AD-A096 450 AERONAUTICAL CONSULTANT ASSOCIATES RANCHO PALOS VERDES CA F/G 16/4
APPLICATION OF THE JOINED WING TO CRUISE MISSILES.(U)
NOV 80 J WOLKOVITCH N00014-79-C-0953
UNCLASSIFIED ONR-CR212-266-1 NL

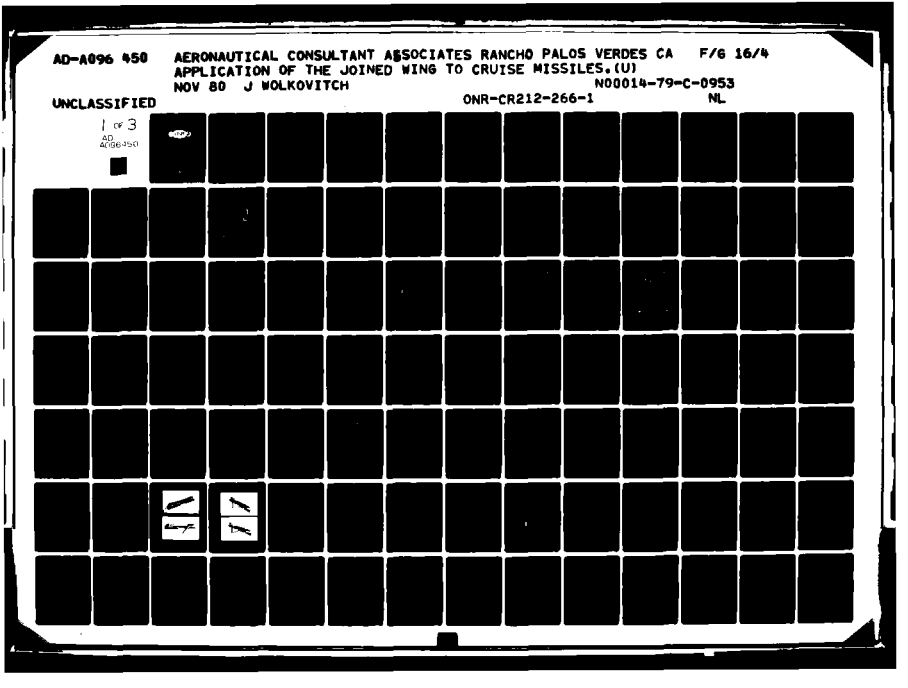

REPORT ONR-CR212-266-1

APPLICATION OF THE JOINED WING TO CRUISE MISSILES

Julian Wolkovitch

Aeronautical Consultant Associates
28603 Trailriders Drive
Rancho Palos Verdes
California 90274

Contract N00014-79-C-0953

November 1980

Final Report for Phase I

Approved for public release; distribution unlimited

Prepared for

Office of Naval Research, 800 N. Quincy St., Arlington, VA 22217

SPECIAL NOTICES

CHANGE OF ADDRESS

Organizations receiving reports on the initial distribution list should confirm correct address. This list is located at the end of the report. Any change of address or distribution should be conveyed to the Office of Naval Research, Code 211, Arlington, VA 22217.

DISPOSITION

When this report is no longer needed, it may be transmitted to other organizations. Do not return it to the originator or the monitoring office.

DISCLAIMER

The findings and conclusions contained in this report are not to be construed as an official Department of Defense or Military Department position unless so designated by other official documents.

REPRODUCTION

UNCLASSIFIED

SECURITY CLASSIFICATION OF THIS PAGE (When Data Entered)

REPORT DOCUMENTATION PAGE	READ INSTRUCTIONS BEFORE COMPLETING FORM
1. REPORT NUMBER: ONR-CR212-266-1	2. GOVT ACCESSION NO.: AD-A096450
	3. RECIPIENT'S CATALOG NUMBER:
4. TITLE (and Subtitle): APPLICATION OF THE JOINED WING TO CRUISE MISSILES	5. TYPE OF REPORT & PERIOD COVERED: Technical Report
	6. PERFORMING ORG. REPORT NUMBER:
7. AUTHOR(s): Julian Wolkovitch	8. CONTRACT OR GRANT NUMBER(s): N00014-79-C-0953
9. PERFORMING ORGANIZATION NAME AND ADDRESS: Aeronautical Consultant Associates, 28603 Trailriders Drive, Rancho Palos Verdes, CA 90274	10. PROGRAM ELEMENT, PROJECT, TASK AREA & WORK UNIT NUMBERS: 62241N, RF41-411
11. CONTROLLING OFFICE NAME AND ADDRESS: Office of Naval Research (Code 210), 800 North Quincy Street, Arlington, VA 22217	12. REPORT DATE: November 1980
	13. NUMBER OF PAGES: 198
14. MONITORING AGENCY NAME & ADDRESS (if different from Controlling Office): F41411	15. SECURITY CLASS. (of this report): Unclassified
	15a. DECLASSIFICATION/DOWNGRADING SCHEDULE:

16. DISTRIBUTION STATEMENT (of this Report)

Approved for public release: distribution unlimited.

17. DISTRIBUTION STATEMENT (of the abstract entered in Block 20, if different from Report)

18. SUPPLEMENTARY NOTES

19. KEY WORDS (Continue on reverse side if necessary and identify by block number)

Cruise Missile, Terrain-Following, Aircraft Design, Joined Wing, Tandem Wing, Optimal Control

20. ABSTRACT (Continue on reverse side if necessary and identify by block number)

The joined wing is a new airplane and missile configuration comprising two wings, a fuselage, and a fin, arranged such that the wings form diamond shapes both in plan view and in front view. Advantages claimed for the joined wing include lightness, stiffness, low induced drag, low wave drag, high trimmed maximum lift coefficient, reduced parasite drag, and good stability and control, plus "built-in" direct lift and sideforce capabilities.

(continued)

DD FORM 1 JAN 73 1473 EDITION OF 1 NOV 65 IS OBSOLETE
S/N 0102-LF-014-6601

UNCLASSIFIED

SECURITY CLASSIFICATION OF THIS PAGE (When Data Entered)

20. ABSTRACT (Concluded)

Comparisons are made of three cruise missile configurations: (1) conventional, (2) joined wing, and (3) joined wing plus canard. The latter configurations yield large advantages in range, maneuverability, and terrain-following. Optimal control theory is employed to calculate the terrain-following accuracy of each configuration.

FOREWORD

The research described in this report was supported by the Office of Naval Research under Contract N00014-79-C-0953, with Dr. Robert E. Whitehead as ONR Contract Technical Monitor.

The author wishes to express his thanks to Mr. George E. Schubert and Lt. Col. Thomas L. Larsen, Ph.D., of the Joint Cruise Missiles Project Office for their valuable guidance and for supplying technical data. Thanks are also due to Mr. W. Martin Waide of Developmental Sciences Inc. for major contributions to solving problems associated with wing folding, and to Dr. Richard F. Whitbeck of Systems Technology Inc. who played a key role in developing the optimal control computer programs presented in this report.

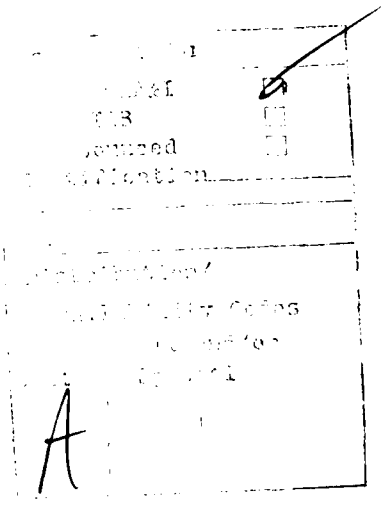

TABLE OF CONTENTS

1.0 BACKGROUND

1.1 OBJECTIVE OF THIS STUDY

The work reported here was performed as Phase I of a study of applications of a new type of wing, known as the joined wing. The particular application studied here is an advanced cruise missile capable of being launched from a standard 21 inch diameter submarine torpedo tube. The present report discusses alternative configurations for joined wing cruise missiles. In Phase II of the study wind tunnel tests will be performed on the most promising of these configurations.

The joined wing concept has previously been described only in patents such as Ref. 1 (other patents are pending), and in reports of limited circulation, e.g., Refs. 2, 3, 4, and 5. Therefore, Section 2 of this report presents a general description of the concept, including aerodynamic and structural aspects. The theoretical and experimental results presented in Section 2 were obtained prior to the present study. Section 2 also summarizes previous work on related configurations.

Section 3 presents some special requirements of cruise missiles and describes how these relate to the joined wing configuration. Section 4 discusses one key aspect of cruise missile design, i.e., the requirement to fly close to the surface of waves or terrain to minimize the probability of being detected by radar. A method of optimizing the missile design for closest terrain-following is described.

Section 5 presents comparisons of cruise performance between a series of conventional advanced cruise missiles and their counterparts employing joined wings. Readers interested in performance rather than guidance and control should read Section 5 before section 4.

Conclusions and recommendations are given in Section 6.

Appendices A, B, and C present detailed material relating to the optimum terrain-following described in Section 4.

2.0 BASIC PRINCIPLES OF THE JOINED WING

2.1 JOINED WING CONFIGURATIONS AND ADVANTAGES

The joined wing is a general concept which involves the combination of two wings, a fuselage, and a fin, such that the wings form a diamond shape both in plan view and in front view. Figure 1 shows a design for a joined wing manned aircraft. Figure 2 illustrates a design for an advanced cruise missile employing a foldable joined wing plus a canard. Many arrangements for joining the wings are possible. Figure 3 shows a design with the joint located inboard of the tips, while Fig. 4 shows that the joint can be a winglet, thus returning some aerodynamic benefit as well as providing the necessary structural tie between the wings.

Advantages claimed for the joined wing include:

- Light weight
- High stiffness
- Low induced drag
- Good transonic area distribution
- High trimmed $C_{L\,max}$
- Reduced wetted area and parasite drag
- Direct lift control capability
- Direct sideforce control capability
- Good stability and control

These claims have been supported by independent analyses, design studies and wind tunnel tests, as described in Sections 2.2. through 2.9.

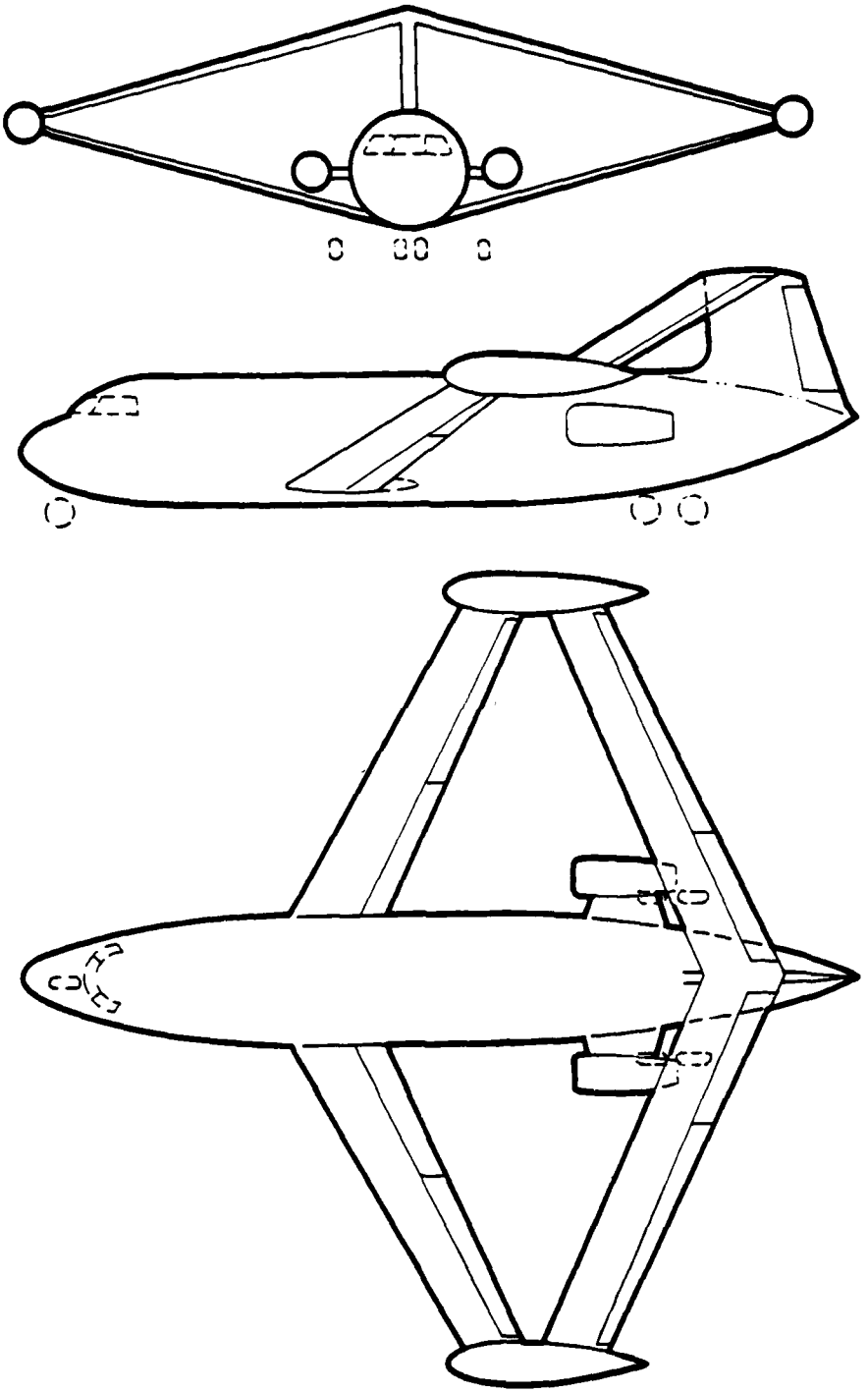

FIGURE 1. JOINED WING AIRPLANE

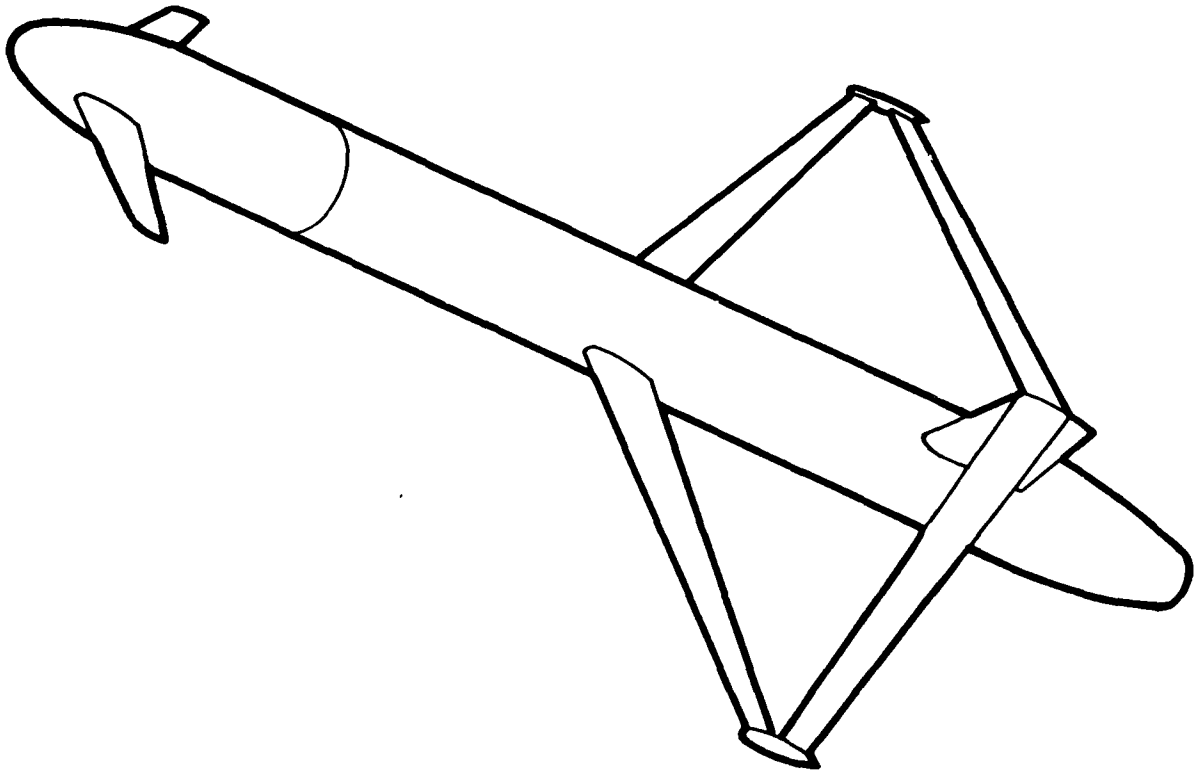

FIGURE 2. ADVANCED CRUISE MISSILE EMPLOYING JOINED WING AND CANARD

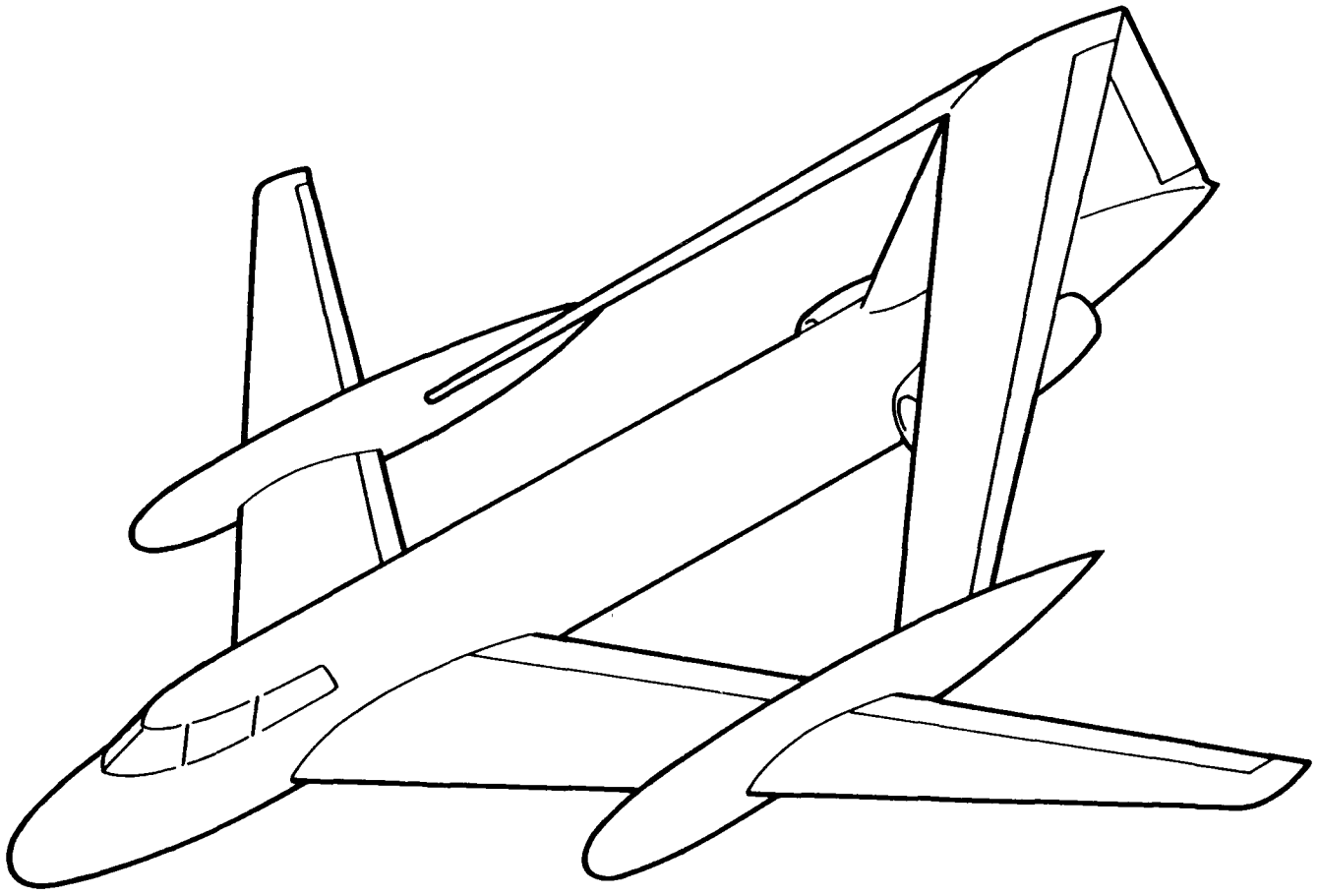

FIGURE 3. INBOARD-JOINT CONFIGURATION

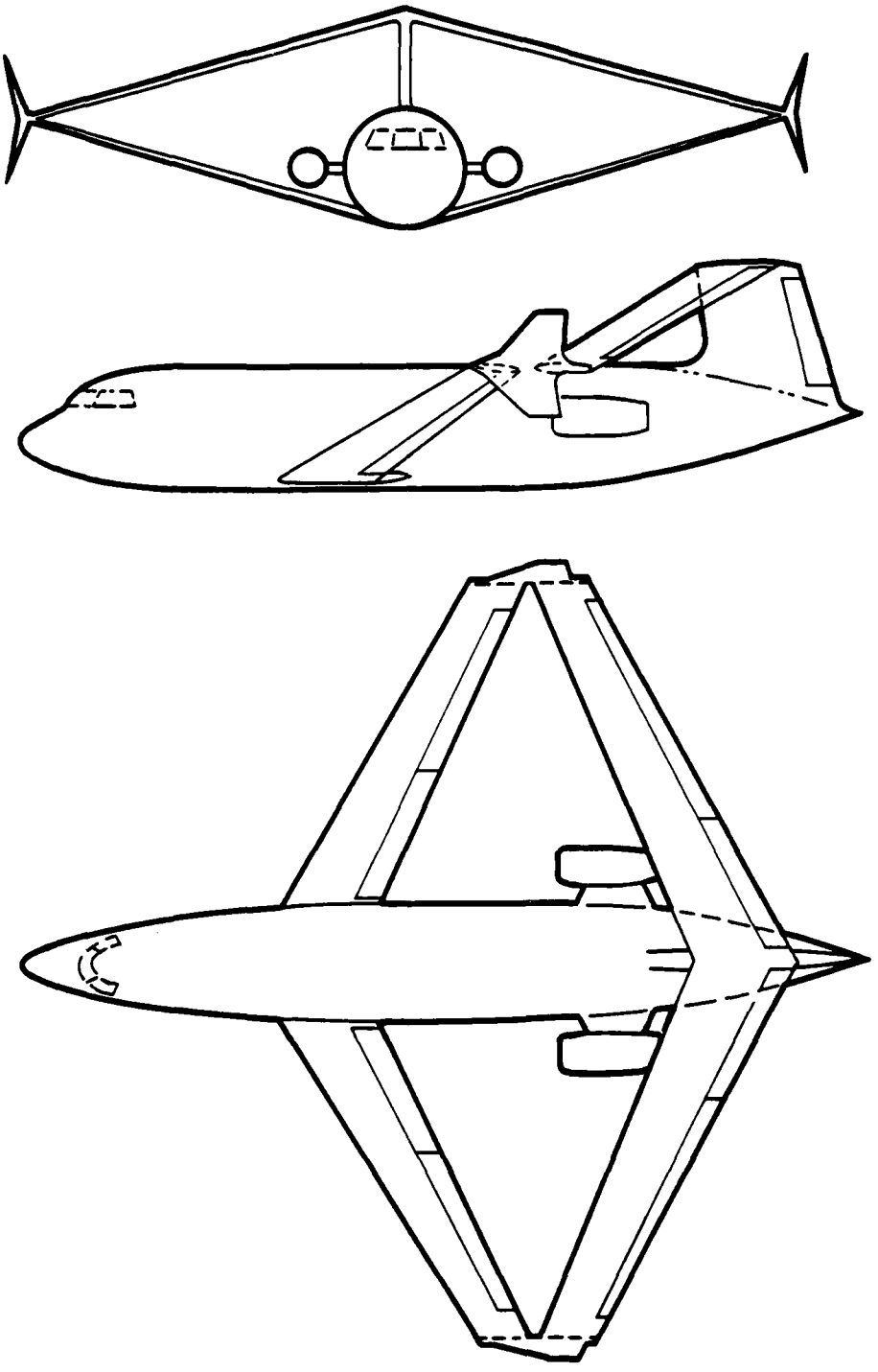

FIGURE 4. JOINED WING AIRPLANE WITH WINGLETS

2.2 STRUCTURAL PRINCIPLES

The internal structure of the joined wing is unconventional, involving chordwise tapering of wing thickness, as shown in Fig. 5. This feature must be clearly understood in order to apply the joined wing concept so that it yields a decisive weight advantage over the conventional wing-plus-tail arrangement. The necessity for chordwise taper of skin thickness is explained below.

Consider Fig. 6. This shows that the lift load acting upon any chordwise section of a joined wing at a distance y from the aircraft's plane of symmetry may be resolved into two components,

(1) An "inplane" component, $\Delta L \sin \theta$, inclined at the local "tilt angle," θ. This component acts within the plane of the truss formed by the joined wings.

(2) An "out-of-plane" component $\Delta L \cos \theta$.

The inplane component is well resisted by the truss structure, but the truss provides no special advantage in resisting the out-of-plane component. Therefore the joined wing structural material must be disposed so that each wing resists out-of-plane loads. This is achieved by concentrating the wing box material at the maximum possible distance from the local plane of the truss (i.e., the plane x-x in Fig. 6). This increases the wing's effective beam depth about its bending axis, as shown in Fig. 7.

The weight advantage resulting from chordwise tapering is considerable. This has been demonstrated by Ref. 3, which compares a conventional airliner aluminum wing-plus-tail with an aluminum joined wing having equal airfoil section and equal parasite and induced drag. Both wings had taper ratios $c_{tip}/c_{root} = 0.3$. Reference 3 employed a finite element structural analysis program to optimize both wing systems for maximum strength/weight. Comparing complete weights (including control surfaces and non-structural components) it was found that the complete

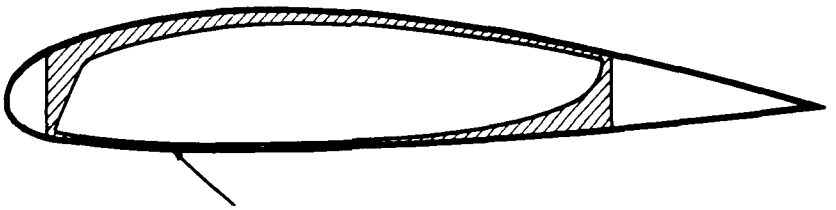

WING BOX EXTENDS FROM 5% TO 75% CHORD

SHADED REGION INDICATES EQUIVALENT SKIN THICKNESS,
ie: AVERAGE OF LOCAL SKINS, STRINGERS AND SPARS.
EQUIVALENT SKIN THICKNESS IS EXAGGERATED FOR
CLARITY, TO EMPHASIZE THE TAPER.

FIGURE 5. CHORDWISE TAPER OF WING SKIN MATERIAL THICKNESS

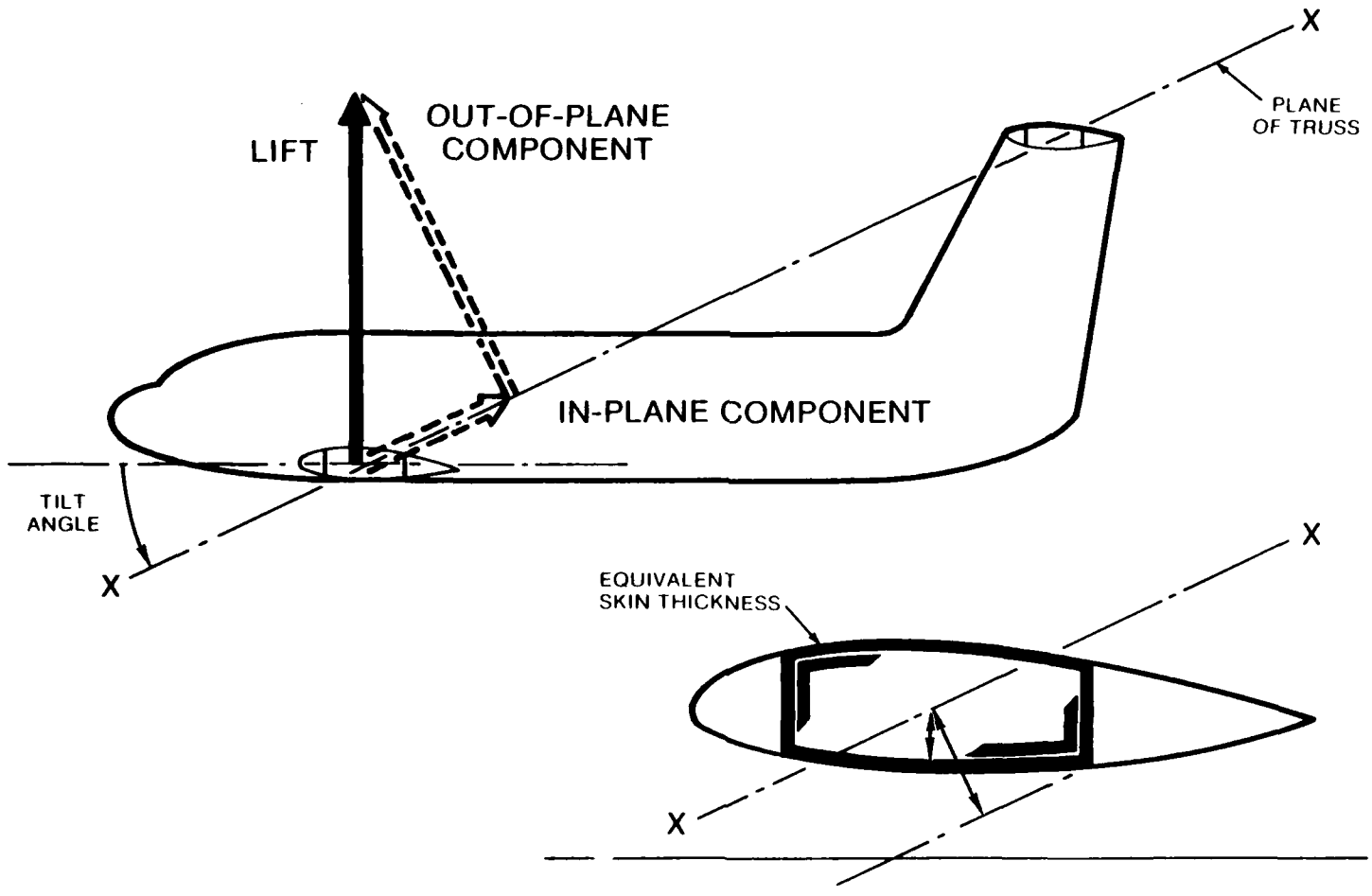

FIGURE 6. IN-PLANE AND OUT-OF-PLANE LIFT COMPONENTS

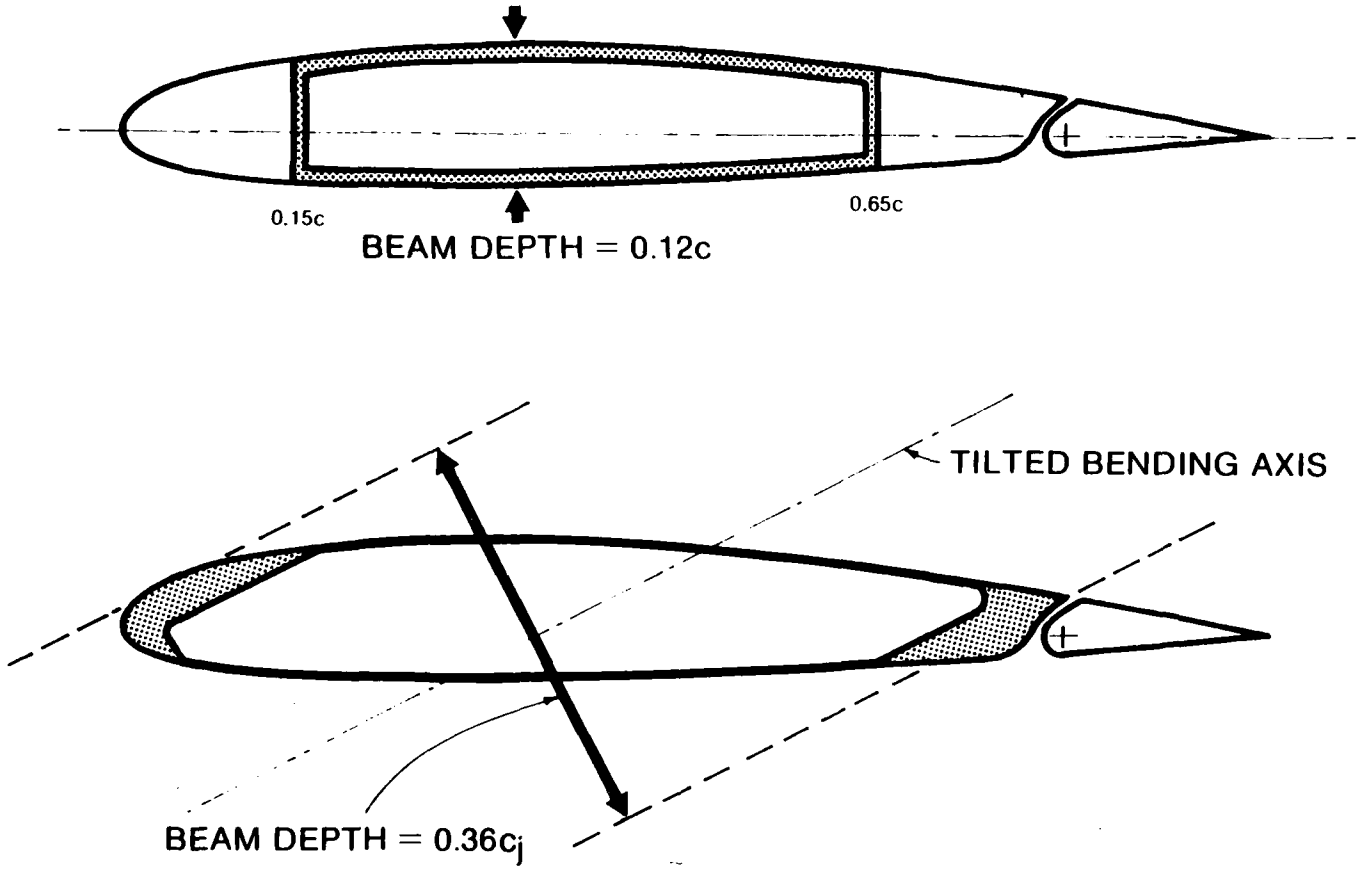

FIGURE 7. LARGE EFFECTIVE BEAM DEPTH/CHORD RATIO OF JOINED WING

joined wing is 24% lighter than the complete conventional wing-plus-tail. It is also much stiffer; as indicated in Fig. 8, the tip deflection of the conventional wing is 2.8 times that of the joined wing.

Reference 3 did not attempt to optimize the taper ratio selected for the joined wing. Further improvements are possible if the taper of the joined wing is decreased to allow for the loads transmitted through the inter-wing joint. (In general, some taper should be retained, unless the cost of manufacture dictates otherwise.)

Because the effective beam depth is primarily determined by the chord of each of the joined wings and their tilt angle, θ, it is possible to employ very thin airfoils. Figure 9 shows a 3% thickness/chord ratio airfoil which has an effective beam depth of 32% of its chord. Thus low drag airfoils can be employed for supersonic flight without the structural weight penalties of thin cantilever wings.

A secondary benefit of the chordwise variation of skin thickness shown in Figs. 7 and 9 is that it thickens the skin (a) near the upper leading edge, where airloads are high and where a good aerodynamic surface contour must be maintained, and (b) around the flap attachment region, where high local loads due to flap airloads occur.

For minimum wing weight a high tilt angle (θ) must be maintained over most of the span. This implies that a tall fin and relatively short fuselage is a desirable combination.

The material distribution shown in Figs. 7 and 9 is not optimum close to the wing centerline and near the inter-wing joint. This is because torsional and other secondary structural loadings become dominant in these regions. Nevertheless, the basic principles described above have been shown (Refs. 3 and 5) to yield joined wing structures which are optimum over most of their spans.

Buckling: Due to the inplane load components the rear wing is in compression during flight at positive "g" load factors. Overall column

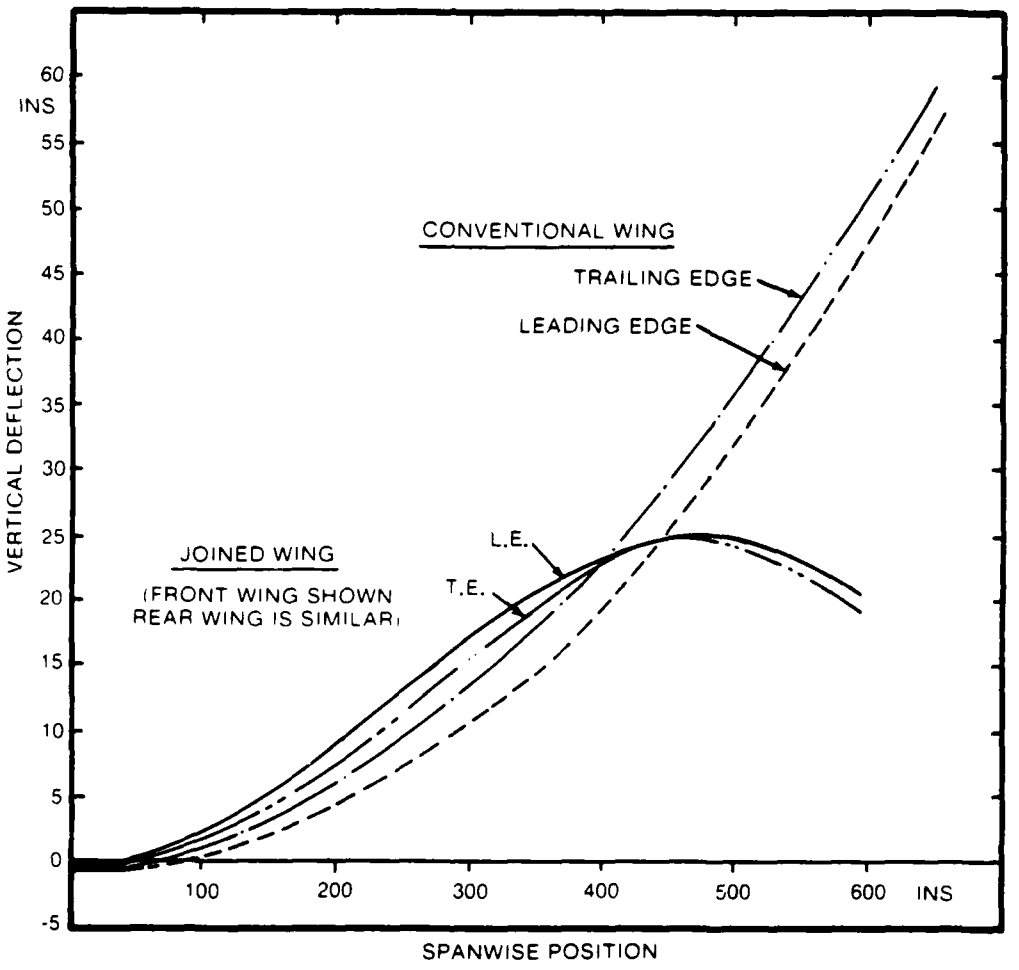

FIGURE 8. DEFLECTIONS OF JOINED AND CONVENTIONAL WINGS HAVING EQUAL TOTAL VERTICAL AIRLOADS AND EQUAL L/D'S, WITH JOINED WING WEIGHT = 0.76 × CONVENTIONAL WING-PLUS-TAIL WEIGHT

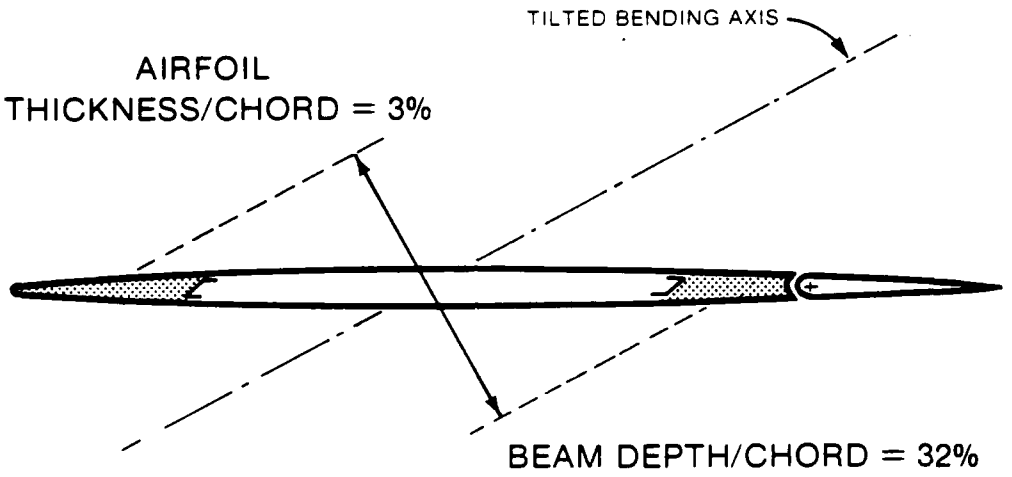

JOINED WING PROVIDES EFFECTIVE BEAM
DEPTH EVEN FOR VERY THIN AIRFOILS

FIGURE 9. CONSTRUCTION OF JOINED WING EMPLOYING THIN AIRFOILS

buckling is therefore theoretically possible. However, this has not proved to be a problem on any configuration studied to date. If buckling should become significant (e.g., for an ultra-high-aspect-ratio vehicle) it could be alleviated by moving the joint inboard, as in Fig. 3.

Torsion: Torsion of the front joined wing is resisted by its own torsional stiffness, and also by flexural stiffness of the rear wing, as shown in Fig. 10. The net result is that the joined wing pair is extremely stiff torsionally and flexurally.

Wing Box Chord: A conventional cantilever box spar structure extending from 15% to 65% chord is definitely not optimum for the joined wing. The box should extend from the leading edge (or as close to it as the de-icing system will permit) to just ahead of the leading edge of the flaps and ailerons.

Fuselage Structure Weight: The joined wing is a special form of the tandem wing. DeYoung (Ref. 6) and Bottomley (Ref. 7) compare fuselage weights of tandem versus conventional configurations. Both these references conclude that for a given total lift, and with a fixed fuselage length, the tandem configuration's fuselage skin is lighter. This is because, as illustrated in Fig. 11, the two uploads of the tandem wings impose less severe bending moments than do opposing wing and tail loads. Figure 11 illustrates the resulting saving in the weight of fuselage structural material.

Since minimum fuselage skin gauge is determined by additional factors such as pressure loads and landing loads, only part of the weight saving shown in Fig. 11 is achieved. However DeYoung (Ref. 6) shows that substantial weight reductions can be achieved despite this limitation. Compared to the tandem wing, the joined wing structure has the further advantage of relieving fuselage torsional and lateral bending moments.

It is desirable that the fuselage should be short, for minimum weight. As shown in Section 2.7 this is compatible with the aerodynamic

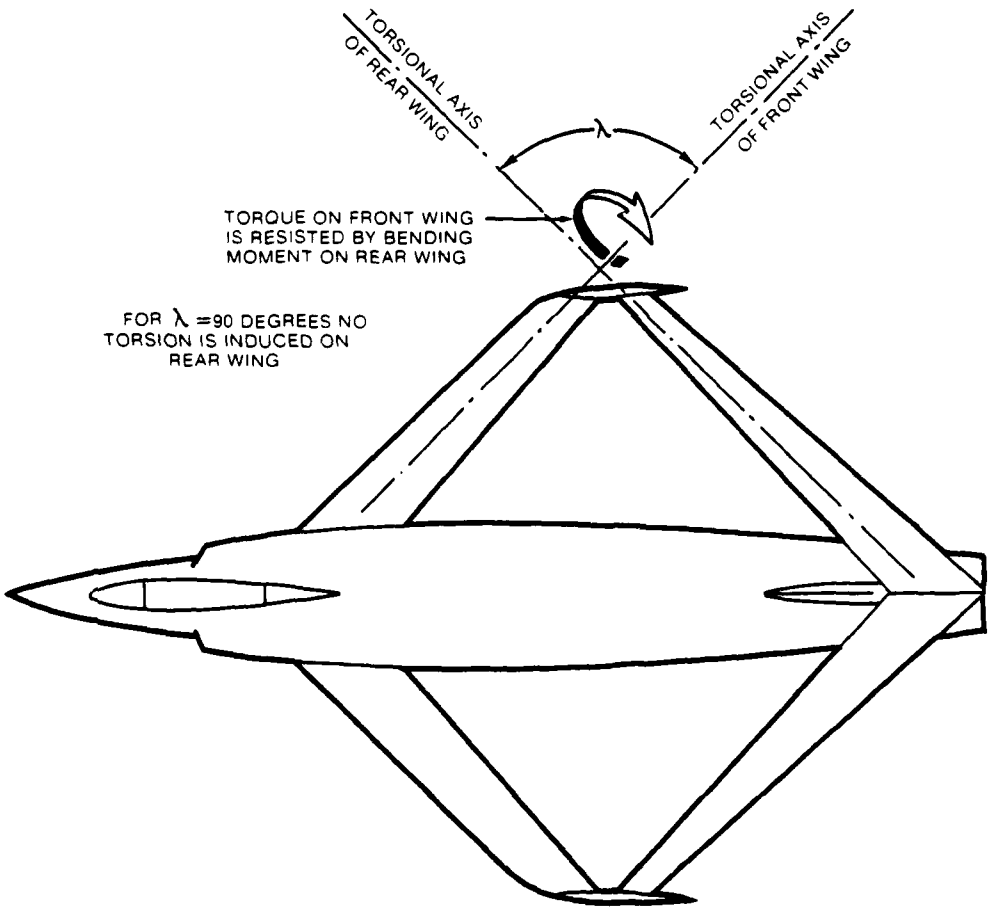

FIGURE 10. BENEFICIAL TORSIONAL/FLEXURAL INTERACTION OF JOINED WINGS

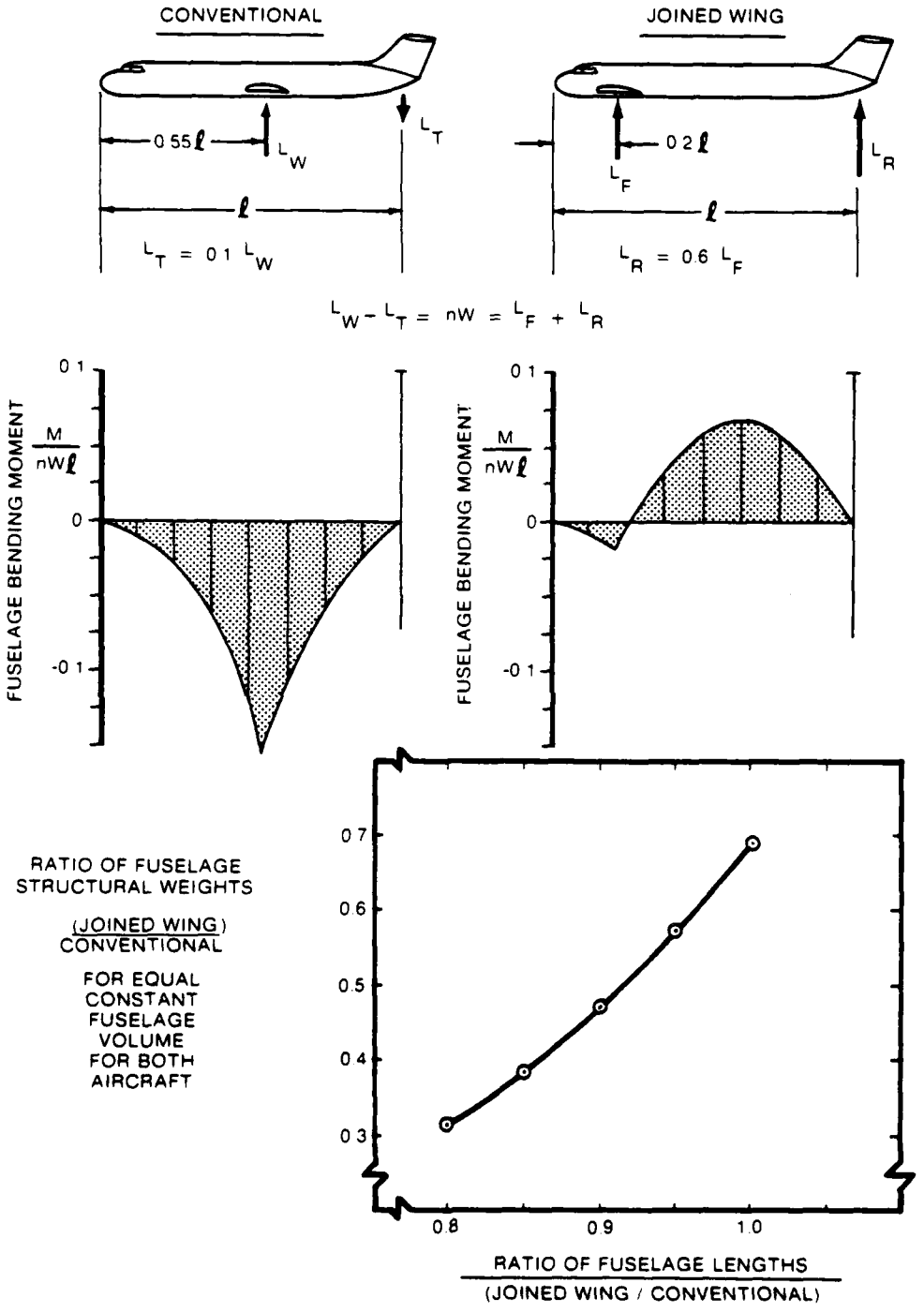

FIGURE 11. REDUCTION IN FUSELAGE WEIGHT THROUGH REDUCED BENDING MOMENTS AND SHORTER FUSELAGE

requirements of joined wing aircraft, primarily because such aircraft do not require a long fuselage to provide a large tail moment arm.

2.3 INDUCED DRAG OF JOINED WINGS

The joined wing yields substantially less induced drag than a conventional monoplane wing of equal lift and span operating at the same dynamic pressure. This has been demonstrated by Prandtl-Munk biplane theory and supporting wind tunnel tests as described below.

For an isolated monoplane wing induced drag is generally expressed in coefficient form as:

$$C_{D_i} = \frac{C_L^2}{\pi e A} \tag{1}$$

or equivalently, in dimensional form as:

$$D_i = \frac{L^2}{\pi q b^2 e} \tag{2}$$

where L = lift; q = dynamic pressure, $(1/2)\rho V^2$; b = span; and the coefficients C_{D_i}, C_L and aspect ratio ($= b^2/S$) are all referred to a common area S. The span-efficiency factor e has an upper limit of 1 for an isolated undihedralled monoplane wing, but as shown by Prandtl and Munk (see, e.g., Ref. 8), for biplane type configurations substantially higher values of e are obtainable.

Equations 1 and 2 are valid for monoplane wings which do not have spanwise variations of incidence or camber (i.e., "untwisted" wings). However, for twisted wings, Ref. 9 shows that an alternative form of induced drag equation, Eq. 3, is more accurate.

$$C_{D_i}{}_{\text{twisted monoplane wing}} = \frac{(C_L - C_{L_x})^2}{\pi A e_x} + (C_{D_i})_{min} \tag{3}$$

where C_{L_x} and e_x are constants. Note that Eq. 3 yields an offset drag polar even though no viscous drag is included. (Offset drag polars also occur for cambered airfoils tested in two-dimensional conditions, but that offset is due to viscous effects and is additional to the inviscid induced drag effects discussed in this section.)

Equation 3 is generally more accurate than Eq. 1. However Prandtl-Munk biplane theory has been developed on the assumption that the induced drag of each wing of a biplane pair can be described by Eq. 1, when that wing is isolated. Therefore, to facilitate reference to the theory, we shall employ Eq. 1 for most of this discussion, explaining at the end how twist and camber corrections can be included.

Prandtl-Munk Biplane Theory: Since the fundamentals of biplane induced drag are well presented in Refs. 8, 10, and 11, only a brief summary will be given here to set the stage for a specialization of the theory for the joined wing.

The induced drag of biplane wings having optimal span loadings is:

$$D_i = \frac{1}{\frac{\pi}{2}\rho V^2}\left[\frac{L_1^2}{b_1^2} + 2\sigma\frac{L_1 L_2}{b_1 b_2} + \frac{L_2^2}{b_2^2}\right] \tag{4}$$

where L_1, L_2 are the lifts on wings of respective spans b_1 and b_2, ρ = air density, V = speed, and σ is a constant, determined by the Trefftz-plane configuration, i.e., the front view of the wings as seen by an observer looking parallel to free-stream direction. Tables of σ for biplane wings are given by Laitone in Ref. 12, which corrects errors in similar tables given in Ref. 10.

For wings of equal spans $b_1 = b_2 = b$ with wing No. 1 carrying a fraction f_1 of the total lift, W;

$$D_i = \frac{(W)^2}{\frac{\pi}{2}\rho V^2 b^2}\left[f_1^2 + 2\sigma f_1(1-f_1) + (1-f_1)^2\right] \tag{5}$$

This expression is minimized by putting $f_1 = 0.5$. However, the minimum is much flatter than the corresponding minimum for a wing-plus-tail combination, as illustrated in Fig. 12. The excess drag above the minimum is trim drag. Hence, trim drag is relatively less important for an equal span staggered biplane (i.e., a tandem wing or joined wing airplane) than for a staggered biplane of very unequal spans (i.e., a conventional aft tail airplane). For preliminary design purposes it will often suffice to neglect trim drag for joined wing aircraft.

Munk's stagger theorem (Refs. 8 and 12) states that the induced drag of a biplane pair of wings carrying lifts L_1 and L_2 maintaining a constant Trefftz-plane configuration is unaffected by displacements of the surfaces parallel to the freestream. The theorem implies that sweep need not affect induced drag, provided span is constant. Munk's stagger theorem has been verified by Lockheed boxplane tests (Ref. 13) and also by Vought tandem wing tests (Ref. 14) both of which are discussed in Section 2.9. Hoerner (Ref. 15, page 7-8) presents some data which appear to contradict the stagger theorem, showing that sweep influences induced drag. However, Hoerner states that "swept wings (or certain other wing shapes) can have the same induced drag as straight wings of the same aspect ratio — provided the lift distribution is the same." To accomplish this, proper twist and camber are required, as was incorporated in the swept tandem wing wind tunnel model described in Ref. 16. The induced drag of this model was found to be in excellent agreement with the minimum achievable induced drag predicted by theory.

Letcher (Ref. 17) has calculated the minimum achievable induced drag of joined wings having optimum twist and camber, and also optimum relative load-sharing factor, f_1. Kuhlman (Ref. 18), by an independent method, verified Letcher's results and extended them to include joined wings with winglets as shown in Fig. 13. Figure 13 indicates that a joined wing fitted with winglets can achieve high values of e. For example, with $d/h = 0.5$ and $h/b = 0.321$ (corresponding to $\pm 20^{\circ}$ dihedral) $e = 1.328$.

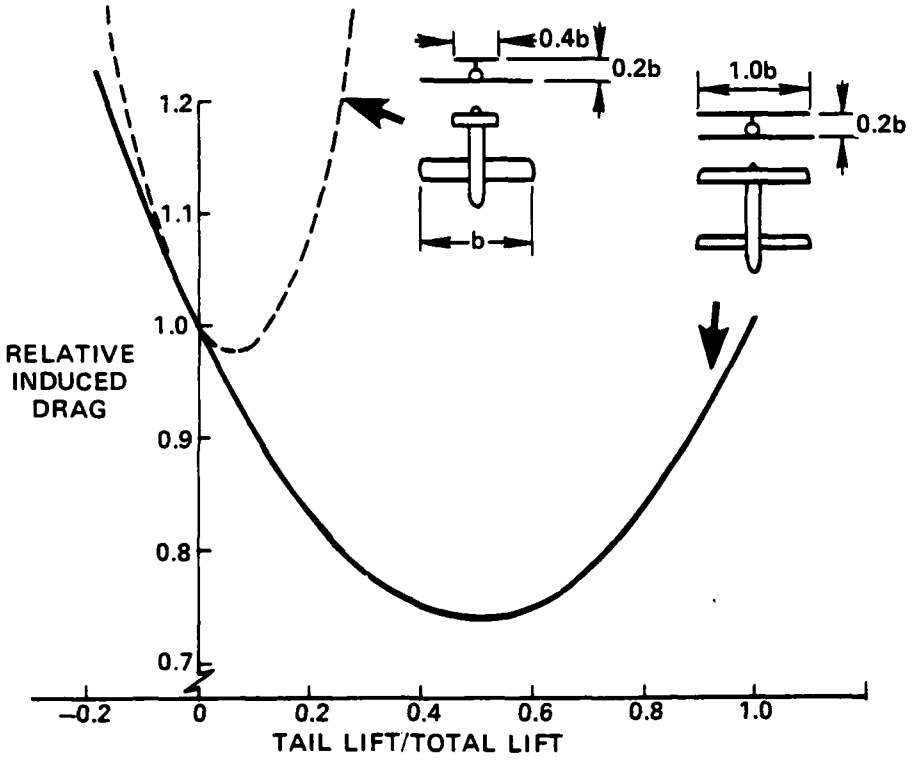

FIGURE 12. INDUCED DRAG OF CONVENTIONAL AND MULTI-WING CONFIGURATIONS WITH OPTIMAL SPAN-LOADINGS

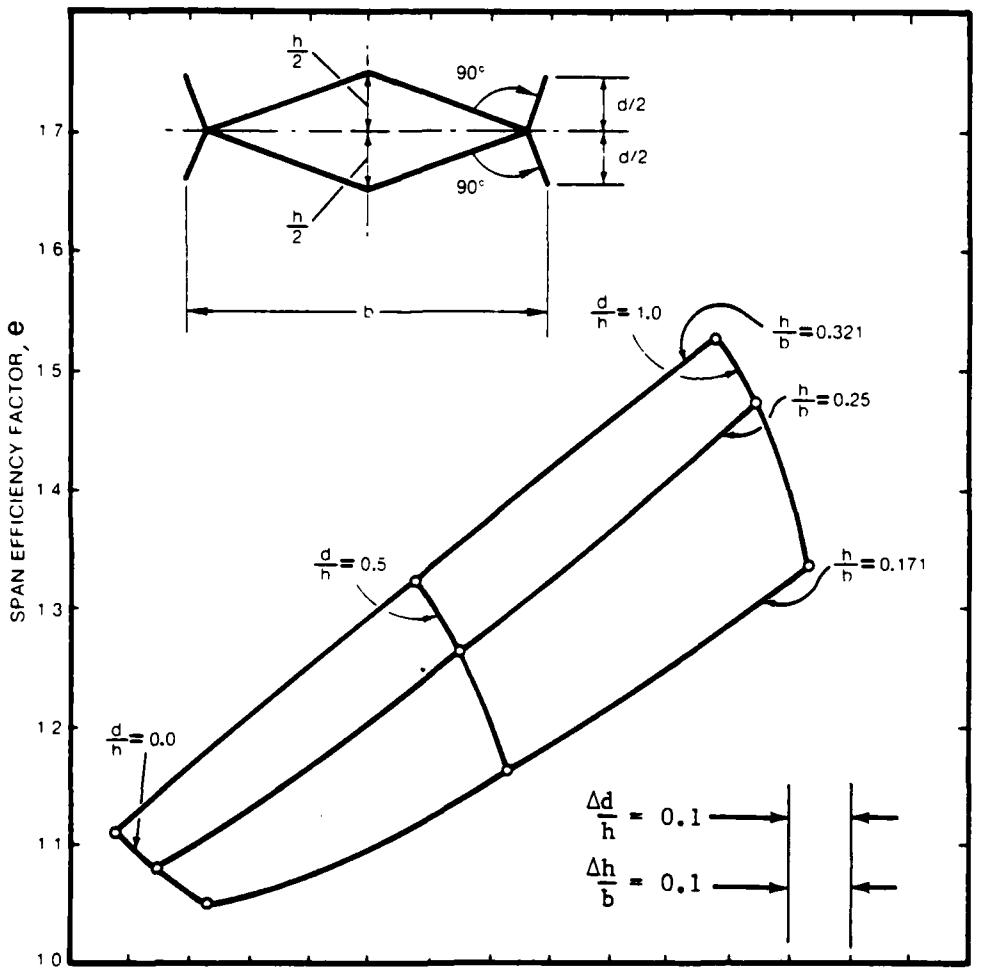

FIGURE 13. CALCULATED SPAN-EFFICIENCY FACTOR FOR JOINED WING WITH SYMMETRIC INCLINED WINGLETS ("CARPET" PLOT)

Corrections to Prandtl-Munk Theory: Even for untwisted wings, two corrections must be applied to values of e calculated by the Prandtl-Munk biplane theory, such as those given in Fig. 13:

(1) A correction for the downward drift of the vortex sheet shed by the front wing (the theory does not allow for this drift).

(2) A correction for wing-body interference and for loss of leading edge suction.

The first correction is significant for configurations having staggered wings of large (vertical) gap. Tandem wing test data analysed in Ref. 14 indicate that the e given by Fig. 13 should be increased by 10% to 14% for typical joined wing configurations, in which the rear wing root is higher than the front wing root.

The second correction is standard for conventional configurations. Typically e is reduced by 10% to 20% at low and moderate C_L's. For the joined wing the second correction should be less than for a conventional configuration since most of the induced drag (typically 2/3 of the total) is developed on the rear wing, which is not intersected by the fuselage. At high C_L's there is an appreciable loss of leading edge suction, and the second correction becomes larger. However, at C_L's within the normal cruise range for most joined wing configurations Corrections (1) and (2) approximately cancel, so Fig. 13 can be employed directly to compute C_{D_i}.

Twisted Wings: As will be explained later, properly designed joined wings have spanwise variations of incidence and camber. Therefore to compute the drag polar accurately over a range of C_L the parameters e_x, C_{L_x}, must be known. These parameters can be found via vortex-lattice methods (e.g., Refs. 19, 20) by computing C_{D_i} for a range of C_L and graphing the results. Often C_{D_i} is required only over a small range of C_L. If the wing is twisted and cambered to yield minimum C_{D_i} at some specified design C_L then in the region of the design C_L it should be sufficiently accurate to compute C_{D_i} from Eq. 1 with e given by Fig. 13, plus the corrections described above.

Experimental Validation: The predictions of the Prandtl-Munk theory relating to induced drag of multi-wing configurations have been compared with wind tunnel test data in Refs. 13, 14, and 16 and have been shown to be in good agreement.

2.4 PARASITE DRAG

Compared to the conventional aircraft the joined wing displays some advantages and some disadvantages with respect to parasite drag.

Adverse effects include:

(1) Lower wing Reynolds numbers.

(2) Increased ratio of wetted area to lifting area due to dihedral cosine effect.

Beneficial effects include:

(1) Reduced wing area due to high trimmed $C_{L\,max}$ (see Section 2.6).

(2) Reduced fuselage wetted area due to reduced length.

(3) Improved wing-fuselage interference.

(4) Smoother fairing of landing gear.

(5) Fin-nacelle integration.

Wing Reynolds Numbers: Comparing a conventional configuration having wing area S_W and tail area S_T with a joined wing configuration of the same total horizontal projected area and the same span yields Reynolds numbers in the ratio $0.5[1 + (S_T/S_W)]$. Typically this yields joined wing Reynolds numbers which are 60% to 65% those of the wing of the conventional airplane. This effect is adverse to the joined wing. A possible benefit would arise if laminar flow control is considered, since it is easier to establish laminar flow at low Reynolds number.

Dihedral Cosine Effect: Considerations of structure weight and induced drag favor the use of steep dihedral angles for joined wings. Such dihedral angles increase wing-plus-tail wetted area by typically 3.5% compared to a conventional configuration.

To overcome these adverse effects joined wing configurations must be designed to take full advantage of the benficial effects discussed below.

High Trimmed $C_{L\,max}$: This is discussed at length in Section 2.6. The aerodynamic design principles given in Section 2.6 permit substantial reductions in joined wing wetted area compared to wetted area of a conventional wing-plus-tail of similar lift capability.

Reduced Fuselage Length: The joined wing airplane can obtain adequate static stability without a long tail moment arm, as shown in Section 2.7. Hence a short fuselage of lower-than-usual fineness ratio (FR) can be employed. Such a fuselage may be advantageous. Figure 14 illustrates this by comparing the drag of fuselages having untapered midsections. At subcritical Mach numbers, for equal volumes, the drag of the FR = 6 fuselage is only 91% of that of the FR = 9.7 fuselage. With proper nose and tail shaping the short fuselage can avoid a significant decrease in drag divergence Mach number.

If fuselage maximum cross-sectional area is fixed (instead of fuselage volume) the drag benefits of a short fuselage are even more striking. The FR = 6 fuselage then has only 67% of the drag of the FR = 9.7 fuselage.

Improved Wing-Fuselage Interference: Attaching the front wing to the fuselage ahead of the maximum fuselage cross-section, as shown in Fig. 15, places the wing root in a favorable pressure gradient. This reduces the boundary layer thickness at the wing-fuselage junction and increases wing root local $C_{L\,max}$.

Smoother Landing Gear Fairing: As explained in Section 2.8, the mainwheels of a joined wing airplane can be located well aft of the c.g.

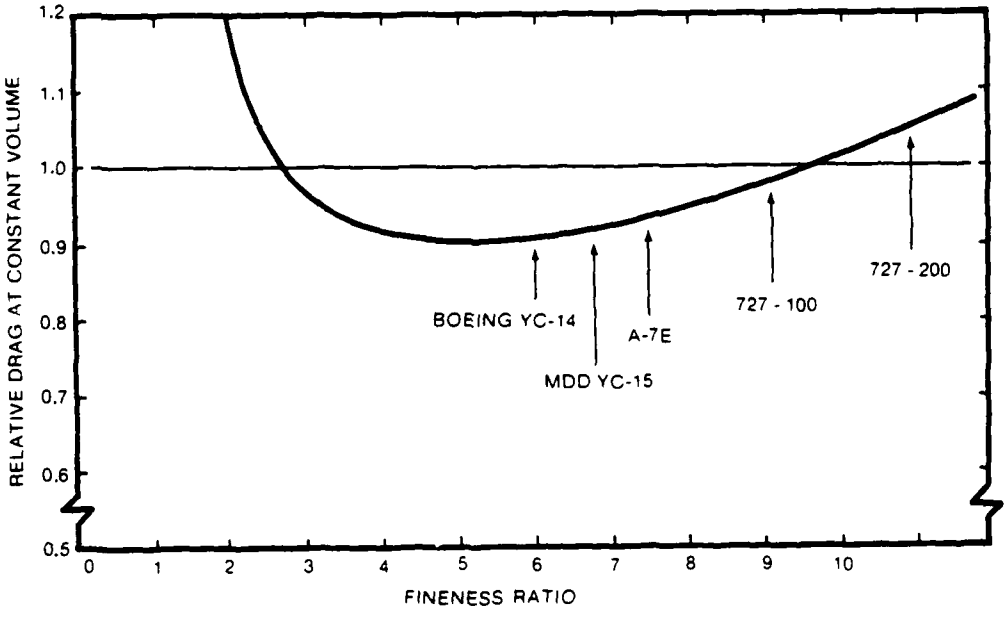

BASED ON DATA FROM REF 15

FINENESS RATIO = LENGTH $/\sqrt{\frac{4}{\pi} \times \text{MAX CROSS-SECTIONAL AREA}}$

FIGURE 14. DRAG OF ISOLATED FUSELAGE AS A FUNCTION OF FINENESS RATIO

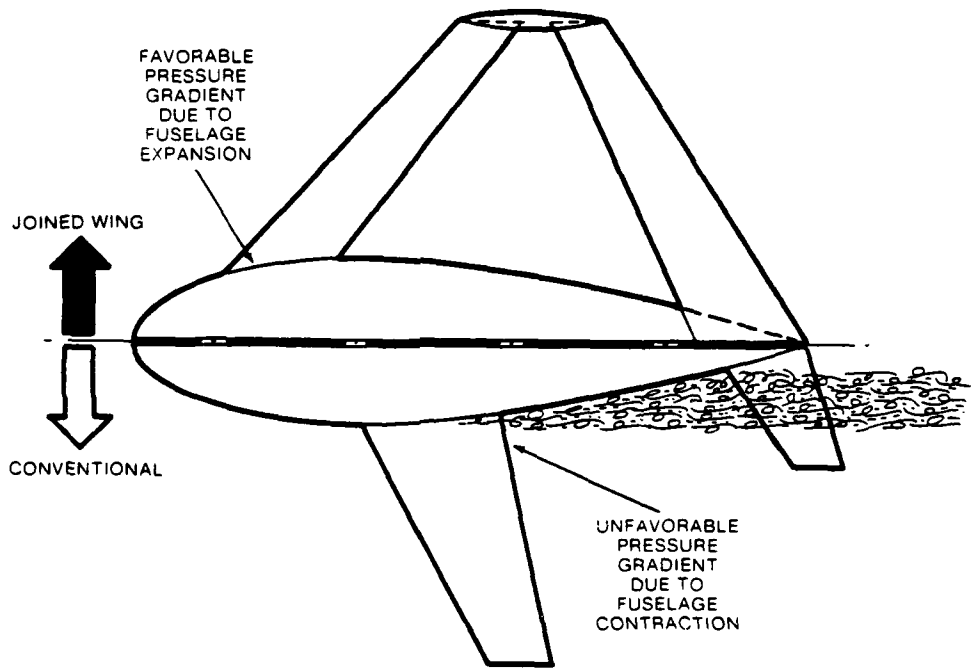

FIGURE 15. WING-FUSELAGE INTERFERENCE COMPARISON

Indeed the main wheels can be retraced into the tail cone, thus avoiding the unsightly and drag-producing "landing gear bump" that characterizes many current transports.

Fin-Nacelle Integration: If properly designed, integration of engine nacelles with the fin can save wetted area, by elimination of pylons and masking of fin area. Fin-nacelle integration is well suited for joined wing aircraft because the fin is not a cantilever structure. Thus more than one engine can be integrated with the fin.

2.5 WAVE DRAG

For transonic and supersonic flight special emphasis should be given to those aspects of the joined wing which yield low wave drag. Appropriate guidelines for design are as follows.

Wave Drag at Zero Lift: As indicated by Fig. 16 the joined wing airplane has an exceptionally *smooth area distribution* around M = 1.0. It is therefore predicted to have a lower transonic drag rise than a conventional configuration. Test data supporting this prediction are analyzed in Ref. 2, p. 13. The data were obtained from transonic tests on a boxplane configuration (Ref. 13) described in Section 2.9.

A most important feature of the joined wing is its compatibility with very thin airfoils (see Fig. 9). As shown in Ref. 15 (Sec. 17, p. 12) and Ref. 21, p. 277, airfoil transonic wave drag coefficient is approximately proportional to $(\text{thickness/chord})^2$, so dramatic drag reductions can be achieved by exploiting this aspect of the joined wing.

Wave Drag Due to Lift: As explained in Ref. 22, wave drag due to lift is minimized by distributing the lifting surfaces over a large fraction of the total airframe length. This design objective is readily achieved using the joined wing.

Wing Interference Drag: The configurations of Figs. 1, 2, 3, and 4 all employ a wing joint arrangement with considerable stagger, so that

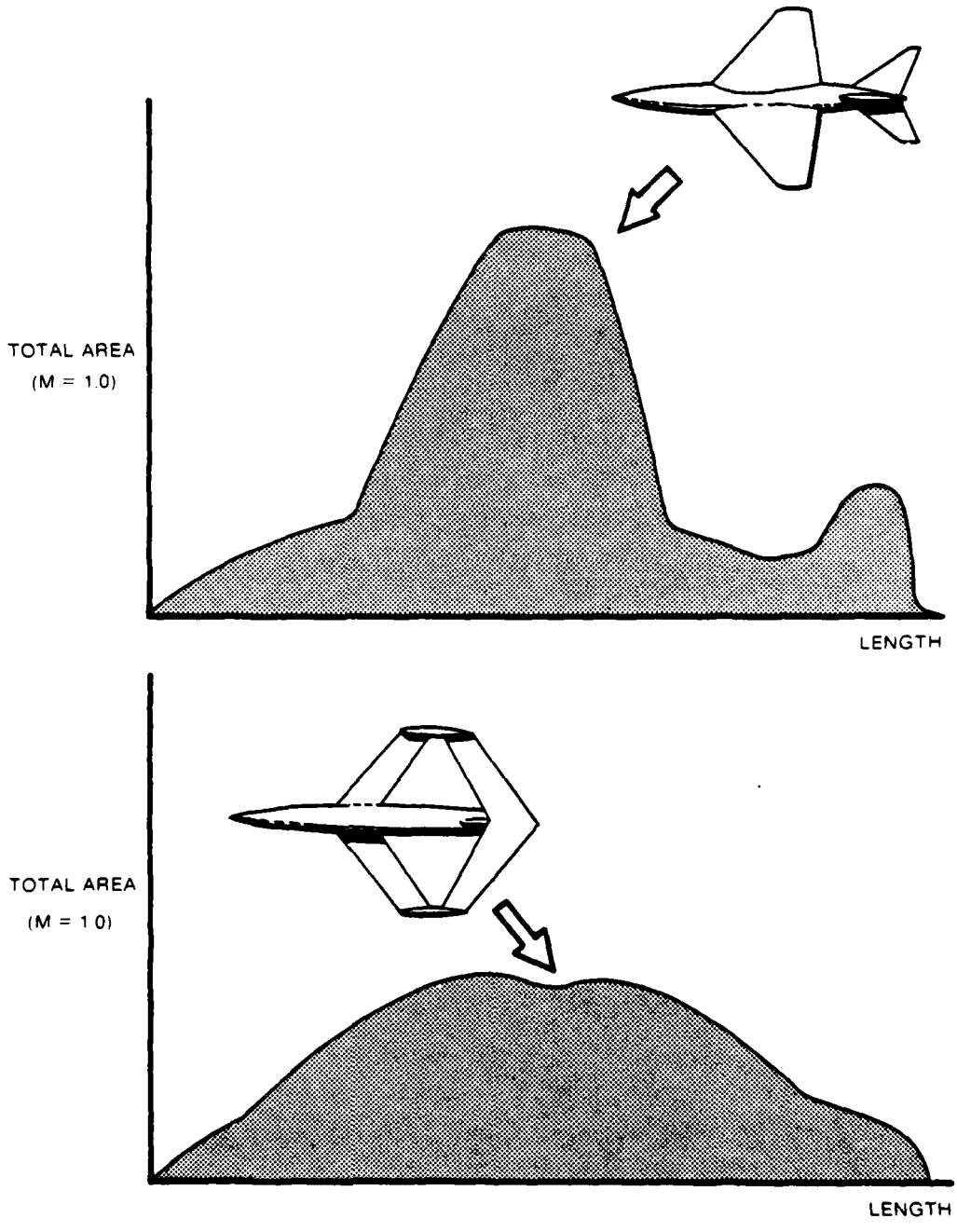

FIGURE 16. COMPARATIVE CROSS-SECTIONAL AREA DISTRIBUTIONS

the wings do not overlap in plan view. This stagger is important: at supercritical speeds it eliminates the possibility of shock waves from one wing impinging on the other, with a consequent shock-induced separation and increase of drag. Staggering the wings at the joint is also desirable at subcritical conditions to avoid the increase of boundary layer thickness that otherwise would occur at the junction of two airfoils.

Figures 1, 2, 3, and 4 show only a few of many possible wing joint arrangements. Others, including "wraparound" continuous curved tips, and "slat" type arrangements are discussed in Ref. 2.

2.6 DESIGN FOR HIGH LIFT

Certain guidelines must be followed to enable the joined wing to obtain high lift without excessive wing area. These guidelines include considerations of trim, as well as flow separation. This subsection first explains the requirements for obtaining high trimmed lift by selecting appropriate overall airframe geometry. Airfoil and flap design considerations are discussed subsequently.

Trim Equations and Their Consequences for Airframe Geometry: Figure 17 shows the lift forces L_F, L_R, acting at the aerodynamic centers of a joined wing pair. When each wing (individually) is producing zero net lift it produces a pitching couple M_O, as indicated. For 1 g steady flight the lift and moment equations about the c.g. become (with notation as in Fig. 17)

$$L_F \ell_F + M_{O_F} + M_{O_R} = L_R \ell_R \tag{6}$$

$$L_F + L_R = W \tag{7}$$

It will be found for almost all statically stable joined wing configurations that when the front wing attains its $C_{L\,max}$ the rear wing lift

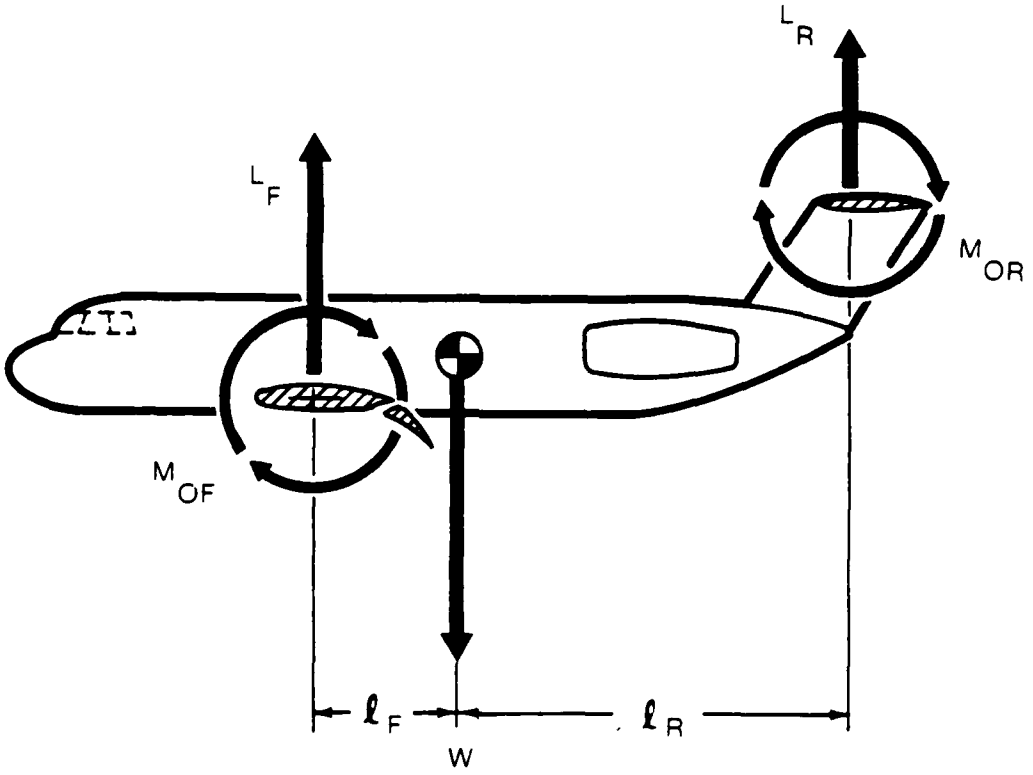

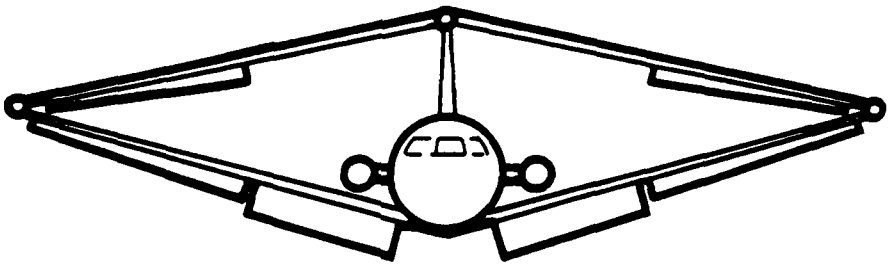

FIGURE 17. TRIMMING FOR MAXIMUM LIFT COEFFICIENT

required to maintain trim is less than the rear wing could generate were trim not required. In other words: "The front wing stalls first." This provides good stall recovery but nevertheless it is undesirable for the front wing to stall while the rear wing is still far from stalling. If this occurs it implies that the rear wing area is oversized from the viewpoint of generating the total maximum lift required to meet the requirements of 1 g and maneuvering flight. One would prefer the front wing to stall when the rear wing is almost at its $C_{L\,max}$. To achieve this, certain principles must be followed in designing the overall airframe geometry, especially the planform. These principles can be derived by manipulating Eqs. 6 and 7 as follows.

From Eq. 6,

$$L_R = L_F \frac{\ell_F}{\ell_R} + \frac{M_{OF} + M_{OR}}{\ell_R} \tag{7}$$

whence:

$$\frac{C_{L_R}}{C_{L_F}} = \frac{S_F}{S_R} \cdot \frac{\ell_F}{\ell_R} + \frac{(M_{OF} + M_{OR})}{C_{L_F} \cdot S_R \ell_R} \tag{8}$$

The first term in the right side of Eq. 8 is always less than unity for a statically stable aircraft. Even for identical front and rear wing areas and equal (positive and negative) sweep angles $\ell_F/\ell_R < 1$, because the overall vehicle aerodynamic center is nearer to the a.c. of the (isolated) front wing than the a.c. of the (isolated) rear wing. This is because the $C_{L\alpha}$ of the rear wing is $(1 - d\varepsilon/d\alpha)$ times its isolated $C_{L\alpha}$. The following principles should be followed to obtain the highest possible value of the first term in Eq. 8.

(1) Decrease the ratio: (frontwing $C_{L\alpha}$)/(rearwing $C_{L\alpha}$) by employing less sweep on the rear wing.

(2) Select front and rear wing airfoils such that the airfoil with the highest two-dimensional $C_{L\alpha}$ is on the rear wing.

(3) Increase the ratio of rear wing/front wing chord to move the a.c. aft.

(4) Reduce the effective $d\varepsilon/d\alpha$ at the rear wing by using a large centerline gap (i.e., make the fin tall). It is also beneficial to employ winglets, since these reduce the average $d\varepsilon/d\alpha$ at the rear wing.

(5) Take advantage of the large pitch damping of the joined wing configuration to move the c.g. aft without sacrificing maneuver margin. (Generally maneuver margin is the key stability parameter, not static margin.) If control configured vehicle (CCV) technology is allowable, it should certainly be employed, so that the maneuver margin can be made negative. This increases trimmed $C_{L\,max}$.

Turning now to the second term in Eq. 8, the key consideration is to make the M_0 terms large and positive. This leads to the following guidelines:

(1) Do not employ equal flap deflections across the span of each wing. Instead employ maximum flap deflections on the inboard section of the front wing and near the outboard section of the rear wing, as shown in the lower half of Fig. 17.

(2) Leading edge devices near the root of the front wing are beneficial.

(3) A low aspect ratio canard can provide appreciable nose-up moment with little forward a.c. shift. (This is discussed in more detail in Section 2.7.)

(4) Where practicable, the fuselage should be shaped (i.e., cambered) and the wing incidence selected to provide positive C_{M_0}.

The foregoing recommendations have emphasized overall airframe geometry rather than local aerodynamic design (e.g., of airfoils and flaps). It is however particularly important that the front wing root airfoil should be selected to give a high local $C_{L\,max}$, as discussed below.

Airfoil Design for High Lift. Figure 18 (reproduced from Ref. 23, p. 16-4) shows how the outward flow in the boundary layer of a swept-back wing increases $C_{L\,max}$ near the wing root. This effect is doubly beneficial for the joined wing because:

(1) It increases $C_{L\,max}$ directly on the front wing.

(2) It provides a nose-up moment which allows the rear wing to be trimmed at a higher C_L.

It is desirable to design joined wings such that this effect is maximized. As shown by experimental data graphed in page 3 of Sec. 16 of Ref. 23 and by Fig. 19, the magnitude of this effect is correlated with the sharpness of the wing leading edge. A sharp-nosed airfoil is beneficial, yielding a 22% increase in $C_{L\,max}$ with 40° sweep.

Design guidelines for airfoil selection thus include:

(1) Near the front wing root use a sharp-nosed airfoil, or a sharp-nosed segmented Kruger flap to generate LE vortex-shedding which will assist sweeping the boundary layer outboard.

(2) Alternatively, employ a leading edge root extension and/or a close-coupled canard. The canard should be of low aspect ratio to avoid excessive forward shift of the a.c. which (for a statically stable aircraft) will limit the lift that can be trimmed on to the rear wing. As discussed in Section 2.7 a highly swept canard with a sharp leading edge is particularly desirable. Use should be made of existing data on close-coupled canard configurations (e.g., Ref. 25).

Induced Camber: Addoms (Ref. 26) has investigated airfoil selection for biplanes. He shows that due to the curvature of the flow induced by each wing of a biplane pair, biplane airfoils require increased camber to achieve $C_{L\,max}$ equal to that attained by monoplane airfoils. For joined

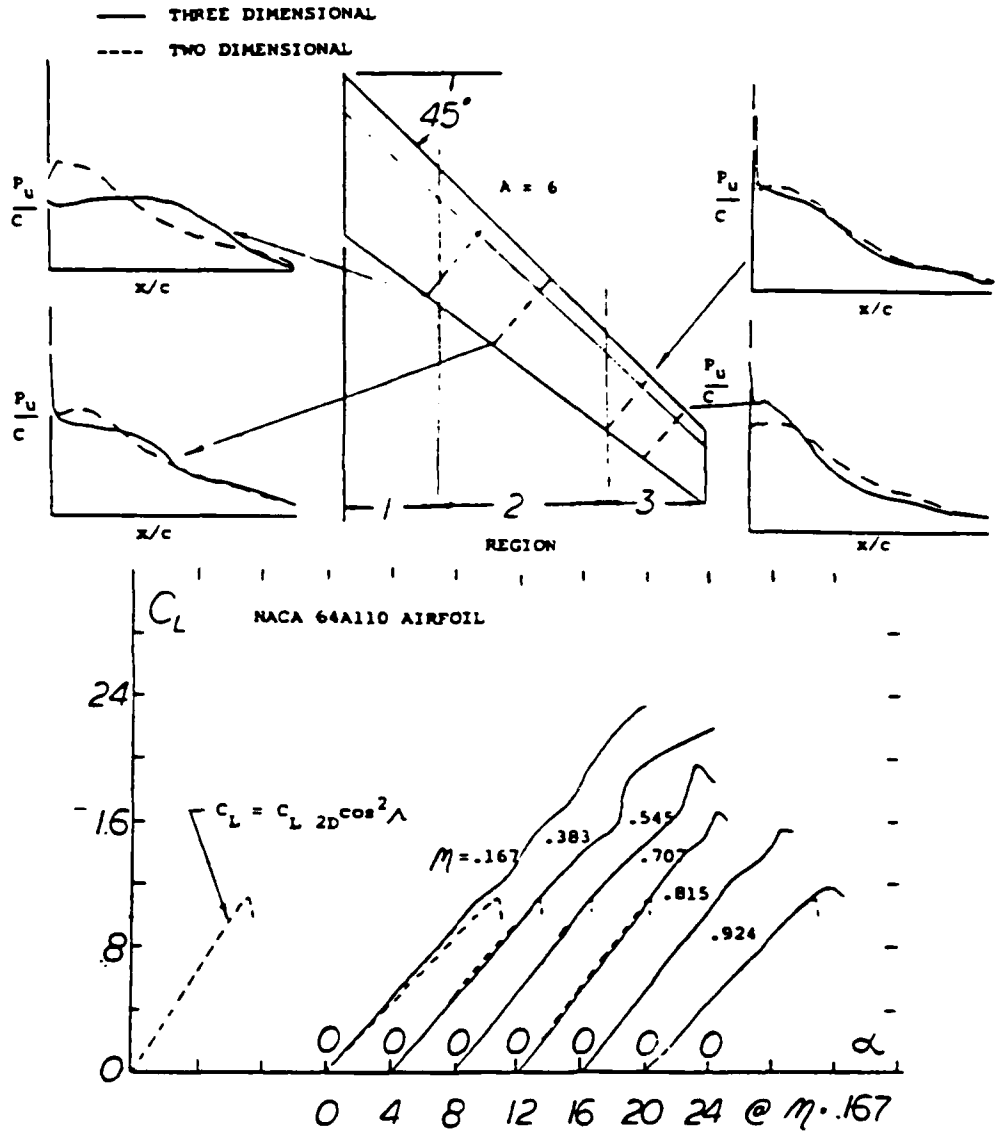

FIGURE 18. LIFT AND PRESSURE DISTRIBUTIONS FOR A SWEPT WING WITH NO FLAPS (REPRODUCED FROM REF. 23)

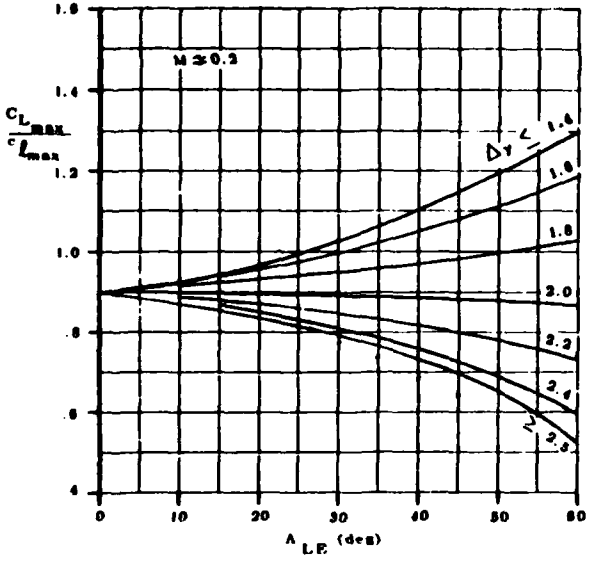

Fig. E-9. Effect of sweep angle on maximum lift (DATCOM method, Ref. E-3)

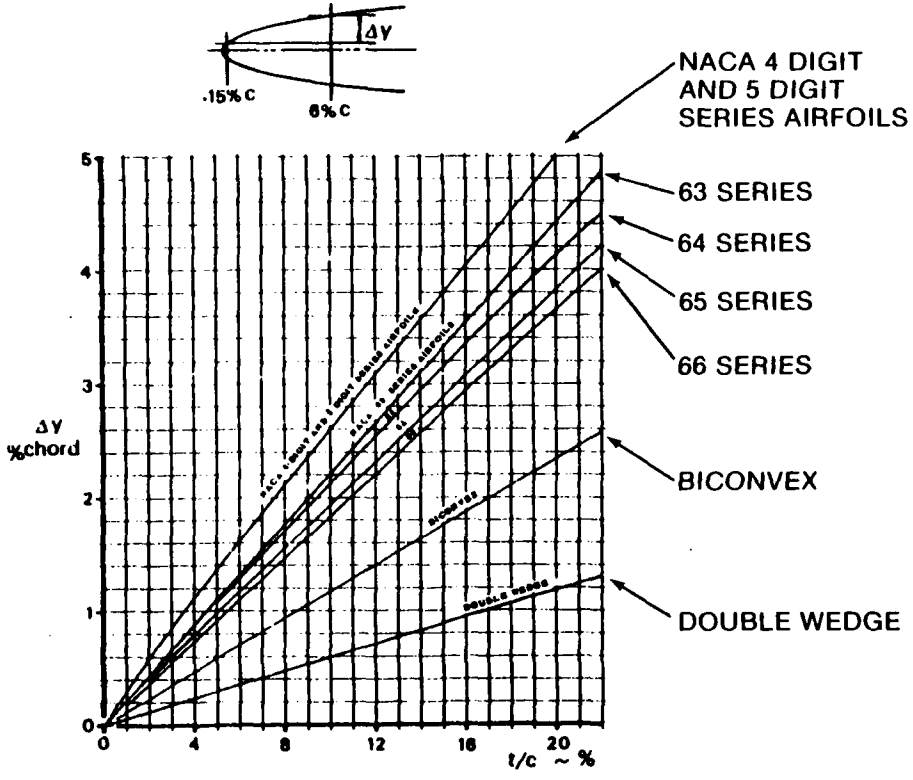

Fig. A-2. Leading edge sharpness parameter of NACA sections (Ref. A-6)

FIGURE 19. INCREASE OF $C_{L\,max}$ WITH SWEEP ANGLE
(REPRODUCED FROM REF. 14)

wings the induced flow curvature varies because of the spanwise variation in gap and stagger of the airfoils. Thus, as shown in Fig. 20 the sign of the flow curvature may change depending on the spanwise ordinate of the joined wing airfoils.

The induced camber effect makes it impossible to perform fair comparisons between monoplanes and multi-wing configurations if identical airfoils are employed for both. For example, in the comparative monoplane vs. boxplane tests described in Ref. 13, identical airfoils were employed for both configurations. As a result, the boxplane model suffered from premature flow separation on the front wing.

Since the induced camber varies with Mach number some compromise may be necessary to obtain high C_L at both high and low Mach numbers. Multi-element and slat airfoil design techniques are appropriate, and the vortex-lattice program of Ref. 20 which yields optimum joined wing twist and camber lines for specified pressure distributions has proven to be useful in airfoil selection.

Apart from induced camber, *multi-plane airfoil systems* experience mutually induced changes in the magnitude of local airspeeds. As explained in Ref. 27 these can be employed with advantage in the design of two-dimensional airfoil-plus-slat combinations, to yield high C_L's. If desired, it should be possible to obtain corresponding advantages by overlapping the tips of joined wings partially so that the front wing tip acts as a slat for the rear wing tip.

2.7 STABILITY AND CONTROL

Longitudinal Stability: Figure 21 shows the location of the aerodynamic center for typical joined wing configurations as predicted by the vortex-lattice program of Ref. 19. Figure 21 also shows C_{m_q}, C_{L_q}, C_{L_α} and C_{ℓ_p} for one configuration, as computed by the above-mentioned vortex-lattice program. The pitch damping $1/4\ \rho S U c^2\ C_{m_q}$ is more than double that of a conventional wing-plus-tail configuration. This large damping causes the maneuver margin to exceed the static margin by a

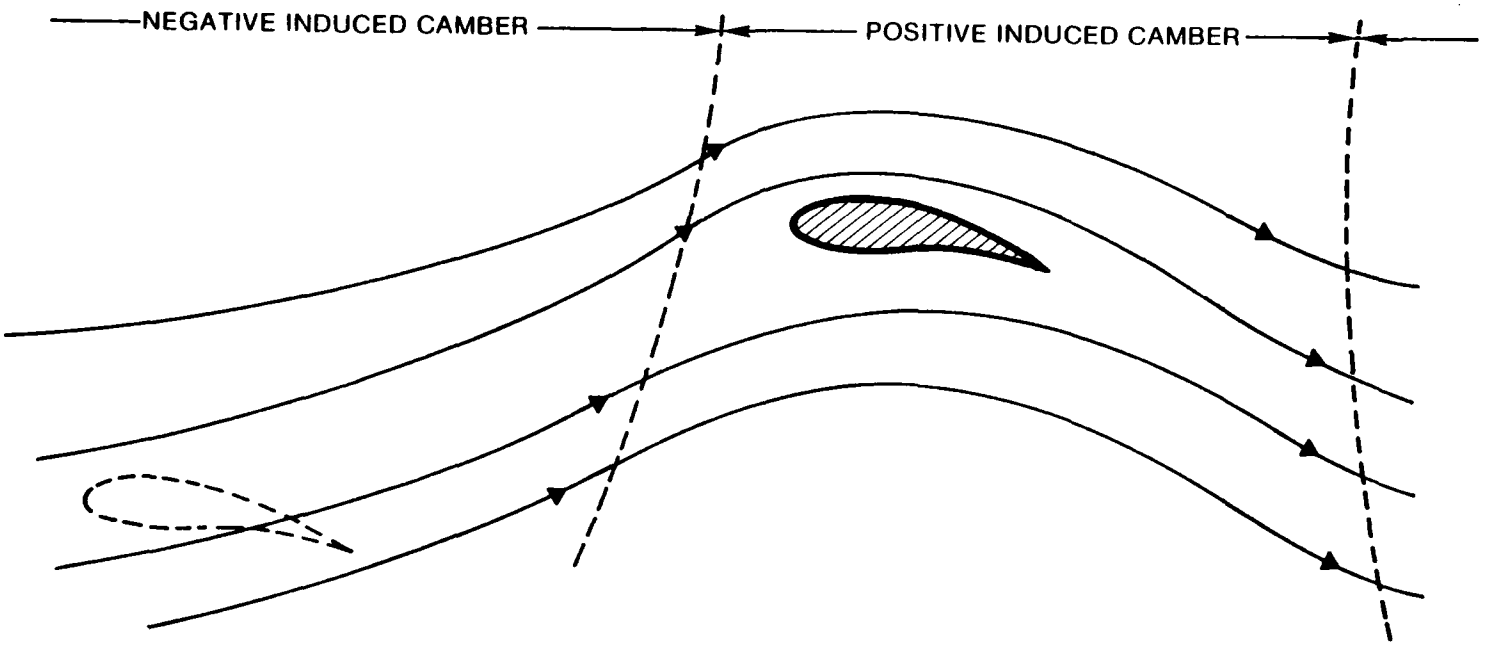

FIGURE 20. INDUCED CAMBER EFFECTS OF REAR WING ON FRONT WING

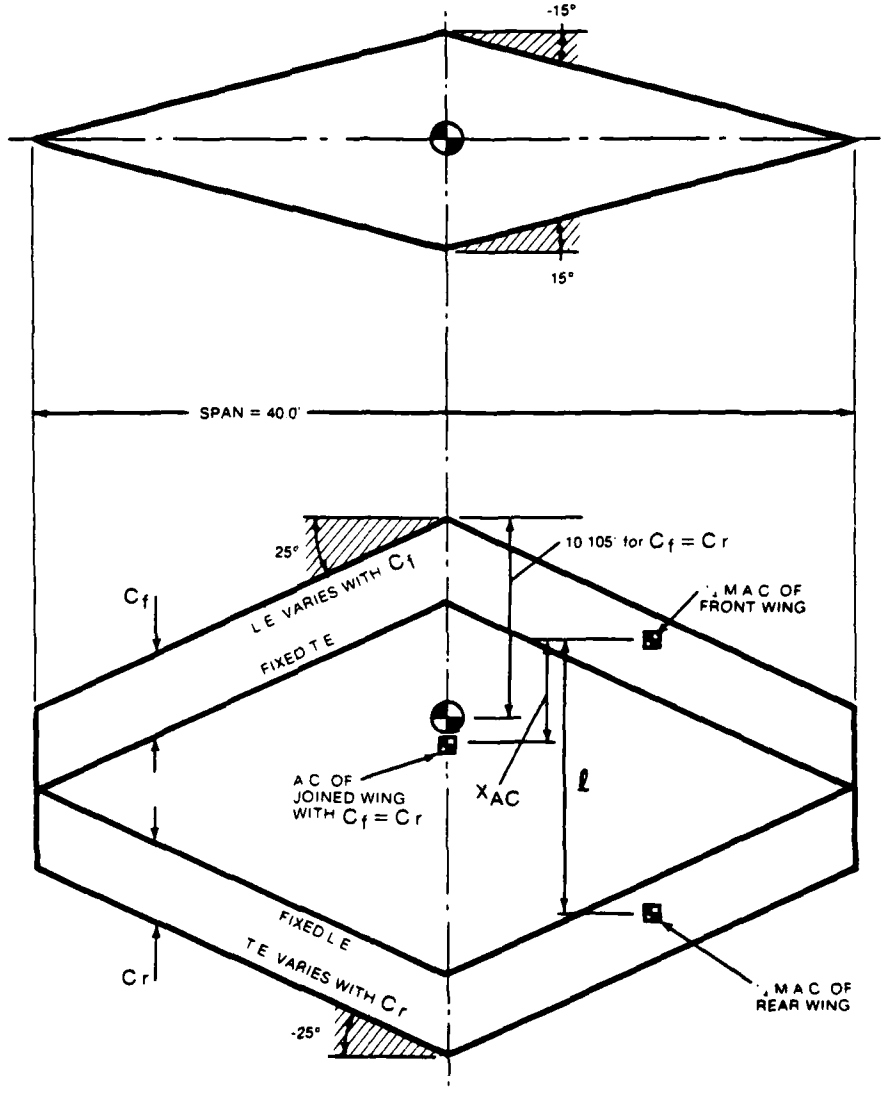

NO TAPER

NO TWIST
NO CAMBER

$C_f + C_r = 8.0' = C_{REF}$

$S_{REF} = 320.0 \square'$

DENOTES MOMENT CENTER
SELECTED FOR COMPUTING C_{mq} (SEE OVERLEAF)
THIS REPRESENTS A POSSIBLE C.G. POSITION, GIVING 0.96' STATIC MARGIN
FOR $C_f = C_r$, AT M=0.75

FIGURE 21(a). JOINED WING AERODYNAMIC CENTER: (a) GEOMETRY

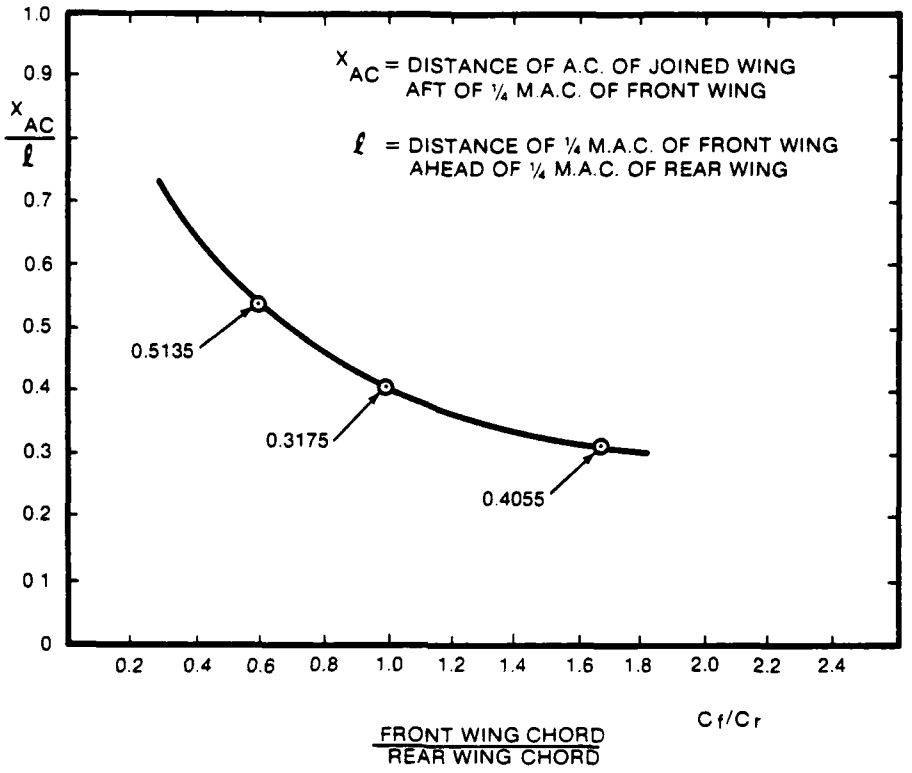

MACH NO. = 0.75, GEOMETRY AS ON PRECEDING PAGE

C_f/C_r	0.6	1.0	1.6
C_{L_α}	4.934	4.973	4.991
C_{m_q} about moment center ◔	N.A	-12.00	N.A
C_{L_q}	N.A.	6.3044	N.A
C_{l_p}	N.A.	0.5231	N.A

FIGURE 21(b). JOINED WING AERODYNAMIC CENTER: (b) RESULTS

greater distance than is typical of conventional aircraft. Hence the joined wing can achieve satisfactory longitudinal stability and control with very small (or even zero) static margin.

Wind tunnel tests on tandem and joined wing configurations (Refs. 4, 14) show reasonable agreement with the a.c. location predicted by vortex-lattice methods at low and moderate C_L's. However at high C_L's the a.c. moves aft and a moderate "pitch down" tendency occurs. (No "pitch-up" trend has been observed.) The pitch-down is of value as a stall preventative, but has the disadvantage that by moving the a.c. aft the static margin may become excessive. This is undesirable because it implies large control deflections for maneuvering and also because it limits trimmed $C_{L\,max}$, as discussed previously. Therefore, if a canard is employed it should be of low aspect ratio and high sweep with a sharp leading edge, to give a large nonlinear (vortex lift) contribution to C_{L_α}. This nonlinear C_{L_α} component can be tailored to correct the rearward shift of the a.c., thus giving essentially constant static margin up to the stall.

Stall Characteristics: Flight tests of joined wing models and of a manned joined wing glider, plus wind tunnel model tests, indicate good stall characteristics with no tendency for wing-dropping.

Lateral Stability: By tailoring the positive and negative dihedral angles of the front and rear wings almost any desired level of dihedral effect (C_{ℓ_β}) can be obtained. Joined wing models show good spiral stability, and display no tendency to Dutch roll. Directional stability also appears to be good, probably because of the endplate effect of the rear wing on the fin.

Control: Versatile control capabilities can be obtained if each wing half is equipped with a control surface. As shown on Fig. 22, this can provide pure pitching moment, direct lift, rolling moment, and direct side-force. Any desired combination of these can be obtained via suitable coupling of the individual control surfaces.

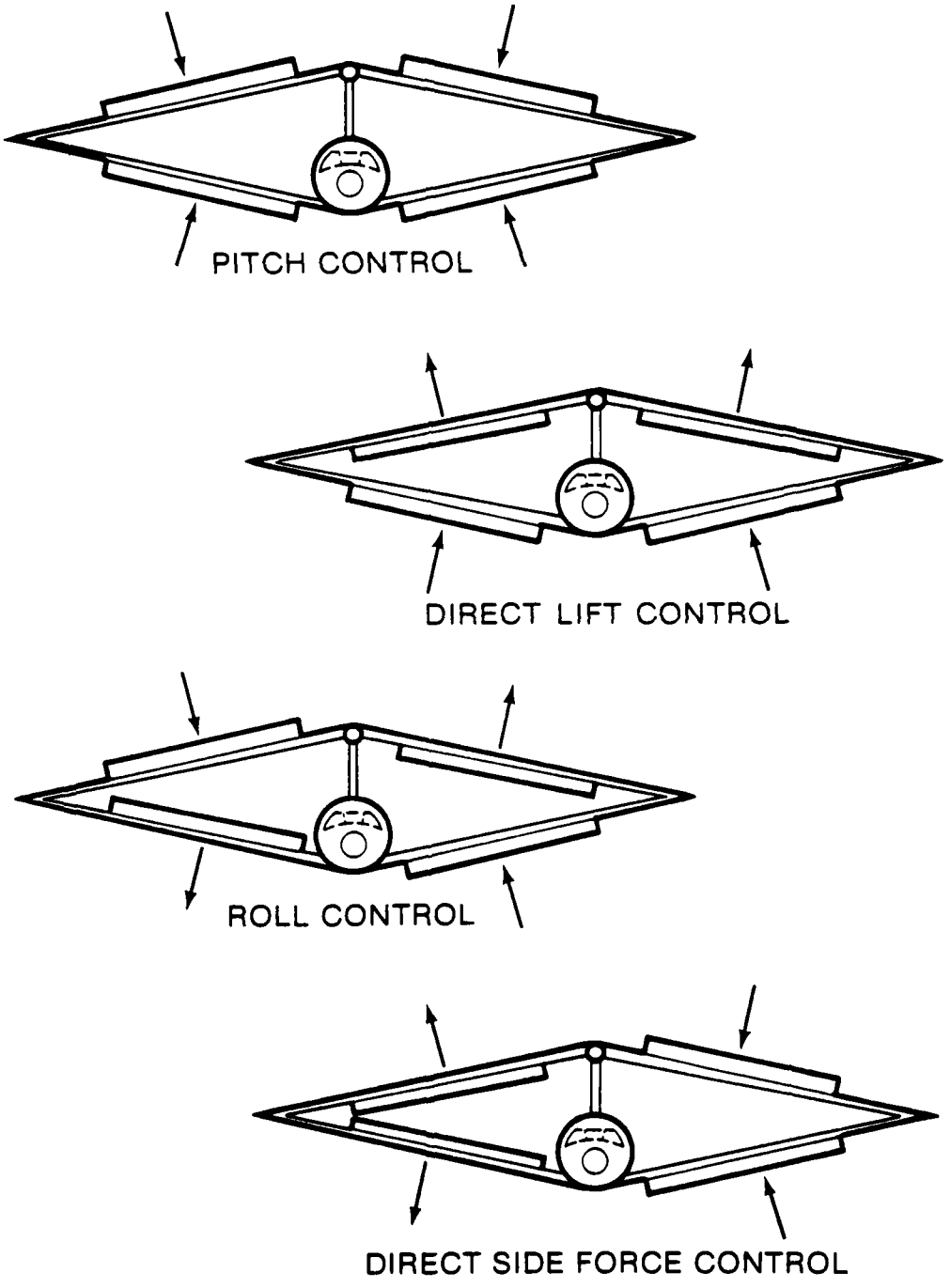

FIGURE 22. VERSATILE CONTROL CAPABILITIES OF JOINED WING AIRPLANE

To demonstrate one advantage of this versatile control arrangement, consider the control required for take-off rotation. By suitable choice of front/rear elevon gearing the longitudinal control can be adjusted to yield a combination of direct lift and pure pitching moment control. Hence the airplane can be rotated for take-off without any net download on the rear wing. This permits the main wheels to be located further aft of the c.g. than on a conventional airplane, at which location it can be conveniently retracted into a part of the fuselage where it does not impinge upon passenger or cargo volume. For example the main wheels could be retracted into the "dead-space" of the fuselage tail cone.

This form of control also yields faster response and more accurate control of the flight path because it avoids the initial wrong-way height response of aft tail airplanes.

The direct side force control shown on Fig. 22 will, in general, produce a side force which does not act exactly through the c.g. Hence some rudder deflection will be required to eliminate the residual yawing moment. Nevertheless this type of control is valuable as a vernier adjustment for precise alignment of the flight path, e.g., on the approach. It may also be of use for remotely piloted vehicles where the remote operator may be confused by the requirement to bank in order to turn. However, we do not advocate this type of control for manned aircraft, where all four elevons should be used as shown in Fig. 22 to produce a rolling moment in order to initiate a turn in the usual manner.

A very effective airbrake can be obtained via the use of a split rudder located near the trailing edge of the rear wing (Fig. 23). The split rudder increases parasite drag and also increases induced drag by degrading the lift distribution on the rear wing. Any resulting nose-up pitching moment can be counteracted by elevons or spoilers on the front wing, or outboard elevons on the rear wing.

Wing Warping: For some applications (e.g., remotely piloted vehicles) wing warping control may be of interest, because it avoids the expense of

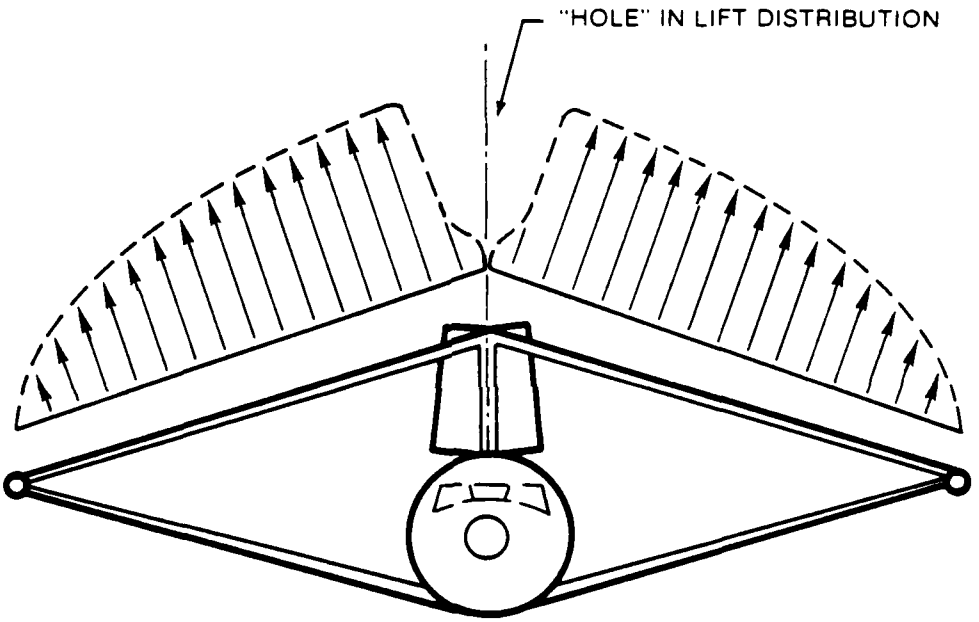

FIGURE 23. SPLIT RUDDER AIRBRAKE

separate control surfaces, and also avoids the increase in radar signature associated with control hinge lines. For the joined wing such control can be simply obtained via actuators inside the fuselage which twist (for example) the front wings against the tip constraint supplied by the rear wings.

2.8 SPECIAL DESIGN ASPECTS

Under this heading we discuss some specialized topics such as joined wing landing gear design, crashworthiness, folding, and suitability for VTOL aircraft.

Landing Gear: The joined wing airplane having elevons on both wings can rotate for take-off without incurring a download on the rear wing. Hence the main wheels can be located far aft of the c.g., possibly even retracting into the tail cone. Thus, as shown in Fig. 24 the legs of the main landing gear can be shorter than those of a conventional airplane, while still providing the necessary ground clearance during rotation. A short landing gear is usually a light landing gear, and retracting it into the tail cone obviates the familiar drag-producing "landing gear bulge."

The feasibility of this type of landing gear depends upon:

(1) Overturning criteria, which demand a wider track for main wheels mounted far aft of the c.g.

(2) Directional stability during take-off and landing, when the airplane may be pivoting in yaw about its main wheels.

Crashworthiness: The joined wing airplane offers a potential advantage in this regard. Placing the front wing root towards the nose of the fuselage enables the joined wings to brace the passenger compartment so that it is less likely to buckle in a crash. The front wing becomes the major energy absorbing structural element.

Ditching characteristics of joined wing aircraft are expected to be satisfactory, since the airplane floats supported by the front wing, winglets, and tip tanks.

CONVENTIONAL AIRPLANE

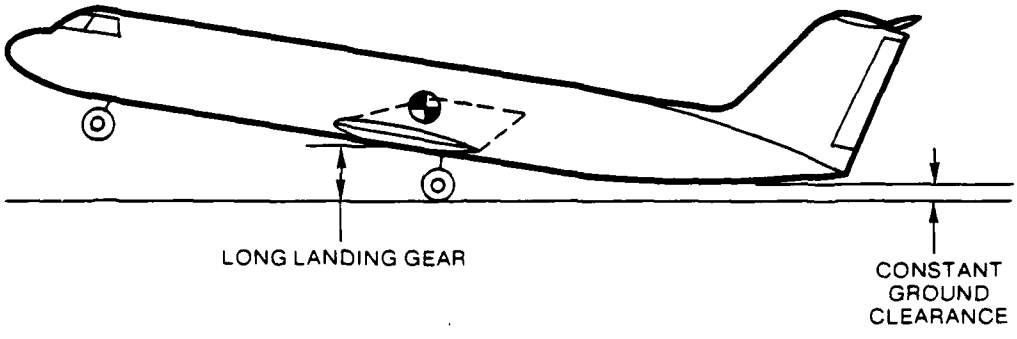

JOINED WING AIRPLANE

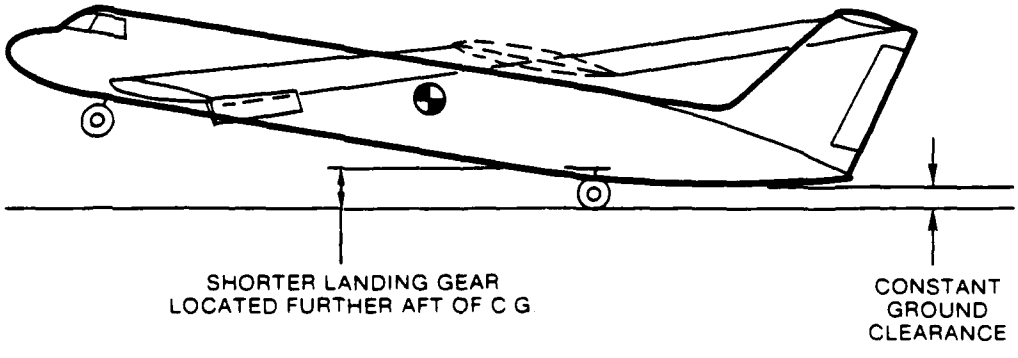

FIGURE 24. EFFECT OF MAINWHEEL/C.G. LOCATION ON LANDING GEAR LENGTH

Folding: Figure 25 illustrates a folding system suitable for manned aircraft. Other systems have been devised for missile applications where it is desired to accommodate the folded wing within the missile fuselage.*

Fuel Volume: For a given thickness/chord ratio the volume of a joined wing is less than that of a conventional wing of similar performance. Thus to ensure adequate fuel volume within the wing structural box it should extend over as large a fraction of the chord as possible. (This is desirable for structural reasons also, as shown in Section 2.2.) The tip joining fairing can also serve as a tip tank. Joined wing fuel volume has not proved to be a significant constraint on any configuration studied to date.

Suitability for VTOL: The joined wing arrangement is well suited to a VTOL aircraft employing two main lifting units displaced laterally from the c.g. This minimizes interference between the wings and the lifting units, which may be ducted fans or propellers.

2.9 PUBLISHED WORK ON RELATED CONFIGURATIONS

The joined wing concept involves complete integration of structural and aerodynamic aspects. In this it differs from the related concepts that have been published. For example, the Lockheed boxplane (Fig. 26) described in Refs. 13 and 28 provides low induced drag, but has less structural rigidity than the joined wing, as indicated by the comparative front views of Fig. 27. Reference 28 shows that the low rigidity of the boxplane yields unacceptable flutter characteristics. The rhomboidal wing of Zimmer (Ref. 29), shown in Fig. 28, achieves a more rigid structure than the boxplane but lacks the structural and aerodynamic benefits obtainable through integrating the fin with the wing, and through the wing structural thickness distribution shown in Fig. 5. Thus the rhomboidal wing configuration has area rule and induced drag characteristics which are only slightly better than those of a conventional configuration.

*A cruise missile folding system is described in Section 3.

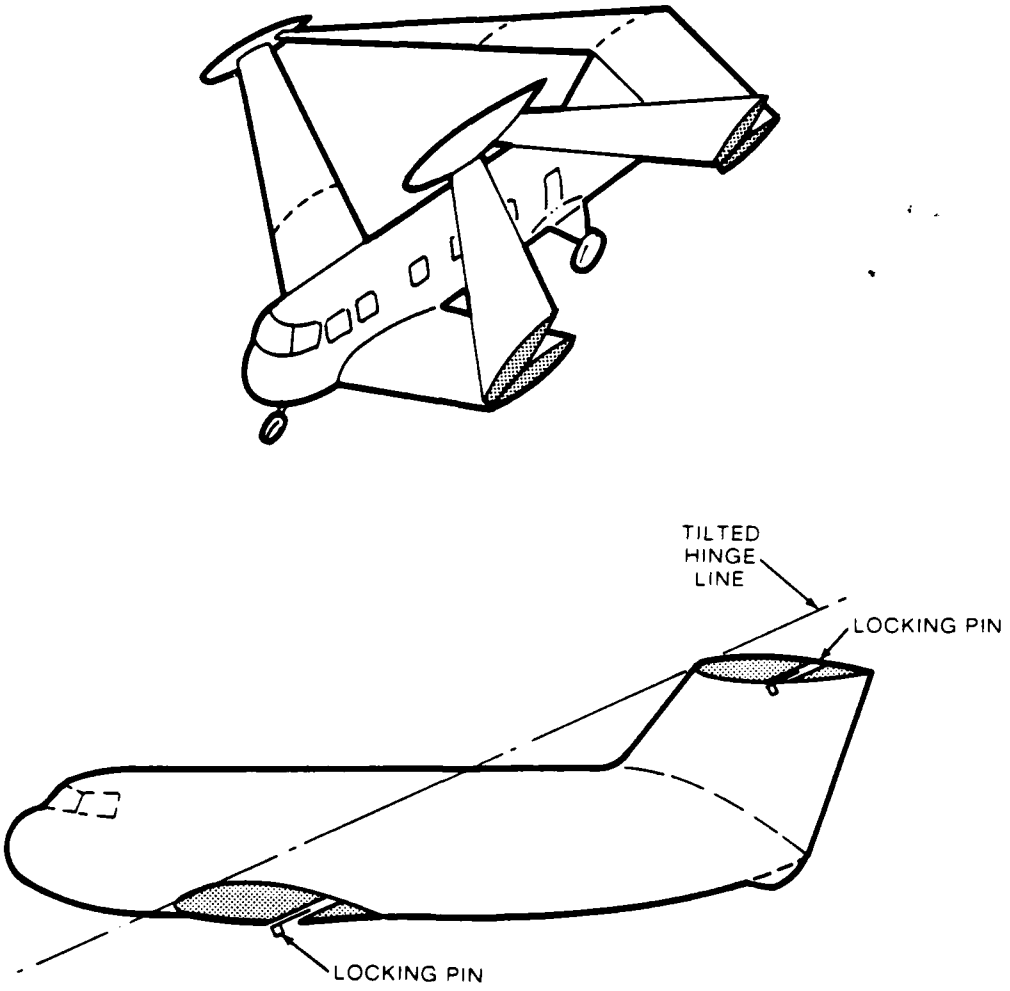

FIGURE 25. A JOINED WING FOLDING ARRANGEMENT

Wing area: 442 58 m^2 (4764 ft^2)
T.O.G.W.: 302 283 kg (666 424 lb)
Operating weight: 128 083 kg (282 376 lb)
Payload 38 465 kg (84 800 lb)

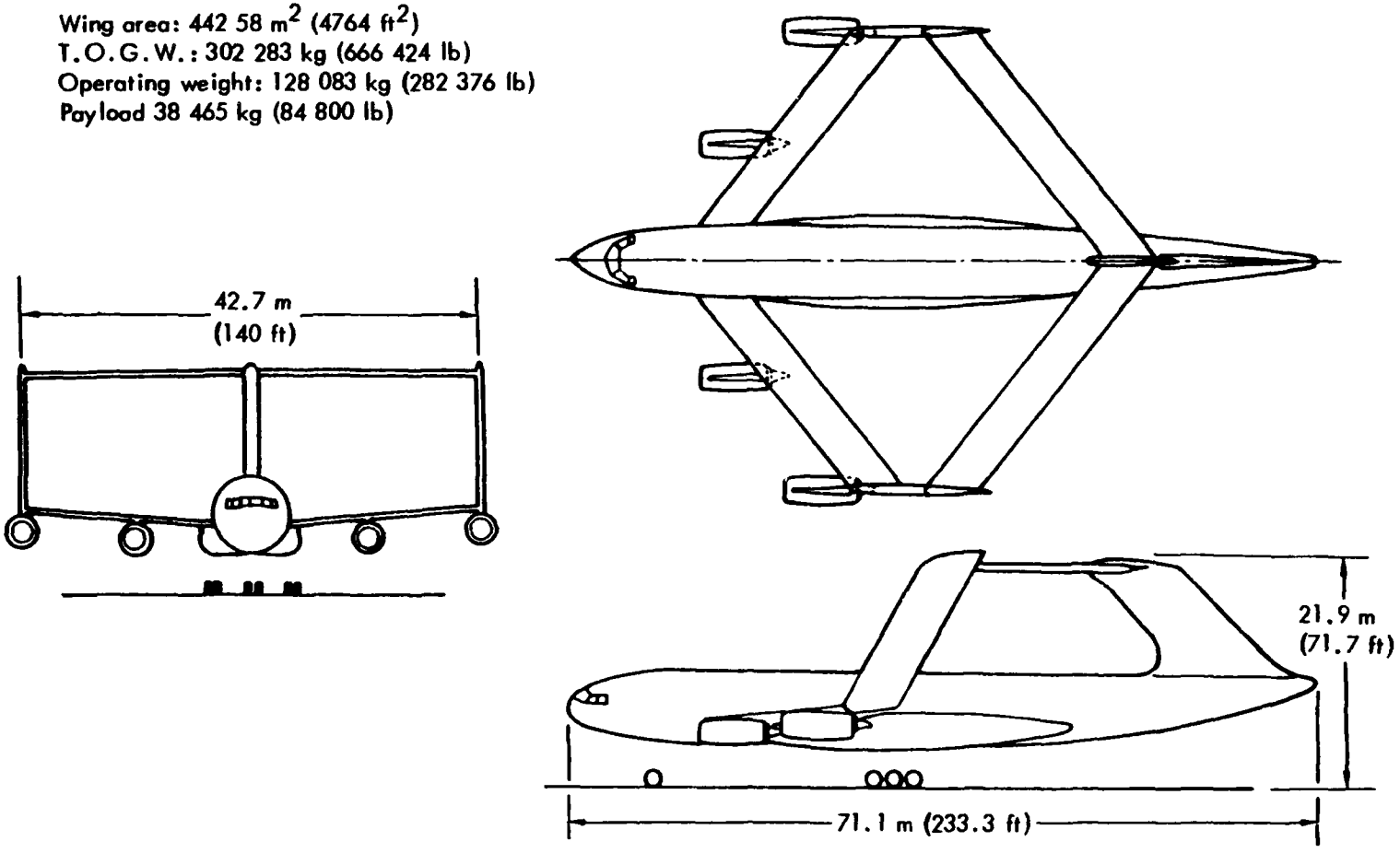

FIGURE 26. LOCKHEED BOXPLANE TRANSPORT DESIGN

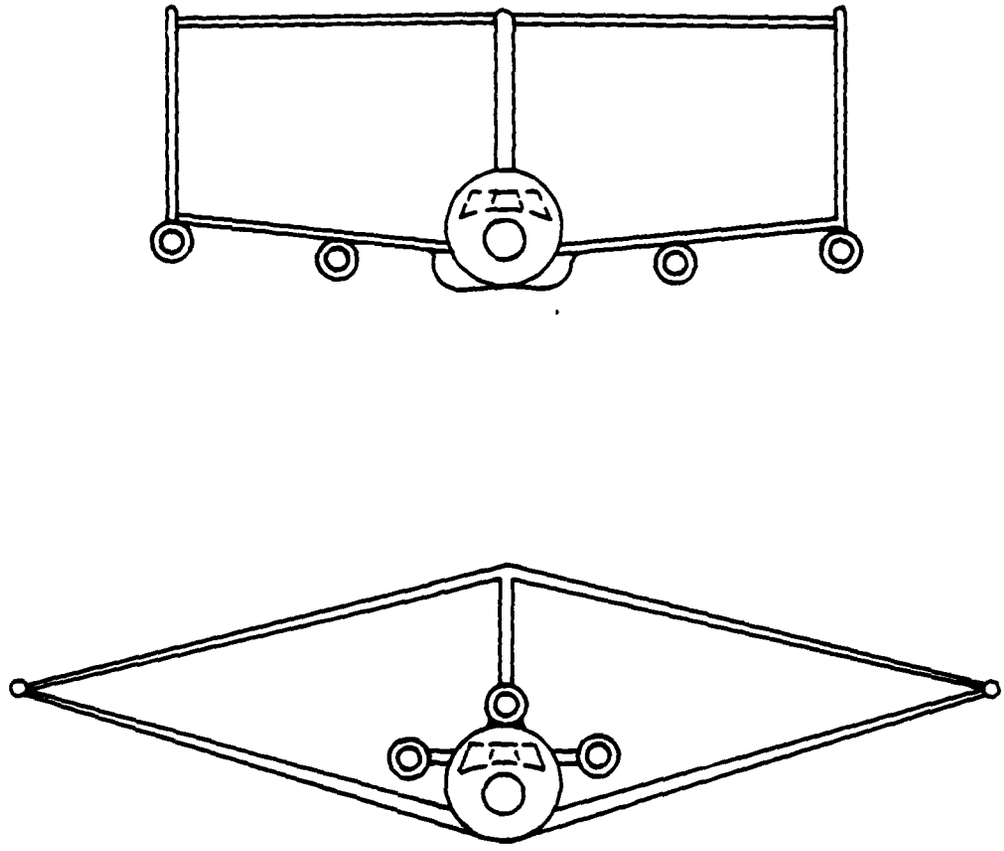

FIGURE 27. COMPARATIVE FRONT VIEWS OF BOXPLANE AND JOINED WING

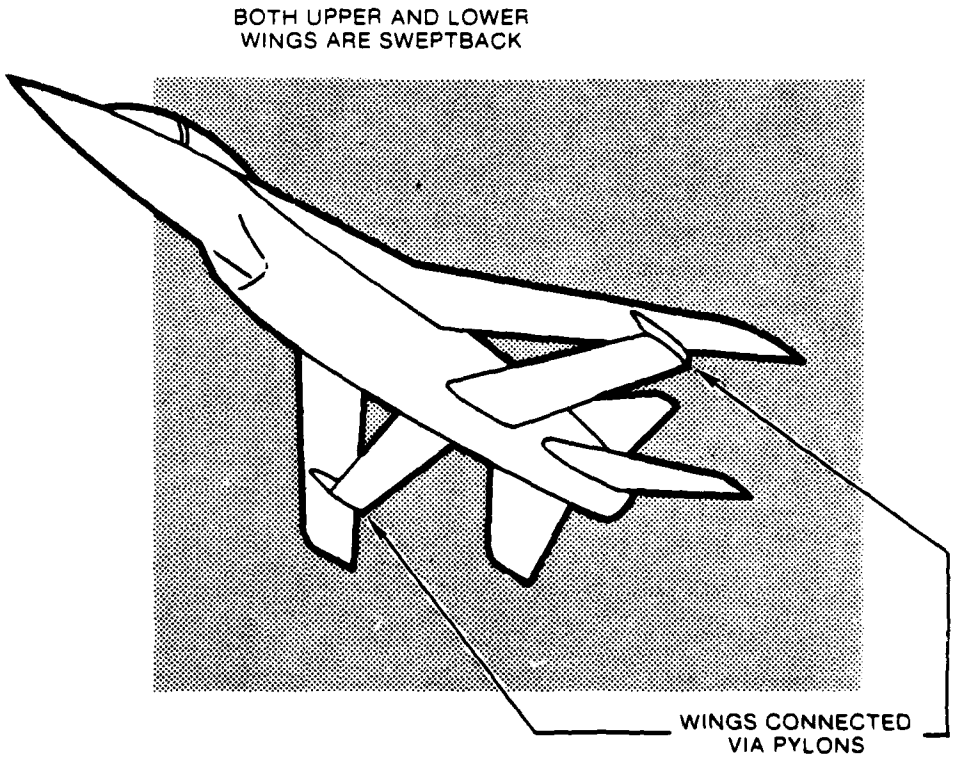

FIGURE 28. RHOMBOIDAL WING CONFIGURATION

Reference 16 describes wind tunnel tests on a boxplane with and without endplates joining the wings. Some additional analysis of the data is given in Ref. 14.

The wind tunnel data presented in Refs. 13, 14, 28 and 29 show good stability and control characteristics and lift and drag characteristics which generally agree with theoretical predictions. The boxplane transonic test results of Ref. 13 show premature separation on the front wing at high C_L's: as explained in Section 2.6 this can be ascribed to the airfoil selected being the same as that of a "baseline" comparable monoplane, thus having insufficient camber to compensate for the "induced camber" effect of the boxplane. (Further analysis of boxplane data is given in Ref. 2.)

Dexter and Cahill (Ref. 30) present tests at Mach numbers between 0.2 and 0.9 on two very similar configurations, one of which is shown in Fig. 29. These configurations had negative tilt angles and contained numerous crudities yielding high drag (e.g., too sharp wraparound radius, flat plate airfoil). As a result the measured span-efficiency factor for the configuration of Fig. 28 was only 0.502. For these reasons, plus the configurational differences, the tests of Ref. 30 have very limited relevance to the joined wing concept.

Apart from the data referenced above, the only other significant data that we have been able to locate on related configurations is an unpublished wind tunnel test report on the Warren-Young wing (Fig. 30). This figure shows one of the wind tunnel models tested at low Mach number by the University of Bath, England. A manuscript copy of the unpublished test report (Ref. 31) was kindly supplied by Dr. J. S. Henderson of that institution. The Warren-Young project differs from the joined wing airplane because it does not take advantage of the height of the vertical tail to obtain a large tilt angle. A further difference is that the Warren-Young arrangement connects the wings by means of a large horizontal tip surface. The wind tunnel tests of Ref. 31 confirmed previous radio-controlled model tests which indicated good flying qualities and

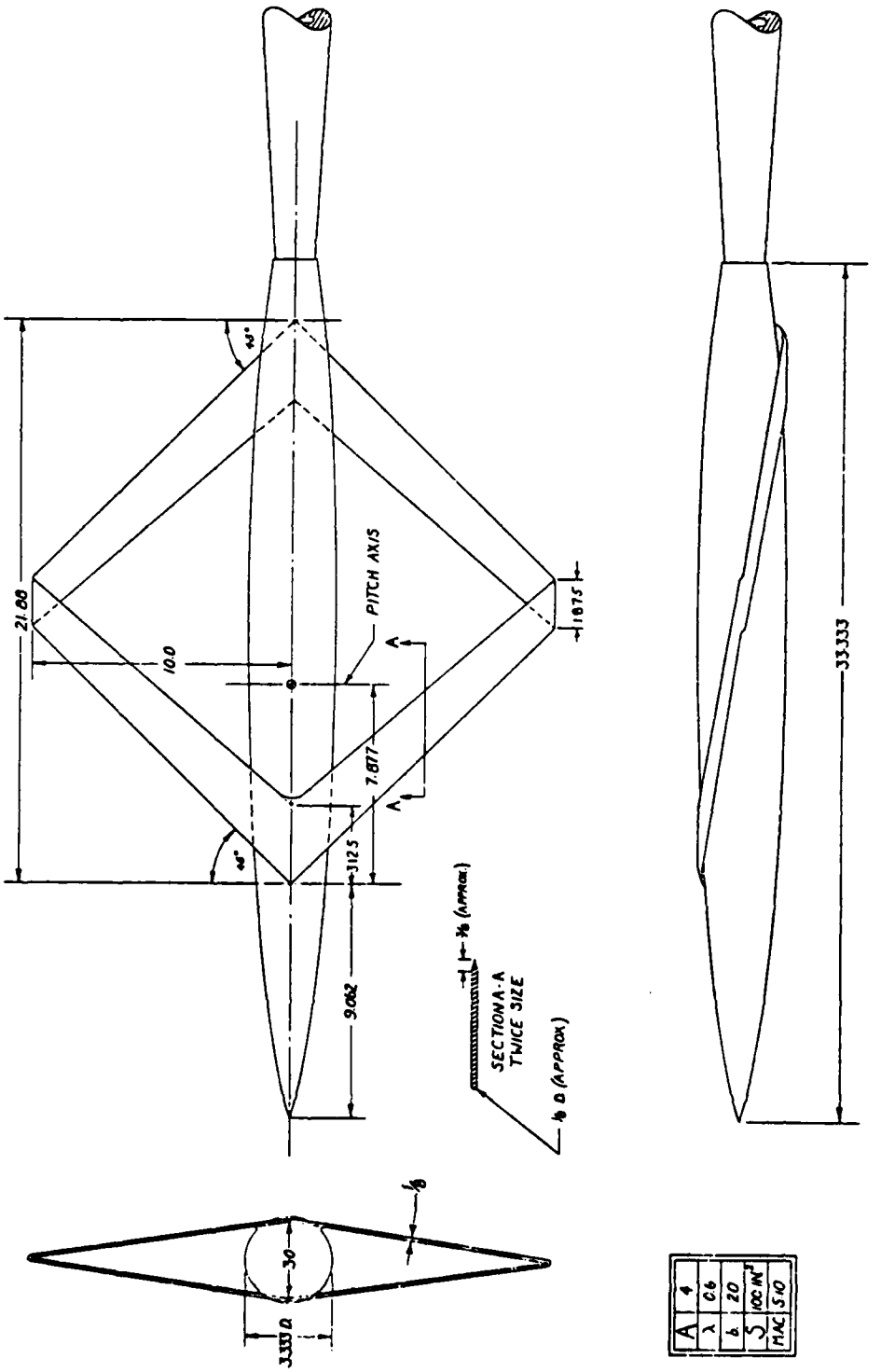

FIGURE 29. WIND TUNNEL MODEL OF REFERENCE 30

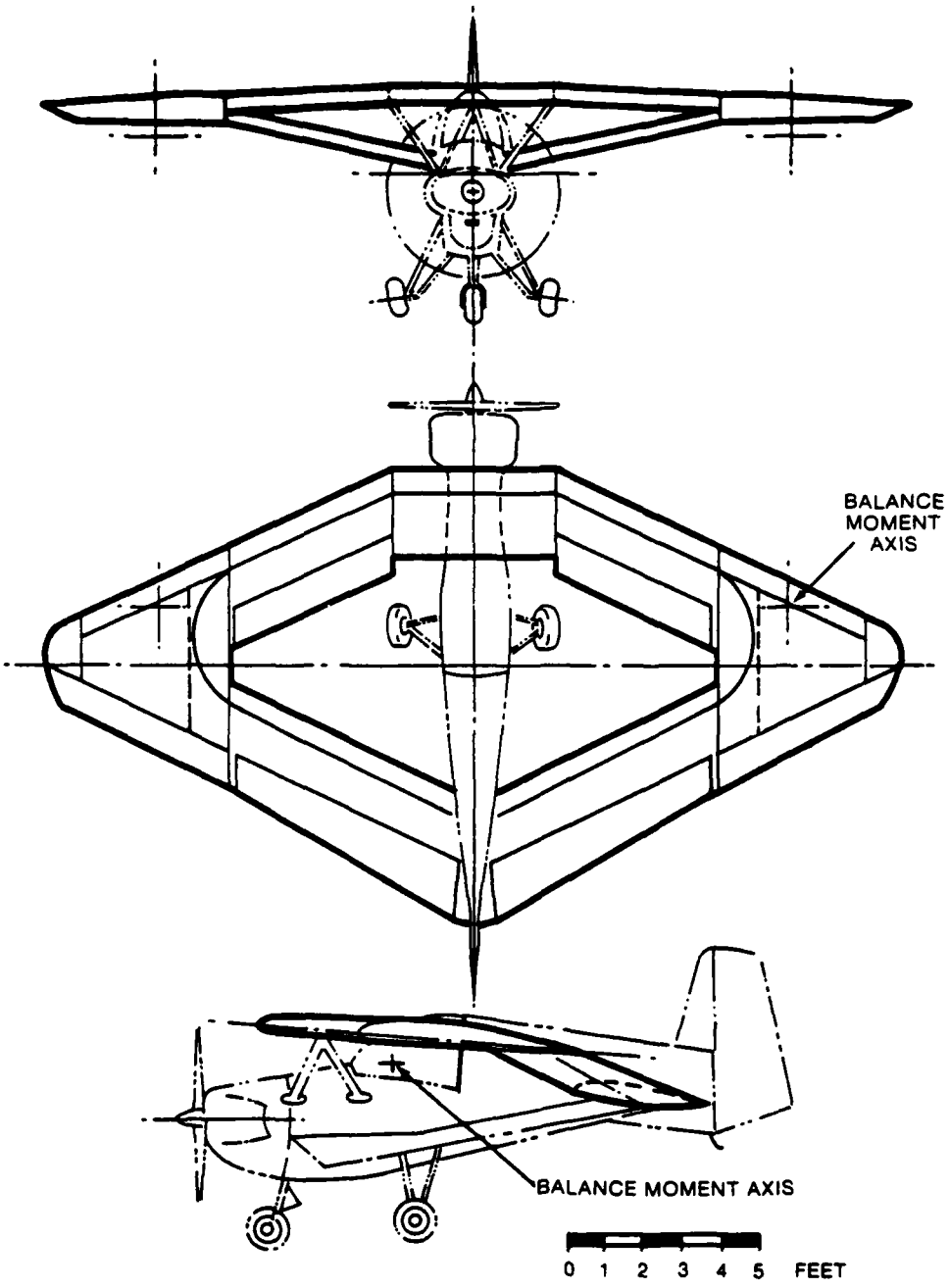

FIGURE 30. WIND TUNNEL MODEL EMPLOYING WARREN-YOUNG TYPE OF WING

gentle stall, but showed a nonlinear C_M - C_L variation below the stall. Between C_L's of 0 and 1.0 (based on total wing area), the aerodynamic center moved aft by approximately 35% of the geometric mean chord (i.e., total area/span). By contrast, the corresponding low Mach number boxplane tests of Refs. 13 and 16 showed very little aerodynamic center shift.

Sketches, photos, and drawings of other configurations related to the joined wing have been published, but the accompanying data have been fragmentary and incomplete. The references cited above are therefore believed to represent the principal sources of technical information on related configurations.

Currently several research programs on the joined wing are being planned. Additional data including further wind tunnel results are explected to be available soon. It is therefore suggested that the author of this report should be contacted to obtain the most complete and up-to-date information.

3.0 JOINED WING CRUISE MISSILE CONFIGURATIONS

3.1 INTRODUCTION: CRUISE MISSILE DESIGN REQUIREMENTS

Having described the basic principles of the joined wing in Section 2, this section applies these principles to the design of cruise missiles. Problems and solutions relating to overall configuration selection and mechanical design are discussed: detailed performance and control analyses are given later, in Sections 4 and 5 of this report.

For the purposes of this report, a "cruise missile" is defined as a missile which spends the major portion of its flight in a "cruise" mode, i.e., flying at nearly constant altitude and nearly constant speed, using aerodynamic lift to support its weight. The advanced cruise missile configurations discussed in this report have launch weights, payloads, and folded dimensions similar to those of Tomahawk class vehicles. The specified low-altitude cruise flight condition (M = 0.7 at sea level) is also similar to that of the Tomahawk. However, the present study is not restricted to vehicles comparable with the Tomahawk; for example, we consider configurations having Tomahawk-like fuselages but wings which are two or three times larger in area than those of the current Tomahawk, to improve maneuverability.

General design requirements for cruise missiles have been well summarized in Refs. 32 and 33. From these references, plus discussions with personnel of the Joint Cruise Missiles Project Office, we formulated the following design goals for an advanced low-altitude cruise missile capable of being launched from a standard 21 inch submarine torpedo tube.

Principal Design Goals

- Low wave (or terrain) clearance to avoid detection
- Low radar signature to avoid detection
- Robustness of the folded vehicle
- Reliable, rapid, and symmetric unfolding
- Simplicity
- Low cost
- High sustained "g" capability for terminal maneuvers
- Long range
- Cruise at M = 0.7, little emphasis on transonic and supersonic capability

The design goals listed above serve as criteria by which the relative merits of joined wing and conventional cruise missiles can be compared.

3.2 COMPARATIVE AIRFRAMES

In order to compare the joined wing versus the conventional wing-plus-tail arrangement, 3 configurations of each type were selected. The conventional configurations (denoted 3GA, 6GA, 9GA) had gross wing areas of respectively 11.5, 23.0, and 34.5 ft^2, as shown in Fig. 31. The joined wing configurations (denoted 3F, 6F, 9F) had gross horizontal projected areas of 10.0, 20.0, and 30.0 ft^2. Figure 32 shows the planforms of these configurations. Figure 33 shows three-views of Configuration 3GA; this configuration is dimensionally similar to the Vought YGBM-110 Tomahawk, but incorporates a pop-down inlet similar to that of the General Dynamics YGBM-109 Tomahawk. Configuration 3GA is a baseline configuration, resembling both, but not identical to either of the existing Tomahawk missiles. Configurations 3GA, 6GA, 9GA have aspect ratios of 9.6: Configurations 3F, 6F, 9F have aspect ratios of 8.35.

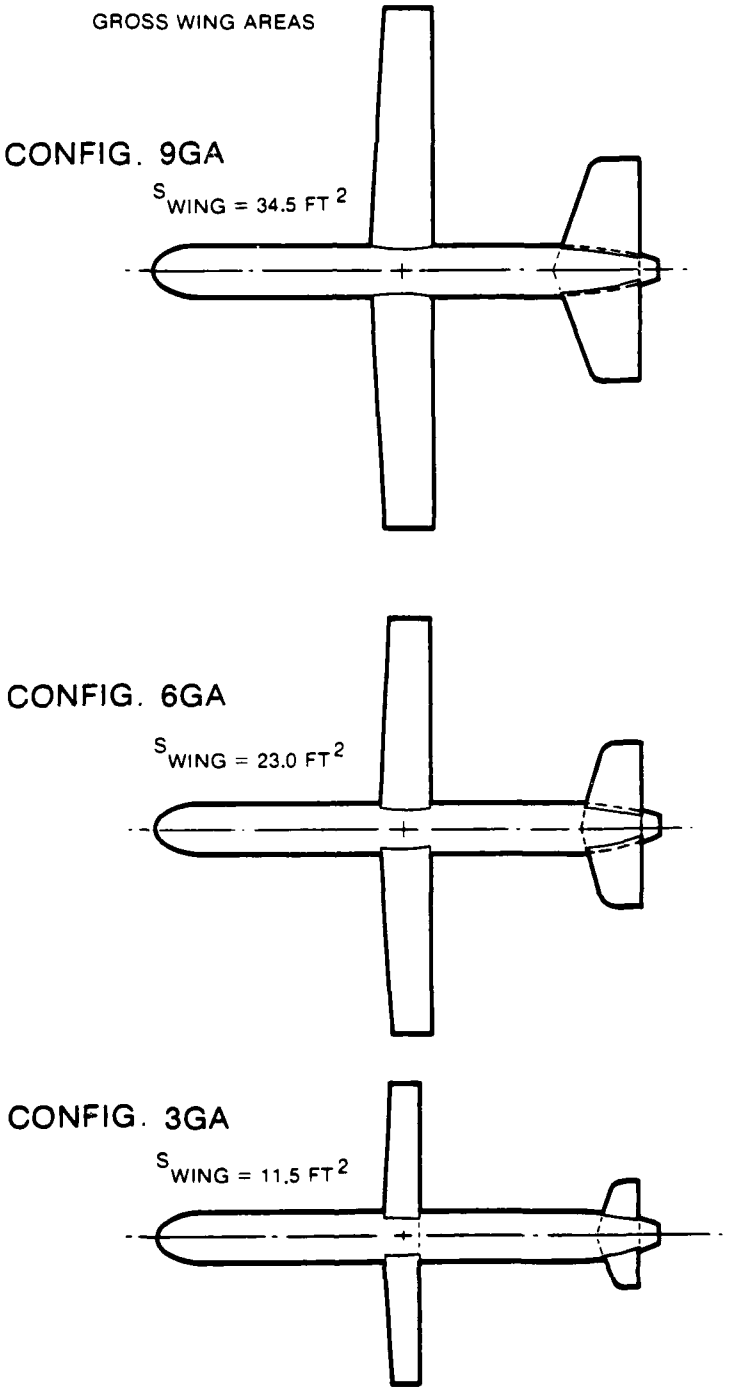

FIGURE 31. CONVENTIONAL (AFT TAIL) CONFIGURATIONS WITH VARIOUS WING AREAS

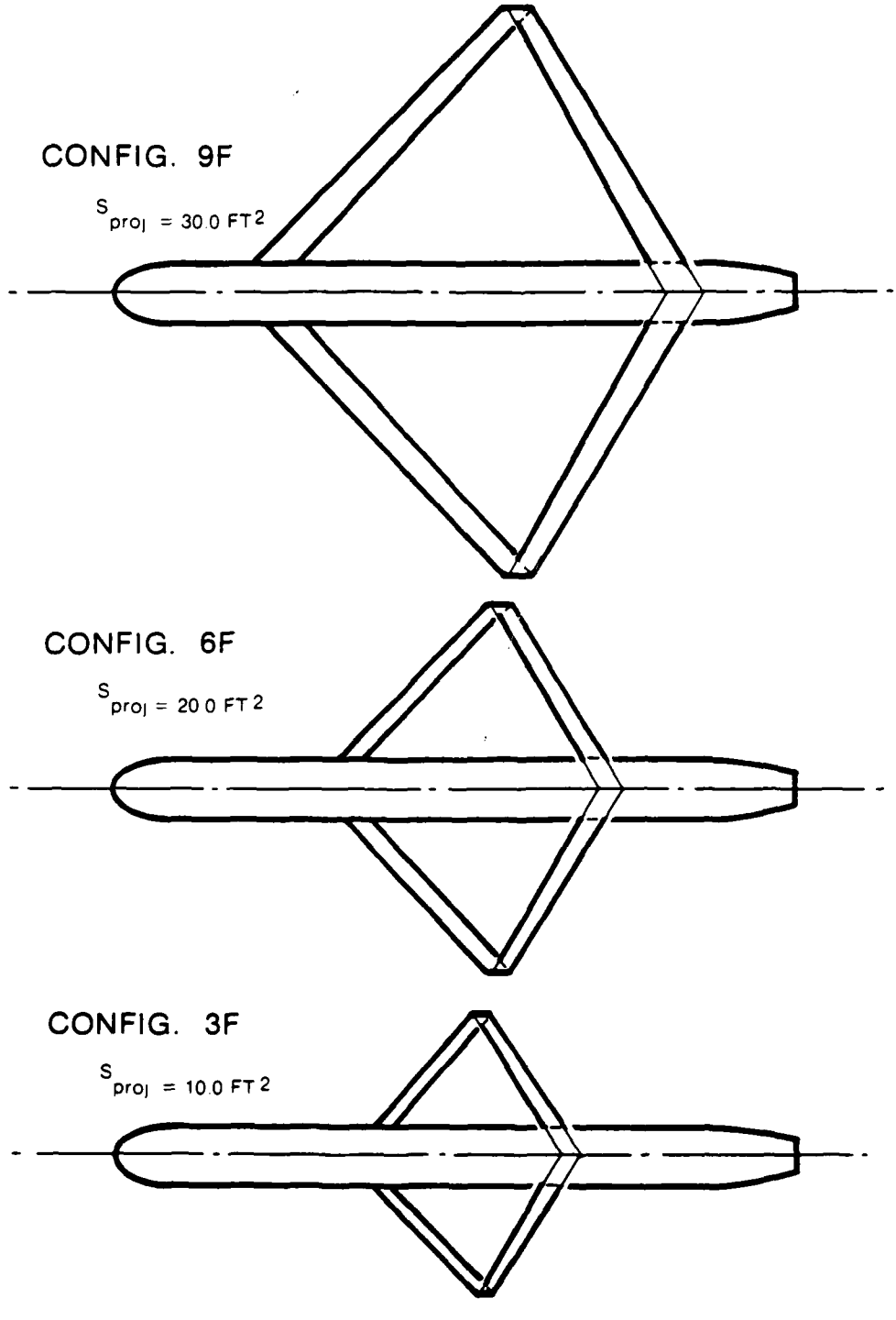

FIGURE 32. PLANFORMS OF JOINED WING CONFIGURATIONS WITH VARIOUS WING AREAS

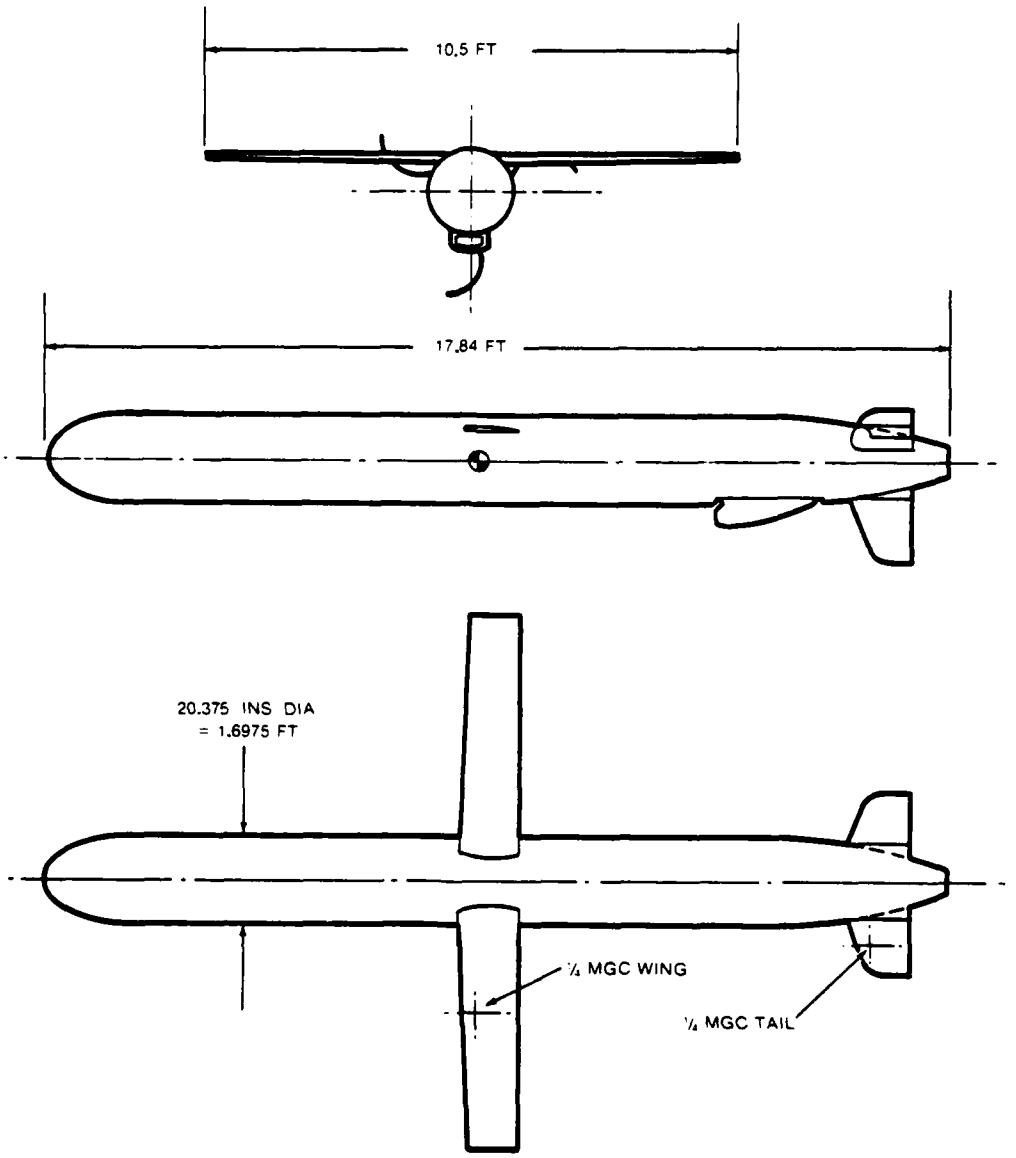

FIGURE 33. CONVENTIONAL CRUISE MISSILE CONFIGURATION 3GA

An additional configuration was also studied. This configuration, denoted as 6H, is shown in Fig. 34. It is a hybrid configuration combining a joined wing with a canard.

The configuration numbers denote very approximately the non-sustained maneuver capability of each configuration at M = 0.7, S.L., maximum weight conditions. Thus, Configurations 3GA, 3F can pull approximately 3 g's, Configurations 6F, 6GA, 6H can pull approximately 6 g's, etc. These values are not necessarily sustained g's. The engine thrust may not be sufficient to overcome the airframe drag during a steady maneuver at the designated number of g's.

The initial cruise weight of all configurations is 2864 lb. Thus the more maneuverable configurations sacrifice some fuel because of the larger weight of their lifting surfaces. (The increased lifting surface volume also reduces fuel tankage, as discussed in Section 5.)

Performance comparisons between the configurations are given in subsequent sections of this report. The remainder of this section discusses some mechanical and configuration design possibilities of joined wing cruise missiles. These include folding, wing-warping type control, variable camber, and staging.

3.3 JOINED WING FOLDING SYSTEM FOR CRUISE MISSILES

For a submarine-launched cruise missile the dimensions of the folded configuration are constrained so that it can fit inside a standard 21" diameter torpedo tube. For the present study it was assumed that the missile is stored within a 21" diameter casing prior to launch, as is the General Dynamics Tomahawk. The fuselage diameter was therefore set equal to that of the G.D. Tomahawk, i.e., 20.375 inches. Thus the wings must fold into a tube of 20.375 inches diameter.

The design goals listed in Section 3.1 profoundly influenced the derivation of the folding system. To attain the design goal of reliable unfolding, the front and rear wings should be connected throughout

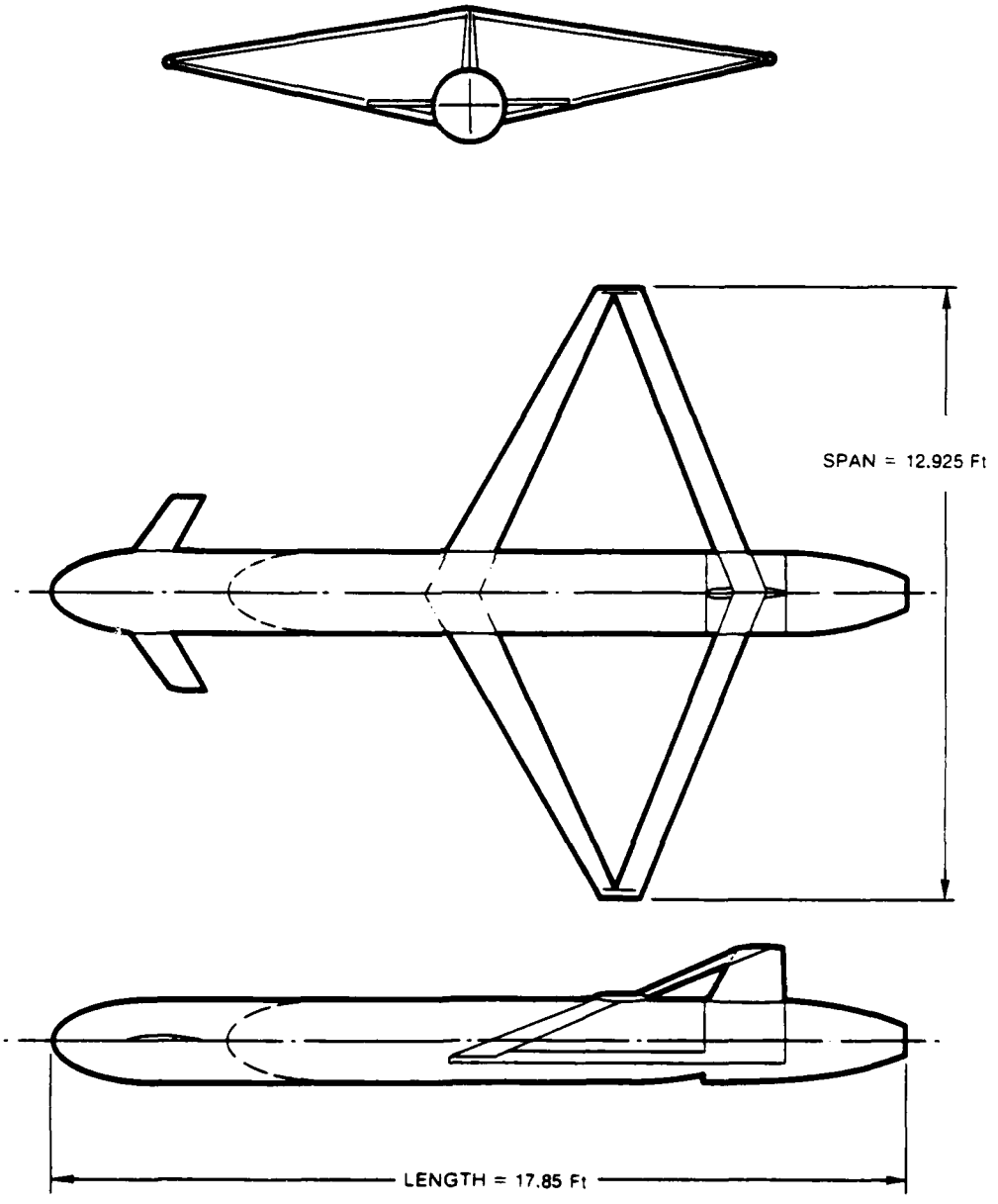

FIGURE 34. HYBRID CONFIGURATION (JOINED WING PLUS CANARD)

deployment. The design goal of symmetric unfolding requires cross-links between port and starboard wings. A further design goal is that the folded configuration should be robust. For example it should be capable of being lashed down for storage in naval vessels which may experience violent accelerations due to attack by bombs or depth charges. This rules out folding systems in which the folded wings rest on top of the fuselage. Since the wings must therefore fold within the fuselage they must do so in a way which does not encroach into the space required for the warhead, the guidance system, or other equipment. The joined wing folding system described below satisfies these requirements, and occupies only 50% of the fuselage volume required by a folded monoplane wing of the same span and area, employing the same airfoil.

The proposed folding system involves three key concepts, illustrated in Figs. 35 through 38, and described below.

(1) Port and starboard fin halves, hinged at their fuselage junctions as shown in Fig. 35, so that they can be rotated in a rolling sense. Figure 35 shows three alternative arrangements: the curved fin arrangement occupies the least fuselage volume, but is less stiff and has higher drag than the twin fin or split single fin arrangement. The latter has the least drag and is also the stiffest configuration.

(2) A two-axis hinge at the root of the rear wing: as shown by photos showing deployment of a half-model (Fig. 36) this two-axis hinge permits the rear wing halves to pivot outwards while the fin halves rotate upwards.

(3) A slot in the lower surface of the rear wing, which, for aerodynamic cleanness, is covered in cruise by a flush-fitting flap. This slot guides a spigot located on the upper surface of the front wing tip, to keep the front and rear wings connected during deployment.

Figures 37 and 38 illustrate other details of the folding system. Both these figures show configurations with joined wings of 31.3 ft^2 total gross projected horizontal area. This is larger than the largest of the configurations shown in Figs. 32 and 34. We selected such a large wing area to demonstrate that the folding system is suitable even for highly maneuverable cruise missiles.

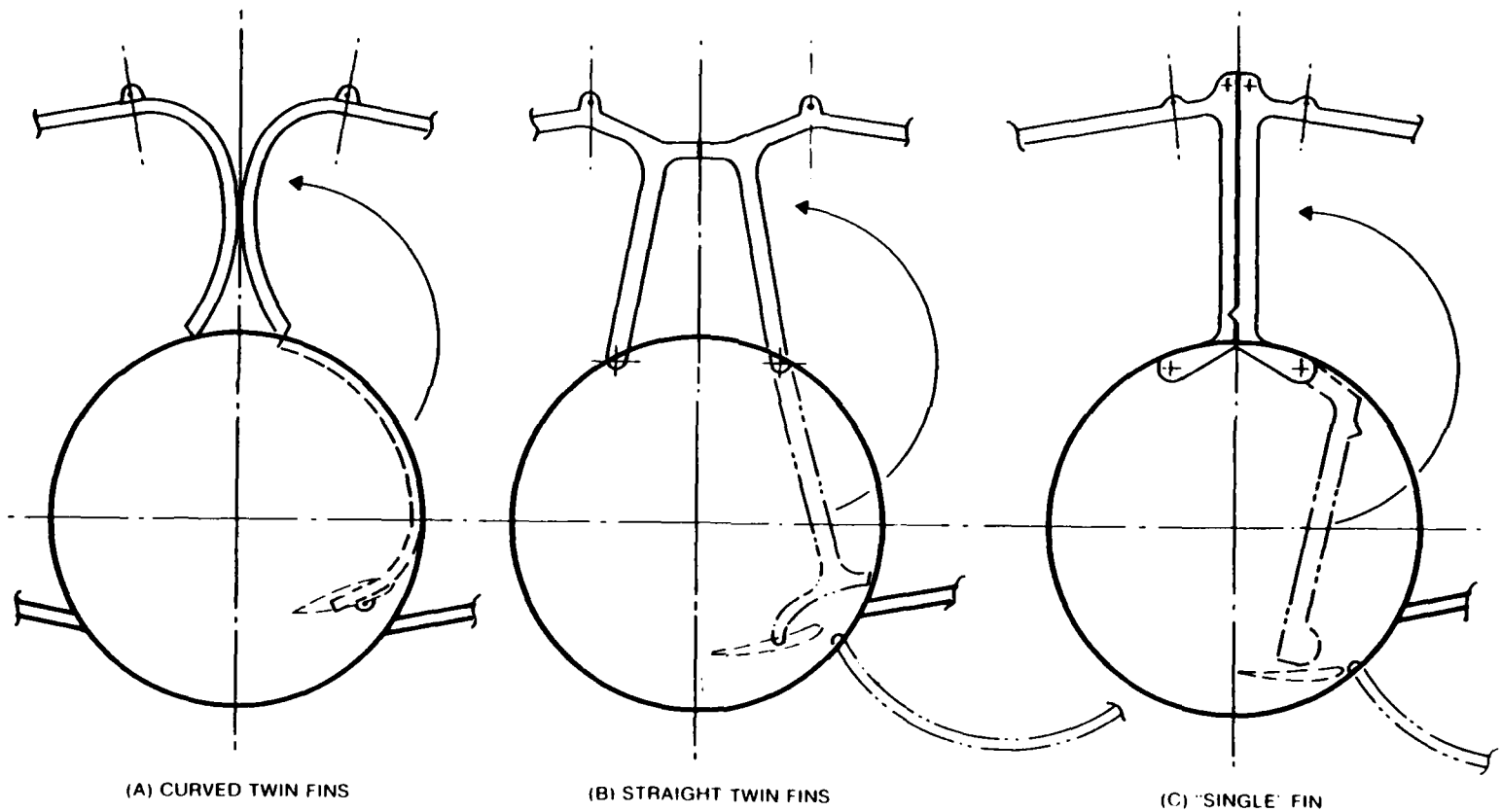

FIGURE 35. ALTERNATIVE FOLDING FIN ARRANGEMENTS

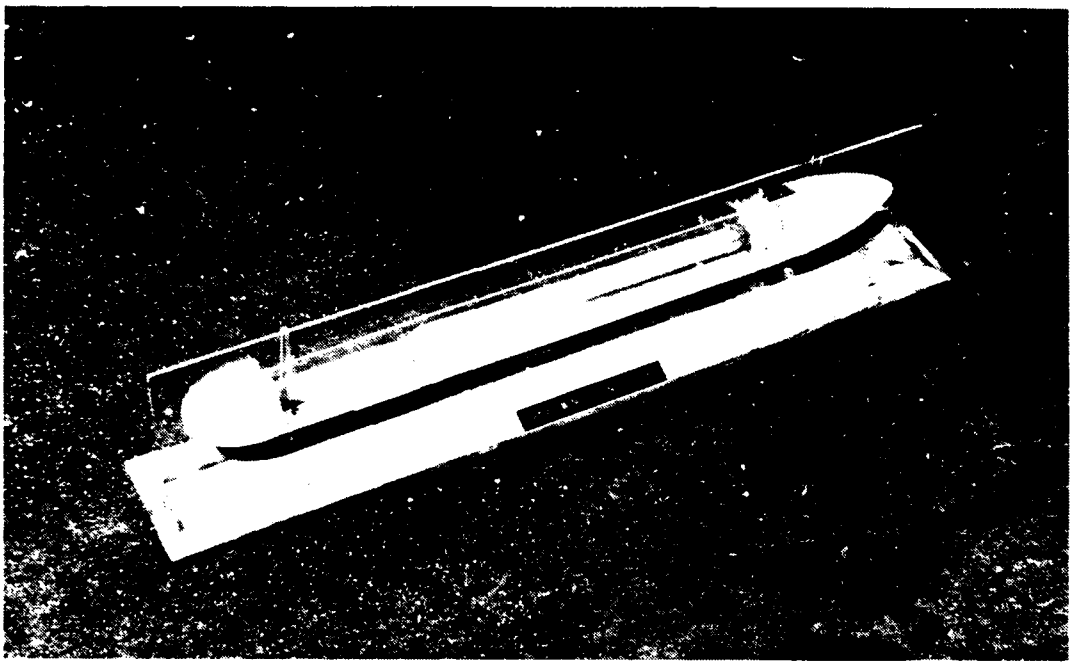

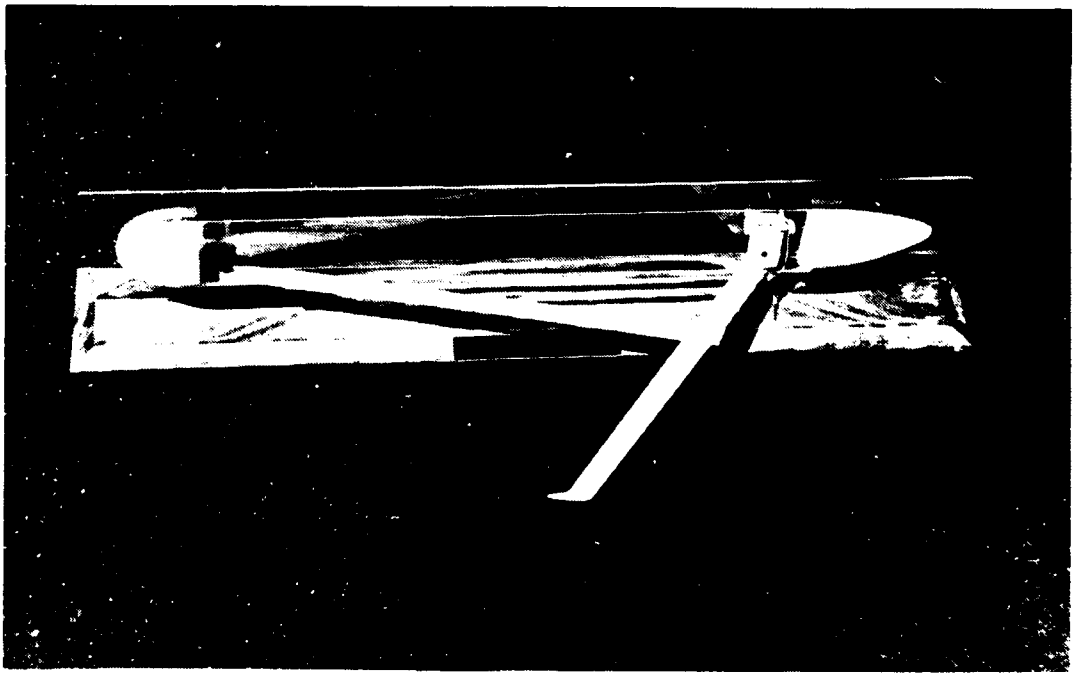

FIGURE 36(a). PHOTOS OF HALF-MODEL OF JOINED WING CRUISE MISSILE SHOWING WING DEPLOYMENT SEQUENCE (CONTINUED OVERLEAF)

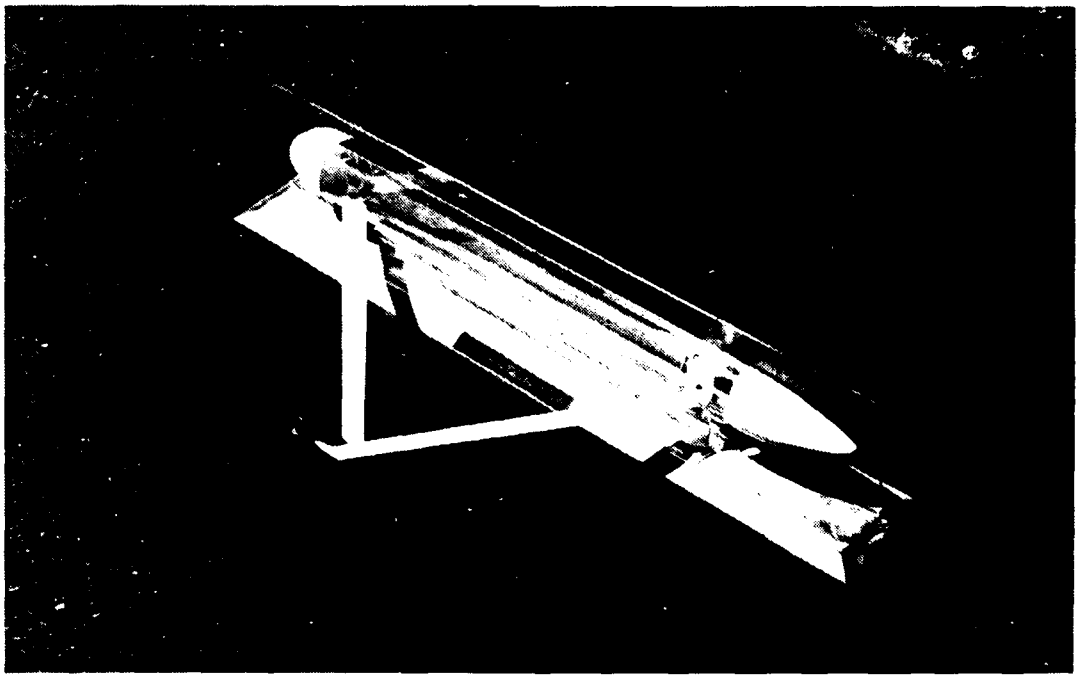

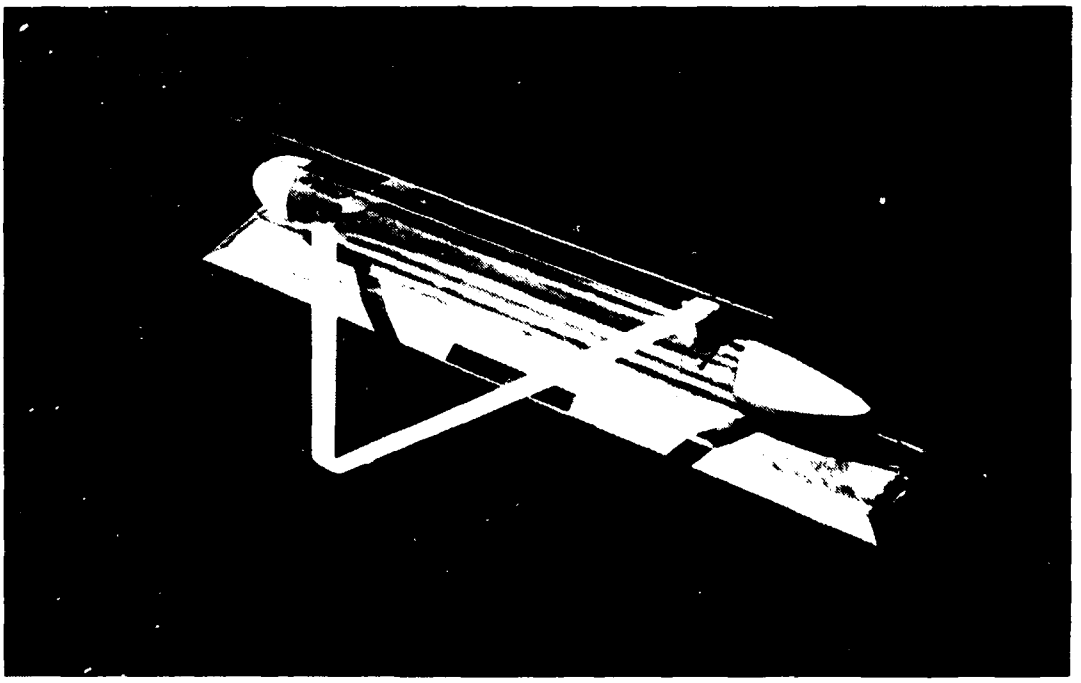

FIGURE 36(b). PHOTOS OF HALF-MODEL OF JOINED WING CRUISE MISSILE SHOWING WING DEPLOYMENT SEQUENCE (CONCLUDED)

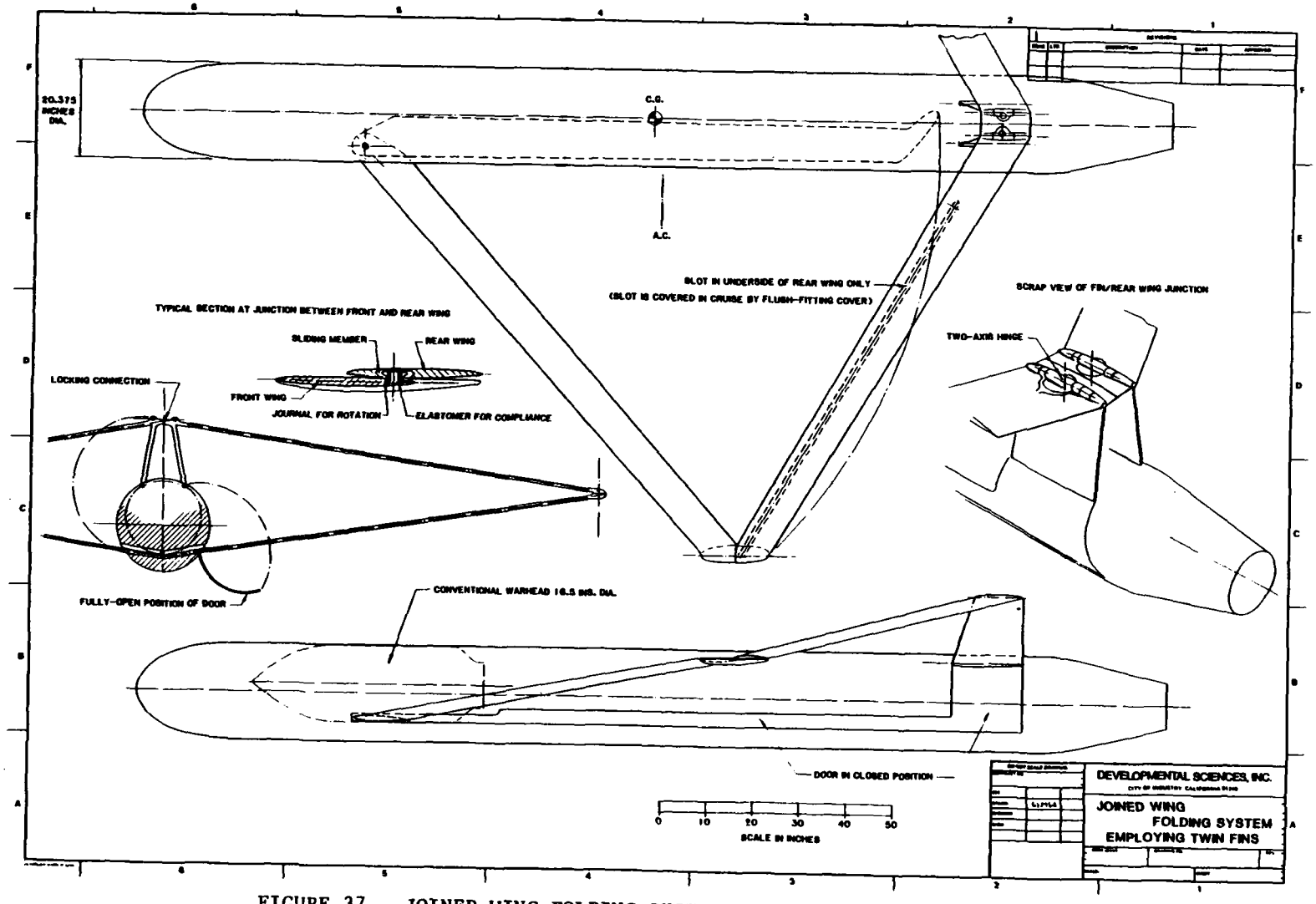

FIGURE 37. JOINED WING FOLDING SYSTEM FOR HIGHLY MANEUVERABLE CRUISE MISSILE (TWIN FIN CONFIGURATION)

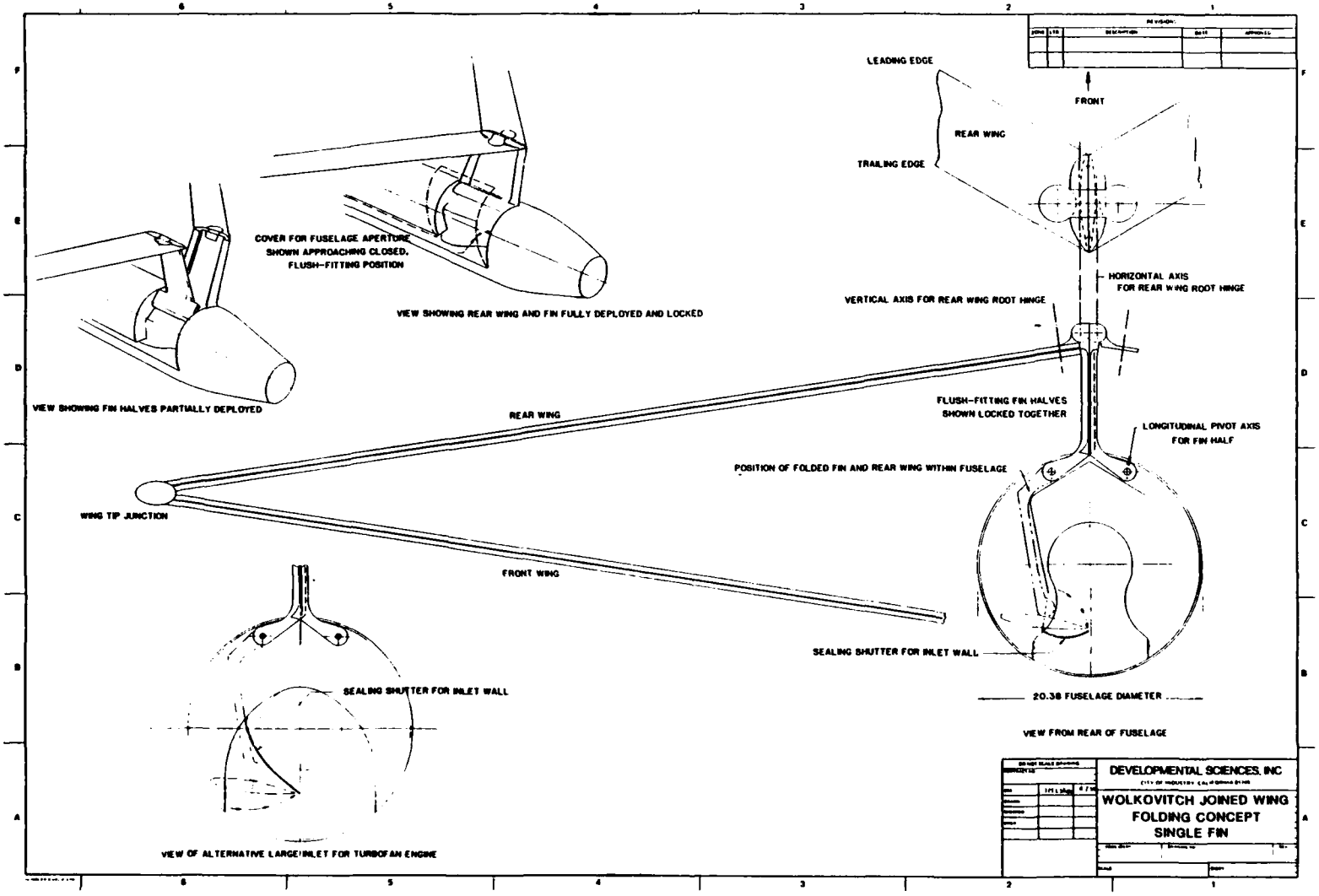

FIGURE 38. JOINED WING FOLDING SYSTEM FOR SINGLE FIN MISSILE CONFIGURATION

The fuselage slot, through which the wings deploy, is covered in cruise by a flush-fitting panel shaped like an elongated letter L. The upright portion of the L seals the cut-out in the fuselage wall through which the fin deploys; the horizontal portion extends as far forward as the trailing edge of the front wing. Sealing the junction of the front wing and fuselage can be done by similar methods to those used on existing conventional missiles with folding wings, e.g., sliding plates or elastomeric seals. Note that, immediately prior to the wings deploying, the L-shaped panel rotates downwards through approximately 180 degrees. The vertical arm of the L thus provides directional stability during deployment until the fins reach their cruise position, after which the L-shaped panel swings back up and closes to provide a smooth fuselage contour.

The model shown in Fig. 36 has demonstrated that deployment and locking can be done rapidly and smoothly, with no tendency for the mechanism to stick at any point before the fully deployed position.

Mode of Operation: In the folded position the fin halves are stored within the fuselage and the rear wing is nested above the front wing. The nested wings do not extend across the full width of the fuselage. The upper and lower portions of the fuselage are connected by a centerline structural connection approximately 1.5" wide which acts as a shear web and can accommodate fuel lines and electrical wiring. By locating the front wing below the fuselage centerline, the conventional warhead can be accommodated. The low front wing location also benefits the joined wing induced drag and structure weight.

Deployment commences with simultaneous opening of the fin and the front wing, causing the folded rear wing to swing out approximately parallel to the fuselage (see Fig. 36). Deployment continues with the overlapping wings rotating in a plane containing the top of the fins and the front wing root. This plane is initially parallel to the fuselage waterline, but as the fins rotate upwards the tilt of this plane increases. The wings are linked by a sliding single axis bearing. This

bearing slides in a slot which is located in the lower surface of the rear wing. Spring-loaded seals (discussed below) close these slots after passage of the bearing. Figure 37 specifies that the inter-wing bearing shall be mounted in an elastomeric block. This block allows the bearing axis to tilt 2 or 3 degrees in the spanwise and fore-and-aft directions to avoid binding resulting from hinge misalignments or from wing flexing.

At the end of deployment the two fins and the front and rear wings are secured by spring-loaded locking pins. The fuselage wall cut-outs are also filled by spring-loaded plates of single curvature, so that the fuselage exterior surface is smooth.

No analyses have been performed of the dynamics of deployment, but the joined wing cruise missile is expected to be as satisfactory as its orthodox counterpart provided the following recommendations are followed.

(1) The port and starboard halves of the front wings should be joined by a cross-linkage to ensure symmetry during deployment. This will also yield approximately symmetrical deployment of the rear wings, even if the two halves of the fin unfold at different rates.

(2) Deployment should be rapid, to provide centrifugal stiffening of the outboard section of the rear wing. (During deployment this section is, in effect, a swept-forward cantilever wing, and as such will be prone to divergence. A helicopter blade encounters a similar dynamic situation during one quadrant of each cycle, but does not diverge due to centrifugal stiffening. Considering the lack of root bending constraint and the high aspect ratio of the helicopter blade, we do not anticipate that divergence will occur for the much stiffer joined wing.)

(3) The booster should remain attached during deployment so that thrust vector control can be retained until the aerodynamic controls become effective.

(4) The flap covering the undersurface slot on the outboard portion of the rear wing should be capable of closing even if the rear wing is bent by airloads. This implies either a hinged flap with the hinge and flap broken up into a number of short segments, or alternatively a sliding cover as sketched in Fig. 39.

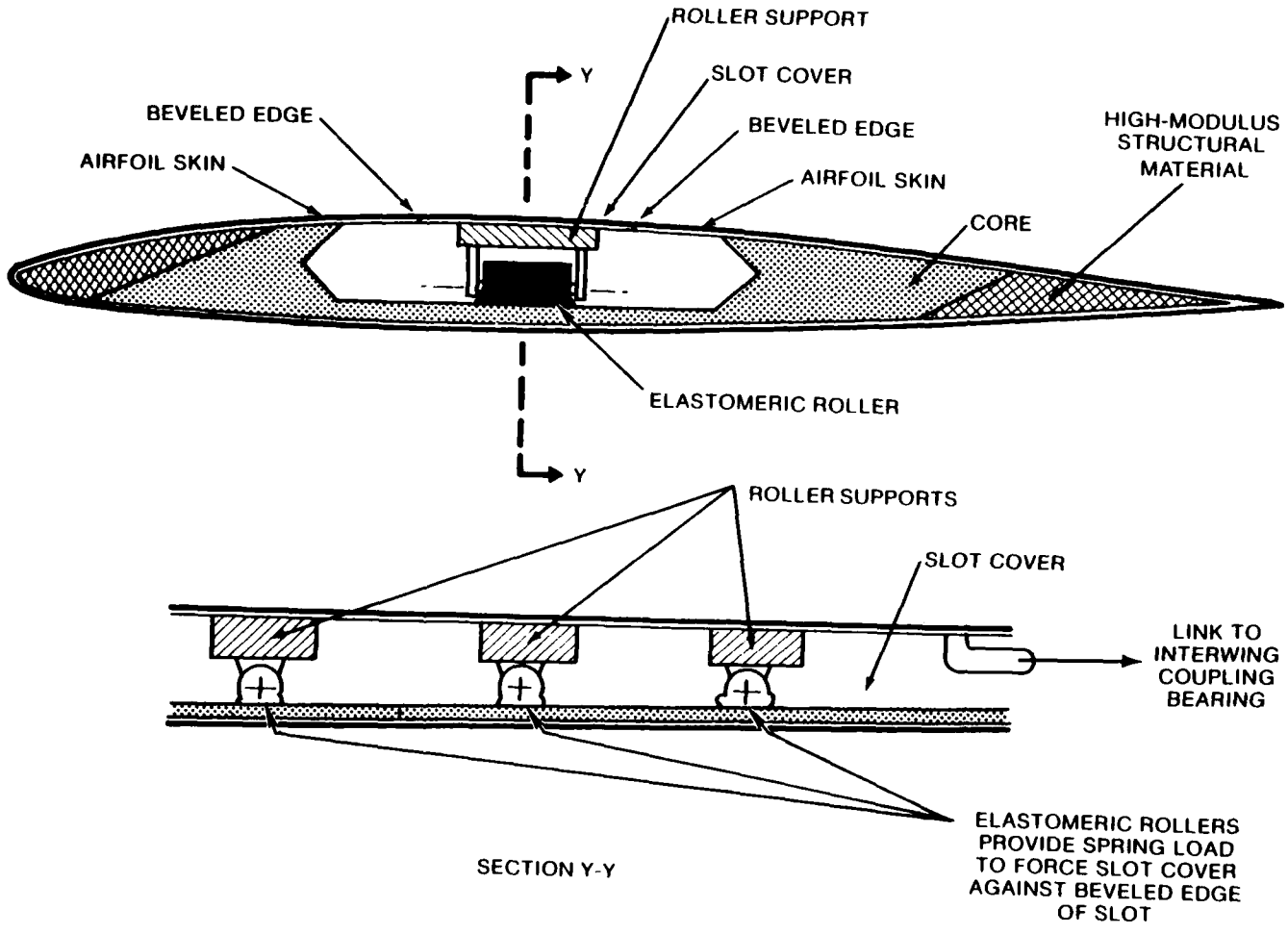

FIGURE 39. SLIDING COVER FOR UNDERSURFACE SLOT IN REAR WING

Comparisons with Conventional Wing Folding Systems: Figure 40 shows schematically two wing folding systems employed on conventional cruise missiles. The Vought Tomahawk employs the "scissors" arrangement, the General Dynamics Tomahawk employs "penknife" type folding with a single post. (Two-post penknife folding has been used on some other airframes, e.g., the Brunswick Samson decoy vehicle, but gives too narrow a root chord for the relatively slender cruise missile.) While the joined wing folding system described here is more complex than the General Dynamics system, it requires only the same total number of hinges.

G. D. Tomahawk	Joined Wing
2 Wing hinges	2 Front wing hinges
2 Horizontal tail hinges	2 (Two-axis) rear wing hinges
1 Upper fin hinge	1 Port fin hinge
1 Under fin hinge	1 Starboard fin hinge
6 = Total	6 = Total

The front joined wing cannot deploy while leaving the rear wing folded. To avoid the corresponding situation (wings, but not tail, deploying) on the conventional cruise missile a special interconnecting wing-tail linkage would have to be incorporated.

Folded joined wings occupy less fuselage volume than comparable conventional wings. This is important for advanced cruise missiles with high maneuver capability (and therefore large wings). Consider a monoplane wing of span b, mean chord c, and thickness/chord ratio t/c. The wing area is $S = bc$ and the volume is $kSc(t/c)$, where k is a constant which depends on the airfoil section. Now suppose we replace this wing by a joined wing pair also of total area S, span b, and employing the same airfoil. The chord of each joined wing is therefore half the original chord. The ratio of wing volumes is:

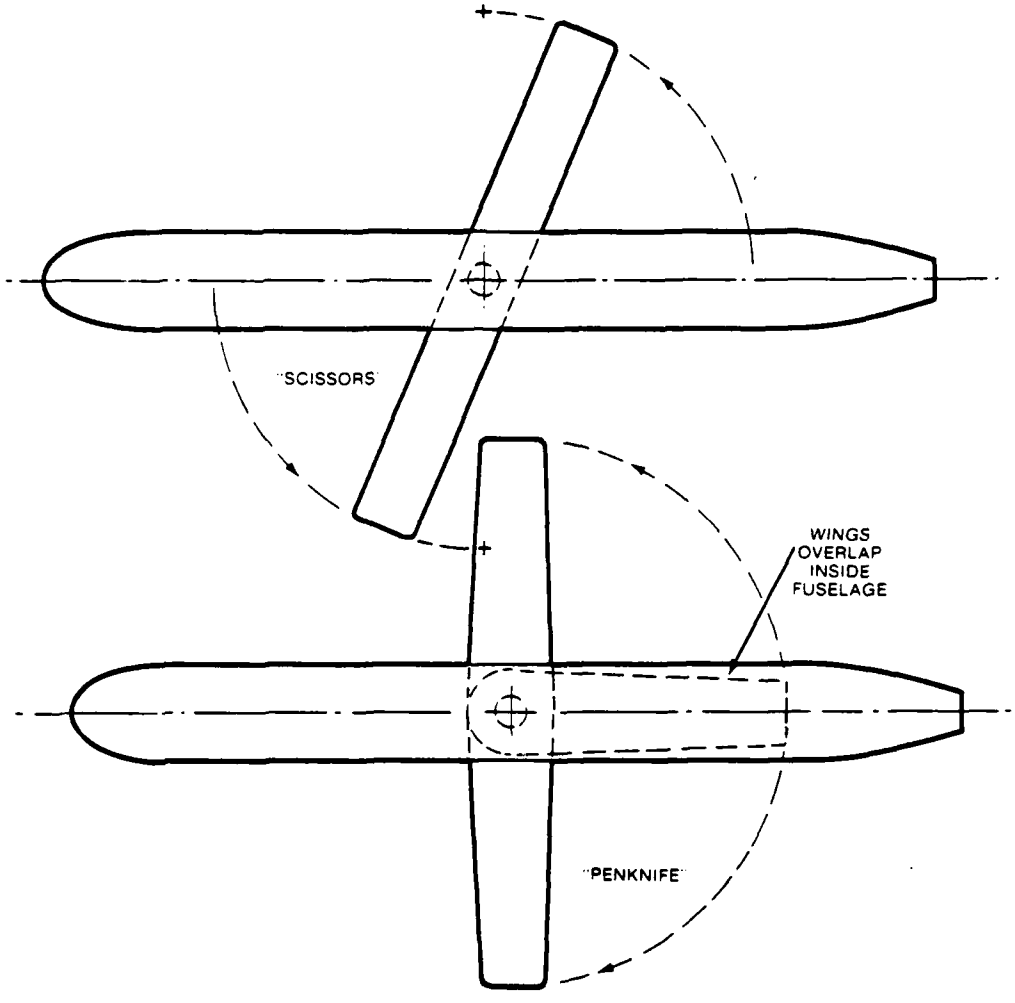

FIGURE 40. CANTILEVER WING FOLDING SYSTEMS

$$\frac{\text{Total joined wing volume}}{\text{Monoplane wing volume}} = \frac{2 \times k \times (S/2) \times (c/2) \times (t/c)}{k \times S \times c \times (t/c)} = 0.5$$

Thus the joined wing occupies only half the fuselage volume of the monoplane wing. More volume is therefore available for fuel.

A more precise calculation than that given above would take into account horizontal tail volume, the relative wing areas required for similar "g" capabilities, and the ullage (unused volume*) associated with each type of wing. As shown in Section 5, these factors do not substantially change the above conclusion.

Wing-folding for highly maneuverable vehicles of conventional layout poses severe mechanical problems. Consider, for example, Configuration 9GA of Fig. 31. The root wing chord at the fuselage sides is 2.0735 ft = 24.88 in. This exceeds the maximum body diameter of 20.375 in. The tip chord (1.98 ft = 23.76 in.) also exceeds the fuselage diameter. To compound the problem, the wing span (18.18 ft) exceeds the fuselage length (17.84 ft). Accommodating this wing inside the fuselage, while also finding room for the tail, may be exceedingly difficult. By contrast, the joined wing shown in Figs. 36-38 has a gross projected area (31.3 ft^2) comparable with the 9GA configuration wing (34.5 ft^2), yet it folds leaving ample room for the warhead, guidance system, fuel, etc. If desired, a still larger joined wing could be employed, by overlapping the folded wings. Wing areas of approximately 60 ft^2 could be accommodated in this way.

Inlet Flap: The flush inlet shown on Figs. 37 and 38 is similar to that employed in the Vought YBGM-110 Tomahawk. The folding system does not encroach upon this inlet, and also is compatible with pop-down inlets such as employed in the G.D. YGBM-109 Tomahawk. Advanced cruise missiles

*Airfoil area is typically 0.60 to 0.65 times the product of chord and maximum thickness. Thus the ullage due to folding an airfoil into a box-shaped compartment of length ℓ is 0.35 to 0.40 times $\ell c^2(t/c)$.

may require larger inlets. This does not present an obstacle to folding the joined wings. All that is required is to incorporate a spring-loaded hinged flap in each side of the inlet, as shown in Fig. 38. The flap hinges inwards when the wings are folded, permitting the wings to occupy the empty space inside the inlet. For inlets with double curvature several short hinged flap segments should be employed.

Wing Taper: Untapered wings are more convenient to fold than tapered wings and are cheaper to manufacture. These advantages are offset by structural weight penalties. Hence, for joined wing configurations having relatively small wing area, untapered wings may be acceptable. (A configuration with untapered wings is described in Section 3.6. This configuration reduces wing area through employing a canard to generate part of the lift.) For initial studies a moderate taper ratio (≈ 0.5) is recommended.

3.4 WING WARPING CONTROL

Since the front wing of a joined wing pair has a constraint at its tip due to the tip joint, it can be warped for pitch and roll control via actuators mounted near its root. Such wing-warping control eliminates hinged control surfaces thus simplifying the wing structure and the control system, and also reduces radar cross-section by eliminating radar reflections from control surface hinge discontinuities. The feasibility of wing-warping has been studied in a preliminary fashion: the results appear promising, as described below.

A structural analysis of the torsional/flexural interactions of the front and aft wings was performed. This was aimed at predicting the spanwise incidence variation induced by torques applied at the front wing root. A number of simplifying assumptions were made, e.g., untapered wings with equal chords and equal (positive and negative) sweep angles, isotropic material properties, and infinitely rigid tip joints were assumed. With these assumptions the spanwise incidence variation was found to be parabolic across both wings. For example, if the front wing root is twisted such that its incidence is increased by 4 degrees, the corresponding

induced incidence at the tip is 1 degree, while at the mid semi-spans the incidences are 2.25 degrees and 0.25 degrees on the front and rear wings respectively. This parabolic variation is typical of untapered wings made of isotropic material. The torsion applied to the front wing is opposed by the flexural stiffness of the aft wing, so by judicious tailoring of fiber orientation other (nonparabolic) variations can be obtained, if desired.

Two prime aspects have been studied: (a) the aerodynamic forces and moments generated by warping; (b) mechanical design of the warping mechanism and integration with the wing folding system. Initial indications regarding (a) are that the steady g's obtained per degree of root twist are typically 1/3 to 2/3 of the g's per degree of aft tail deflection for the aft tail cruise missile having the same total lifting surface area. For the Vought Tomahawk the aft tail pitch control deflection was limited to ±5 degrees. It appears reasonable to allow a larger limit for wing root twist (e.g., 15 degrees) hence adequate longitudinal control is expected to be available from wing warping provided premature flow separation does not occur near the root of the front wing. To ensure this the root airfoil must be properly designed and a good wing root seal must be maintained. The importance of proper sealing of the wing root for maintaining good fuselage "carry-over" of wing lift has been demonstrated by wind tunnel test data on a folding missile given in Ref. 34.

The wing warping mechanism must satisfy some difficult spatial constraints since it should be located within the fuselage below the front wing root in order to leave the space above the root free for warhead or fuel. In addition, it is desirable that the actuators and gears remain fixed during deployment. In the scheme shown in Fig. 41, the front wing is mounted in a yoke which has a transverse bearing to permit wing deployment. The yoke can be rotated about an axis parallel to the wing quarter chord line by means of a spur gear segment driven by a reversible servo motor. The conceptual design shown in Fig. 41 complies with the spatial constraints listed above. It is also mechanically and structurally

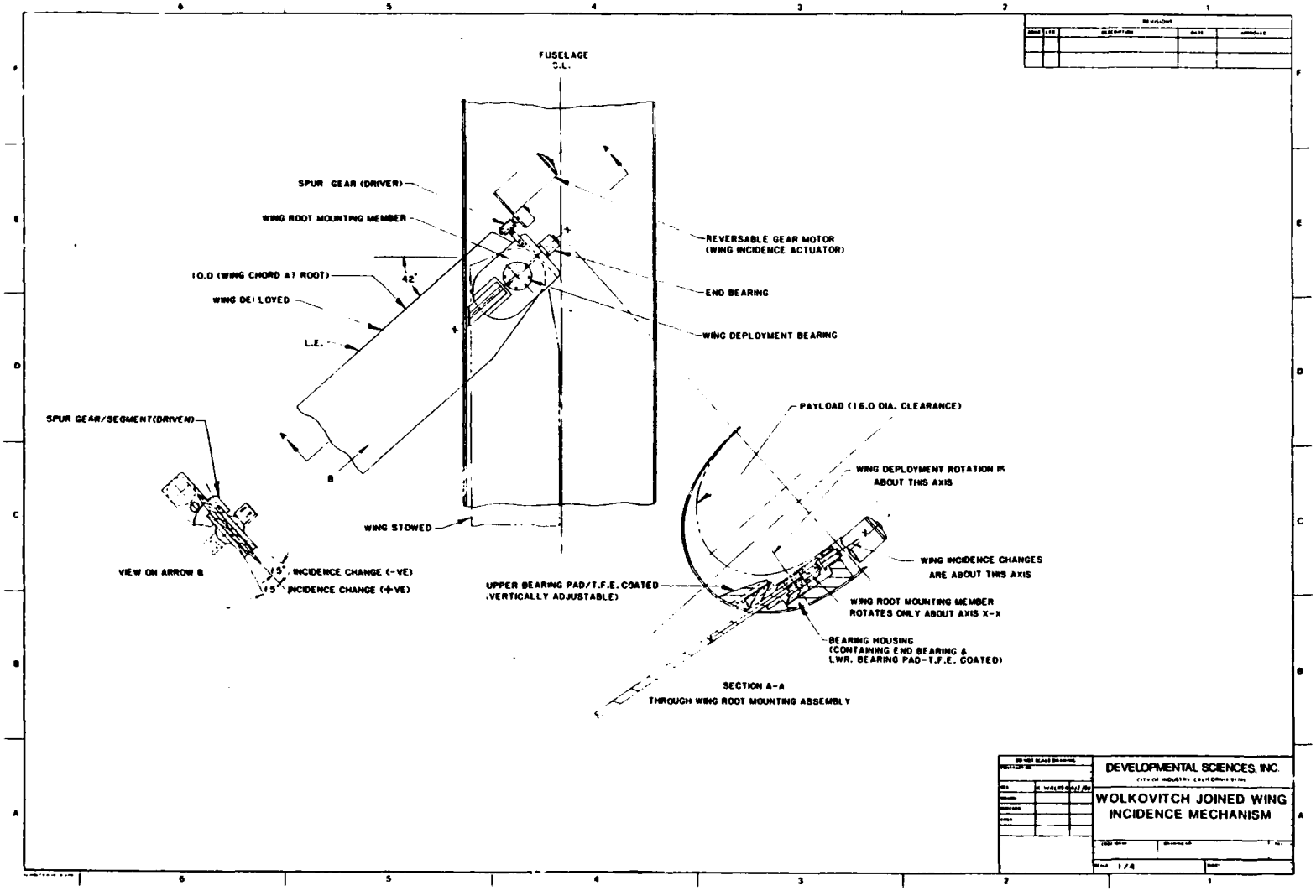

FIGURE 41. WING-WARPING CONTROL SYSTEM

simple and should have less backlash than conventional control systems, which use push-rods to actuate hinged flaps, elevators, and ailerons.

3.5 VARIABLE CAMBER

Variable camber has long been recognized as yielding significant aerodynamic advantages for aircraft that must develop high L/D over a wide range of lift coefficients. Unfortunately, a conventional cantilever wing presents considerable mechanical difficulties in mechanizing variable camber. This is because numerous actuators must be mounted within the wings. For a joined wing the possibility exists of varying camber via two sets of actuators, one set located within the fuselage at the wing root, the other set located inside the tip joint fairing. Such a system would not induce constant camber across the entire span, but conceivably the spanwise variation of camber might be small, and acceptable in view of the saving in the numbers of actuators required. Additionally, since the actuators are outside the airfoils, thin airfoils could be employed (e.g., for supersonic cruise).

For a cruise missile the prime benefit of variable camber is that, as fuel is consumed, and wing loading reduced, camber can be reduced to maintain the highest possible L/D, thus maximizing range. This possibility was considered in the present study but was not pursued because:

(1) To demonstrate the feasibility of variable camber would have required more extensive mechanical design studies than could be justified for the funds available.

(2) An attractive alternative form of variable geometry exists, which is well suited to the joined wing; this is "staging," which is described below.

3.6 STAGED JOINED WING CONFIGURATION

Figure 42 shows a configuration employing joined wings which deploy similarly to those of Fig. 36. The configuration also includes a canard surface which is attached to a nose tank which is ejected when empty.

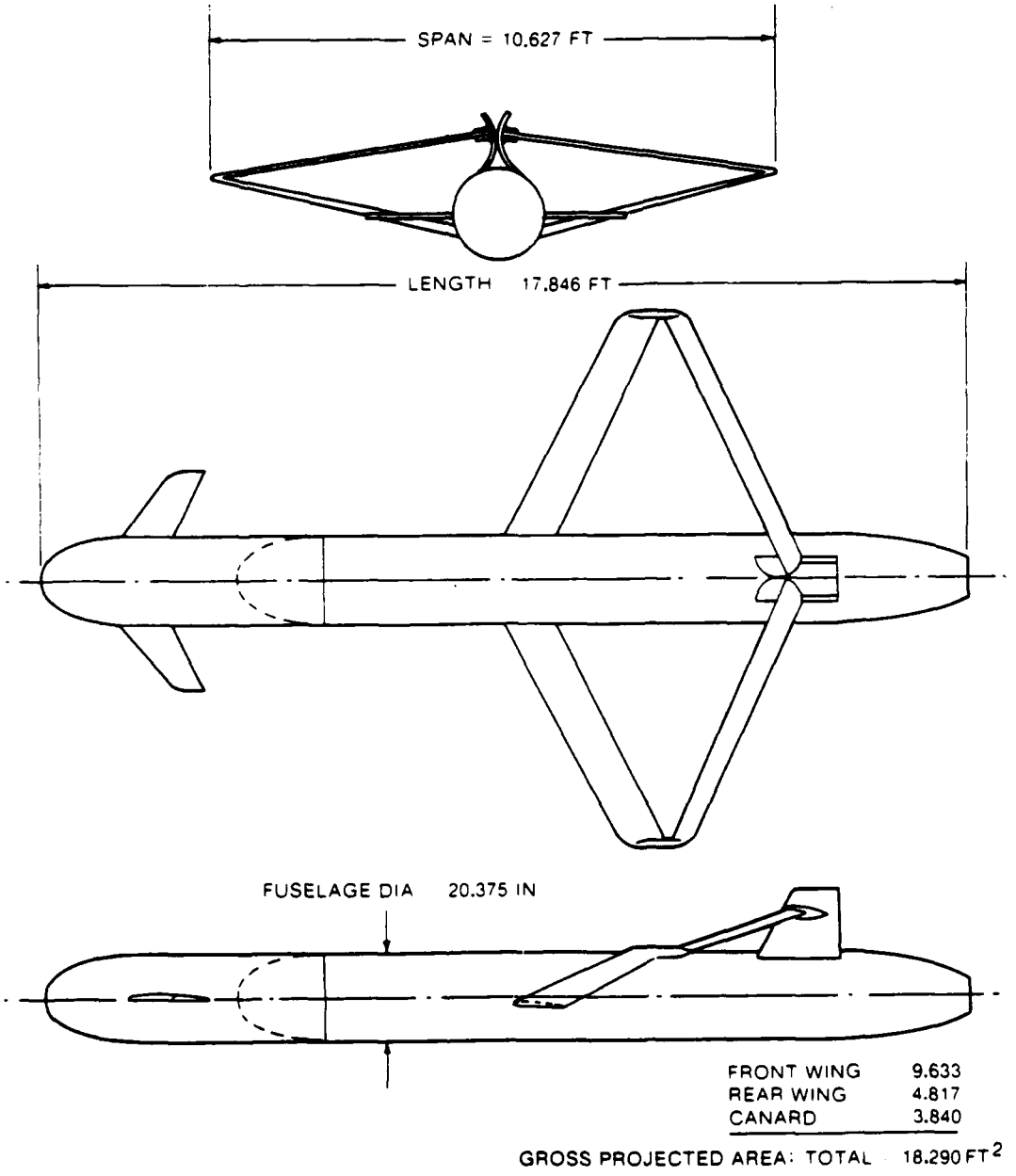

FIGURE 42. HYBRID TWO-STAGE CONFIGURATION WITH UNTAPERED JOINED WINGS

Such a configuration is feasible with the downward-looking guidance and terrain-following system (TERCOM) used in current Tomahawk cruise missiles and projected cruise missiles.* The objectives of this staged configuration are:

(1) To improve range, speed and maneuverability by reducing missile drag and weight during the latter portion of the mission.

(2) To reduce radar cross-section.

(3) To reduce the required operating range of C_L on the joined wings, permitting the use of airfoils of lower drag coefficient.

(4) To reduce the fuselage volume taken up by the folded lifting surfaces (for a given thickness/chord ratio and given total area three lifting surfaces occupy less volume than two, or one).

(5) To provide a modular missile in which the lifting surfaces do not intrude on the fuselage sections occupied by the guidance equipment and warhead. Figure 43 shows an inboard profile which illustrates this advantage. Such a modular arrangement facilitates the use of alternative warheads and guidance systems.

(6) To provide a decoy capability. If desired, the nose section can be powered (e.g., by a booster) so that, as the missile closes with its target, the nose section flies off, thus providing an additional radar signal to confuse the enemy during a critical phase of the attack. By using the canard plus pop-out fins, the decoy can maneuver.

Figure 44 illustrates the proposed method of fairing the nose tank. This leaves a smooth fuselage contour after the nose has separated. Experimental data given on p. 5-7 of Ref. 15 indicates that the drag penalty for the 1/32" step surface irregularity that exists before separation should be small, representing only a 1.2% increase over the drag of a smooth fuselage. For conservatism, the performance calculations of Section 5 assume a 2% drag increase, corresponding to a 1/20" step.

*Downward-looking radar altimeter systems are preferred to forward-looking systems because they give a smaller radar signature to the enemy.

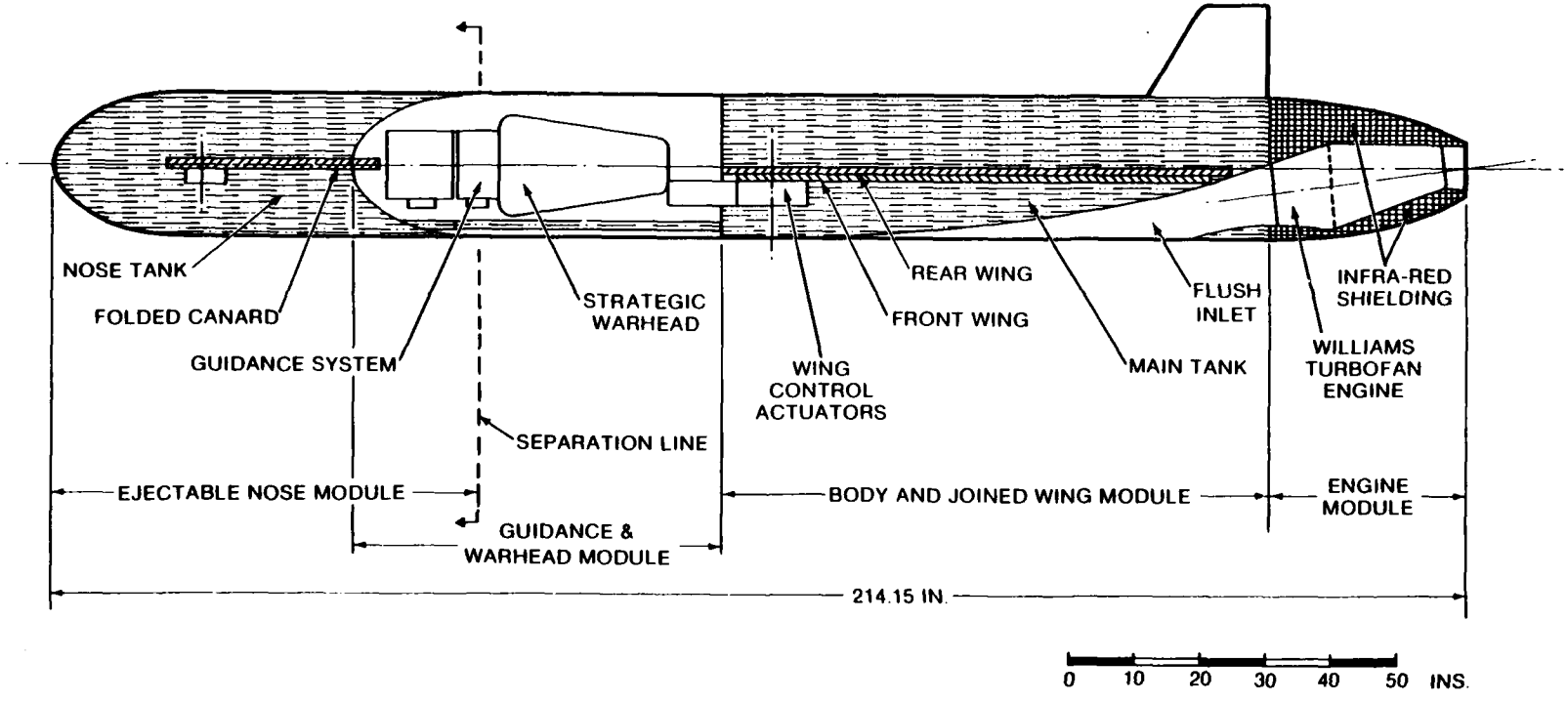

FIGURE 43. INBOARD PROFILE OF HYBRID CONFIGURATION OF FIG. 42

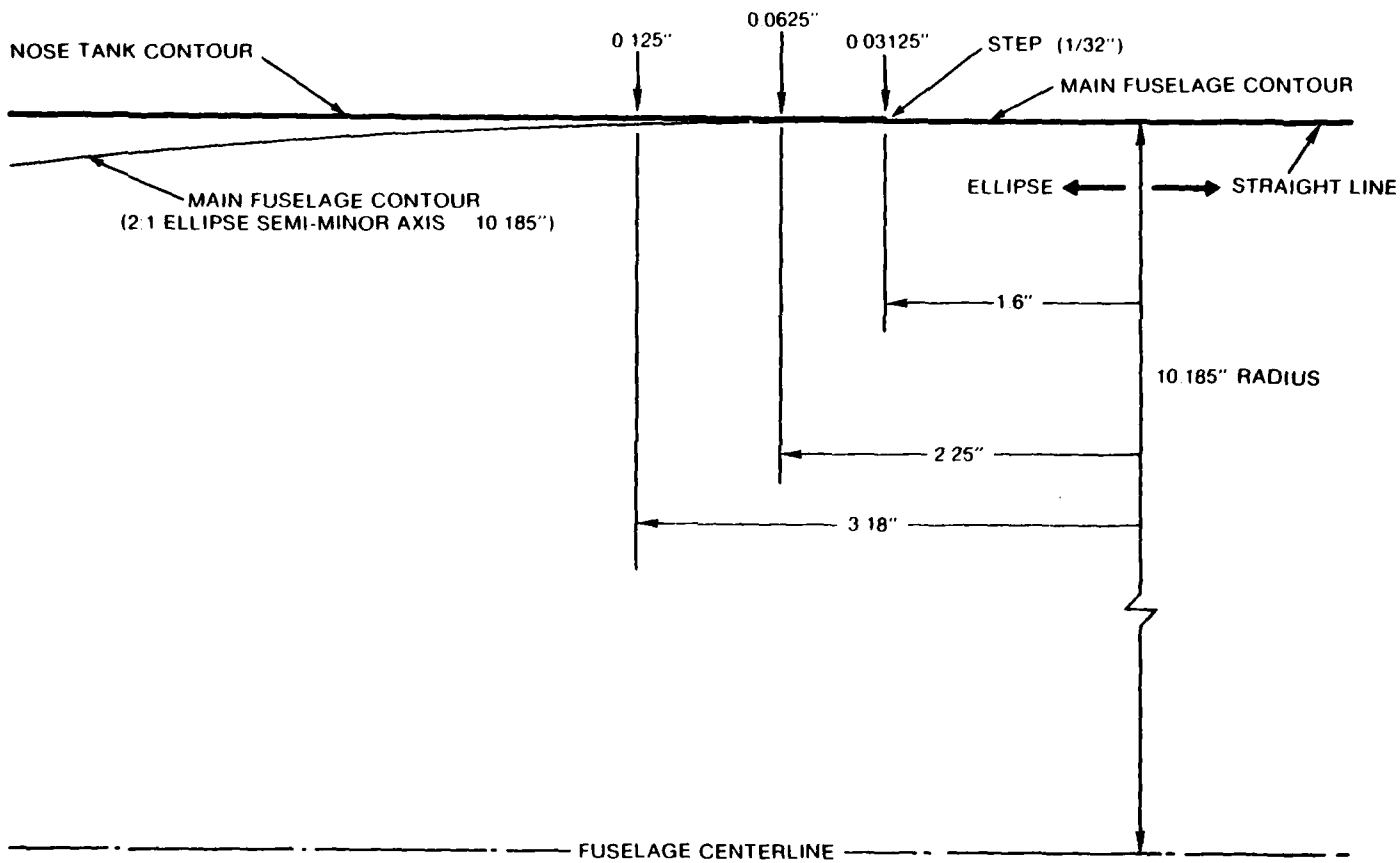

FIGURE 44. DETAIL OF NOSE TANK ATTACHMENT GEOMETRY FOR TWO-STAGE CONFIGURATION

For the configuration shown in Fig. 42, ejecting the nose tank reduces the missile's total wetted area by 19% and empty weight by 5%. Detailed estimates of the performance benefits of staging are given in Section 5.

A key factor determining the practicality of staging is the longitudinal stability of the configuration. This is best measured by the maneuver margin, but for initial studies the static margin provides an acceptable index of stability. Figures 45 and 46 illustrate the effect of fuel consumption and staging on static margin for the configuration of Fig. 42. Figure 45 applies for the canard surface having a fixed sweep angle, $\Lambda_{c/4} = 35^{o}$ as drawn in Fig. 42. Figure 46 applies for a canard having a sweep angle which progressively increases from 35^{o} as the nose tank is emptied.

With constant canard sweep the static margin becomes unstable as the nose tank is emptied, as shown by the upper lines in Fig. 45. Immediately after ejecting the nose tank the static margin becomes slightly unstable, but it becomes much more stable as the aft fuel is consumed.

Although a slightly unstable static margin is tolerable, it would be preferable to have a small positive static margin throughout the flight. Figure 46 shows how this can be obtained by varying the canard sweep as nose fuel is burned. The lower part of Fig. 46 illustrates how excessively large static margin can be delayed via fuel management, i.e., splitting the aft fuel into two tanks and emptying the more forward tank first. A similar benefit can be obtained with a single aft tank by trimming the missile to fly more nose up as fuel is consumed. (This can be done via the direct lift capability of the joined wing.) Neither fuel management nor attitude adjustment can change the static margin when the fuel tanks are nearly empty. However this limitation is not expected to be serious because:

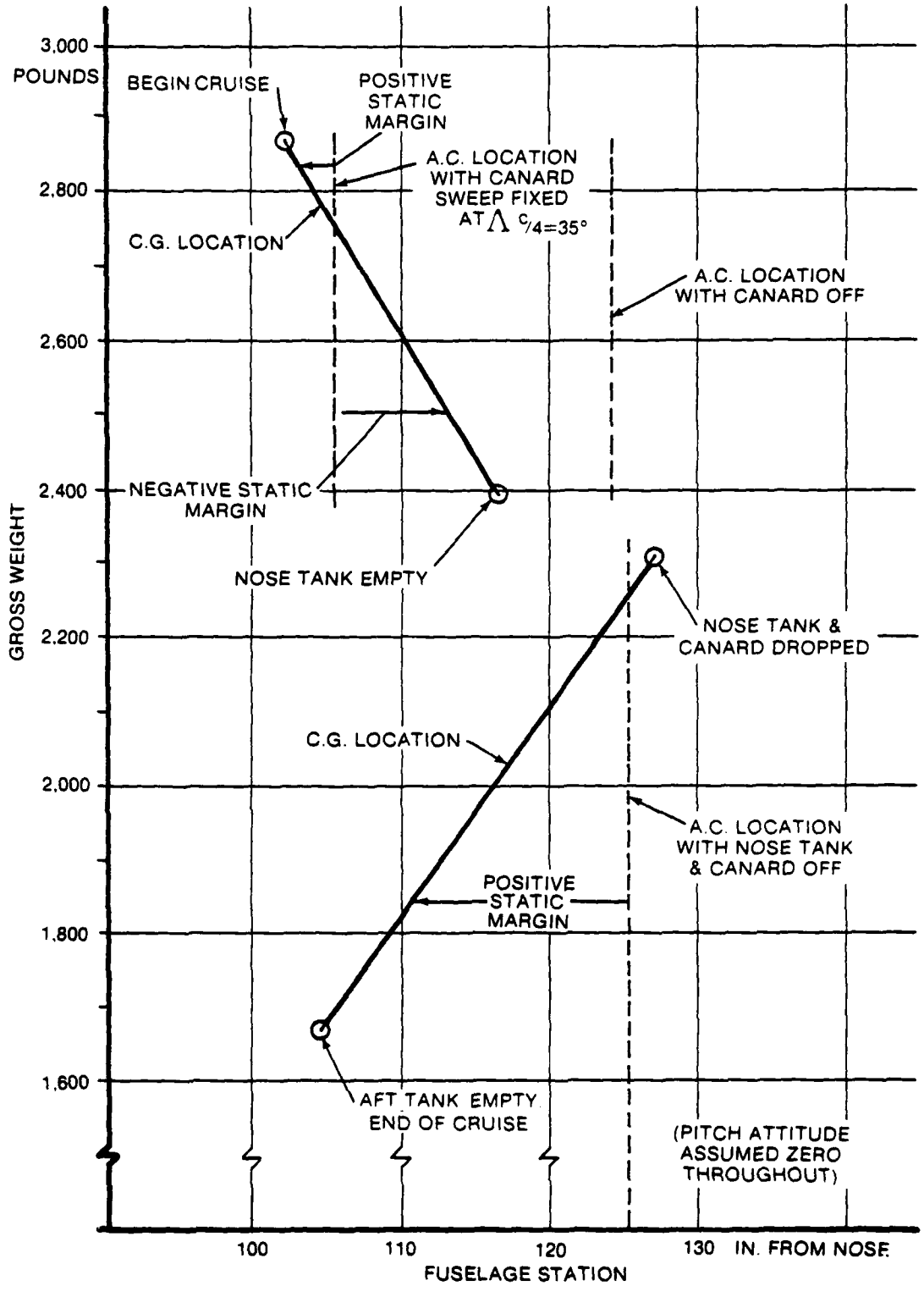

FIGURE 45. STATIC MARGIN VARIATION WITH WEIGHT: FIXED CANARD SWEEP ANGLE

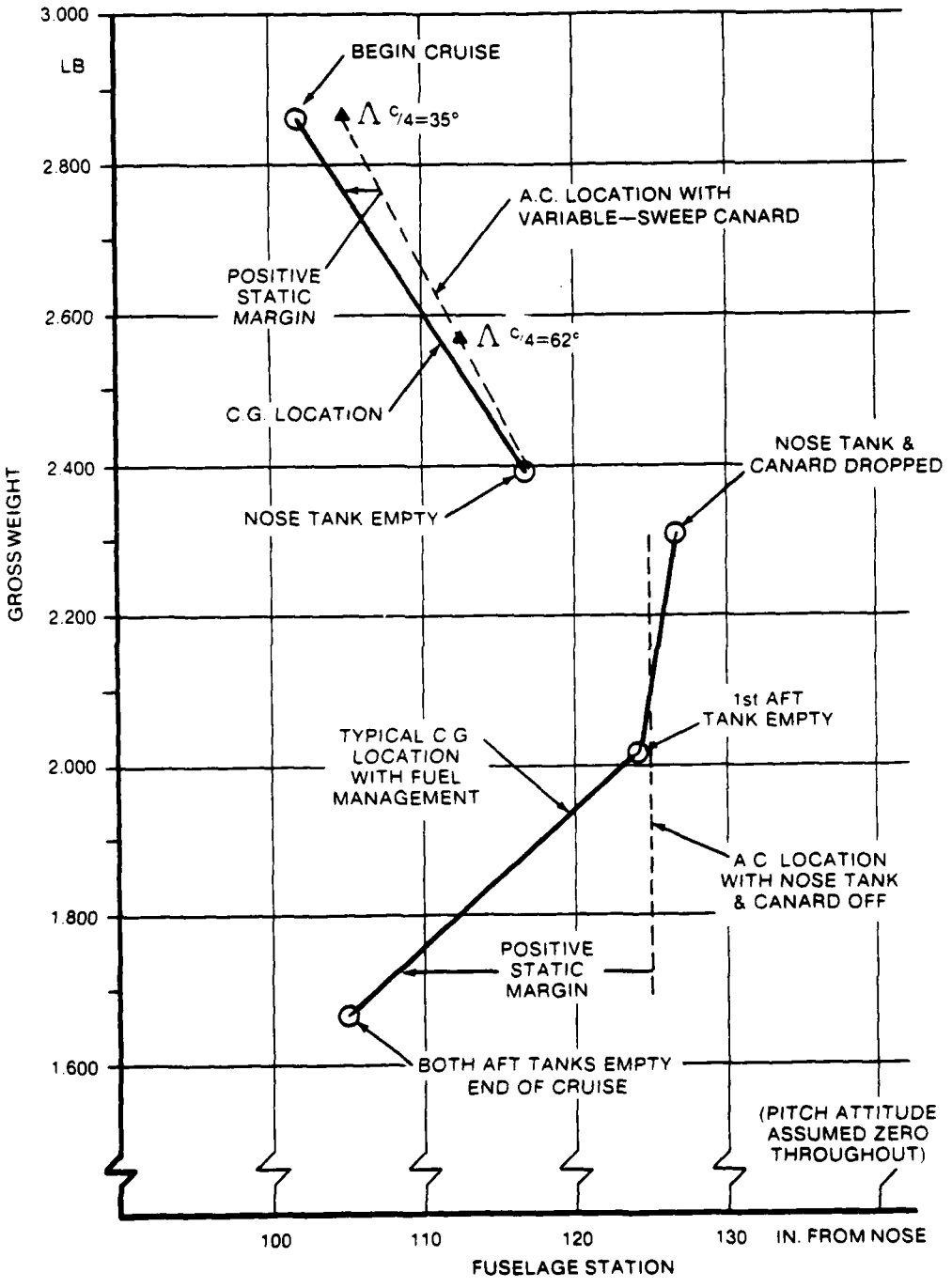

FIGURE 46. STATIC MARGIN VARIATION WITH WEIGHT: VARIABLE CANARD SWEEP ANGLE

(1) Only a small percentage of missions will require maximum range.

(2) Near maximum range the low gross weight will improve maneuverability.

(3) With direct lift control, excessive static margin does not impair maneuverability as much as it does for aft tail control.

From the above discussion, staging appears to be practical and promising. The joined wing configuration is particularly well suited to staging because of the inherently wide c.g. range over which it can be trimmed. (If desired, 100% of the lift can be carried on the front wing.)

Staging is not suitable for aft tail configurations because the c.g. range shown on Figs. 45 and 46 (approximately 25") is large compared to the normal trim range (with conventional tail/wing area ratios). It does not appear feasible to alleviate this situation by variable wing sweep, e.g., going from sweepforward to sweepback as the c.g. moves aft. This demands excessive sweep angle variations and/or spans.

The next section of this report discusses terrain-following. Readers who are interested in performance rather than guidance and control may prefer to read Section 5 before Section 4.

4.0 AIRFRAME DESIGN FOR TERRAIN-FOLLOWING

4.1 APPLICATION OF OPTIMAL CONTROL THEORY

A cruise missile, like a submarine, depends critically on stealth. This is achieved by:

(1) Designing the vehicle to have low observables.

(2) Flying close to the surface of the sea or terrain.

In this section we investigate the consequences of Requirement (2) on the best selection of missile airframes.

If very low altitude flight is to be performed successfully the flight path of the missile must reflect the irregularities of the terrain or waves. Terrain-following with low clearance requires an effective guidance system. However as will be shown, even with an optimum guidance system, terrain-following accuracy is limited by the dynamic response characteristics of the airframe. Hence, comparing the terrain-following accuracy of joined wing and conventional airframes, each having individually optimized guidance systems, provides one facet of an overall comparison of airframes. To perform such a comparison, criteria for optimality must first be defined. This can be done as follows.

Current and projected cruise missiles employ downward-looking terrain-following systems which measure the missile's clearance above the terrain, i.e., h_c in Fig. 47. (Downward, rather than forward-looking guidance is employed because it is less easily detected by the enemy.) A bias setting is incorporated in the guidance logic, corresponding to a desired constant clearance h_B. The difference between h_B and h_c, at any instant, is the height error, h_e. If h_e has a symmetrical statistical distribution, the mean value of h_e, $E(h_e)$, may be assumed to be zero. To achieve stealth h_B should be low and upward deviations from h_B should be small. With a low h_B, downward deviations from h_B must also be small

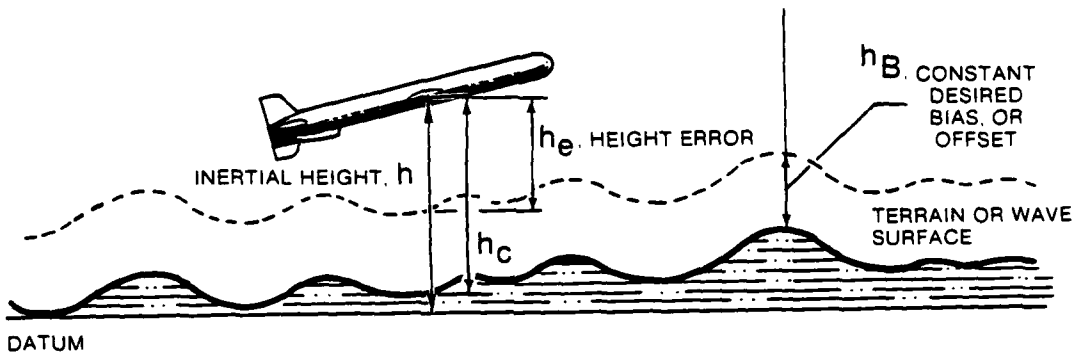

FIGURE 47. CRUISE MISSILE FLYING ABOVE TERRAIN

to reduce the probability of hitting the terrain (usually called "probability of clobber," p_c). Therefore a reasonable optimality criterion for the guidance system is that it should minimize the mean square height error, $E(h_e^2)$. This criterion has the advantage of being mathematically convenient, and it is widely employed in Optimal Control Theory. This theory shows how to compute the guidance system that (for a given airframe) yields minimum $E(h_e^2)$. The theory also yields short-cut methods for computing the minimum $E(h_e^2)$ and also the associated mean square control deflection $E(\delta^2)$.

While there are advantages to employing minimum $E(h_e^2)$ as a criterion for terrain following, it should be realized that the minimum $E(h_e^2)$ system is only an approximation to the minimum p_c system. This is because p_c depends on the frequency characteristics of h_e as well as its statistical amplitude distribution. For example, consider two Gaussian h_e time histories, having identical $E(h_e^2)$ but with the first having a higher bandwidth than the second. For equal flight durations, the high-bandwidth h_e will have the greater number of exceedances of any specified boundary value. (For further discussions of the relative utility of $E(h_e^2)$ and p_c as optimization criteria see Ref. 36. References 37 and 38 are also of interest: these explain some of the difficulties and high computer time requirements involved in computing p_c.) Although $E(h_e^2)$ is a less precise measure of system merit than p_c, it provides a valid and cost-effective basis for comparison of alternative preliminary configuration designs and will be used here for that purpose.

In the remainder of this section we present power spectra for terrain to be followed (actually ocean waves) and also for atmospheric turbulence appropriate to low altitudes. Transfer functions are then given for the alternative joined wing, hybrid (i.e., joined wing + canard), and conventional airframes shown in Figs. 31 through 34. The best achievable terrain-following performance of each configuration is then calculated (i.e., the minimum achievable $E(h_e^2)$. It is shown that the hybrid and the joined wing configurations are potentially capable of closer-terrain

following than the conventional aft tail configurations. This advantage is due to the fact that the aft tail airframes initially move in the wrong direction following elevator commands intended to change altitude. By contrast, the joined wing configurations have responses which are always in the desired direction. Finally, it is shown that, for the wind and wave conditions specified, practical realization of this advantage requires height to be controlled by two control surfaces. Thus the hybrid configuration requires simultaneous control of front wing flaps and canard incidence for closest terrain-following. The basic joined wing configuration requires the lift generated on each wing to be controlled, e.g., by flaps on each wing.

4.2 SYSTEM DESCRIPTION

Under this heading we describe the mathematical models employed to represent the airframe, its atmospheric turbulence environment, and the "terrain" (sea surface). A more complete description of each of these is given in Appendix A: only the bare essentials are presented here.

Airframe Equations of Motion: Short-period longitudinal equations are employed; it is assumed that airspeed variations are suppressed perfectly by an outer throttle loop not shown on Fig. 48. The equations of motion are transformed from the standard form given in Ref. 39: they are written in terms of height perturbations (h) and pitch angle perturbations (θ) as:

$$\begin{bmatrix} s - Z_w & -Z_\alpha \\ -\dot{M_w}s - M_w & s^2 - (M_q + \dot{M_\alpha})s - M_\alpha \end{bmatrix} \begin{bmatrix} -sh \\ \theta \end{bmatrix} = \begin{bmatrix} Z_\delta \\ M_\delta \end{bmatrix} \delta + \begin{bmatrix} -Z_w + Z_q s/U_o \\ -\dot{M_w} + M_q s/U_o - \dot{M_w}s \end{bmatrix} w_g \tag{10}$$

δ denotes a single control surface deflection, subsequently multiple controls are denoted as δ_1, δ_2. w_g is the vertical component of turbulence. The terms $Z_q s/U_o$, $M_q s/U_o$ multiplying w_g are "gust-gradient" terms (Ref. 39, p. 251). Following customary practice the Z_q term is neglected, since $Z_q << U_o$.

AD-A096 450 AERONAUTICAL CONSULTANT ASSOCIATES RANCHO PALOS VERDES CA F/G 16/4
APPLICATION OF THE JOINED WING TO CRUISE MISSILES.(U)
NOV 80 J WOLKOVITCH N00014-79-C-0953
UNCLASSIFIED ONR-CR212-266-1 NL

2 OF 3
AD
A096450

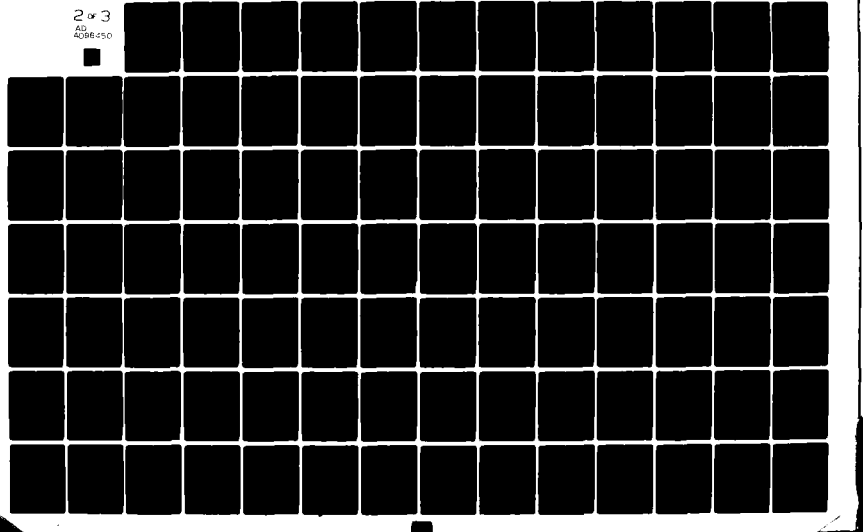

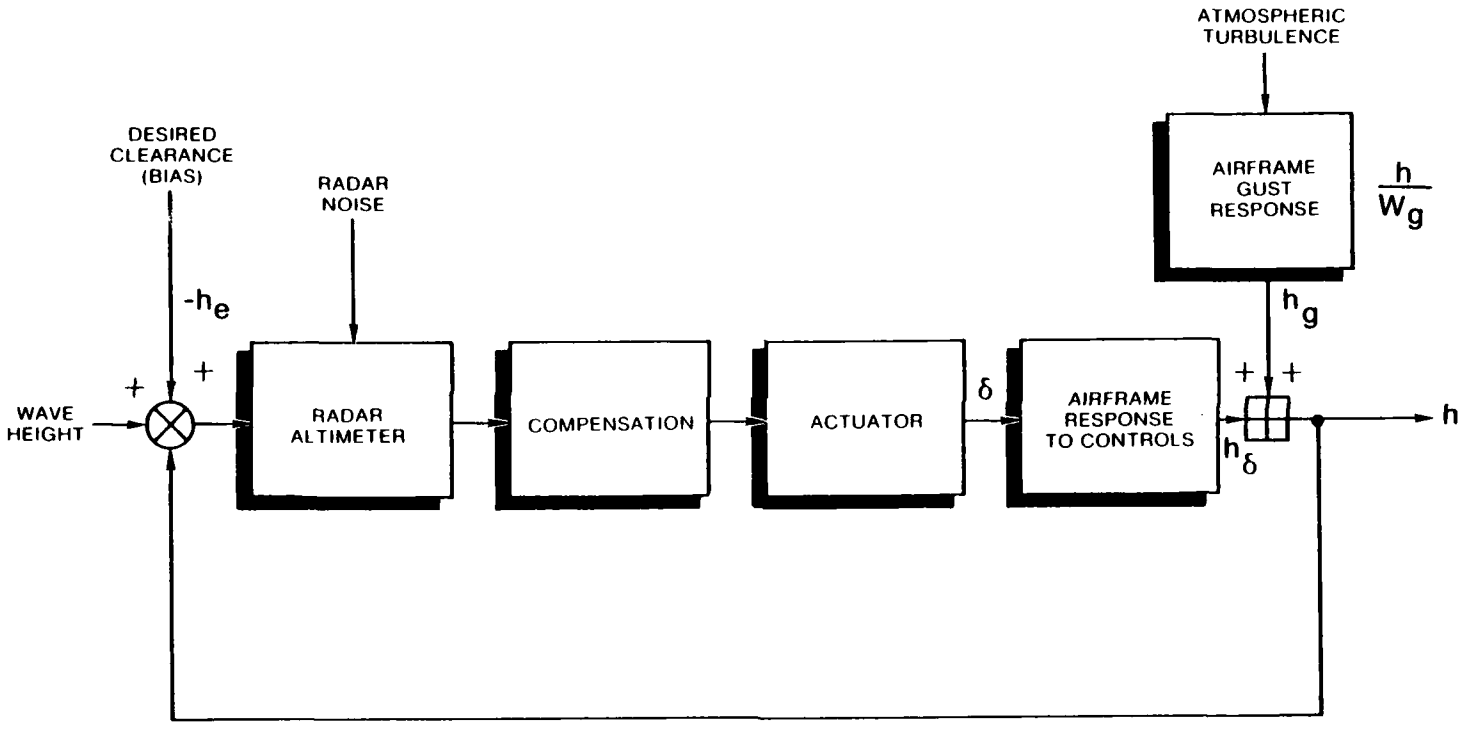

FIGURE 48. TERRAIN-FOLLOWING SYSTEM BLOCK DIAGRAM

The principal transfer functions of interest are those describing the height response to control and also to vertical gust components.

$$\frac{h}{\delta} = \frac{-Z_\delta s^2 + Z_\delta(M_q + M_{\dot\alpha})s + Z_\delta M_\delta - M_\delta Z_\alpha}{s^2[s^2 - (M_q + M_{\dot\alpha} + Z_w)s - M_\alpha + M_q Z_w]} \tag{11}$$

$$\frac{h}{w_g} = \frac{Z_w(s - 2M_q)}{s^2[s^2 - (M_q + M_{\dot\alpha} + Z_w)s - M_\alpha + M_q Z_w]} \tag{12}$$

For brevity, the denominator of these transfer functions will be written $s^2(s^2 + Bs + C)$. Initially "single-controller" systems are considered, so δ is a scalar quantity. "Multi-controller" systems involving controls δ_1, δ_2, ... will be discussed in Section 4.4.

Sea Spectrum: As explained in Appendix A, a modified Bretschneider spectrum is employed, appropriate to a short-crested sea, of Sea State 5, and a 20 knot windspeed. For a missile traversing this sea at M = 0.7, flying into the inertial wind direction, the wave height encountered frequency characteristics are described by the following power spectrum:

$$\phi_{h_w h_w} = \left(\frac{818.9\ \omega_e^2}{(\omega_e^2 + 6.3^2)^2}\right)^2 \tag{13}$$

where

h_w = Wave height above mean sea level, ft

ω_e = Frequency of encounter, rad/sec

Figure 49 graphs this spectrum. Note that it is of relatively narrow bandwidth, with most of the power concentrated in the region 2.0 → 20.0 rad/sec. This is different from typical land terrain spectra

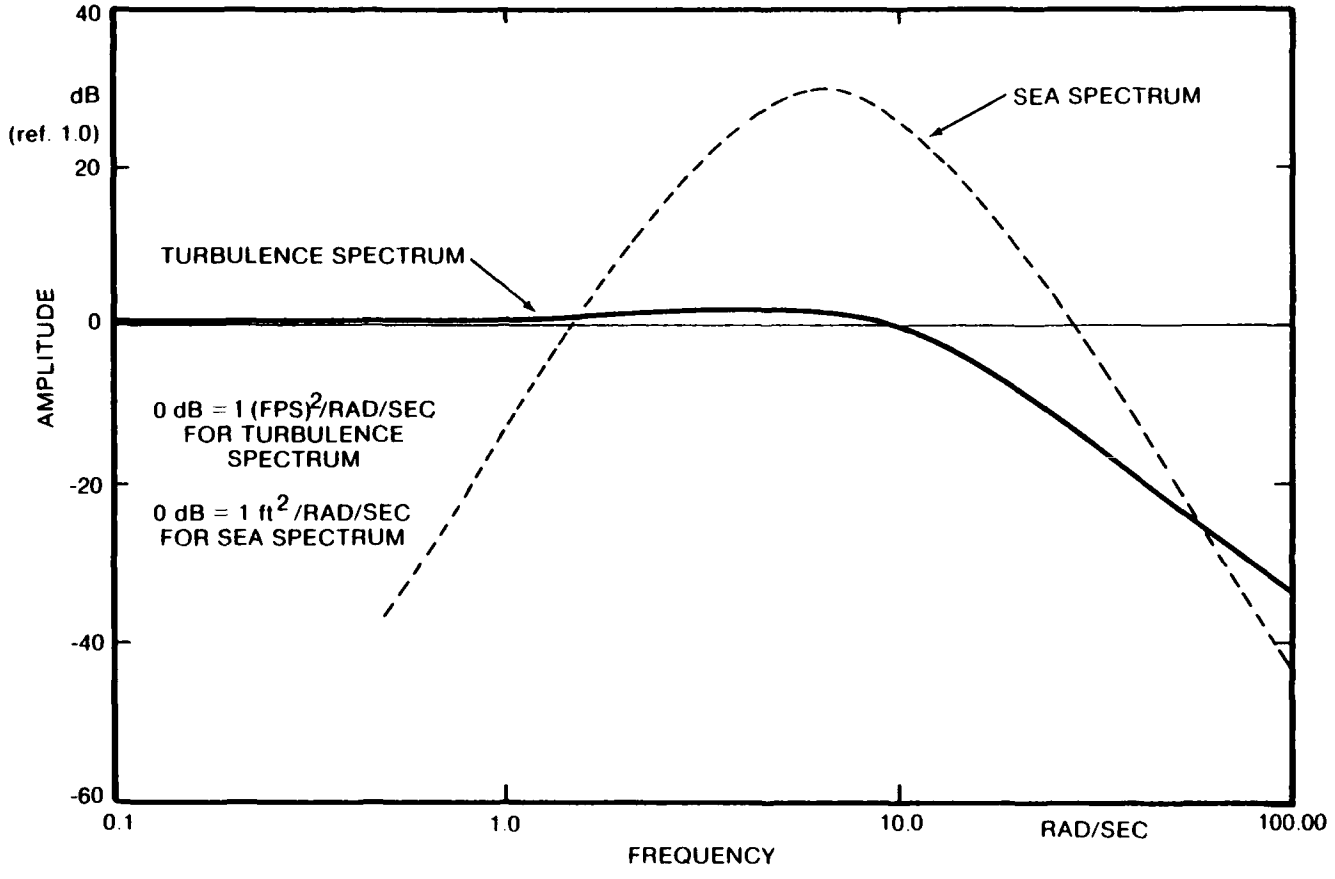

FIGURE 49. COMMAND AND DISTURBANCE SPECTRA

(Refs. 37 and 38) which do not attenuate at low frequencies. The rms wave height is 9.18 ft.

Turbulence Spectrum: The well-known Dryden spectrum is employed. As shown in Appendix A, for the assumed flight condition this reduces to:

$$\phi_{w_g w_g} = \frac{(14.0438)^2(\omega^2 + 4.5143)^2}{(\omega^2 + 7.819^2)^2} \tag{14}$$

The rms value of w_g is 2.9 fps. This spectrum is also shown on Fig. 49.

Stability Derivatives: Stability derivatives were calculated for each of the configurations 3GA, 6GA, 9GA, 3F, 6F, 9F, and 6H shown in Figs. 31 through 34. In all cases a positive static margin was assumed as listed on Table 1, which also gives weights and inertias. The vortex-lattice computer program of Ref. 19 was employed to calculate the lifting surface contribution to the joined wing derivatives, with fuselage corrections from standard texts (e.g., Ref. 23). For the conventional configuration 3GA, full-scale M = 0.7 A.E.D.C. Tullahoma wind tunnel data on the closely similar Vought YGBM-109 Tomahawk cruise missile were employed (Ref. 45): these were scaled to Configurations 6GA and 9GA by standard methods (Ref. 23). The hybrid configuration planform involves three lifting surfaces and therefore cannot be modeled by the vortex-lattice program of Ref. 19 which is limited to two planforms. However, a later version of this program, originally developed by J. S. Luckring for oblique-wing planforms, avoids this restriction and was utilized to compute derivatives for the hybrid configuration. Table 2 lists the derivatives and the h/δ and h/w_g transfer functions in the forms:

$$\frac{h}{\delta} = \frac{A_{h_\delta} s + B_{h_\delta} s + C_{h_\delta}}{s^2(s^2 + Bs + C)} \tag{15}$$

$$\frac{h}{w_g} = \frac{A_{h_{w_g}} s + B_{h_{w_g}}}{s^2(s^2 + Bs + C)}$$

TABLE 1. FLIGHT CONDITIONS FOR TERRAIN-FOLLOWING ANALYSIS

Mach No. = 0.7

Altitude = Sea Level

For all configurations

% Total Fuel Used = 50.5%, for Configurations 3GA, 6GA, 9GA, 3F, 6F, 9F

= 6.2%, for Configuration 6H

Configuration	3GA	3F	6GA	6F	6H	9GA	9F
Weight (lb)	2234.9	2077.69	2396.8	2183.52	2771.5	2622.7	2320.58
Pitch Inertia (sl-ft^2)	1620.0	1591.03	1815.6	1644.2	2363.54	1983.5	1789.7
Static Margin (ins.)	4.175	2.012	5.907	1.992	2.0	7.23	2.0562
Reference Area* (ft^2)	11.5	10.0	23.0	20.0	15.9992	34.5	30.0
C_L at 1 g	0.2673	0.2858	0.1434	0.1502	0.238	0.1046	0.1064
g Per Degree of Control Deflection†	1.1341	1.1907	1.5478	3.0099	2.5817	2.8766	4.5531

*The reference area is the area employed to define C_L. For Configurations 3GA, 6GA, 9GA it equals the gross wing area, for Configurations 3F, 6F, 6H, and 9F it equals the gross horizontal projected area of the joined wings (excluding the canard for 6H).

†"Control" = all-moving tail for 3GA, 6GA, 9GA; wing-warping (measured at front wing root) for 3F, 6F, 9F, and all-moving canard only for 6H.

TABLE 2. DERIVATIVES AND TRANSFER FUNCTIONS

(Flight Conditions Specified in Table 1)

	CONFIG. 3GA	CONFIG. 6GA	CONFIG. 9GA	CONFIG. 3F	CONFIG. 6F	CONFIG. 9F	CONFIG. 6H*
MALPHA	-14.30900000	-36.14000000	-60.76000000	-3.97450000	-7.36460000	-10.00340000	-5.24880000
MW	-0.01830000	-0.04620000	-0.07770000	-0.00510000	-0.00940000	-0.01280000	-0.00671200
ZALPHA	-959.8800000	-1,790.900000	-2,345.450000	-588.7485000	-1,003.024900	-1,444.244800	-864.7700000
ZW	-1.22760000	-2.29040000	-3.14040000	-0.75300000	-1.38510000	-1.84710000	-1.10600000
MA DOT	-0.12480000	-0.22230000	-0.29620000	-0.07560000	-0.21080000	-0.41330000	-0.27900000
MW DOT	-0.00015960	-0.00028430	-0.00037880	-0.00009670	-0.0002 ,960	-0.00052850	-0.00035700
MDELTA	0.59050000	1.12900000	1.56460000	0.25000000	0.70510000	1.21540000	0.57070000
ZDELTA	1.81860000	3.81859000	5.60510000	-3.13910000	-6.03610000	-8.43150000	-1.31800000
MQ	-0.40800000	-0.72450000	-0.98000000	-0.25180000	-0.70270000	-1.37750000	-0.69800000
B	1.76040000	3.23720000	4.41660000	1.00040000	2.29860000	3.63790000	2.08300000
C	14.80986000	37.79939480	63.83759200	4.16410540	8.33790977	12.54778025	6.01998800
A, H DELTA	-1.81860000	-3.81859000	-5.60510000	3.13910000	6.03610000	8.43150000	1.31800000
B, H DELTA	-0.96895000	-3.61544101	-7.15322862	1.02774134	5.51397735	15.09913020	1.28768600
C, H DELTA	540.7867926	1,883.922257	3,501.231194	159.6634780	808.0943191	1,839.678797	500.4411030
A, H WG	-1.22760000	-2.29040000	-3.14040000	-0.75300000	-1.38510000	-1.84710000	-1.10600000
B, H WG	-1.00172160	-3.31878960	-6.15518400	-0.37921080	-1.94661954	-5.08876050	-1.54397600

*With canard 1/4-chord sweep angle $\Lambda_{c/4}$ = 35 deg.

Table 1 indicates that although the static margins of all the configurations studied are positive they are not equal. This variation was expected to have little effect on terrain-following performance of single-controller systems: this expectation was verified by performing the calculations of terrain-following accuracy twice, first with the static margin indicated and secondly with zero static margin. Only slight differences in terrain-following accuracy were found. The reason for this insensitivity is that varying static margin has little effect on the numerator coefficients of the h/w_g and h/δ transfer functions, and affects the denominators of these transfer functions equally, by varying the C coefficient. [Varying static margin can have significant effects, however, if a multicontroller (e.g., flaps-plus-elevator) height control system is employed. This is discussed in Section 4.4.]

4.3 LIMITS ON OPTIMUM TERRAIN-FOLLOWING PERFORMANCE

For a given airframe, the guidance system can be designed to minimize $E(h_e^2)$ through the use of Optimal Control Theory. This yields the guidance system that gives the minimum achievable $E(h_e^2)$ for a specified level of mean square elevator deflection $E(\delta^2)$. (This constraint may be generalized for multicontroller systems, e.g., elevator-plus-flap control, and additional constraints, e.g., g-limits may be introduced.)

It might be thought that any desired level of $E(h_e^2)$, even zero, could be obtained by allowing $E(\delta^2)$ to increase. This is not true for conventional (aft tail) configurations in which elevator is employed to control height. Such configurations have height-to-elevator transfer functions which incorporate one or more right-half-plane zeros. (Transfer functions of this kind are called "nonminimum phase.") It has been shown (Ref. 40) that for a system having a nonminimum phase transfer function the error cannot be reduced to zero even if infinitely large mean square control deflections are permitted. For such a system there is a finite minimum achievable mean square error.

From the Laplace transform initial and final value theorems it can shown that the presence of a right-half-plane transfer function zero of

the height/elevator transfer function implies that the initial direction of the airframe's height-to-elevator response is in the opposite direction to the ultimate response. This occurs because, in order to climb, a download must be applied to the elevator. This download causes the initial response of the airframe c.g. to be downwards.

By contrast, for a canard or joined wing configuration this reversal of response can be avoided, by placing the elevator control on the front wing, ahead of the c.g. Thus, potentially, such "minimum phase" configurations can follow given terrain more closely than conventional (aft tail) configurations.

The foregoing discussion has omitted many details such as the effects of digital processing and actuator lags, possibilities of multicontroller systems (e.g., elevators-plus-flaps), forward-looking guidance, airframe flexibility, et. These will be discussed in Section 4.4. First, however, we present the results of some optimal control calculations for downward-looking single-controller guidance systems, without lags, applied to a variety of joined wing and conventional cruise missile configurations.

Optimum Single-Controller System: Appendix A derives the equations for the optimal single-controller system, i.e., the system that minimizes the performance index, J.

$$J = E(h_e^2) + k^2 E(\delta^2) \tag{17}$$

Our principal interest here lies not in the details of the optimal compensation in Fig. 48, but rather in the question: "How good is the optimum system," i.e., how closely does it follow the terrain. Thus for a given k^2 we wish to know the value of $E(h_e^2)$ obtained, and the associated mean square control deflection $E(\delta^2)$. As shown in Appendix A, these values are given by expressions of the type:

$$E(h_e^2)_{opt} = \frac{1}{2\pi j} \int_{-j\infty}^{j\infty} \left\{ W_1 \phi_{RR} \overline{W}_1 + W_2 \phi_{dd} \overline{W}_2 \right\} dj\omega \qquad (18)$$

$$\text{Associated } E(\delta^2) = \frac{1}{2\pi j} \int_{-j\infty}^{j\infty} \left\{ W_a \phi_{RR} \overline{W}_a + W_b \phi_{dd} \overline{W}_b \right\} dj\omega \qquad (19)$$

In each expression the first term gives the contribution to J that stems from the portion of h_e or δ that is correlated with the terrain. The second term gives the contribution due to the portion of h_e or δ that is correlated with the atmospheric turbulence. Only two terms appear in each expression: there are no cross-correlation terms involving ϕ_{Rd}, ϕ_{dR} because it has been assumed that the terrain (waves) and turbulence are uncorrelated.

$E(h_e^2)_{opt}$ and the associated $E(\delta^2)$ were calculated by the computer program described in Appendices A and C, for each of the configurations in Figs. 31 through 34. The results are presented below.

Conventional (Aft Tail) Configurations: Figure 50 shows the mean square height error, $E(h_e^2)$, for aft tail configurations 3GA, 6GA, and 9GA graphed versus the corresponding mean square control deflection $E(\delta^2)$ required by the optimal control system. Values of the weighting parameter k are indicated on the graphs. (The control deflection, δ, indicates deflection of the all-moving tail surfaces in units of degrees.) At high values of k (i.e., "expensive control") corresponding to the left side of the graphs the control deflections are small and have little effect on the missile, which flies more or less in a straight line with the preponderant part of the height error being due to the waves. Thus the asymptote of $E(h_e^2)$ for $k \to \infty$ is essentially equal to the mean square wave height, 81.2 ft^2. As k is decreased the system accuracy increases, but for reasonable values of $E(\delta^2)$, e.g., of the order of 10 deg^2, the gain in accuracy is slight. For example, Configuration 3GA reduces its mean square error only to 74/81.2 = 0.91 of its open-loop value. If much larger $E(\delta^2)$ could be produced or if the control effectiveness

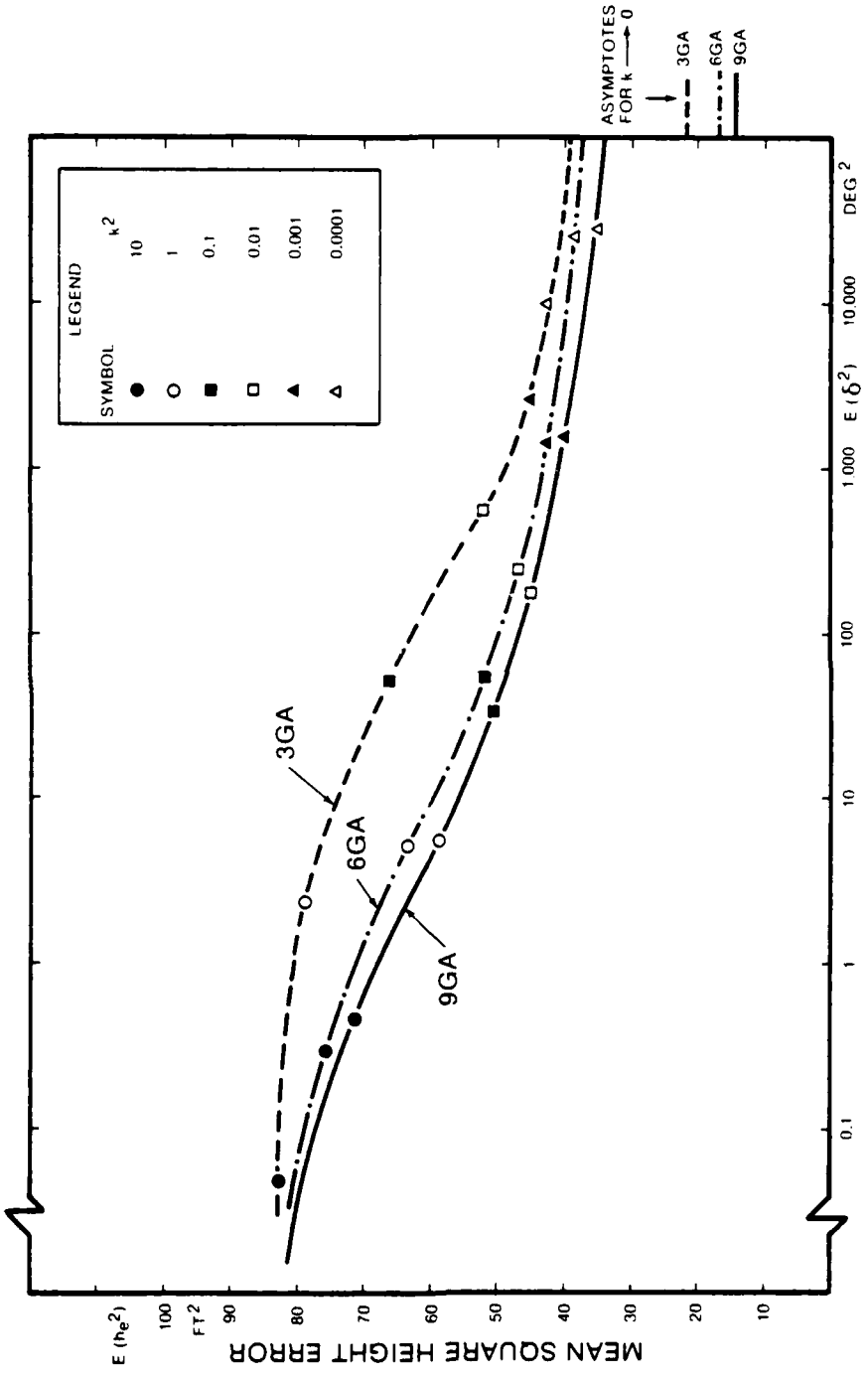

FIGURE 50. OPTIMAL TERRAIN-FOLLOWING PERFORMANCE OF SINGLE-CONTROLLER AFT TAIL CONFIGURATIONS

parameters C_{L_δ}, C_{M_δ}, could be increased the accuracy could be improved, but even with infinite mean square control deflections the best accuracy that can be achieved with airframe 3GA is only $E(h_e^2) = 22\ ft^2$, i.e., 0.27 of the open-loop mean square error.*

This situation is only slightly improved by selecting a larger wing area, as shown by the graphs for Configurations 6GA and 9GA in Fig. 50. Nor is any significant improvement gained by reducing static margin. This expedient was studied by recalculating the optimum system performance with M_α set equal to zero, and the remaining derivatives unchanged. For any given k the zero static margin values of $E(h_e^2)$ and $E(\delta^2)$ were, when graphed on Fig. 50, virtually coincident with the points graphed for the normal static margins listed in Table 1.

It is clear from the above results that even with ideal guidance system dynamics (e.g., no actuator lags, no digital processing delays) the gain in accuracy resulting from terrain following is meager for the aft tail configurations. The root of the problem can be traced to the nonminimum phase characteristics inherent in any airframe controlled by an aft tail. To demonstrate this, the magnitude of the nonminimum phase zero in the h/δ transfer function was varied parametrically, and the asymptotic value of $E(h_e^2)$ was recalculated. That is, the h/δ transfer function (Eq. 15) was expressed as:

$$\frac{h}{\delta} = \frac{A_{h_\delta}(s + a)(s - b)}{s^2(s^2 + Bs + C)} \quad , \quad b > 0 \qquad (20)$$

and b was varied parametrically. The resulting $E(h_e^2)$ was calculated from Eqs. B34 and B35 of Appendix B. Figure 51 illustrates the result of parametrically varying b. It shows that for $1.0 > b > 100.0$ the asymptotic

*The asymptotes shown in Fig. 50 have been verified by an independent method given in Appendix B.

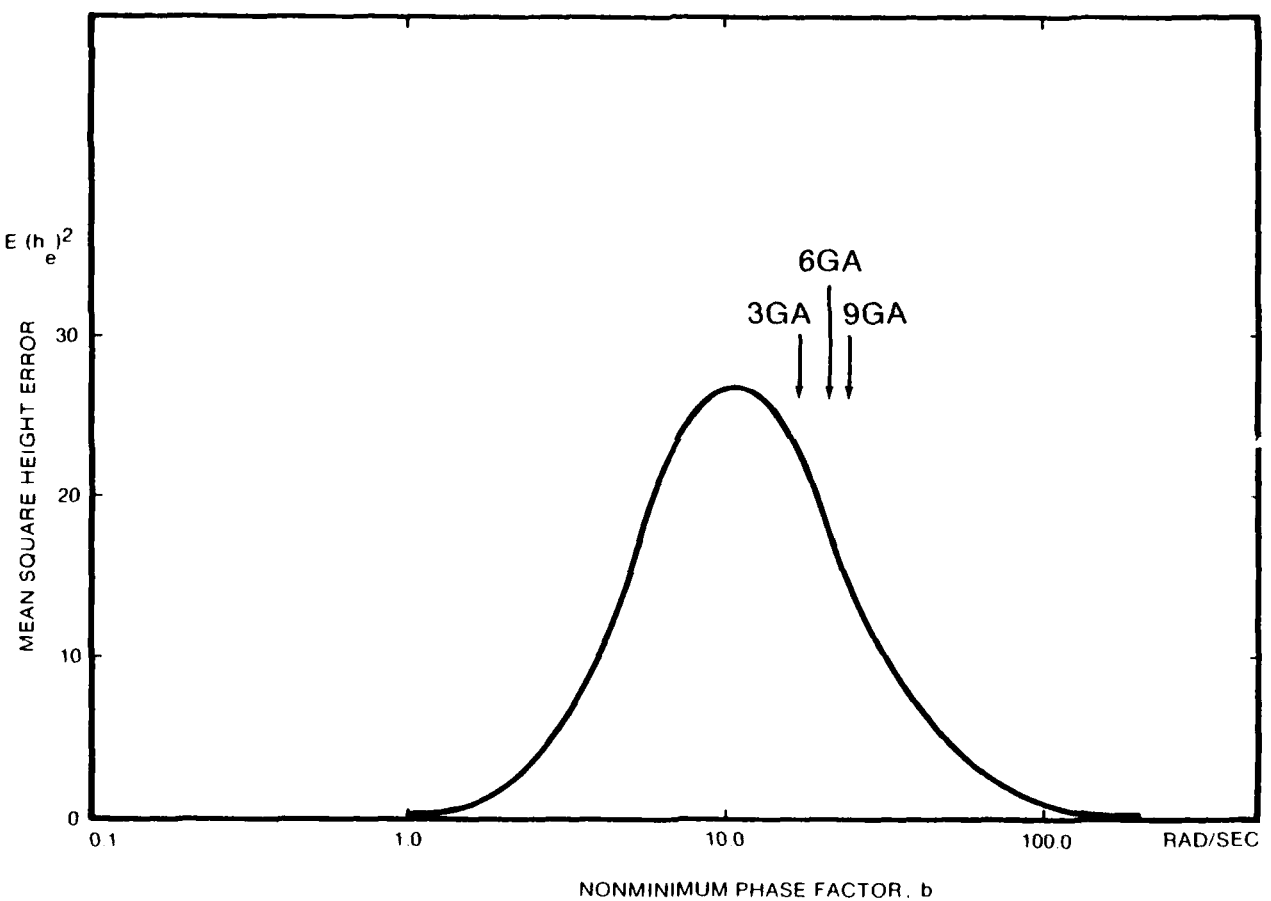

FIGURE 51. MINIMUM ACHIEVABLE MEAN SQUARE ERROR FOR AFT TAIL CONFIGURATIONS

error is very small. Unfortunately, each one of the configurations 3GA, 6GA, 9GA has values of b which fall near the peak of the graph in Fig. 51.

There is no simple remedy for this limitation of aft tail configurations. Varying static margin has only a slight effect on b; even reducing the static margin to zero induces only a slight change in the value of b, which is primarily determined by the tail moment arm. To effectively vary b requires feedback to a second controller, i.e., the guidance system should simultaneously control tail incidence plus one other control, e.g., flaps. This is discussed in Section 4.4 where it is shown to be of only limited effectiveness.

Effect of Varying Terrain: Since the above results have been derived for a particular sea spectrum it is necessary to investigate the effects of deviating from this spectrum. For example, a different command spectrum would be appropriate over land. The effects of varying the command spectrum can be found as explained in Appendix B, Eqs. B34 through B38. These equations can be applied to determine the asymptotic mean square error of a nonminimum phase missile flying over land terrain, as follows.

Various forms of land terrain spectra are in use (see Refs. 37, 38, and 41) but the simplest and most convenient form for our purpose is a first-order Butterworth form, thus:

$$(\phi_{RR})^{+} = \frac{\sqrt{2a[E(R^2)]}}{s + a} \tag{21}$$

In this equation $E(R^2)$ is the mean square terrain height variation, and a is the encounter break frequency, which depends on the terrain roughness and the missile's speed. From Eq. B34, the component of mean square height error due to terrain-following has a minimum value for zero control weighting ($k \to 0$) which is given by

$$E(h_e)_R^2 = \frac{1}{2\pi j} \int_{-j\infty}^{j\infty} \left[\frac{Q}{\bar{Q}} \; (\phi_{RR})^+\right]_- \left[\frac{\bar{Q}}{Q} \; (\phi_{RR})^-\right]_+ \; dj\omega \qquad (22)$$

where $Q/\bar{Q} = (b + s)/(b - s)$, with b being the nonminimum phase factor. Since

$$\left[\frac{Q}{\bar{Q}} \; (\phi_{RR})^+\right]_- = \sqrt{2a[E(R^2)]} \cdot \frac{2b}{b + a} \cdot \frac{1}{b - s} \qquad (23)$$

$$\frac{E(h_e)_R^2}{E(R^2)} = \frac{4ab}{(b + a)^2} = \frac{4(b/a)}{[1 + (b/a)]^2} \qquad (24)$$

Equation 24 is of value because it enables us to state limits on the performance of single-controller systems in terms related to terrain roughness. For example, consider two types of terrain:

(1) Rolling terrain, with a spatial correlation distance a_s = 2,000 ft. (a_s is the average distance between two samples differing in magnitude by a factor of 1/e = 0.368.)

(2) Rough terrain, with a_s = 500 ft.

For a vehicle traversing the terrain at M = 0.7 (781.9 fps) the corresponding values of a in Eq. 24 are a = 781.9/2,000 = 0.39 sec^{-1} and a = 781.9/500 = 1.563 sec^{-1} for rolling and rough terrain respectively. For Configuration 3GA, which is approximately representative of current Tomahawk class missiles, factoring the transfer functions given in Table 2 yields b = 16.9799 rad/sec. Hence from Eq. 24, for rolling terrain:

$$\frac{\text{Minimum Achievable Mean Square Height Error}}{\text{Mean Square Terrain Height Variation}} = \frac{4 \times 0.39 \times 16.9799}{(0.39 + 16.9799)^2} = 0.008 \qquad (25)$$

For rough terrain:

$$\frac{\text{Minimum Achievable Mean Square Height Error}}{\text{Mean Square Terrain Height Variation}} = \frac{4 \times 1.563 \times 16.9799}{(1.563 + 16.9799)^2} = 0.308 \qquad (26)$$

A "worst case" type of terrain would be one yielding a = b, for which Eq. 24 attains its maximum value of 1.0. In this situation the optimal feedback is zero, i.e., the best strategy is to fly the missile controls-fixed in a straight-line flight path, making no attempt to follow the undulations of the terrain. For a Tomahawk class missile flying at M = 0.7 the spatial correlation distance of such terrain is $a_s = U_o/b = 46.0$ ft. This corresponds to exceedingly jagged terrain which would rarely be encountered. The "rough" terrain quoted above is more probable: for that terrain rms height error exceeds 50% of the rms terrain altitude variation.

From the above results and those presented in Fig. 51, it is concluded that, for aft tail single controller missiles flying over land or sea the maximum achievable closeness with which the terrain can be followed is severely limited, due to the vehicle's initial wrong-way height response.

Atmospheric Turbulence Response: The Dryden spectrum employed to describe low altitude turbulence (Eq. 14) is widely employed in aircraft guidance and control studies. The mean square height error due to turbulence was much smaller than that due to terrain for all the configurations studied. Therefore the effect of varying the Dryden spectrum appears to be secondary, hence no parametric variations were performed. However three points of detail should be noted for future studies.

(1) The Dryden spectrum has a finite d.c. value, which may sometimes cause convergence difficulties for optimization procedures. Since the

ultra-low frequency behavior is of little interest it is suggested that the spectrum should be attenuated at low frequencies (e.g., below 0.01 rad/sec) to remove the d.c. component.

(2) The use of gust-gradient terms (see Eq. 10) in connection with the standard Dryden spectrum, or any other turbulence spectrum that has a finite d.c. value, requires consideration. These terms provide only a first approximation to the complex interactions of the airframe with time-varying and spatially-varying atmospheric velocity components (see Ref. 42 for more exact but more complicated representations). As a check, we repeated most of our optimization calculations with the gust gradient terms removed. Only minor differences in the results were observed. It is recommended that such checks should always be performed.

(3) Our calculations show that the height error induced by turbulence is much smaller than that due to terrain. It does not necessarily follow that the turbulence-induced normal accelerations are much less than those due to terrain-following. If subsequent, more detailed studies are performed the "g" response of the optimally controlled system should be assessed. The performance index can be extended, if desired, to include terms relating to normal acceleration.

Terrain-Following Performance of Single-Controller Joined Wing Configuration: The joined wing configurations 3F, 6F, 9F obtain pitch control via wing-warping, as described in Section 3. With a parabolic variation of twist, corresponding to uniform torsional modulus GJ along both wings, the center of pressure of the lift induced by twist is ahead of the c.g., and hence the height/twist transfer function is minimum phase. However, as is apparent from Fig. 32, the pitching moment arm is small for Configuration 3F. For the hybrid configuration, 6H (Fig. 34), a long moment arm is obtained by employing an all-moving canard as the primary pitch control.

Figure 51 shows the terrain-following performance of these configurations when optimally controlled. The gust and wave spectra are identical to those employed previously. Comparing Fig. 52 with Fig. 50 it is

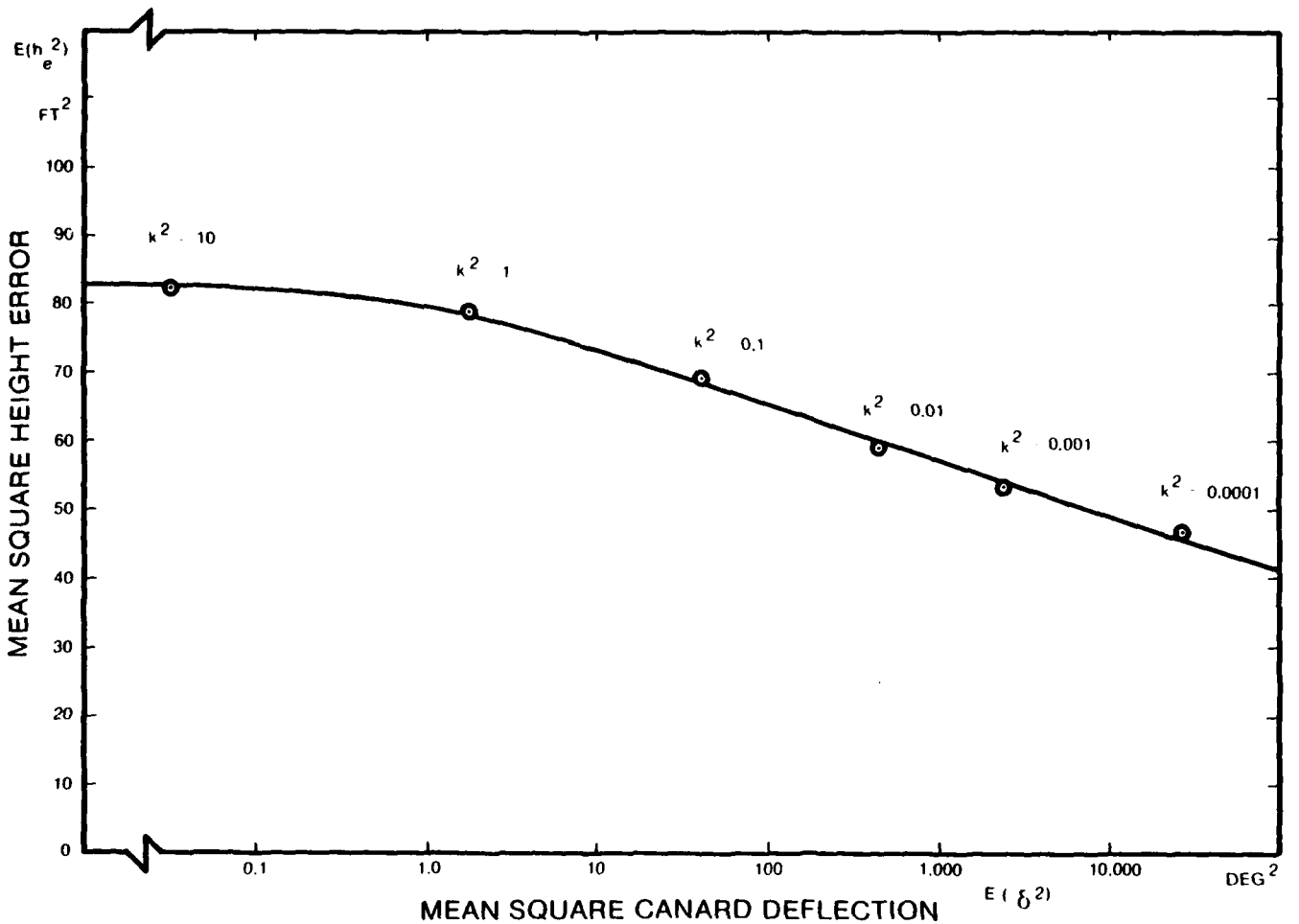

FIGURE 52(a). OPTIMAL TERRAIN-FOLLOWING PERFORMANCE OF HYBRID CONFIGURATION

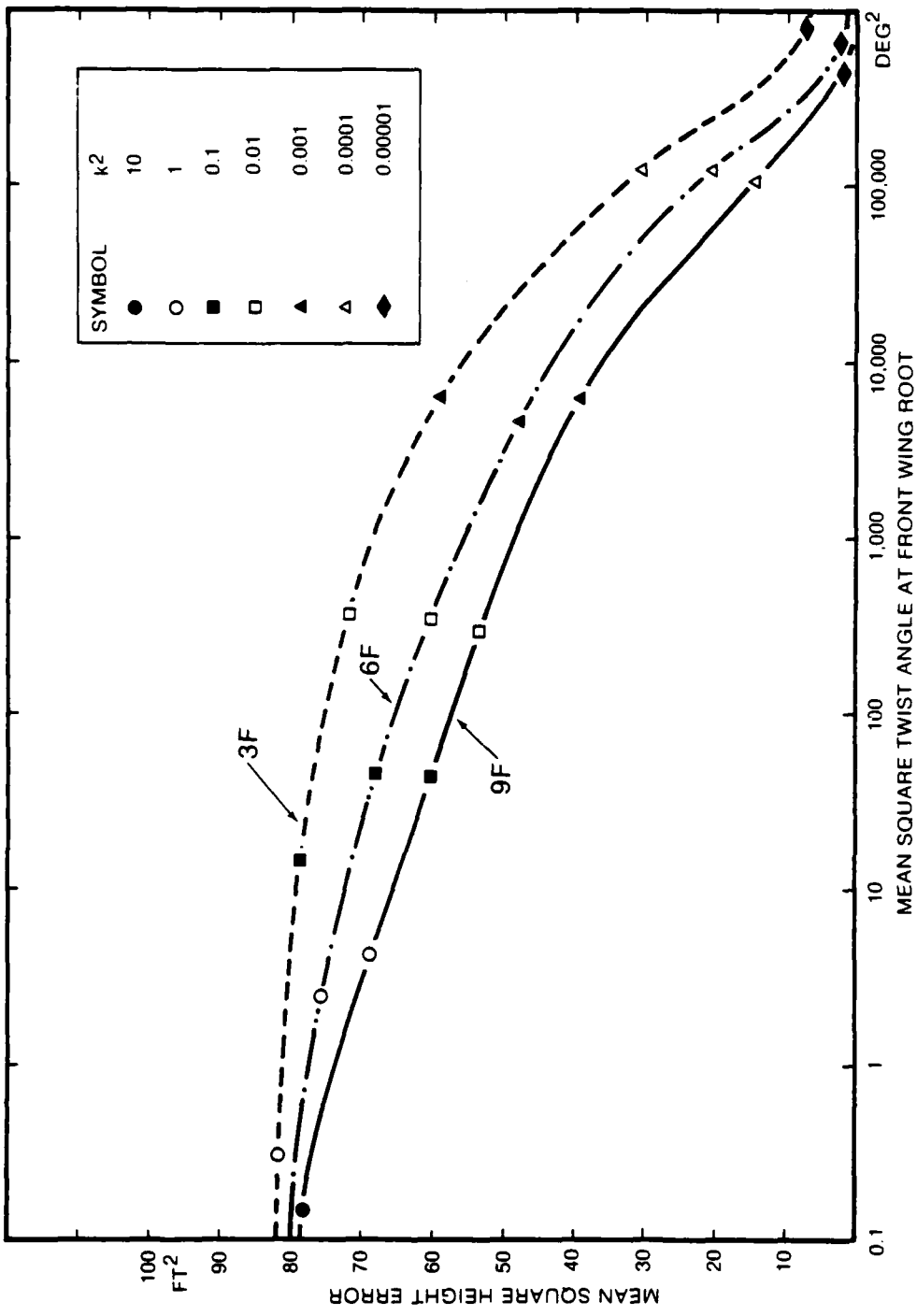

FIGURE 52(b). OPTIMAL TERRAIN-FOLLOWING PERFORMANCE OF JOINED WING CONFIGURATIONS

seen that, as predicted, the joined wing and hybrid configurations yield a mean square height error which tends to zero as $k \to 0$. Unfortunately, the associated magnitudes of control deflection $E(\delta^2)$ are impractically large. Two remedies are possible: (1) increase control effectiveness; (2) employ multiple controls (e.g., flaps plus elevator).

Increased control effectiveness implies increasing both M_δ and Z_δ to n times their original levels.* This yields a mean square height error equal to that provided by $(1/n)^2$ times the original control deflection of the original optimized system, for a given value of k. Thus for the aft tail configuration the limit on terrain following accuracy remains unchanged; however, it is approached more closely. The chances of achieving substantially increased control effectiveness are slim, although some gains could be made by the following expedients:

(1) (For the aft tail and hybrid configurations) gearing an anti-servo tab to the all-moving tail (or canard) is done on many light planes (e.g., the Piper Cherokee series).

(2) (For the joined wing configurations) augmenting or replacing the wing warping control with deflections of a flap mounted on the front wing.

On balance it appears to be more desirable to employ a multicontroller system, as described below. This provides large improvements in terrain-following ability for the hybrid and joined wing configurations, but only smaller improvements for the aft tail configurations.

---

*The effect of reducing static margin to zero was also studied. This yielded negligible benefits because, as shown in Fig. 53, it does not change the h/δ transfer function much in the frequency region around 6.3 rad/sec where the wave spectrum has its peak. Reducing static margin would be effective if the command (terrain) spectrum is of the type that has large low-frequency components, e.g., land terrain.

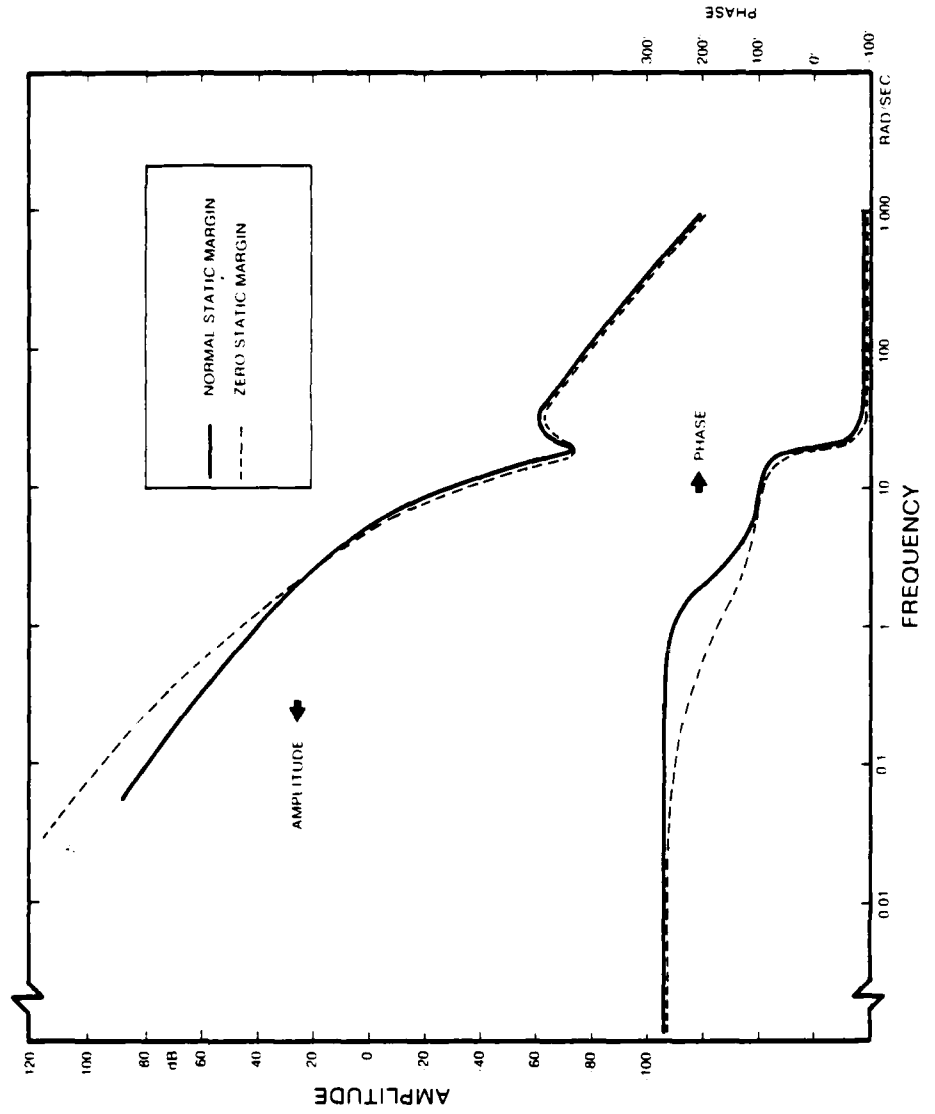

FIGURE 53. HEIGHT/CANARD DEFLECTION TRANSFER FUNCTION FOR HYBRID CONFIGURATIONS

4.4 MULTICONTROLLER SYSTEMS: HYBRID CONFIGURATION

We use the term "multicontroller" to denote systems employing two separate controls, e.g., flaps plus elevator. The benefits of multicontroller systems are most easily understood by first ascertaining the reason for the large control deflections demanded by the single-controller systems. Consider Fig. 53 which shows the h/δ transfer function for Configuration 6H, where δ = deflection of the all-moving canard, measured in degrees. The equation for h/δ, from Table 2, is

$$\frac{h}{\delta} = \frac{1.318s + 1.287687s + 500.441103}{s^2(s^2 + 2.083s + 6.019988)} = \frac{1.318(s + 0.4885 \pm 19.4797j)}{s^2(s^2 + 2.083s + 6.019988)} \quad (27)$$

The Bode diagram of Eq. 25, given on Fig. 53, exhibits a pronounced dip around 19.5 rad/sec, due to the light damping of the numerator factors. This dip unfortunately attenuates the h/δ response in the region where it is most needed, i.e., in the region around the peak of the wave spectrum. If the dip is eliminated (or smoothed) the response improves dramatically. This can be demonstrated by putting

$$\frac{h}{\delta} = \frac{100}{s^2}$$

Below frequencies of 2 rad/sec this has an amplitude characteristic similar to the basic h/δ transfer function (Eq. 27). However, its terrain-following performance is much superior, as shown in Fig. 54, which graphs the results of optimal control calculations similar to those illustrated in Figs. 50 and 52. Note that close terrain following can be achieved with moderate control deflections, e.g., $E(h_e^2) = 45.1$ ft^2 with $E(\delta^2) = 6.8$ deg^2. For zero static margin the results are even better: removing the dip from the zero static margin line on Fig. 53 yields:

$$\frac{h}{\delta} = \frac{1,000}{s^2}$$

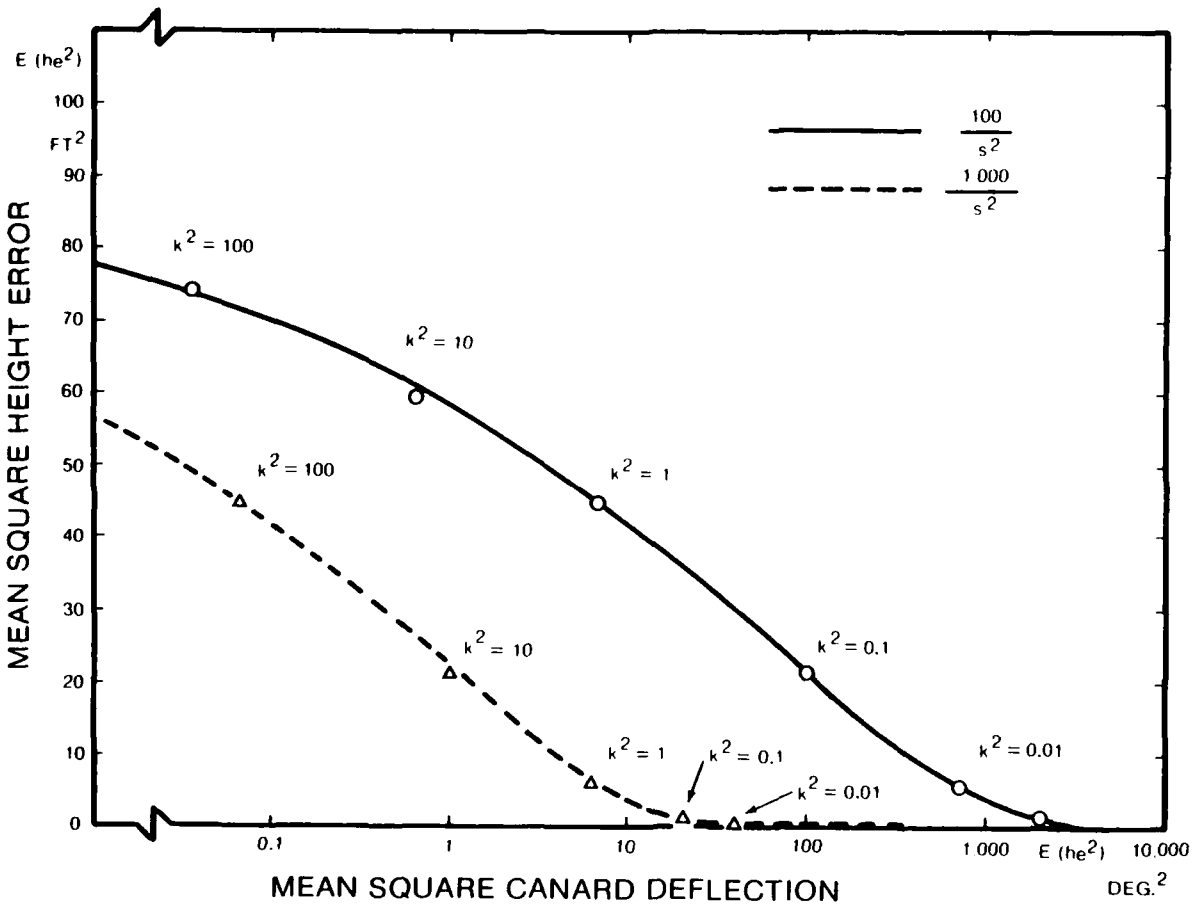

FIGURE 54. TERRAIN-FOLLOWING PERFORMANCE OF MULTICONTROLLER SYSTEMS

Figure 54 illustrates that this achieves $E(h_e^2) = 21.9$ ft^2 with only 1.00 deg^2 of mean square canard deflection.

The desirable forms of transfer functions, presented above, can be realized by employing two controls. This will be demonstrated for the hybrid configuration 6H controlled via canard incidence and front wing flaps. It will also be shown that, for aft tail configurations, desirable forms of transfer functions cannot be physically realized through the combined use of aft tail and wing flap deflections.

Consider Fig. 55. This shows a multicontroller system suitable for Configuration 6H, in which two controls are actuated by the optimal control system. These controls are canard incidence (δ_1 degrees) and deflection of front wing flaps (δ_2 degrees). The flap control derivatives are M_{δ_2}, Z_{δ_2}, and the crossfeed in Fig. 55 has transfer function C(s). It is desired that the overall transfer function of the blocks enclosed by dashed lines should be $100/s^2$. Then, from Eqs. 11 and 15:

$$\frac{100}{s^2} = \frac{CZ_{\delta_2}\{s^2 - (M_q + M_{\dot{\alpha}})s - [M_\alpha - (M_{\delta_2}/Z_{\delta_2})Z_\alpha]\} + A_{h\delta_1}s^2 + B_{h\delta_1}s + C_{h\delta_1}}{s^2(s^2 + Bs + C)} \tag{31}$$

Substituting numerical values for Configuration 6H from Table 2, and manipulating Eq. 31 yields the required crossfeed transfer function as:

$$C = \frac{98.682s^2 + 207.0123s + 101.5649}{-Z_{\delta_2}\{s^2 + 0.977s + [5.248 - 864.77(M_{\delta_2}/Z_{\delta_2})]\}} \tag{32}$$

C must not be unstable, if it is to be constructed physically. This condition implies that

$$5.248 - 864.77(M_{\delta_2}/Z_{\delta_2}) \geq 0$$

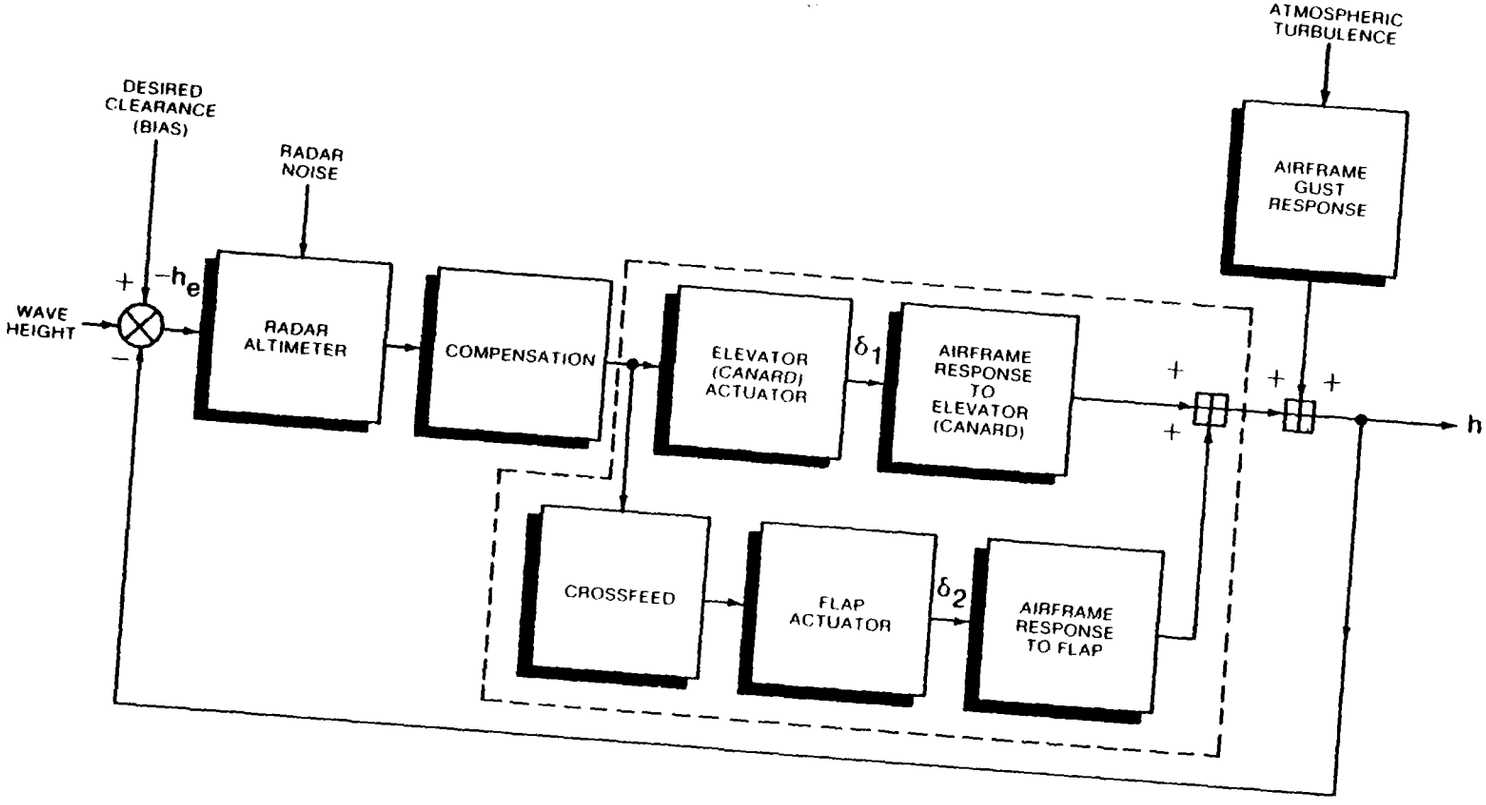

FIGURE 55. MULTICONTROLLER SYSTEM BLOCK DIAGRAM

A controller located forward of the c.g., such as inboard flaps on the front wing, has $(M_{\delta_2}/Z_{\delta_2}) < 0$ and satisfies this condition automatically. For trailing edge flaps occupying the entire span of the front wing $M_{\delta_2} \approx 0$, and $Z_{\delta_2} = -4.31$, whence:

$$C = \frac{98.682(s + 0.7821)(s + 1.3157)}{4.31(s + 0.4885 \pm 2.2382j)} \qquad (33)$$

Figure 56 graphs the Bode diagram of this transfer function. In the frequency range of most interest (1 to 10 rad/sec) the amplitude ratio is typically 30 dB, i.e., a linear ratio of 31.6. From Fig. 54 this implies that to obtain a mean square height error of, for example, 74.87 ft^2 the canard rms deflection would be $\sqrt{0.0369} = 0.192$ deg and the rms flap deflection would be of the order of $31.6 \times 0.192 = 6.07$ deg. This performance is considerably better than that of the single controller system. Still further gains could be achieved by tailoring the form of C and/or reducing static margin. These gains would involve permitting higher rms canard deflections, e.g., 5 degrees, while maintaining rms flap deflection at approximately 6 degrees. This could be done either by applying optimal control theory for multicontroller systems, or by iterative classical methods of control systems design.

In summary, the use of combined flap and canard controls enables the hybrid configuration to achieve substantially better terrain-following performance than can be attained using canard control alone. Similar benefits cannot be obtained for the aft tail configuration through the combined use of flaps and elevator, as will be shown below.

Multicontroller Aft Tail Configuration: The inherent limitation of aft tail configurations for close terrain following with combined control flap and elevator (or all-moving tail) becomes apparent upon attempting to repeat the procedure demonstrated above for the hybrid configuration, whereby an effective transfer function of the desired

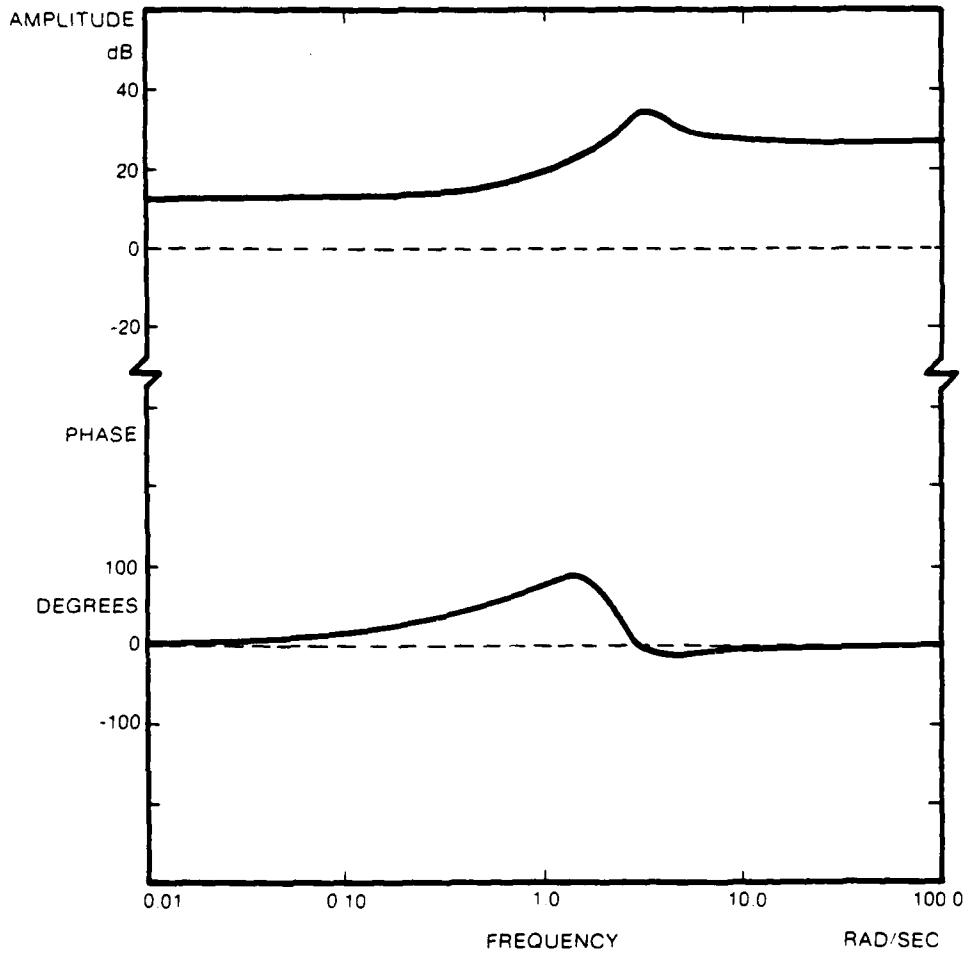

FIGURE 56. BODE DIAGRAM OF CROSSFEED TRANSFER FUNCTION

form (Eq. 28) was realized. Configuration 6GA is selected to provide a numerical example.

Substituting the appropriate numbers for Configuration 6GA (from Table 2) in Eq. 31 yields an equation for the crossfeed transfer function, C, which relates flap deflection to aft tail deflection. Equation 31 thus becomes, for Configuration 6GA,

$$\frac{100}{s^2} = \frac{-CZ_{\delta_3}\left|s^2 + 0.9468s + 36.14 - 1{,}790.9(M_{\delta_3}/Z_{\delta_3})\right|}{-3.81859s^2 - 3.615s + 1{,}883.92} \qquad (34)$$
$$s^2(s + 3.2372s + 37.7993948)$$

where δ_3 denotes flap deflection.

Manipulating Eq. 34 similarly to Eq. 31 yields the following necessary condition for C to be stable

$$36.14 - 1{,}790.0\,\frac{M_{\delta_3}}{Z_{\delta_3}} > 0 \qquad (35)$$

i.e.,

$$\frac{M_{\delta_3}}{Z_{\delta_3}} < 0.02017 \qquad (36)$$

Let the center of pressure of the lift due to flap deflection be located a distance ℓ_F aft of the c.g. By definition:

$$\frac{M_{\delta_3}}{Z_{\delta_3}} = \frac{W}{g} \cdot \frac{\ell_F}{I_y} = \frac{2{,}396.8}{32.2} \cdot \frac{\ell_F}{1{,}815.6} = 0.4099\,\ell_F \qquad (37)$$

Hence the maximum value of ℓ_F is given by

$$(\ell_F)_{max} = 0.02017/0.04099 = 0.49 \text{ feet} \qquad (38)$$

This distance is 0.317 times the mean wing chord of Configuration 6GA. Thus if the vehicle c.g. is at 0.25 $\bar{c}$, for C to be stable the incremental lift due to flap deflection must have its center of pressure forward of 0.567 $\bar{c}$. As shown in Ref. 43, p. 244, most trailing edge flap configurations yield incremental center of pressure locations which are further aft than this value. Offsetting this, the tail load induced by flap downwash moves the c.p. forward, but only after a lag of approximately 0.01 seconds (the time required for the downwash to reach the tail). Hence, even if the aft-mounted control attains $\ell_F < 0.49$ feet, it still has a slower response than a forward-mounted control. Note that ℓ_F should be substantially less than 0.49 feet, because if the inequality condition (Eq. 36) is only just satisfied C will be large in the region $\omega \approx [36.14 - 1{,}790.0(M_{\delta 3}/Z_{\delta 3})]^{1/2}$ and the system will be impracticable because it will demand excessively large flap deflections.

It is interesting to examine the effect of reducing static margin on the feasibility of aft tail multicontroller systems. If we let the static margin become zero then in Eq. 34 the M_α term (≈ -36.14) vanishes. As a result the stability condition becomes $M_{\delta 3}/Z_{\delta 3} < 0$, which condition cannot be satisfied by any trailing edge flap system. Thus reducing static margin only worsens the situation for the aft tail airframe.

Multicontroller Non-Hybrid Joined Wing Configurations: The hybrid is more attractive than the pure joined wing configuration for multicontroller terrain following, because of the long moment arm of the canard. If staging is employed, as shown in Figs. 34, 42, and 43, the canard is no longer available to the post-staged configuration. To obtain close terrain following after staging has occurred it may be desirable to mount the canard aft of the nose tank, so that the vehicle remains a hybrid configuration throughout its flight.

If the canard cannot be used, consideration should be given to:

(1) Combined deflections of rear wing flaps and front wing flaps, with the larger deflections on the front wing flaps, to keep the c.p. of the added airload forward of the c.g.

(2) Movable leading edge devices (e.g., Kruger flaps, controllable L.E. droop) mounted on the inboard part of the front wing.

Canard Configurations. It may be asked whether a canard configuration would follow terrain as closely as the hybrid configuration 6H. Penalties of structure weight, induced drag, and increased wing volume would ensue if the joined wing of 6H were replaced by a monoplane wing. Even if these penalties are disregarded, the control moment arm available from such a wing would be less than that provided by a comparable joined wing. Furthermore flaps mounted on such a wing would be aft of the c.g., thus producing an initially wrong-way response which, as has been shown, is detrimental to terrain-following. It therefore appears that no advantage would be gained by adopting a canard configuration employing cantilever lifting surfaces.

4.5 CONCLUDING REMARKS

This section has shown how configuration size and geometry affect terrain-following accuracy. Seven airframe configurations were studied, but only a single type of terrain was considered: a short-crested sea. It would be of interest to apply the techniques described here to terrain-following over land. One would expect greater improvements to be possible over land because of the larger amplitude and smaller high-frequency content of land terrain spectra.

The system models presented here are simplified in that they omit such things as actuator lags, digital processing lags, radar altimeter noise, and airframe structural dynamics. Because of these simplifications the accuracy of terrain-following calculated here tends to be optimistic. Further, more detailed, studies should be performed to study these effects.

5.0 PERFORMANCE COMPARISON

5.1 INTRODUCTION

This section presents comparisons of calculated range and maneuverability for the joined wing, conventional and hybrid configurations 3GA, 6GA, 9GA, 3F, 6F, 9F, and 6H shown in Figs. 31 through 34. The comparisons are based on:

(1) Range at sea level at M = 0.7.

(2) Range at 40,000 ft altitude at M = 0.7.

(3) Sustained maneuvering "g" capability at sea level, M = 0.7.

All configurations are assumed to have an initial cruise weight of 2864.0 lb. This is the configuration's weight when the booster separates, hence all configurations employ the same size of booster. The assumed powerplant characteristics are generally representative of projected small turbofans of the class used in current Tomahawk cruise missiles, but do not correspond to any specific existing engine.

The geometry of the airframe configurations has been described in Section 3. A point that requires additional comment is the increase in the ratio of horizontal projected tail area S_T to wing area for Configurations 6GA and 9GA, compared to Configuration 3GA. This is required to maintain adequate tail volume ratio $\bar{v} = \ell_T S_T / Sc$. The mean chord, c, is proportional to $S^{1/2}$, because a constant aspect ratio is retained. The tail moment arm ℓ_T is approximately constant, since fuselage length is fixed. For constant $\bar{v}$, S_T would be proportional to $S \times S^{1/2}$, i.e., $S^{1.5}$. However since part of the function of the tail is to overcome fuselage destabilizing moments, and since the fuselage size is fixed, a less extreme variation of tail size was adopted: $S_T \propto S^{1.17}$. This gives the tail areas tabulated overleaf and illustrated on Fig. 31. For Configurations 6GA and 9GA the curved folding tail of 3GA (Fig. 33) is not used: instead a Y-tail arrangement having straight surfaces spaced at 120 degrees is employed, with multiple hinges for folding.

	3GA	6GA	9GA
Gross horiz. tail proj. area, ft^2	4.83	10.868	17.51
Gross wing area, ft^2	11.5	12.0	34.5
Tail area/wing area	0.42	0.4725	0.5075
ℓ_T/mean geometric chord	7.57	4.569	3.92
Tail-volume ratio	3.18	2.16	1.99

The vertical tail area was varied similarly to the horizontal tail area. (An increase in wing span, even with no fuselage change, requires an increase in vertical tail area for proper turn coordination, as shown in Ref. 46.)

For drag estimation purposes it was assumed that all configurations had identical flush inlets. As noted previously the joined wing and hybrid concepts can be employed with either flush or protruding inlets, as desired.

5.2 DRAG ESTIMATION

The procedure employed for estimating drag is generally similar to the methods of Linden and O'Brimski (Ref. 44) and Torenbeek (Ref. 24) in that (1) wetted area and form factors are employed as a basis for calculating minimum drag, and (2) an offset drag polar is used with minimum drag at $C_L = C_{L_x} \neq 0$.

$$C_D = C_{D\,min} + \frac{(C_L - C_{L_x})^2}{\pi A e_x} + \begin{matrix}\text{Additional terms} \\ \text{at high } C_L\text{'s}\end{matrix} \qquad (39)$$

The accuracy of the method was checked by computing the drag of the Vought YGBM-110 Tomahawk missile. Full-scale wind tunnel measurements taken on an actual YGBM-110 at M = 0.7 S.L. conditions are given in Ref. 45. Figure 57 compares the measured drag polar with the results

of our calculations.* This figure shows that although the predicted variation of drag with lift is reasonably accurate, the calculated $C_{D\,min}$ is approximately 1.1 times the measured value. This can be ascribed to our assumption of 100% turbulent flow, i.e., transition at all leading edges. It would have been simple to modify the method by assuming transition at 10% chord on all surfaces, which assumption would yield results closely matching the wind tunnel data. However it was decided to retain the assumption of fully turbulent flow (1) for conservatism and (2) to allow for the "drag rectification" effect caused by positive and negative control deflections which cause a small drag increase regardless of sign. A further consideration is that the surface finish of an operational vehicle may be inferior to that of a factory-fresh vehicle selected for wind tunnel testing.

Table 3 shows the calculated minimum drag at Sea Level Standard Conditions for the joined wing and conventional configurations: the hybrid configuration results are given on Table 4. For the 40,000 ft condition the minimum drag values were calculated by varying the weighted Ryenolds numbers shown on Tables 3 and 4 proportionately to the Re/ft of the high-altitude flight condition.

Drag Due to Lift: For all configurations drag due to lift is expressed as:

$$C_D - C_{D\,min} = \frac{(C_L - C_{L_x})^2}{\pi A e_x} \qquad \text{for } C_L < C_{L_s} \qquad (40)$$

$$C_D - C_{D\,min} = \frac{(\overline{C_L - C_{L_x}} + \overline{C_L - C_{L_s}})^2}{\pi A e_x} \qquad \text{for } C_L \geq C_{L_s} \qquad (41)$$

*The YGBM-110 has a fuselage diameter of 20.875 in. Configuration 3GA is generally similar, but has a smaller fuselage diameter (20.375 in.). This diameter was selected to equal that of the General Dynamics YGBM-109, which employs a protective steel casing for underwater launch, and therefore is appreciably smaller in diameter than the 21 inch torpedo tube from which it is launched.

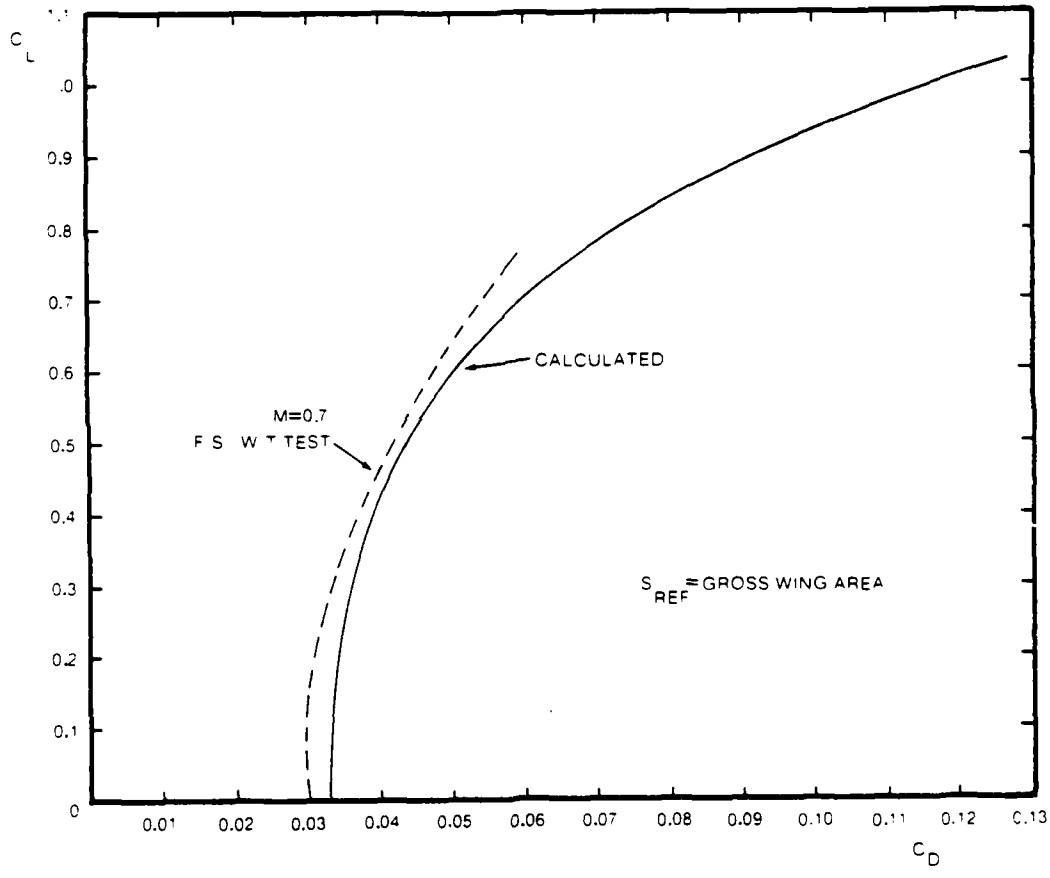

FIGURE 57. CALCULATED AND MEASURED DRAG POLARS FOR VOUGHT YGBM-110 CRUISE MISSILE

TABLE 3. MINIMUM DRAG AT M = 0.7, SEA LEVEL STANDARD CONDITIONS

Config.	Component	S_{wet} (ft^2)	$Re \times 10^{-6}$	C_f Turbulent Flat Plate	Form Factor	C_{fe}	D_{min} (lb)
3F	Front wing	10.059	2.85	0.0037	1.267	0.0047	34.3
	Rear wing	9.680	2.56	0.0038	1.267	0.0048	33.6
	Fin	8.800	6.2	0.0032	1.267	0.0041	26.3
	Fuselage	87.769	89.3	0.00216	1.324	0.0028	182.4
	TOTAL	116.308	68.32*			0.003274*	276.6
6F	Front wing	18.870	4.05	0.00349	1.267	0.0044	60.6
	Rear wing	13.360	3.63	0.00355	1.267	0.0045	43.7
	Fin	8.914	6.22	0.00324	1.267	0.0041	26.6
	Fuselage	87.769	89.3	0.00216	1.324	0.0028	182.4
	TOTAL	128.91	62.2*			0.00332*	313.3
9F	Front wing	29.148	4.985	0.003366	1.267	0.00427	90.4
	Rear wing	29.040	4.44	0.003432	1.267	0.00435	91.8
	Fin	13.37	7.59	0.00314	1.267	0.00398	38.7
	Fuselage	87.769	89.3	0.00216	1.324	0.0028	182.4
	TOTAL	159.327	51.6*			0.00345*	403.3
3GA	Wing	20.6	5.32	0.00333	1.267	0.00422	63.2
	Tail	10.272	5.30	0.00333	1.267	0.00422	31.5
	Fuselage	87.769	89.3	0.00216	1.324	0.0028	182.4
	TOTAL	118.641	67.44*			0.00317*	277.1
6GA	Wing	41.2	7.45	0.00315	1.267	0.00399	119.5
	Tail	24.43	8.86	0.00306	1.267	0.00388	68.9
	Fuselage	87.769	89.3	0.00216	1.324	0.0028	182.4
	TOTAL	153.399	54.5*			0.00329*	370.8
9GA	Wing	61.8	9.197	0.00304	1.267	0.00386	173.3
	Tail	40.56	10.77	0.00297	1.267	0.00376	110.9
	Fuselage	87.769	89.3	0.00216	1.324	0.0028	182.4
	TOTAL	190.129	46.51*			0.00335*	466.6

*"Total" indicates weighted $Re = \Sigma Re\, S_{wet} / \Sigma S_{wet}$ and similarly weighted C_{fe}.

TABLE 4

HYBRID CONFIGURATION MINIMUM DRAG AT M = 0.7, SEA LEVEL STANDARD CONDITIONS

Config.	Component	S_{wet} (ft^2)	$Re \times 10^{-6}$	C_f Turbulent Flat Plate	Form Factor	C_{fe}	D_{min} (lb)
Initial Cruise	Fuselage	87.769	89.3	0.00216	1.35	0.0029	186.0
	Canard †	4.112	4.17	0.00347	1.267	0.0044	13.1
	Front wing	19.190	3.58	0.00356	1.267	0.0045	62.9
	Rear wing	13.226	2.48	0.00379	1.267	0.0048	46.2
	Fin	3.006	6.29	0.00324	1.267	0.0041	9.0
	TOTAL	127.303	62.65*			0.00342*	317.2
Before Staging	Fuselage	87.769	89.3	0.00216	1.35	0.0029	186.0
	Canard §	2.93	5.65	0.0033	1.267	0.00418	8.9
	Front wing	19.190	3.58	0.00356	1.267	0.0045	62.9
	Rear wing	13.226	2.48	0.00379	1.267	0.0048	46.2
	Fin	3.006	6.29	0.00324	1.267	0.0041	9.0
	TOTAL	126.12	63.14*			0.00340*	313.0
After Staging	Fuselage	67.851	70.6	0.00224	1.324	0.00296	150.0
	Front wing	19.190	3.58	0.00356	1.267	0.0045	62.5
	Rear wing	13.226	2.48	0.00379	1.267	0.0048	42.7
	Fin	3.006	6.29	0.00324	1.267	0.0041	8.96
	TOTAL	103.273	47.55*			0.00352*	264.2

*"Total" indicates weighted $Re = \Sigma Re\, S_{wet}/\Sigma S_{wet}$ and similarly weighted C_{fe}.

† $\Lambda = 35^{\circ}$, at 1/4-chord line.

§ $\Lambda = 62^{\circ}$, at 1/4-chord line.

where C_{L_s} is the lift coefficient at which massive separation occurs. C_{L_s} is approximately equal to the buffet lift coefficient: it was found that almost all the range and maneuver results of interest here did not involve flight at $C_L > C_{L_s}$, so Eq. 40 was adequate. Table 5 lists the key parameters describing drag due to lift. For the joined wing configurations e_x and C_{L_x} were estimated using wind tunnel test data as described in Section 1. Note that, before staging, the hybrid configuration has an e_x only slightly better than that of the conventional configurations: this is because the lift carried by the canard is distributed over a much shorter span than of the joined wing. The canard lift decreases as the nose tank is emptied, but its span also decreases because its sweep must be increased throughout cruise to maintain a positive static margin. After staging, the hybrid regains the full induced drag benefits of the joined wing.

TABLE 5. DRAG-DUE-TO-LIFT PARAMETERS

Configuration:	3GA	3F	6GA	6F	$6H_1$*	$6H_2$*	9GA	9F
C_{L_x}	0.066	0.126	0.066	0.126	0.126	0.126	0.066	0.126
e_x	0.528	0.755	0.528	0.755	0.528	0.766	0.528	0.755
Span, b, ft	10.5	9.1395	14.84	12.925	12.925	12.925	18.18	15.83
Reference area, S, ft^2	11.5	10.0	23.0	20.0	15.9992	15.9992	34.5	30.0
A	9.6	8.35	9.6	8.35	10.44	10.44	9.6	8.35
C_{L_s}	0.9	1.1	0.9	1.1	1.1	1.1	0.9	1.1

*Subscripts 1 and 2 denote pre-staging and post-staging configurations, respectively.

Figure 58 presents calculated drag polars and $(L/D)_{max}$ values for all the above configurations.

5.3 ENGINE PERFORMANCE

As noted previously, the assumed specific fuel consumption characteristics are representative of turbofan engines projected for advanced cruise missiles, but do not correspond to the S.F.C. characteristics of any particular engine. For flight at M = 0.7 S.L. the following equation for S.F.C. was assumed:

$$\underset{\text{(lb Fuel/lb Thrust/hr)}}{\text{S.F.C.}} = 1.57597295 - 0.30258\left(\frac{T}{100}\right) + 0.0369\left(\frac{T}{100}\right)^2 \tag{42}$$

when T = installed thrust in lb. This gives a S.F.C. of 1.31 at T = 100 lb, reaching a minimum of 0.955 at T = 410 lb. For flight at M = 0.7, 40,000 ft the S.F.C. was taken as 0.842 times the value calculated from the above equation. The maximum installed thrust at M = 0.7, S.L. was assumed to be 500 lb.

5.4 ESTIMATED WEIGHTS

Table 6 gives weight breakdowns for each configuration. Standard weight estimation procedures (Ref. 24) plus published data were employed to derive component weights for the conventional configurations. The estimates given are necessarily approximate — this is particularly true for Configuration 9GA where the wing folding system is bound to be complex in view of the large dimensions of the wing relative to the fuselage. The weight penalty for such a folding system can only be determined accurately after it has been designed in detail. For current cruise missiles wing weight is determined by stiffness rather than static strength requirements. In view of the high stiffness of the joined wing (see Fig. 8) this should permit considerable weight saving compared to the conventional wing-plus-tail. It has been assumed here that the joined

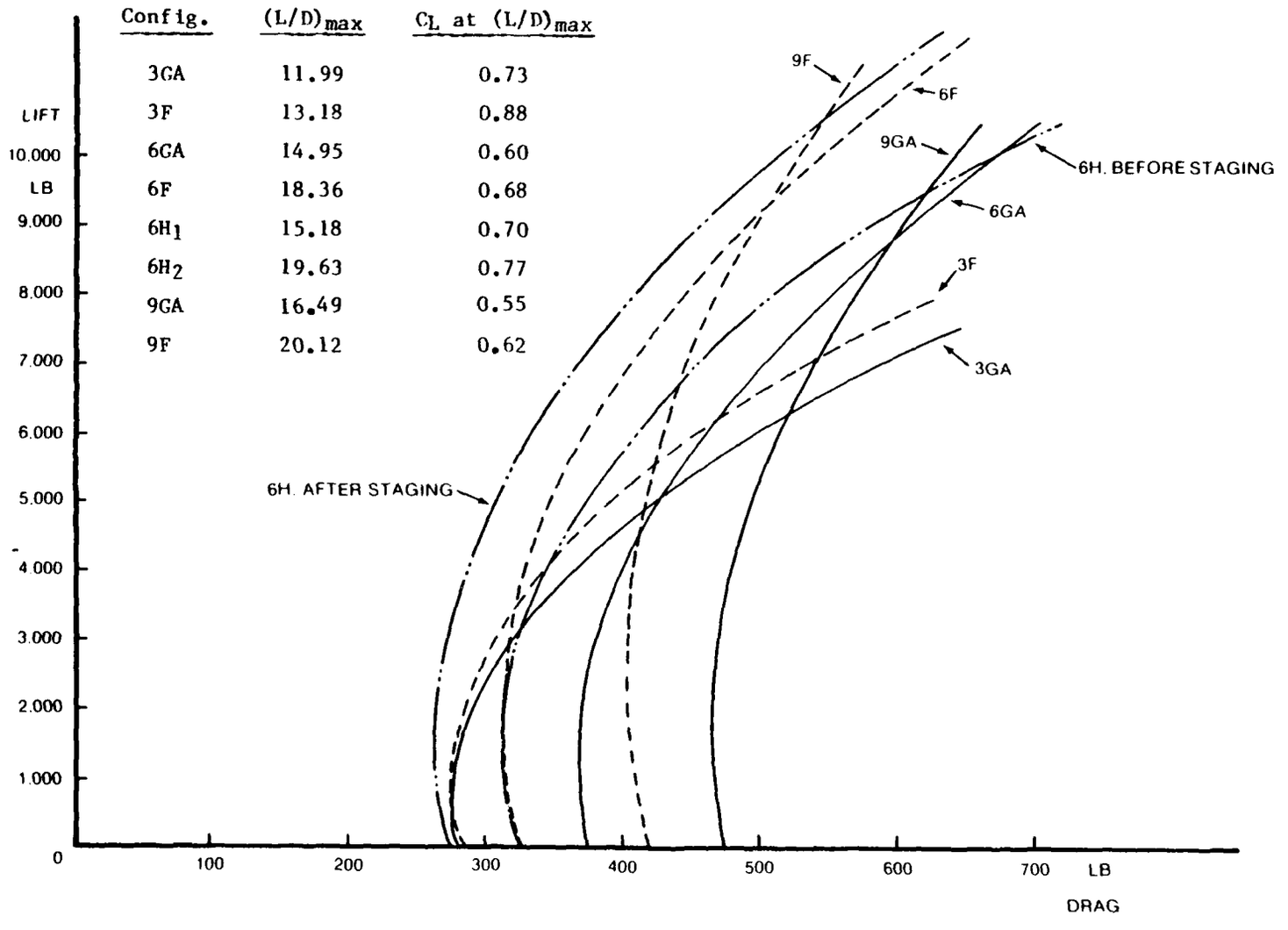

FIGURE 58. SEA LEVEL DRAG POLARS FOR CONFIGURATIONS 3GA, 6GA, 9GA, 3F, 6F, 9F, AND 6H (BEFORE AND AFTER STAGING)

TABLE 6. WEIGHT SUMMARY

(Weights given in lb)

Configuration:	3GA	3F	6GA	6F	6H	9GA	9F
Wing(s)	117.	117.	330.8	330.8	242.8	607.7	607.7
Tail	42.5	--	155.9	--	--	334.4	--
Fuselage and fin	686.0	686.0	686.0	686.0	686.0	686.0	686.0
Remainder*	467.5	467.5	467.5	467.5	467.5	467.5	467.5
Weight empty	1,313.0	1,270.5	1,640.2	1,484.3	1,386.3	2,095.6	1,761.2
Payload	275.0	275.0	275.0	275.0	275.0	275.0	275.0
Oil	5.0	5.0	5.0	5.0	5.0	5.0	5.0
Weight after staging	--	--	--	--	2,303.1	--	--
Fuel	1,271.0	1,313.5	943.8	1,099.7	636.8	488.4	822.8
Canard	--	--	--	--	39.1	--	--
Nose and tank	--	--	--	--	50.0	--	--
Weight before staging	--	--	--	--	2,392.2	--	--
Nose Fuel	--	--	--	--	471.8		
Initial cruise weight	2,864.0	2,864.0	2,864.0	2,864.0	2,864.0	2,864.0	2,864.0

*"Remainder" includes: propulsion (226), power generation (44), orientation (43), guidance (113), environmental system (8), armament (3), and miscellaneous (30.5), totalling 467.5 lb.

wing weight is equal to that of the conventional wing. From the analysis of Ref. 3 this assumption is quite conservative.

The fuel weights listed in Table 5 yield initial cruise weights of 2864.0 lb for each configuration. On this basis the fuel weights for the large-wing configurations are obviously less than those for configurations employing smaller and lighter wings. Because of this fuel weight reduction, adequate fuel tank volume is available even for the large-winged configurations where much fuselage volume is occupied by the folded wings. If the initial cruise weight were allowed to increase, volumetric fuel capacity would become a limiting factor, particularly for the conventional configurations. This is discussed in Section 5.5.

5.5 RANGE AND MANEUVERABILITY COMPARISONS

Since payload and Mach number have been fixed for all configurations, the major performance comparisons relate to range and sustained g's. These have been calculated for each configuration, and the results are compactly presented on Figs. 59 and 60. In these figures "sustained g's" denotes the normal acceleration at which the drag equals the maximum installed thrust (500 lb). The weight assumed for calculating sustained g's equals the weight of the missile, plus payload, oil, and 10% of the initial cruise fuel. In both Figs. 59 and 60 the sustained g's shown are appropriate to M = 0.7 at sea level, however in Fig. 60 the range shown applies for cruise at M = 0.7, 40,000 ft. The ranges given do not include allowances for headwinds, loiter, climb and descent, and unusable fuel (which is typically 1% of total fuel tankage).

Figure 59 shows that for the conventional configuration increasing wing area does not significantly increase sustained g capability (although it raises non-sustained g capability). This is because the parasite drag of the increased wing area approximately cancels the reduction of induced drag obtained through the reduced span-loading. This result is of course dependent on altitude and also on the maximum engine thrust assumed, but

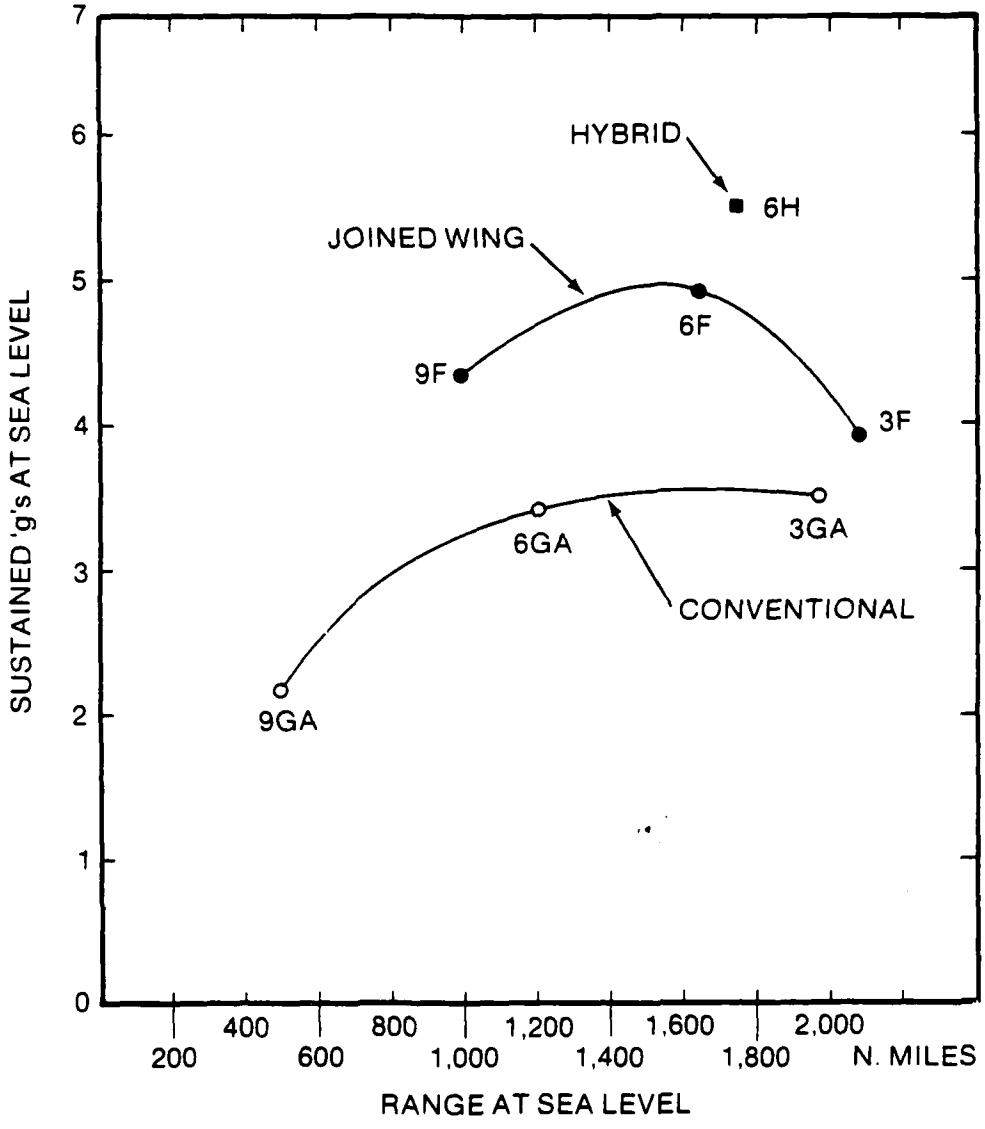

FIGURE 59. MANEUVERABILITY VS. RANGE AT SEA LEVEL

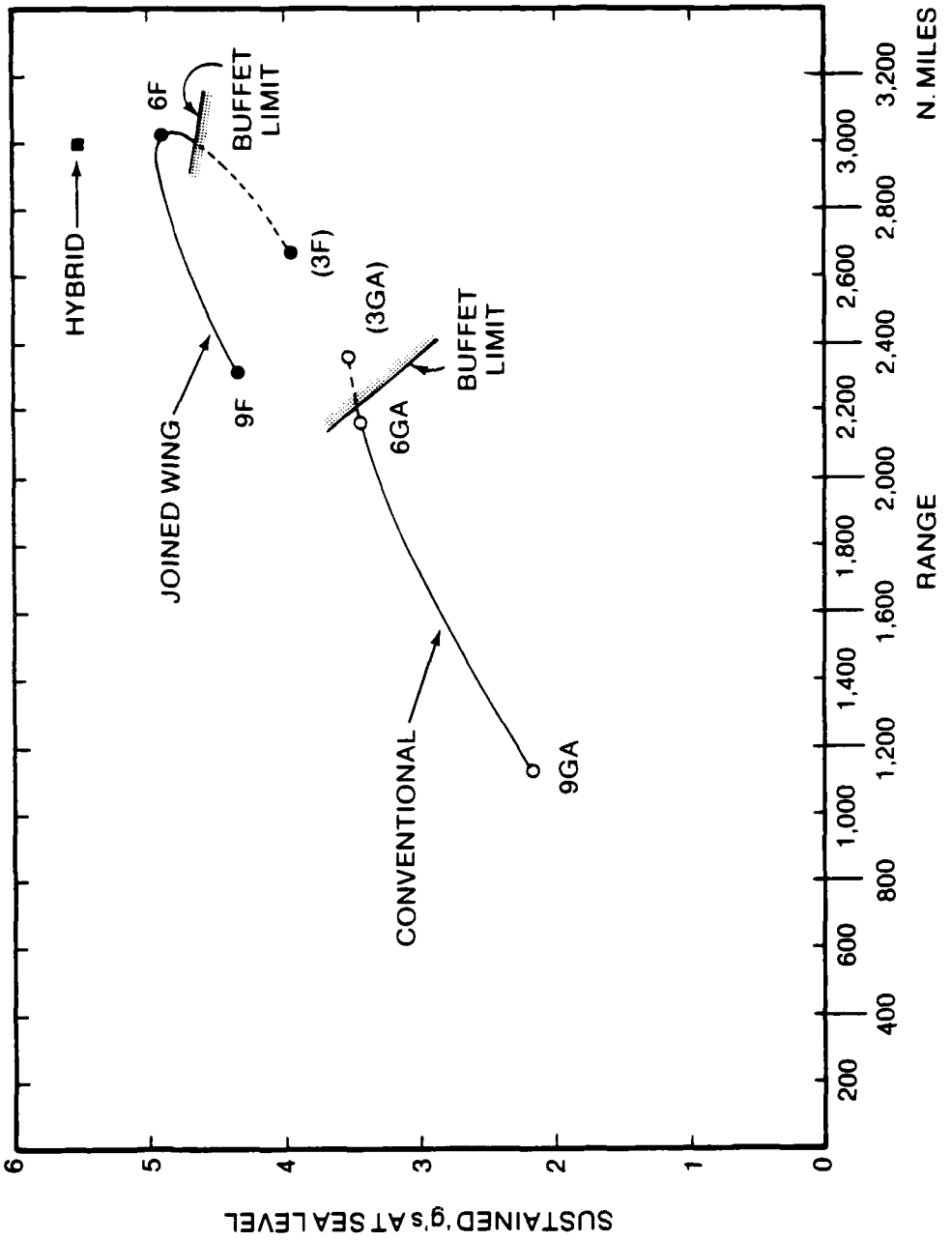

FIGURE 60. MANEUVERABILITY VS. RANGE AT 40,000 FT ALTITUDE

for sea level maneuvering, changes of ±10% in maximum thrust will not greatly affect this conclusion. To improve maneuverability it is necessary to employ either a higher aspect ratio monoplane configuration, or a joined wing or hybrid configuration, in order to get lower induced drag. For 1800 n.m. range the gain in maneuverability offered by the joined wing and hybrid configurations is considerable, as shown below:

Configuration	Conventional	Joined Wing	Hybrid
Sustained g capability	3.5	4.7	5.5
Ratio	1.0	1.34	1.57

Figure 60 illustrates the high altitude range performance of the configurations studied. It is necessary to employ wing areas of at least 20 ft^2 in order to stay below the buffet limit (C_{L_s}) during the initial cruise. The low induced drag of the joined wing configuration 6F is the main factor providing 1.38 times the range of its conventional counterpart (6GA). The hybrid configuration 6H has a maneuverability advantage, but no range advantage over 6F. This is because only a single hybrid configuration was studied. The maneuverability advantage can be traded for a range advantage by varying the hybrid wing area. Parametric variations of canard/front/rear wing geometry would also yield improved range for the hybrid configuration, since Configuration 6H was sized for stability and control, and convenient folding rather than for maximum range or maneuverability.

The range advantage of the joined wing configuration can be summarized by comparing the 6F and 6GA ranges in nautical miles graphed on Figs. 59 and 60, thus:

$$\frac{\text{Range of Joined Wing Config.}}{\text{Range of Conventional Config.}} = \frac{1636}{1206} = 1.36 \quad \text{at sea level}$$

$$= \frac{3020}{2166} = 1.39 \quad \text{at 40,000 ft}$$

The advantage of the joined wing decreases as wing area is reduced. However, it should be noted that the wing areas of the 6F and 6GA configurations approximately equal the minimum wing areas for which flight at 40,000 ft is possible.

In summary, the joined wing configuration has a marked advantage in range for missiles that are required to cruise at high altitude and/or to maneuver above the 3 g level at low altitude.

Volume Constraints: As shown in Section 3, joined wings have less volume than equivalent conventional wings. This offers a potential range advantage for a cruise missile since the total vehicle volume is limited by the dimensions of the torpedo tube from which it is launched. The range advantage could be significant for a tactical type of cruise missile, equipped with a large (non-nuclear) warhead which leaves relatively little volume available for fuel tanks. For the strategic type of missile considered here the benefits are modest, as shown below.

Assuming a 30% ullage factor, the volume occupied by the folded wings is subtracted from the total volume available for wings-plus-fuel tanks (23.013 ft^3). The remainder is the available fuel volume:

Configuration:	3GA	3F	6GA	6F	9GA	9F
1.3 × wing volume (ft^3)	1.063	0.4697	3.007	1.3285	5.524	2.4406
Available fuel volume (ft^3)	21.95	22.543	20.006	21.6845	17.489	20.5724
Ratio of fuel volumes	1.0 : 1.027		1.0 : 1.084		1 : 1.176	

Other things being equal (e.g., L/D, initial cruise weight) the range of the joined wing configuration would be greater than that of the corresponding conventional configuration in (approximately) the ratio indidated. No attempt was made to exploit this advantage in the performance calculations presented above because it would have necessitated raising the initial cruise weight above the uniform value of 2864 lb selected for all configurations. This would introduce new factors (such as different sizes of boosters) which would complicate the performance comparisons. However the low volume of the joined wing facilitates the task of accommodating payload and systems within the vehicle and would be more significant for a short-range, densely-packed missile in which the available fuel volume is critical. For all configurations discussed here the fuel volume was adequate to contain the fuel appropriate to the assumed initial cruise weight of 2864 lb.

6.0 CONCLUSIONS AND RECOMMENDATIONS

6.1 CONCLUSIONS

1. The joined wing concept has been described, and its application to cruise missile design has been studied. For cruise missiles the joined wing yields significant gains in range and maneuverability. It is also simple to fold and occupies much less volume inside the missile body than a comparable cantilever wing.

2. A study has been made of terrain-following, comparing the accuracy of joined wing and conventional cruise missiles, each equipped with optimal terrain-following guidance systems. The joined wing yields closer terrain-following provided that two forward-mounted controls are employed. This can be done by combining a joined wing with a canard to form a hybrid configuration, having control surfaces on the canard and on the front wing.

3. If desired, the hybrid configuration can be staged by employing a jettisonnable nose tank to which the canard is attached. Staging improves range and maneuverability and also reduces the size of the missile during its terminal phase so that it is less easily detected.

6.2 RECOMMENDATIONS

The joined wing is a highly integrated concept involving structures and aerodynamics. Further research in both these areas is required, as indicated below.

(1) Wind tunnel tests (subsonic, transonic and supersonic).

(2) Extension of monoplane airfoil design methods tc joined wings.

(3) Development of procedures for calculating induced drag and trimmed $C_{L\,max}$ of joined wing and hybrid configurations.

(4) General structural analyses to determine the optimum joined wing geometry for maximum stiffness and minimum weight. In particular, studies should be made of the effect of taper ratio and spanwise location of the wing joint on stiffness and weight.

(5) More detailed analyses of terrain-following, including the effects of control system lags and alternative terrain spectra.

(6) Design studies of joined wing alternatives to current and projected aircraft and missiles.

REFERENCES

1. Wolkovitch, J., Joined Wing Aircraft, U.S. Patent 3,942,747, 1976.

2. Wolkovitch, J., An Introduction to the Joined Wing Airplane, EEC Rept. No. 771, Engel Engineering Co., 28603 Trailriders Drive, Rancho Palos Verdes, CA 90274, 1977.

3. Fairchild, M. P., Structural Weight Comparison of a Joined Wing and a Conventional Wing, M.S. Thesis in Engineering Mechanics, University of Texas at Arlington, Arlington, TX, 1980.*

4. White, E. R., Preliminary Force Test Data for a Joined-Wing Aircraft Configuration, Internal Memo File V-19100/0LTR-094, NASA Langley Research Center, Hampton, VA, 8 April 1980.

5. Robertson, F. H., et al., Report on Comparison Between the Joined Wing and Orthodox Layouts When Applied to a Long Range V.I.P. Transport Airplane Design, Vought Rept. No. 2-31200/8R-51546, Vought Corporation, Dallas, TX, 1978.

6. DeYoung, J., Fuselage Structural Efficiency of N-Plane Compared with Single Wing Transport Aircraft, Vought (Hampton Tech. Center) Memo V-19000/5NASA-368, Dec. 1975.

7. Bottomley, J. W., "The Tandem-Wing Concept Applied to Modern Transports," Aeronautical J., Nov. 1974, pp. 523-524.

8. Reid, E. G., Applied Wing Theory, McGraw-Hill, 1932.

9. Igoe, W. B., R. J. Re, and M. D. Cassetti, Transonic Aerodynamic Characteristics of a Wing-Body Combination Having a 52.5 deg Sweptback Wing of Aspect Ratio 3 with Conical Camber and Designed for a Mach Number of $\sqrt{2}$, NASA TN D-817, May 1961.

10. Durand, W. F., Aerodynamic Theory, 1936; reprinted by Dover Press, New York, 1963 (section by L. V. Kerber).

11. Glauert, H., The Elements of Aerofoil and Airscrew Theory, Cambridge University Press, England, 1926.

12. Laitone, E. V., "Positive Tail Loads for Minimum Induced Drag of Subsonic Aircraft," J. Aircraft, Vol. 15, Dec. 1978, pp. 837-842.

13. Miranda, L. R., and G. L. Dougherty, Transonic Wind Tunnel Testing of a Low Induced Drag Lifting System, Vols. I and II. Contract N00019-73-C-0499, Lockheed Aircraft Corp., Burbank, CA, Feb. 1974.

---

*Published in a shortened form as AIAA Paper 81-0366, with the same title.

14. Wolkovitch, J., "Subsonic VSTOL Aircraft Configurations with Tandem Wings," J. Aircraft, Sept. 1970, pp. 605-611.

15. Hoerner, S. F., Fluid-Dynamic Drag, Hoerner Fluid Dynamics, Brick Town, NJ, 1965.

16. Henderson, W. P., and J. K. Huffman, Aerodynamic Characteristics of a Tandem Wing Configuration at a Mach Number of 0.30, NASA TM X-72779, Oct. 1975.

17. Letcher, J. S., "V-Wings and Diamond-Ring Wings of Minimum Induced Drag," J. Aircraft, Aug. 1972, pp. 605-607.

18. Kuhlman, J. M., and T. J. Ku, Numerical Optimization Techniques for Bound Circulation Distribution for Minimum Induced Drag of Non-planar Wings, NASA Tech. Progress Rept., Grant NSG1357, Nov. 1979.

19. Margason, R. J., and J. E. Lamar, Vortex-Lattice Fortran Program for Estimating Subsonic Aerodynamic Characteristics of Complex Planforms, NASA TN D-6142, 1971.

20. Lamar, J. E., A Vortex-Lattice Method for the Mean Camber Shapes of Trimmed Noncoplanar Planforms with Minimum Vortex Drag, NASA TN D-8090, 1976.

21. McCormick, B. W., Aerodynamics, Aeronautics, and Flight Mechanics, Wiley, New York, 1979.

22. Ashley, H., Engineering Analysis of Flight Vehicles, Addison-Wesley, Reading, MA, 1974.

23. Hoerner, S. F., and H. V. Borst, Fluid-Dynamic Lift, Hoerner Fluid Dynamics, Brick Town, NY, 1975.

24. Torenbeek, E., Synthesis of Subsonic Airplane Design, Delft University Press, Holland, 1976.

25. Lacey, D. W., Aerodynamic Characteristics of the Close-Coupled Canard as Applied to Low-to-Moderate Swept Wings. Vol. 2: Subsonic Speed Regime, David W. Taylor Naval Ship Research and Development Center, Bethesda, MD, Rept. DTNSRDC-79/002, 1979.

26. Addoms, R. B., and F. W. Spaid, "Aerodynamic Design of High Performance Biplane Wings," J. Aircraft, Vol. 12, No. 8, Aug. 1975, pp. 629-630.

27. Smith, A. M. O., "High-Lift Aerodynamics," J. Aircraft, June 1975, pp. 501-530.

28. Lange, R. H., et al., Feasibility Study of the Transonic Biplane Concept for Transport Aircraft Application, NASA CR-132462, June 1974.

29. Zimmer, H., Das Hochauftriebsverhalten Beim Rautenflügelkonzept, Dornier GMBH, Friedrichshafen, Germany, DGLR Rept. No. 78-114, 1978.

30. Cahill, J. F., and D. H. Stead, Preliminary Investigation at Subsonic and Transonic Speeds of Aerodynamic Characteristics of a Biplane Composed of a Swept-Back and Swept-Forward Wing Joined at the Tip, NACA RM L53L34B, Mar. 1954.

31. Henderson, J. S., Wind Tunnel Tests of a Model of a Warren-Young Wing Aircraft, unpublished report, Department of Engineering, University of Bath, England, 1976.

32. Nicolai, L. M., "A Perspective on the Requirements and Design for Advanced Cruise Missiles," AIAA Paper 79-1817, 1979.

33. Cronvich, L. L., and H. P. Liepman, Advanced Missile Technology: A Review of Technology Improvement Areas for Cruise Missiles, NASA CR-3187, 1979.

34. Washington, W. D., R. E. Wittmeyer, and W. H. Appich, Jr., "Body Slot Effects on Wing-Body and Wing-Tail Interference of a Typical Cannon-Launched Projectile," AIAA Paper 80-0260, 1980.

35. Levinsky, E. S., et al., Semispan Wind Tunnel Test Evaluation of a Computer-Controlled Variable Geometry Wing (Self-Optimizing Flexible Technology Wing Program), AEDC-TR-78-51, 1978.

36. Magdaleno, R. E., and J. Wolkovitch, Performance Criteria for Linear Constant-Coefficient Systems with Random Inputs, USAF ASD TR 62-470, ASTIA 297805, 1962.

37. Cunningham, E. P., "Probability of Crashing for a Terrain-Following Missile," J. Spacecraft and Rockets, Vol. 11, No. 4, April 1974, pp. 257-260.

38. Cunningham, E. P., "Probability of Crashing from Monte Carlo Simulation," J. Spacecraft and Rockets, Vol. 16, No. 5, Sept.-Oct. 1979, pp. 348-350.

39. McRuer, D., I. Ashkenas, and D. Graham, Aircraft Dynamics and Automatic Control, Princeton University Press, Princeton, N.J., 1973.

40. Kwakernaak, H., and R. Sivan, "The Maximally Achievable Accuracy of Linear Optimal Regulators and Linear Optimal Filters," IEEE Trans. A.C., Vol. AC-17, Feb. 1972, pp. 79-86.

41. Cunningham, E. P., "Single-Parameter Control for Terrain Following," To be published in J. Aircraft, Dec. 1980.

42. Etkin, B., "The Turbulent Wind and Its Effect on Flight," AIAA Paper 80-1836, 1980.

43. Abbott, I. H., and A. E. von Doehnhoff, Theory of Wing Sections, Dover, N. Y., 1960.

44. Linden, J. E., and F. J. O'Brimski, "Some Procedures for Use in Performance Prediction of Proposed Aircraft Designs," SAE Paper 650800, 1965.

45. Sanders, M. E., and D. E. Wieduwilt, Performance, Stability and Control Characteristics of the Full-Scale Navy/Vought Tomahawk Sea-Launched Cruise Missile (YGBM-110) at Subsonic Mach Numbers, AEDC-TR-77-18, 1977 (UNCLASSIFIED).

46. Larrabee, E. E., "The Aerodynamic Design of Sailplane Tail Assemblies," Technical Soaring, Vol. V, No. 1, 1977.

APPENDIX A

CALCULATION OF OPTIMUM TERRAIN-FOLLOWING PERFORMANCE

A1. GENERAL OBJECTIVES

Figure A1 shows a cruise missile flying above terrain. As discussed in the main text the missile is assumed to have a downward-looking terrain-following system, schematically illustrated in Fig. A2. The purpose of this system is to maintain the missile close to a desired clearance above the terrain. This desired clearance (or height bias) is denoted as h_B.

We are interested in the question of what is the minimum value of h_B that can be employed. This depends upon the statistical variation of the height error h_e, which at any instant is given by:

$$h_e = h - (h_w + h_B)$$

whence

h_w = Wave (or terrain) inertial height,

h = Inertial height of some specified point on the airframe

If we assume that the atmospheric turbulence and the wave or terrain height have Gaussian distributions, then to minimize h_B for a given probability of clobber, p_c, the control system should be designed to minimize the average value of h_e^2. Applying the ergodic hypothesis reduces the problem to a standard type of optimization problem, i.e., to find the control system that minimizes $E(h_e^2)$, where E denotes expected value.

Chang (Ref. A1) and numerous other references describe how such a control system can be found by application of optimal control theory. Two alternate types of solution techniques are available:

1. Time-domain methods (popularized by Kalman, et al.)
2. Frequency-domain methods (popularized by Weiner, et al.)

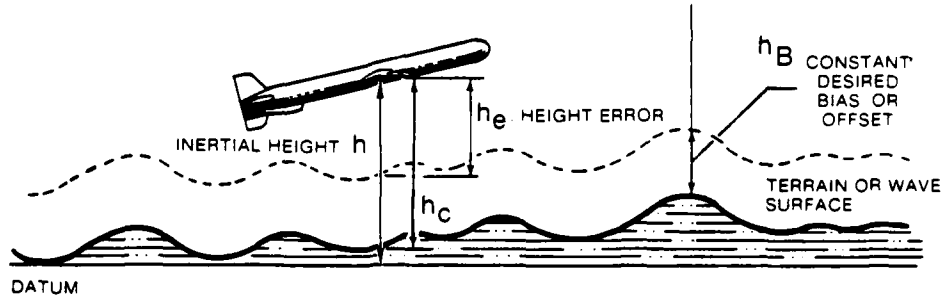

FIGURE A1. CRUISE MISSILE FLYING ABOVE TERRAIN

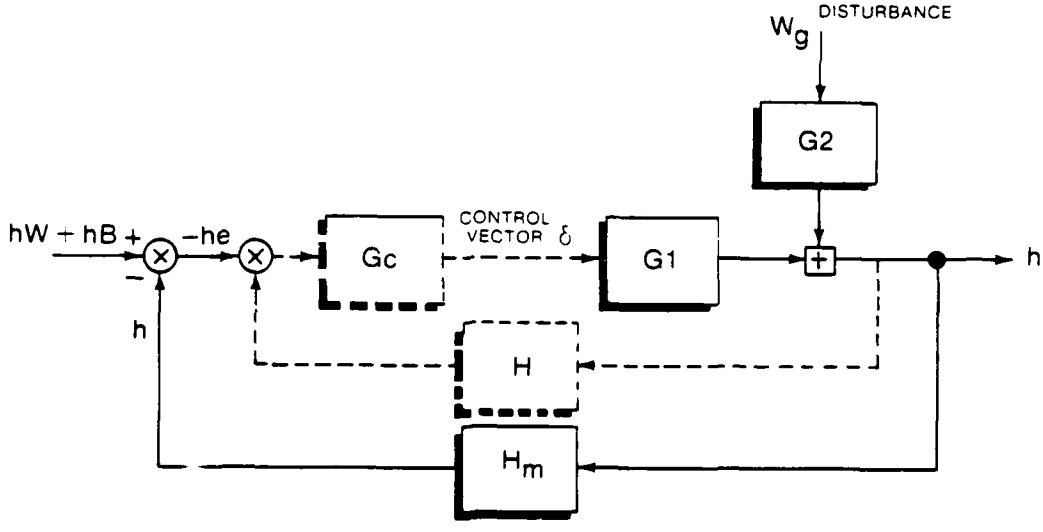

FIGURE A2. TERRAIN-FOLLOWING SYSTEM BLOCK DIAGRAM

For our purposes the frequency-domain approach is preferable, since it clearly identifies the airframe characteristics which (for some configurations) limit the closeness with which the airframe can follow the terrain. The frequency domain method is admissible since it may be assumed that the statistical properties of the signal (terrain) and noise (atmospheric turbulence) are both stationary.

This appendix presents the details of the optimization calculation. It should be noted that our principal interest is in the performance of the optimum system rather than how it is mechanized. Thus we are primarily concerned with $E(h_e^2)$ and the mean square control deflection $E(\delta^2)$ rather than the form of the compensation transfer functions G_c and H in Fig. A2.

In the following sections we discuss:

1. The mathematical model of the airframe.
2. The mathematical model of the "terrain" (sea surface).
3. The mathematical model of atmospheric turbulence.
4. Solution for the optimum system.
5. Calculation of the performance of the optimum system.

This appendix presents the required mathematical models and theory. Program listings for the HP-41C computer are given in Appendix C. Results of the optimization calculations are presented in the main text of this report.

A2. MATHEMATICAL MODEL OF THE AIRFRAME

It is assumed that the missile is equipped with a speed control (via the throttle) such that it flies over the terrain at essentially constant inertial speed. Thus the missile's longitudinal dynamics can be approximated by the short-period equations of motion (Ref. A2). These equations are written in terms of pitch attitude (θ) and angle of attack (α), however it is more convenient to rewrite the equations in terms of θ and height of the center of gravity (h), where $h = \int U_o(\theta - \alpha)\, dt$. The desired form of the short-period equations then becomes:

$$\begin{bmatrix} s - Z_w & -Z_\alpha \\ -M_{\dot{w}}s - M_w & s^2 - (M_q + M_{\dot{\alpha}})s - M_\alpha \end{bmatrix} \begin{bmatrix} -sh \\ \theta \end{bmatrix} = \begin{bmatrix} Z_\delta \\ M_\delta \end{bmatrix} \delta \qquad \text{(A1)}$$

whence

$$\frac{h}{\delta} = \frac{-Z_\delta s^2 + Z_\delta(M_q + M_{\dot{\alpha}})s + Z_\delta M_\alpha - M_\delta Z_\alpha}{s^2[s^2 - (M_q + M_{\dot{\alpha}} + Z_w)s - M_\alpha + M_q Z_w]} \qquad \text{(A2)}$$

$$\frac{\theta}{\delta} = \frac{(Z_\delta M_{\dot{w}} + M_\delta)s + Z_\delta M_w - M_\delta Z_w}{s[s^2 - (M_q + M_{\dot{\alpha}} + Z_w)s - M_\alpha + M_q Z_w]} \qquad \text{(A3)}$$

Also of interest are the transfer functions giving the response of the airframe to vertical gusts of velocity w_g fps. These transfer functions are formed following the procedure of Ref. A2, page 251, which accounts for gust gradient effects by replacing the right side of Eq. 27 by

$$\begin{bmatrix} -Z_w + Z_q s/U_o \\ -M_w + M_q s/U_o - M_{\dot{w}}s \end{bmatrix} w_g$$

Since $Z_q << U_o$ it may be neglected over the frequency range of interest here, whence, after some reduction:

$$\frac{h}{w_g} = \frac{Z_w(s - 2M_q)}{s\Delta_{sp}} \qquad \text{(A4)}$$

where

$$\Delta_{sp} = s^2 - (M_q + M_{\dot{\alpha}} + Z_w)s - M_\alpha + M_q Z_w$$

$$\frac{\theta}{w_g} = \frac{1}{U_o} \cdot \frac{s^2(M_q - M_{\dot{\alpha}}) + s(-M_\alpha - M_q Z_w)}{s\Delta_{sp}} \qquad \text{(A5)}$$

A3. WAVE SPECTRA

Fortenbaugh (Ref. A3) discusses various wave power spectra for short-crested (confused) seas and recommends the Bretschneider spectrum, which has the equation

$$S_w(\omega) = \frac{A}{\omega^5} \cdot e^{-B/\omega^4} \qquad \text{(A6)}$$

where

ω = Wave frequency in rad/sec

$A = 483.5\ H_s^2/T_o^4$

$B = 1944.5/T_o^4$

T_o = Modal wave period (sec)

H_s = Significant wave height (ft)

The parameters T_o and H_s are correlated with sea state and wind condition in Ref. A3, page 19. We shall assume a Sea State 5 with a 20 knot head-wind as a typical condition. This gives H_s = 12 ft, T_o = 12.07 sec, whence:

$$S_w = \frac{3.28}{\omega^5}\ e^{-0.09162/\omega^4} \qquad \text{(A7)}$$

For a moving observer the encountered wave frequency, ω_e, is related to ω by

$$\omega_e = \omega\left(1 \pm \frac{\omega V}{g} \cos \mu_s\right) \qquad \text{(A8)}$$

where

V = Inertial speed (fps)

μ_s = The observer's heading with respect to the predominant wave direction

For a cruise missile flying at airspeed corresponding to M = 0.7 directly into a 20 knot headwind the inertial speed is 748.12 fps. For this condition the Bretschneider spectrum is shifted in frequency, as shown in Fig. A3. The amount of the shift varies with the frequency, hence the shape of the spectrum changes. This is shown in Fig. A3 which compares Bretschneider spectra for a stationary observer and for an observer moving at 748.12 fps inertial speed.

The formula for the Bretschneider spectrum is inconvenient for optimization calculations; for such calculations it is desirable to employ spectra which can be expressed as ratios and products of linear factors of the frequency variable $j\omega$, i.e.,

$$\text{Power Spectrum} = \frac{\Pi_p (a_i + j\omega_e)(a_i - j\omega_e)}{\Pi_q (b_i + j\omega_e)(b_i - j\omega_e)} \quad , q > p \tag{A9}$$

Figure A3 shows such an approximation

$$S_w = 2{,}238{,}721.0 \frac{\omega_e^8}{(\omega_e^2 + 6.3^2)^6} \tag{A10}$$

For our optimization calculation Eq. A10 was modified to increase the power at low frequencies. This was done to model the long waves and swells characteristic of fully developed seas (as opposed to the confused seas modeled by the Bretschneider spectrum), and also to model possible maneuvering commands (e.g., for evasive action). Such commands are expected to be

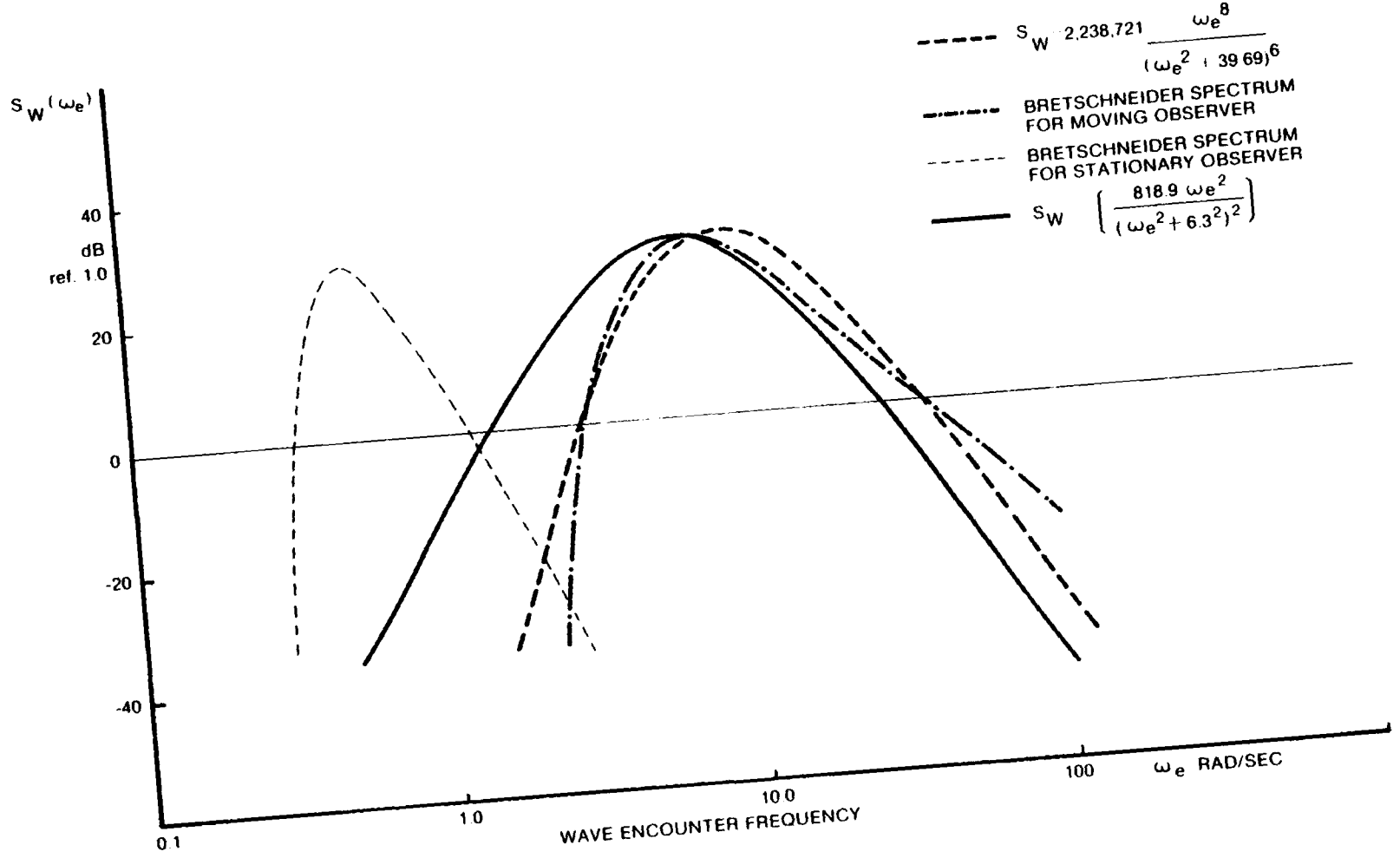

FIGURE A3. COMPARATIVE WAVE SPECTRA

largely in the 1 − 10 rad/sec frequency range. Accordingly the input command spectrum $\phi_{h_w h_w}$ employed is:

$$\phi_{h_w h_w} = 670{,}628.8 \frac{\omega_e^4}{(\omega_e^2 + 6.3^2)^4} = \left(\frac{818.9\ \omega_e^2}{(\omega_e^2 + 6.3^2)^2}\right)^2 \qquad \text{(A11)}$$

Equation 23 is also graphed on Fig. A3. $E(h_w^2)$ equals 81.2 ft^2.

A4. ATMOSPHERIC TURBULENCE

Only the vertical component of turbulence, w_g, is modeled. The well-known Dryden spectrum (Ref. A4)* gives this as:

$$(\phi_{w_g w_g})^+ = \sigma_{w_g} \cdot \sqrt{L_3} \cdot \frac{1 + j\sqrt{3}\ L_3\Omega_3}{1 + 2jL_3\Omega_3 + L_3^2(j\Omega_3)^2} \qquad \text{(A12)}$$

where

Ω_3 = Spatial frequency (rad/ft)

L_3 = Turbulence scale length (ft)

σ_{w_g} = rms turbulence intensity (fps)

*Note that the spectrum convention employed in Ref. A4 differs by a factor of π from the definition used here. The necessary corrections have been made throughout the present report.

We shall assume L_3 = 100 ft. For the missile flying parallel to the inertial wind direction at airspeed V_A fps, the encounter frequency in rad/sec is given by:

$$\omega_e = \Omega V_A \tag{A13}$$

The vertical gust r.m.s. amplitude is assumed to be 2.9 fps, based on data presented in Ref. A5, page 427, whence:

$$(\phi_{w_g w_g})^+ = \frac{1.037(1 + 0.221518j\omega_e)}{1 + 0.255787j\omega_e + 0.016357(j\omega_e)^2}$$

$$= \frac{14.0438(s + 4.5143)}{(s + 7.819)^2} \tag{A14}$$

In essence, the purpose of the optimization is to find the system that will achieve the best possible compromise between following the commands and not being excessively disturbed by atmospheric turbulence.

A5. OPTIMAL CONTROL SYSTEM

For purposes of this report the control system is assumed to be noise-free, e.g., the measured height of the missile above the local wave surface is assumed to be known precisely. Furthermore, internal system lags due to digital effects and actuator lags are neglected. Such effects are important in designing real hardware, but can be neglected for comparative studies of joined wing versus conventional airframe configurations.

The performance index selected is

$$J = E(h_e^2) + k^2 E(\delta^2) \tag{A15}$$

where

k is a constant, discussed below

δ = Control deflection (from trim position)

Only a single (inner-loop) control is considered, e.g., deflection of the all-moving tail on the conventional configuration. Combined elevator-plus-flap control is not considered (see discussion in main text). However, it is assumed that throttle is employed as an outer-loop control to maintain constant airspeed, thus suppressing phugoid motions.

The form of performance index given in Eq. A15 reflects our views on what aspects of system performance we consider to be important. Obviously it is desired to minimize $E(h_e^2)$, but at the same time it is undesirable that this should be accomplished at the cost of excessive control deflections. The parameter k^2 represents this tradeoff, and we shall obtain solutions for a wide range of k^2 to illustrate its effects. As shown in Ref. A1, additional parameters can be introduced into the performance index. For example, we could select an index of the form

$$J = E(h_e^2) + k_\delta^2 E(\delta^2) + k_n^2 E(n_z - 1)^2 \qquad \text{(A16)}$$

where k_δ, k_n are constants and n_z = normal acceleration measured in g's. Such an index would direct penalize systems which require the airframe to operate near its maximum "g" capability for a large portion of the flight. However, increasing the complexity of the performance index introduces unwelcome complications into the optimization procedure. It should also be realized that the weighting $E(\delta^2)$ also implicitly weights $E(n_z - 1)^2$. Hence Eq. A16 appears to be adequate for the present study.

A6. DERIVATION OF THE OPTIMAL CONTROL SYSTEM

The derivation given below draws upon concepts and techniques presented by Whitbeck in Ref. A5, which should be consulted for a more detailed discussion.

For the system shown on Fig. A2 the control deflection can be written in vector form as

$$\delta = [I + G_c(H + H_m)G_1]^{-1} G_c R - [I + G_c(H + H_m)G_1]^{-1} G_c(H + H_m)G_2 d \quad \text{(A17)}$$

or more compactly

$$\delta = W_a R + W_b d \quad \text{(A18)}$$

Equation A18 defines W_a and W_b.

The corresponding expression for the height error vector h_e is

$$h_e = R - C = R - G_2 d - G_1[W_a R + W_b d] \quad \text{(A19)}$$

$$= [1 - G_1 W_a]R - (G_2 + G_1 W_b)d \quad \text{(A20)}$$

$$= W_1 R + W_2 d \quad \text{(A21)}$$

Equation A21 defines W_1 and W_2.

The performance index is, by definition,

$$J = E\left\{\text{trace } h_e h_e^T + k^2 \text{ trace } \delta\, \delta^T\right\} \quad \text{(A22)}$$

Put

$$\delta = [W_a \,\vdots\, W_b]\begin{bmatrix} R \\ \cdots \\ d \end{bmatrix} \triangleq W R_1 \quad \text{(A23)}$$

$$h_e = [(1 - G_1 W_a) \,\vdots\, -(G_2 + G_1 W_b)]\begin{bmatrix} R \\ \cdots \\ d \end{bmatrix} \triangleq G_A R_1 \quad \text{(A24)}$$

$$= [I, \,\vdots\, -G_2]\begin{bmatrix} R \\ \cdots \\ d \end{bmatrix} - G_1[W_a \,\vdots\, W_b]\begin{bmatrix} R \\ \cdots \\ d \end{bmatrix} \triangleq G_B R_1 - G_1 W R_1 \quad \text{(A25)}$$

R_1, G_A, G_B, W are defined by the above equations.

$$J = E\left\{R_1^T[G_B - G_1W]^T\,[G_B - G_1W]R_1 + k^2R_1^TW^TWR_1\right\} \tag{A26}$$

where ^{T} denotes transpose

To form the equivalent expression for stationary random inputs R and d, having power spectra ϕ_{RR} and ϕ_{dd}, we employ the principle of the transient analog (Ref. A7) which for the scalar h_e and δ considered here yields J as the following frequency-domain integral

$$J = \frac{1}{2\pi j}\int_{-j\infty}^{-j\infty}\left\{W_1\phi_{RR}\bar{W}_1 + W_2\phi_{dd}\bar{W}_2 + k^2[W_a\phi_{RR}\bar{W}_a + W_b\phi_{dd}\bar{W}_b]\right\}\,dj\omega \tag{A27}$$

where

ϕ_{RR} = Terrain spectrum

ϕ_{dd} = Turbulence spectrum

ω = Frequency variable, rad/sec

$j = \sqrt{-1}$

and the superposed bars ($\bar{W}_1$, $\bar{W}_2$, $\bar{W}_a$, $\bar{W}_b$) denote complex conjugate quantities

In Eq. A27 the first two terms give the mean square height error, while the second two terms give R times the mean square control deflection. The principal focus of the discussion of this appendix relates to computing the integrals

$$\frac{1}{2\pi j}\int_{-j\infty}^{-j\infty}(W_1\phi_{RR}\bar{W}_1 + W_2\phi_{dd}\bar{W}_2)\,dj\omega$$

and

$$\frac{1}{2\pi j}\int_{-j\infty}^{-j\infty}(W_a\phi_{RR}\bar{W}_a + W_b\phi_{dd}\bar{W}_b)\,dj\omega$$

for the condition when W_a and W_b are jointly selected to give the minimum possible performance index J, for a specified value of the weighting parameter k^2.

To derive the Wiener-Hopf equation for the optimal system first differentiate Eq. A26 with respect to W^T

$$J = E\left\{[R_1^T G_B^T - R_1^T G_1^T W^T][G_B R_1 - G_1 W R_1] + k^2 R_1^T W^T W R_1\right\} \tag{A28}$$

$$= E\left\{R_1^T G_B^T G_B R_1 - R_1^T G_B^T G_1 W R_1 - R_1^T G_1^T W^T G_B R_1 + R_1^T G_1^T W^T G_1 W R_1 + k^2 R_1^T W^T W R_1\right\} \tag{A29}$$

$$\frac{\partial J}{\partial W^T} = E\left\{-R_1^T G_1^T G_B R_1 + R_1^T G_1^T G_1 W R_1 + k^2 R_1^T [W R_1]^T\right\} \tag{A30}$$

$$= E\left\{-R_1^T G_1^T (G_B - G_1 W) R_1 + k^2 W R_1 R_1^T\right\} \tag{A31}$$

$$\left[\frac{\partial J}{\partial W^T}\right]^T = E\left\{-[G_1^T (G_B - G_1 W) R\ ] R_1^T + k^2 W R_1 R_1^T\right\} \tag{A32}$$

For the variation to vanish we must have the standard Wiener-Hopf condition:

$$E\left\{[k^2 + G_1^T G_1] W R_1 R_1^T - G_1 G_B R_1 R_1^T\right\} = \psi \tag{A33}$$

where ψ is a vector that exists only for negative time, as explained in Ref. A6.

Substituting $G = [1 \mid -G_2]$, $W = [W_a \mid W_b]$ yields:

$$E\left\{[k^2 + G_1^T G_1][W_a \mid W_b] \begin{bmatrix} RR^T & Rd^T \\ dR^T & dd^T \end{bmatrix} - G_1^T [1 \mid -G_2] \begin{bmatrix} RR^T & Rd^T \\ dR^T & dd^T \end{bmatrix}\right\} = \psi \tag{A34}$$

Applying the principle of the transient analog yields a corresponding spectral matrix equation which reduces to two scalar equations since the wave "command" R and atmospheric turbulence "disturbance" d are uncorrelated, i.e., $\phi_{Rd} = \phi_{dR} = 0$. The scalar equations are:

$$[k^2 + \bar{G}_1 G_1]W_a\phi_{RR} - \bar{G}_1\phi_{RR} = \psi_1 \tag{A35}$$

$$[k^2 + \bar{G}_1 G_1]W_b\phi_{dd} + \bar{G}_1 G_2\phi_{dd} = \psi_2 \tag{A36}$$

where ψ_1, ψ_2 are functions of s that have only right half plane poles. Both Eqs. A35 and A36 have the form

$$\bar{F}FWG\bar{G} + N = \psi \tag{A37}$$

which has the standard Wiener-Hopf solution (Ref. A6):

$$W = -F^{-1}\left[(\bar{F})^{-1} N (\bar{G})^{-1}\right]_+ G^{-1} \tag{A38}$$

Equation A38 is applied below to write solutions for the specific W_a and W_b of interest here.

A7. SPECIFIC OPTIMAL CONTROL SYSTEMS

For the system considered here we have:

$$(\phi_{RR})^+ = \frac{818.9s^2}{(s + 6.3)^4} \quad , \qquad G_1 = \frac{N_1}{s^2 D}$$

$$(\phi_{dd})^+ = \frac{14.0438(s + 4.5143)}{(s + 7.819)^2} \quad , \quad G_2 = \frac{N_2}{sD}$$

Substituting in Eq. A36 yields after reduction:

$$W_a = \frac{s^2 D}{k^2 \Delta}\left[\frac{\bar{N}_1 s^2}{\bar{\Delta}(s+6.3)^4}\right]_+ \frac{(818.9)(s+6.3)^4}{(818.9)s^2} \tag{A39}$$

$$= \frac{D}{k^2 \Delta}\left[\frac{\bar{N}_1 s^2}{\bar{\Delta}(s+6.3)^4}\right]_+ (s+6.3)^4 \tag{A40}$$

whence

$$(\phi_{RR})^+ W_a = \frac{818.9D}{k^2 \Delta}\left[\frac{\bar{N}_1 s^2}{\bar{\Delta}(s+6.3)^4}\right]_+ \tag{A41}$$

$$W_b = -\frac{s^2 D}{\Delta k^2}\left[\frac{\bar{N}_1 N_2 (s+4.5143)}{sD\bar{\Delta}(s+7.819)^2}\right]_+ \frac{(s+7.819)^2}{(s+4.5143)} \tag{A42}$$

Now let us define two polynomials in s, L_a and L_b, as follows:

$$\left[\frac{\bar{N}_1 s^2}{\bar{\Delta}(s+6.3)^4}\right]_+ = \frac{L_a}{\bar{\Delta}(s+6.3)^4} \tag{A43}$$

$$\left[\frac{\bar{N}_1 N_2 (s+4.5143)}{sD\bar{\Delta}(s+7.819)^2}\right]_+ = \frac{L_b}{sD\bar{\Delta}(s+7.819)^2} \tag{A44}$$

The solutions for W_a and W_b can then be written as:

$$W_a = \frac{DL_a}{k^2\Delta} \tag{A45}$$

$$W_b = \frac{-sL_b}{k^2\Delta(s + 4.5143)} \tag{A46}$$

The method of solution for L_a and L_b will now be described. It is relatively lengthy; this is a consequence of the repeated factors in ϕ_{RR} and ϕ_{dd}, which complicate the task of forming partial fraction expansions.

A8. CALCULATION OF RESPONSE OF OPTIMUM SYSTEM

In this subsection we outline the equations employed to calculate the mean square values of h_e^2 and δ^2 from Eq. A27 (which see). Appendix C presents computer programs for solving these equations. The programs are written for the HP 41C calculator system. For ease of reference to these programs the notation used in these sections indicates the registers in which parameters are stored, e.g., the h/δ transfer function (Eq. A2) is written as:

$$\frac{h}{\delta} = G_1 = \frac{R_{01}s^2 + R_{02}s + R_{03}}{s^2(s^2 + R_{04}s + R_{05})} \tag{A47}$$

This indicates that in Eq. A2 the quantity $-Z_\delta$ is stored in Register No. 01, while $Z_\delta(M_q + M_{\dot{\alpha}})$ is stored in Register No. 02, etc., etc. Because of the limited memory of the HP-41C it has been necessary to reassign some registers during the program. Hence, where $R_{01} - R_{05}$ are reassigned, h/δ is correspondingly reassigned as follows:

$$\frac{h}{\delta} = G_1 = \frac{R_{31}s^2 + R_{32}s + R_{33}}{s^2(s^2 + R_{34}s + R_{35})} \tag{A48}$$

It will be clear from the context whether Eq. A47 or Eq. A48 is being employed.

The gust response transfer function (Eq. A4) is written as:

$$\frac{h}{w_g} = G_2 = \frac{R_{42}s + R_{43}}{s(s^2 + R_{34}s + R_{35})} \tag{A49}$$

A.8.1 Root Square Locus (Programs "OCT", "POLY", "Z↑1/N", and "QR"

The first step in the optimization is to calculate the variation of the poles of Y (Eq. A50) as a function of $1/k^2$.

$$Y = \left(1 + \frac{k^2}{G\bar{G}_1}\right)^+ = \left(1 + \frac{D\bar{D}}{\left(\frac{1}{k^2}\right)N_1\bar{N}_1}\right)^+ \tag{A50}$$

where N_1 and D_1 are respectively the numerator and denominator of Eq. A2. Rearranging Y gives

$$Y = \left(\left(\frac{1}{k^2}\right)N_1\bar{N}_1 + D_1\bar{D}_1\right)^+ = \Delta \tag{A51}$$

Chang (Ref. A1) describes a graphical procedure analogous to root locus construction for finding the roots of $Y\bar{Y}$ as functions of $1/k^2$. This procedure is known as the "root square locus" method. The graphical aspects of the method are not of interest here, but the mathematical methods are employed to find the poles of Y. We put

$$\begin{aligned} \Delta\Delta &= s^4D\bar{D} + (1/k^2)N_1\bar{N}_1 \\ &= \lambda^4 + R_{03}\lambda^3 + R_{02}\lambda^2 + R_{01}\lambda + R_{00} \end{aligned} \tag{A52}$$

where $\lambda = s^2$.

The calculation procedure is as follows:

1. $\Delta\bar{\Delta}$ is calculated (by Program "OCT").
2. The four λ-roots of $\Delta\bar{\Delta}$ are found (by Program "POLY").
3. The eight s-roots of $\Delta\bar{\Delta}$ are found (by Program "Z↑1/N").
4. The four s-roots with L.H.P. real parts are used to form factors of Δ (by Program "QR").
5. The factors are multiplied to give Δ in polynomial form:

$$\Delta = s^4 + R_{06}s^3 + R_{07}s^2 + R_{08}s + R_{09} \tag{A54}$$

where $R_{06} \rightarrow R_{09}$ are given as output of Program "QR".

A.8.2 Solution for W_a (Program "AB")

Equation A43 can be generalized to:

$$\frac{\bar{N}_1 s^2}{\bar{\Delta}(s+6.3)^4} = \frac{L_a}{(s+6.3)^4} + \frac{R_a}{\bar{\Delta}} \tag{A55}$$

$$= \frac{A}{(s+6.3)^4} + \frac{B}{(s+6.3)^3} + \frac{C}{(s+6.3)^2} + \frac{D}{(s+6.3)} + \frac{R_a}{\bar{\Delta}} \tag{A56}$$

We require expressions for A, B, C, and D. These expressions should preferably be recursive, i.e., B = f(A), C = f(A,B), D = f(A,B,C) to reduce the amount of computation required.

A can be found by multiplying both sides of Eq. A56 by $(s+6.3)^4$ and then putting s = -6.3, yielding

$$A = \left.\frac{\bar{N}_1 s^2}{\bar{\Delta}}\right|_{s=-6.3} = \frac{R_{14}R_{00}^2}{R_{10}} = R_{17} \tag{A57}$$

The symbols $R_{14}(=\bar{N}_1)_{s=-6.3}$, $R_{00}(=6.3)$, $R_{10}(=\bar{\Delta})$, R_{17}, indicate storage register allocations in the program "AB" described later. The coefficients B, C, D are found as follows.

Rearranging Eq. A56 yields

$$\bar{N}_1 s^2 - A\bar{\Delta} = B\bar{\Delta}(s+6.3) + C\bar{\Delta}(s+6.3)^2 + D\bar{\Delta}(s+6.3)^3 + R_a(s+6.3)^4 \qquad (A58)$$

Differentiating with respect to s

$$\begin{aligned} 2\bar{N}_1 s + s^2\bar{N}_1' - A\bar{\Delta}' = {} & B\bar{\Delta}'(s+6.3) + B\bar{\Delta} \\ & + 2C\bar{\Delta}(s+6.3) + C\bar{\Delta}'(s+6.3)^3 \\ & + 3C\bar{\Delta}(s+6.3)^2 + D\bar{\Delta}'(s+6.3)^3 \\ & + 4R_a(s+6.3)^3 \end{aligned} \qquad (A59)$$

Putting s = -6.3 yields the desired result

$$B = (2\bar{N}_1 s + s^2\bar{N}_1' - A\bar{\Delta}')\Big/\bar{\Delta} \qquad (A60)$$

Differentiating Eq. A59 with respect to s and putting s = -6.3 yields:

$$C = \frac{2\bar{N}_1 + 4s\bar{N}_1' + s^2\bar{N}_1'' - A\bar{\Delta}'' - 2B\bar{\Delta}'}{2\bar{\Delta}} \qquad (A61)$$

Similarly, differentiating Eq. A59 twice yields, with s = -6.3

$$D = \frac{6\bar{N}_1' + 6s\bar{N}_1'' - A\bar{\Delta}''' - 3B\bar{\Delta}'' - 6C\bar{\Delta}'}{6\bar{\Delta}} \qquad (A62)$$

The storage register allocations for Eqs. A60, A61, and A62 are as indicated below.

$$B = R_{18} = (2R_{00}R_{14} + R_{00}^2R_{15} - R_{17}R_{11}) / R_{10} \quad \text{(A63)}$$

$$C = R_{16} = \frac{2R_{14} + 4R_{00}R_{15} + 2R_{00}^2R_{01} - 2R_{18}R_{11} - R_{17}R_{12}}{2R_{10}} \quad \text{(A64)}$$

$$D = R_{15}^* = \frac{6(R_{15} + 2R_{00}R_{01}) - R_{17}R_{13} - 3R_{18}R_{12} - 6R_{16}R_{11}}{6R_{10}} \quad \text{(A65)}$$

where the asterisk indicates that register R_{15} is filled twice (first with $\bar{N}_1'$, which is subsequently cleared and replaced with D).

Having obtained A, B, C, D, as described above, these are now combined to form L_a in Eq. A55.

$$L_a = A + B(s + 6.3) + C(s + 6.3)^2 + D(s + 6.3)^3$$

The storage register assignments require clearing R_{00} (formerly $R_{00} = s = -6.3$) and putting $R_{00} = -s = 6.3$, giving

$$L_a = R_{15}(s^3 + 3R_{00}s^2 + 3R_{00}^2s + R_{00}^3) + R_{16}(s^2 + 2R_{00}s + R_{00}^2) + R_{18}(s + R_{00}) + R_{17} \quad \text{(A66)}$$

The coefficients of powers of s in Eq. A66 are evaluated and stored as follows.

$$L_a = R_{10}s^3 + R_{11}s^2 + R_{12}s + R_{13} \quad \text{(A67)}$$

A.8.3 Solution for $(\phi_{RR})^+ W_a$

The spectrum of that portion of the control deflection that is correlated with the terrain is given by $\phi_{RR}W_a\bar{W}_a$. Integrating this spectrum over the complete frequency range gives the appropriate component

of mean square control deflection. The integration is most easily performed by splitting the spectrum into left-half plane and right-half plane factors, thus:

$$\phi_{RR}W_a\bar{W}_a = (\phi_{RR})^{+}W_a \times (\phi_{RR})^{-}\bar{W}_a$$

This subsection describes the evaluation of the left-half plane factor $(\phi_{RR})^{+}W_a$.

From Section A6 we have

$$W_a(\phi_{RR})^{+} = \frac{(818.9/k^2)s^2DL_a}{\Delta(s + 6.3)^4} \tag{A68}$$

To evaluate the denominator of Eq. A68 put

$$(s+6.3)^4 = s^4 + 25.2s^3 + 238.14s^2 + 1{,}000.188s + 1{,}575.2961 \tag{A69}$$

$$= s^4 + R_{20}s^3 + R_{21}s^2 + R_{22}s + R_{23} \tag{A70}$$

Multiplying the right-hand side of Eq. A70 by the right-hand side of A54 and assigning appropriate registers yields:

$$\Delta(s+6.3)^4 = s^8 + R_{24}s^7 + R_{25}s^6 + R_{26}s^5 + R_{27}s^4 + R_{28}s^3 + R_{29}s^2 + R_{30}s + R_{31} \tag{A71}$$

To evaluate the numerator of Eq. A68 put

$$s^2 DL_a = \underbrace{(s^4 + R_{04}s^3 + R_{05}s^2)}_{\text{From Eq. A47}} \underbrace{(R_{10}s^3 + R_{11}s^2 + R_{12}s + R_{13})}_{\text{From Eq. A67}}$$

$$= R_{33}s^7 + R_{34}s^6 + R_{35}s^5 + R_{36}s^4 + R_{37}s^3 + R_{38}s^2 \qquad \text{(A72)}$$

Finally, put $R_{32} = 818.9/k^2$ and multiply Eq. A72 appropriately, reassigning R_{33}-R_{38} and adding zeros in R_{39} and R_{40}. This yields the desired result as:

$$W_a(\phi_{RR})^+ = \frac{R_{33}s^7 + R_{34}s^6 + R_{35}s^5 + R_{36}s^4 + R_{37}s^3 + R_{38}s^2 + R_{39}s + R_{40}}{s^8 + R_{24}s^7 + R_{25}s^6 + R_{26}s^5 + R_{27}s^4 + R_{28}s^3 + R_{29}s^2 + R_{30}s + R_{31}} \qquad \text{(A73)}$$

A.8.4 Integration of Spectral Factors (Program "I8N")

Given the LHP and RHP factors of the numerator and denominator of a power spectrum of a variable in the form of polynomials A and B as follows:

$$\phi_{pp} = \frac{A(s)}{B(s)} \times \frac{A(-s)}{B(-s)} \quad , \quad s = j\omega \qquad \text{(A74)}$$

The mean square value of p is, by Parseval's theorem (Ref. A8)

$$E(p^2) = \frac{1}{2\pi j} \int_{-j\infty}^{-j\infty} \frac{A(s)A(-s)}{B(s)B(-s)}\, ds \quad , \quad s = j\omega \qquad \text{(A75)}$$

Reference A8 gives formulas for evaluating $E(p^2)$ in terms of the coefficients of A(s) and B(s). For the 8th order denominators of interest here these formulas proved to be ill-conditioned. Attempts to evaluate the I_8 formula of Ref. A8 were made using first the HP-41C and subsequently the CDC 6600 computers. Neither computer was able to give

reliable results. For example, negative values of $E(p^2)$ were obtained. The problem may be associated with the repeated denominator roots of the command and disturbance spectra.

After repeated attempts to employ the formulas of Ref. A8 proved fruitless it was decided to approximate Eq. A75 by:

$$E(p^2) = \frac{1}{\pi j} \int_0^{100} \frac{A(j\omega)A(-j\omega)}{B(j\omega)B(-j\omega)} \, dj\omega \tag{A76}$$

$$= \frac{1}{\pi} \int_0^{100} \frac{A(j\omega)A(-j\omega)}{B(j\omega)B(-j\omega)} \, d\omega \quad , \quad \omega \text{ in rad/sec} \tag{A77}$$

As will be described, Program "I8N" is employed to compute $W_a \phi_{RR} \bar{W}_a$ as a function of ω. The integration was then performed by a standard HP-41C math module routine "INTG". An interval ($\Delta\omega$) of 1 rad/sec was employed, giving 100-step integration: no significant gain in accuracy was obtained by increasing the number of steps. Some checks were made regarding the effect of the finite upper limit in Eq. A77. It was found that the value of the integral typically changed less than 1% if the upper limit of integration was raised to 200 rad/sec.

The "I8N" program employs nested expressions to reduce computer time. Thus the RHS of Eq. A73 is rewritten as:

$$\frac{(((-R_{34}\omega^2 + R_{36})\omega^2 - R_{38})\omega^2 + R_{40}) + j\omega(((-R_{33}\omega^2 + R_{35})\omega^2 - R_{37})\omega^2 + R_{39})}{((((\omega^2 - R_{25})\omega^2 + R_{27})\omega^2 - R_{29})\omega^2 + R_{31}) + j\omega(((-R_{24}\omega^2 + R_{26})\omega^2 - R_{28})\omega^2 + R_{30})}$$

ω is stored in R_{11}, other register assignments are obvious from the listing of "I8N" given later.

The next subsection describes the method used to calculate the mean square value of the second part of the control deflection of the optimally-controlled system, i.e., that part which is correlated with the atmospheric turbulence. The procedure follows similar procedures to those demonstrated above for computing the mean square value of the component of control deflection correlated with the command (terrain) input. It was found that the latter was dominant for all cases considered here and, as a first approximation, the turbulence-correlated component could be neglected. In general it will not be known a priori that one component is negligible, hence the second component of control deflection should be calculated as described below.

A.8.5 Solution for $(\Phi_{dd})^{+} W_B$ (Program "WBC")

Equations A46 and A44 yield:

$$(\Phi_{dd})^{+} W_B = \frac{(14.0438/k^2)(-sL_b)}{\Delta(s+7.819)^2} \tag{A80}$$

where

$$L_b = sD\bar{\Delta}(s+7.819)^2 \left[\frac{\bar{N}_1 N_1 (s+4.5143)}{sD\bar{\Delta}(s+7.819)^2}\right]_{+} \tag{A90}$$

To calculate the $[\ ]_{+}$ term, first expand its kernel thus:

$$\frac{\bar{N}_1 N_2(s + 4.54143)}{sD(s + 7.819)^2 \bar{\Delta}} = \frac{L_4 s^4 + L_3 s^3 + L_2 s^2 + L_1 s + L_0}{sD(s + 7.819)^2}$$

$$+ \frac{-L_4 s^3 + B_2 s^2 + B_1 s + B_0}{\bar{\Delta}} \qquad \text{(A91)}$$

The $-L_4$ term in Eq. A91 arises because the LHS of Eq. A91 comprises a 4th order numerator whereas the denominator is 9th order. Thus Eq. A91 can be written as:

$$\bar{N}_1 N_2(s + 4.54143) = (L_4 s^4 + L_3 s^3 + L_2 s^2 + L_1 s + L_0)\bar{\Delta}$$

$$+ (-L_4 s^3 + B_2 s^2 + B_1 s + B_0) sD(s + 7.819)^2 \qquad \text{(A92)}$$

with storage register assignments as follows:

$$N_2 = R_{42} s + R_{43} \quad , \quad \bar{N}_1 = R_{01} s^2 - R_{02} s + R_{03} \quad , \quad D = s^2 + R_{04} s + R_{05} \quad ,$$

$$(s + 7.819)^2 = s^2 + R_{10} s + R_{11}$$

Program "WBC" solves Eq. A92 for L_4, L_3, L_2, L_1, L_0 by equating coefficients of equal powers of s. The register assignments are:

$$sD(s + 7.819)^2 = s^5 + R_{12} s^4 + R_{13} s^3 + R_{10} s^2 + R_{11} s \qquad \text{(A93)}$$

$$4.5143 = R_{18} \qquad \text{(A94)}$$

The LHS of Eq. A92 is expanded as follows:

$$\bar{N}_1 N_2 = (R_{01} s^2 - R_{02} s + R_{03})(R_{42} s + R_{43}) \qquad \text{(A95)}$$

$$= R_{14} s^3 + R_{15} s^2 + R_{16} s + R_{17} \qquad \text{(A96)}$$

$$\bar{N}_1 N_2 (s + 4.5143) = R_{14}s^4 + R_{20}s^3 + R_{15}s^2 + R_{16}s + R_{17} \qquad \text{(A97)}$$

The RHS of Eq. A92 is expanded making use of Eq. A93 to yield a polynomial formed by the sum of the terms listed below:

s^8	s^7	s^6	s^5	s^4	s^3	s^2	s	Const.
L_4	L_3	L_2	L_1	L_0				
$-L_4$	$-R_{06}L_4$	$-R_{06}L_3$	$-R_{06}L_2$	$-R_{06}L_1$	$-R_{06}L_0$			
$(\Sigma = 0)$	$-R_{12}L_4$	$R_{07}L_4$	$R_{07}L_3$	$R_{07}L_2$	$R_{07}L_1$	$R_{07}L_0$		
		$-R_{13}L_4$	$-R_{08}L_4$	$-R_{08}L_3$	$-R_{08}L_2$	$-R_{08}L_1$	$-R_{08}L_0$	
		$R_{12}B_2$	$-R_{10}L_4$	$R_{09}L_4$	$R_{09}L_3$	$R_{09}L_2$	$R_{09}L_1$	$R_{09}L_0$
		B_1	$R_{13}B_2$	$-R_{11}L_4$	$R_{11}B_2$	$R_{11}B_1$	$R_{11}B_0$	
			$R_{12}B_1$	$R_{10}B_2$	$R_{10}B_1$	$R_{10}B_0$		
			B_0	$R_{13}B_1$	$R_{13}B_0$			
				$R_{12}B_0$				

Evaluating this polynomial to the RHS of Eq. A96 yields immediately

$$R_{09}L_0 = R_{17} \qquad \text{(A98)}$$

$$L_0 = \frac{R_{17}}{R_{09}} = R_{19} \qquad \text{(A99)}$$

The remaining terms $L_4 \ldots L_1$, $B_2 \ldots B_0$ are given by the following matrix equation.

$$\left[\begin{array}{cccc|ccc} -(R_{12}+R_{06}) & 1 & 0 & 0 & 1 & 0 & 0 \\ (R_{07}-R_{13}) & -R_{06} & 1 & 0 & R_{12} & 1 & 0 \\ -(R_{10}+R_{08}) & R_{07} & -R_{06} & 1 & R_{13} & R_{12} & 1 \\ (R_{09}-R_{11}) & -R_{08} & R_{07} & -R_{06} & R_{10} & R_{13} & R_{12} \\ \hline 0 & R_{09} & -R_{08} & R_{07} & R_{11} & R_{10} & R_{13} \\ 0 & 0 & R_{09} & -R_{08} & 0 & R_{11} & R_{10} \\ 0 & 0 & 0 & R_{09} & 0 & 0 & R_{11} \end{array}\right]\left[\begin{array}{c} L_4 \\ L_3 \\ L_2 \\ L_1 \\ \hline B_2 \\ B_1 \\ B_0 \end{array}\right] = \left[\begin{array}{c} 0 \\ 0 \\ 0 \\ R_{14}-L_0 \\ \hline R_{20}+R_{06}L_0 \\ R_{15}-R_{07}L_0 \\ R_{16}+R_{08}L_0 \end{array}\right] \tag{A100}$$

The first step in the solution is to reassign the RHS elements of Eq. A100 thus:

$$RHS = [0,\ 0,\ 0,\ R_{14},\ \vdots\ R_{20},\ R_{15},\ R_{16}]^T \tag{A101}$$

The most straightforward way to solve Eqs. A100 and A101 is to invert the matrix by use of the HP-41C math module "SIMEQ" routine. This routine was not available at the time when program "WBC" was written, hence Eq. A101 was solved by a partitioning method which is briefly summarized below, for the benefit of readers who wish to check the listing of "WBC" given later. Other readers should skip this, and go directly to Eq. A114.

1. The matrix is partitioned as indicated, giving with obvious notation

$$\left[\begin{array}{c|c} P_{11} & P_{12} \\ \hline P_{21} & P_{22} \end{array}\right]\left[\begin{array}{c} L_b \\ \hline B \end{array}\right] = \left[\begin{array}{c} Y_1 \\ \hline Y_2 \end{array}\right] \tag{A102}$$

whence

$$P_{22}B + P_{21}L_b = Y_2 \tag{A103}$$

2. P_{22}^{-1} is calculated algebraically

$$P_{22}^{-1} = \begin{bmatrix} 1/R_{11} & -R_{10}/R_{11}^2 & (R_{10}^2 - R_{11}R_{13})/R_{11}^3 \\ 0 & 1/R_{11} & -R_{10}/R_{11}^2 \\ 0 & 0 & 1/R_{11} \end{bmatrix} = \begin{bmatrix} R_{17} & R_{18} & R_{21} \\ 0 & R_{17} & R_{18} \\ 0 & 0 & R_{17} \end{bmatrix} \tag{A104}$$

3. Since

$$B = P_{22}^{-1}\{Y_2 - P_{21}L\} \tag{A105}$$

B can be expressed, after reassignment of many registers, as:

$$[B] = \begin{bmatrix} B_2 \\ B_1 \\ B_0 \end{bmatrix} = \begin{bmatrix} R_{20} \\ R_{15} \\ R_{16} \end{bmatrix} - \begin{bmatrix} 0 & R_{22} & R_{23} & R_{21} \\ 0 & 0 & R_{22} & R_{23} \\ 0 & 0 & 0 & R_{23} \end{bmatrix} \begin{bmatrix} L_4 \\ L_3 \\ L_2 \\ L_1 \end{bmatrix} \tag{A106}$$

4. From Eq. A102

$$P_{12}B + P_{11}L_b = Y_1 \tag{A107}$$

Substitute Eq. A107 into Eq. A106; reassign the first column of P_{11} as $[R_{24}, R_{25}, R_{26}, R_{27}]^T$, and multiply out. After reassignment this yields:

$$\begin{bmatrix} R_{24} & R_{28} & R_{32} & R_{36} \\ R_{25} & R_{29} & R_{33} & R_{37} \\ R_{26} & R_{30} & R_{34} & R_{38} \\ R_{27} & R_{31} & R_{35} & R_{39} \end{bmatrix} \begin{bmatrix} L_4 \\ L_3 \\ L_2 \\ L_1 \end{bmatrix} = \begin{bmatrix} R_{13} \\ R_{12} \\ R_{11} \\ R_{10} \end{bmatrix} \tag{A108}$$

5. Solve for $[L_4, L_3]^T$ in terms of $[L_2, L_1]^T$ by partitioning and inverting the resulting 2×2 submatrices, yielding after reassignment:

$$\begin{bmatrix} L_4 \\ L_3 \end{bmatrix} = \begin{bmatrix} R_{16} \\ R_{17} \end{bmatrix} - \begin{bmatrix} R_{12} & R_{14} \\ R_{13} & R_{15} \end{bmatrix} \begin{bmatrix} L_2 \\ L_1 \end{bmatrix} \tag{A109}$$

Substituting Eq. A109 in Eq. A108 yields after reduction:

$$\left[\begin{array}{c|c} R_{34} - R_{26}R_{12} - R_{30}R_{13} & R_{38} - R_{26}R_{14} - R_{30}R_{15} \\ \hline R_{35} - R_{27}R_{12} - R_{31}R_{13} & R_{39} - R_{27}R_{14} - R_{31}R_{15} \end{array}\right] \begin{bmatrix} L_2 \\ L_1 \end{bmatrix} = \begin{bmatrix} R_{11} - R_{26}R_{16} + R_{38}R_{17} \\ R_{10} - R_{27}R_{16} - R_{39}R_{17} \end{bmatrix} \tag{A110}$$

After reassigning registers this becomes

$$\begin{bmatrix} R_{20} & R_{22} \\ R_{21} & R_{23} \end{bmatrix} \begin{bmatrix} L_2 \\ L_1 \end{bmatrix} = \begin{bmatrix} R_{11} \\ R_{10} \end{bmatrix} \tag{A111}$$

Solving Eq. A111 and reassigning $L_0 = R_{19}$, $L_2 = R_{11}$, $L_1 = R_{10}$ yields, from Eq. A109

$$L_4 = R_{16} - R_{12}R_{11} - R_{14}R_{10} = R_{13} \tag{A112}$$

$$L_3 = R_{17} - R_{13}R_{11} - R_{15}R_{10} = R_{12} \tag{A113}$$

whence the desired result:

$$L_b = L_4s^4 + L_3s^3 + L_2s^2 + L_1s + L_0 = R_{13}s^4 + R_{12}s^3 + R_{11}s^2 + R_{10}s + R_{14} \tag{A114}$$

The next subsection describes the procedure employed to calculate the mean square value of that component of mean square height error correlated with the terrain. For the cases considered here this proved to be the dominant component; the turbulence-correlated component was negligible in comparison.

A.8.6 Solution for $(\phi_{RR})^+ W_1$ (Program "DE")

Referring back to Eq. A27 it can be seen that the portion of the mean square height error that is correlated with the terrain (wave) input is determined by $(\phi_{RR})^+ W_1$. From Eq. A20 this can be written as:

$$(\phi_{RR})^+ W_1 = \frac{(818.9)\left(s^2\Delta - \frac{N_1 L_a}{k^2}\right)}{\Delta(s + 6.3)^4} \tag{A78}$$

The first term in the numerator parentheses is:

$$s^2\Delta = s^6 + R_{06}s^5 + R_{07}s^4 + R_{08}s^3 + R_{09}s^2$$

The second term is:

$$\frac{N_1 L_a}{k^2} = \frac{1}{R_{41}} (R_{10}s^3 + R_{11}s^2 + R_{12}s + R_{13})(R_{01}s^2 + R_{02}s + R_{03})$$

where

$$\frac{1}{k^2} = R_{41}$$

The complete numerator of Eq. A78, including the 818.9 factor (stored as R_{34}) is given by Program "DE" as follows. The lead term R_{33} is zero, as explained below.

$$R_{33}s^7 + R_{34}s^6 + R_{35}s^5 + R_{36}s^4 + R_{37}s^3 + R_{38}s^2 + R_{39}s + R_{40}$$

R_{33} is zero: this is a dummy term required for compatibility with the "I8N" program. R_{33} through R_{40} are overwritten, since these registers were previously used for the numerator of $W_a(\phi_{RR})^+$. The denominator of $(\phi_{RR})^+W_1$ is identical with that of $(\phi_{RR})^+W_a$ so registers 24 through 31 need not be overwritten.

The calculation of $\phi_{RR}W_1\overline{W}_1$ is performed using Program "I8N" as for $\phi_{RR}W_a\overline{W}_a$, and the subsequent integration is performed by Program "INTG", as previously.

Having found L_b, it can be substituted in Eq. A80, giving

$$(\phi_{dd})^+W_b = \frac{-(14.0438/k^2)(R_{13}s^5 + R_{12}s^4 + R_{11}s^3 + R_{10}s^2 + R_{14}s)}{\Delta(s + 7.819)^2} \qquad \text{(A114)}$$

The denominator of this expression is:

$$(s^4 + R_{06}s^3 + R_{07}s^2 + R_{08}s + R_{09})(s^2 + R_{15}s + R_{16})$$

$$= s^6 + R_{20}s^5 + R_{21}s^4 + R_{22}s^3 + R_{23}s^2 + R_{24}s + R_{25} \qquad \text{(A115)}$$

The numerator of Eq. 114 is written as

$$-(R_{26}s^5 + R_{27}s^4 + R_{28}s^3 + R_{29}s^2 + R_{30}s + R_{31})$$

whence

$$-(\phi_{dd})^{+}W_b = \frac{R_{26}s^5 + R_{27}s^4 + R_{28}s^3 + R_{29}s^2 + R_{30}s + R_{31}}{s^6 + R_{20}s^5 + R_{21}s^4 + R_{22}s^3 + R_{23}s^2 + R_{24}s + R_{25}} \quad \text{(A116)}$$

A.8.7 Integration of Spectral Factors (Program "I6N")

Section A.8.6 describes the ill-conditioning problems encountered with integration of $W_a\phi_{RR}\bar{W}_a$. To avoid a recurrence of these difficulties in the evaluation of $\phi_{dd}W_b\bar{W}_b$, a numerical integration procedure was employed, similar to the "I8N" program. The program for evaluating $\phi_{dd}W_b\bar{W}_b$ as a function of frequency, ω, is labeled "I6N". It represents Eq. A116 as a nested expression.

$$-(\phi_{dd})^{+}W_b = \frac{((R_{27}\omega^2 - R_{29})\omega^2 + R_{31}) + j((R_{26}\omega^2 - R_{28})\omega^2 + R_{30})\omega}{(((-\omega^2 + R_{21})\omega^2 - R_{23})\omega^2 + R_{25}) + j((R_{20}\omega^2 - R_{22})\omega^2 + R_{24})\omega} \quad \text{(A117)}$$

This is multiplied by its complex conjugate and integrated between limits of $\omega = 0$ and $\omega = 100$ rad/sec using the HP-41C math module subroutine "INTG" with 100 intervals of 1 rad/sec, similarly to the integration of the "I8N" program output described in Section A.8.4.

A.8.8 Solution for $(\phi_{dd})^{+}W_2$ (Program "W2C",

From Eq. A20

$$W_2 = -(G_2 + G_1W_b) \quad \text{(A120)}$$

$$W_2 = -\begin{bmatrix} \dfrac{R_{42}s + R_{43}}{s(s^2 + R_{04}s + R_{05})} & \dfrac{-(R_{01}s^2 + R_{02}s + R_{03})s\ L_b}{s^2(s^2 + R_{04}s + R_{05})k^2\Delta(s + 4.5143)} \end{bmatrix} \tag{A121}$$

$$= \frac{(1/k^2)(R_{01}s^2+R_{02}s+R_{03})(R_{13}s^4+R_{12}s^3+R_{11}s^2+R_{10}s+R_{14})-\Delta(s+4.5143)(R_{42}s+R_{43})}{s(s^2 + R_{04}s + R_{05})\Delta(s + 4.5143)} \tag{A122}$$

The second term in the numerator of Eq. 122 is evaluated by assigning 4.5143 to R_{15}, subsequently reassigning R_{15} as indicated below.

$$(R_{42}s + R_{43})(s + R_{15}) = R_{17}s^2 + R_{16}s + R_{15} \tag{A123}$$

Other storage registers are reassigned as indicated below.

$$(R_{17}s^2 + R_{16}s + R_{15})(s^4 + R_{06}s^3 + R_{07}s^2 + R_{08}s + R_{09}) \tag{A124}$$
$$= R_{17}s^6 + R_{18}s^5 + R_{19}s^4 + R_{26}s^3 + R_{27}s^2 + R_{16}s + R_{15}$$

The complete numerator of Eq. A122 is computed as follows, using $(1/k^2) = R_{41}$

$$(R_{01}s^2 + R_{02}s + R_{03})(R_{13}s^4 + R_{12}s^3 + R_{11}s^2 + R_{10}s + R_{14})R_{41}$$
$$- R_{17}s^6 - R_{18}s^5 - R_{19}s^4 - R_{26}s^3 - R_{27}s^2 - R_{16}s - R_{15} \tag{A125}$$
$$= R_{17}s^6 + R_{18}s^5 + R_{19}s^4 + R_{26}s^3 + R_{27}s^2 + R_{16}s + R_{15}$$

We now have

$$W_2 = \frac{R_{17}s^6 + R_{18}s^5 + R_{19}s^4 + R_{26}s^3 + R_{27}s^2 + R_{16}s + R_{15}}{s(s^2 + R_{04}s + R_{05})\Delta(s + 4.5143)} \tag{A126}$$

It can be shown that R_{15} should be zero. The proof of this is given in Section A.8.9, to avoid a digression at this point. Due to roundoff errors the computed R_{15} will not be exactly zero. The program "W2C" prints out R_{15} as an indication of the magnitude of the roundoff errors.

With R_{15} dropped, $(\phi_{dd})^+ W_2$ is computed using Eq. A14 with $d = w_g$

$$(\phi_{dd})^+ = \frac{14.0438(s + 4.5143)}{(s + 7.819)^2} \tag{A127}$$

$$W_2(\phi_{dd})^+ = \frac{14.0438(R_{17}s^5 + R_{18}s^4 + R_{19}s^3 + R_{26}s^2 + R_{27}s + R_{16})}{(s^2 + R_{04}s + R_{05})(\Delta)(s + 7.819)^2} \tag{A128}$$

The denominator factors $(\Delta)(s + 7.819)^2$ are already stored from Program "WBC" as:

$$(\Delta)(s + 7.819)^2 = s^6 + R_{20}s^5 + R_{21}s^4 + R_{22}s^3 + R_{23}s^2 + R_{24}s + R_{25}$$

Multiplying by $(s^2 + R_{04}s + R_{05})$ yields the complete denominator as:

$$s^8 + R_{24}s^7 + R_{25}s^6 + R_{26}s^5 + R_{27}s^4 + R_{28}s^3 + R_{29}s^2 + R_{30}s + R_{31}$$

The "W2C" program prints out R_{24} through R_{40} to identify $W_2(\phi_{dd})^+$ in the following form

$$(\phi_{dd})^{+}W_2 = \frac{R_{33}s^7 + R_{34}s^6 + R_{35}s^5 + R_{36}s^4 + R_{37}s^3 + R_{38}s^2 + R_{39}s + R_{40}}{s^8 + R_{24}s^7 + R_{25}s^6 + R_{26}s^5 + R_{27}s^4 + R_{28}s^3 + R_{29}s^2 + R_{30}s + R_{31}} \tag{A129}$$

Integration. Since $(\phi_{dd})^{+}W_2$ has an eighth-order numerator it can be integrated by Program "I8N" exactly as described in Section A.8.4.

A.8.9 Proof That s Is a Factor of the Numerator of W_2

This proof is required for the simplification of Eq. A126. From Eqs. A120 and A46,

$$W_2 = -G_2 - G_1W_B = \frac{-N_2}{sD} + \frac{N_1}{s^2D}\,\frac{s\,L_b\,(1/k^2)}{\Delta(s + 4.5143)} \tag{A130}$$

$$W_2 = \frac{-N_2 s\Delta(s + 4.5143) + N_1 s L_b\,(1/k^2)}{s^2 D\,\Delta\,(s + 4.5143)} \tag{A131}$$

But from Eqs. A91 and A44,

$$L_b \cdot \bar{\Delta} + B \cdot sD(7.819)^2 = \bar{N}_1N_2(s + 4.5143) \tag{A132}$$

where $B = -L_4s^3 + B_2s^2 + B_1s + B_0$ in Eq. A91. If $s = 0$ is a factor of the numerator of W_2 then

$$[-N_2\Delta(s + 4.5143) + N_1L_b(1/k^2)]_{s=0} = 0 \tag{A133}$$

But from Eq. 132, for $s = 0$, $L_b\bar{\Delta} = \bar{N}_1N_2(s + 4.5143)$

$$\left[-N_2\Delta(s + 4.5143) + \frac{N_1\bar{N}_1N_2(s + 4.5143)}{k^2\bar{\Delta}}\right]_{s=0} = 0 \qquad \text{(A134)}$$

$$\left[\frac{-N_2(s + 4.5143)}{\bar{\Delta}}\left(\Delta\bar{\Delta} - \frac{1}{k^2}N_1\bar{N}_1\right)\right]_{s=0} = 0 \qquad \text{(A135)}$$

But from Eq. A52, by definition,

$$\Delta\bar{\Delta} = s^4D\bar{D} + \frac{1}{k^2}N_1\bar{N}_1$$

whence the term in the inner parentheses in Eq. A135 becomes

$$s^4D\bar{D} + \frac{1}{k^2}N_1\bar{N}_1 - \frac{1}{k^2}N_1\bar{N}_1 = 0 \quad , \quad \text{for } s = 0 \qquad \text{(A136)}$$

REFERENCES FOR APPENDIX A

A1. Chang, S. S. L., Synthesis of Optimum Control Systems, McGraw-Hill, New York, 1961.

A2. McRuer, D., I. Ashkenas, and D. Graham, Aircraft Dynamics and Automatic Control, Princeton University Press, Princeton, N.J., 1973.

A3. Fortenbaugh, R. L., "Progress in Mathematical Modeling of the Operational Environment of DD Class 963 Ships," paper presented at AIAA Atmospheric Flight Mechanics Conference, Boulder, Colo., 1979.

A4. Anon., Military Specification — Flying Qualities of Piloted Airplanes, MIL-F08785B(ASG), 1969.

A5. Houbolt, J. C., "Atmospheric Turbulence," AIAA J., Vol. 11, No. 4, April 1973, pp. 421-437.

A6. Whitbeck, R. F., Wiener-Hopf Approaches to Regulator, Filter/Observer, and Optimal Coupler Problems, ONR Contract N00014-78-C-0391, Final Report, Systems Technology, Inc., 1980.

A7. Magdaleno, R. E., and J. Wolkovitch, Performance Criteria for Linear Constant-Coefficient Systems with Random Inputs, USAF ASD TR62-470, ASTIA 297805, 1962.

A8. Newton, G. C., L. A. Gould, and J. F. Kaiser, Analytical Design of Linear Feedback Controls, Wiley, New York, 1957.

APPENDIX B

SYSTEM PERFORMANCE WITH ZERO COST OF CONTROL

B.1 BASIC RELATIONSHIPS

The performance index is:

$$J = E(h_e^2) + k^2 E(\delta^2) \tag{B1}$$

For a nonminimum phase airframe J_{min} does not tend to zero as $k^2 \to 0$. The value of $E(h_e^2)$ achieved for $k^2 \to 0$ is of interest because it is the minimum possible mean square height error achievable with a single control δ.

With the same symbols employed in Appendix A, the total mean square height error is given by:

$$E(h_e^2) = \int^* (W_1 \phi_{RR} \overline{W}_1 + W_2 \phi_{dd} \overline{W}_2) \tag{B2}$$

where

$$\int^* (\ ) \quad \text{denotes} \quad \frac{1}{2\pi j} \int_{-j\infty}^{-j\infty} (\ )\, dj\omega$$

The mean control square control deflection is given by:

$$E(\delta^2) = \int^* (W_a \phi_{RR} \overline{W}_a + W_b \phi_{dd} \overline{W}_b) \tag{B3}$$

From Eq. A20

$$W_1 = 1 - G_1 W_a \tag{B4}$$

$$W_2 = -G_2 - G_1 W_b \tag{B5}$$

With $k^2 = 0$, from Eqs. A35 and A36,

$$\bar{G}_1 G_1 W_a \phi_{RR} - \bar{G}_1 \phi_{RR} = \psi_1 \tag{B6}$$

$$\bar{G}_1 G_1 W_b \phi_{dd} + \bar{G}_1 G_2 \phi_{dd} = \psi_2 \tag{B7}$$

Write G_1 as $G_1 = N\bar{Q}/D$, where $\bar{Q}$ is the product of all RHP factors, e.g.,

$$G_1 = \frac{K(s + a)(s - b)}{s^2(s^2 + 2\zeta\omega_n s + \omega_n^2)} \tag{B8}$$

where $N = K(s + a)$, $D = s^2(s^2 + 2\zeta\omega_n s + \omega_n^2)$, $\bar{Q} = (s - b)$. Then Eq. B7 can be written as:

$$\frac{\bar{Q}\bar{N}}{\bar{D}} \cdot \frac{QN}{D} \cdot W_a \cdot (\phi_{RR})^- (\phi_{RR})^+ - \frac{Q\bar{N}}{\bar{D}} \phi_{RR} = \psi_1 \tag{B9}$$

From Eq. A38

$$W_a = \frac{-D}{QN} \cdot \frac{1}{(\phi_{RR})^+} \left[\left(\frac{\bar{D}}{\bar{Q}\bar{N}} \right) \left(\frac{-\bar{N}Q}{\bar{D}} \right) \left(\frac{1}{(\phi_{RR})^-} \right) \right]_+ \tag{B10}$$

$$= \frac{-D}{QN} \frac{1}{(\phi_{RR})^+} \left[\frac{Q}{\bar{Q}} (\phi_{RR})^+ \right]_+ \tag{B11}$$

Whence

$$W_1 = 1 - G_1 W_a = 1 - \frac{\bar{Q}\cancel{N}}{\cancel{D}} \cdot \frac{\cancel{D}}{QN} \cdot \frac{1}{(\phi_{RR})^+} \left[\frac{Q}{\bar{Q}} (\phi_{RR})^+ \right]_+ \tag{B12}$$

$$= 1 - \frac{\bar{Q}}{Q} \frac{1}{(\phi_{RR})^+} \left[\frac{Q}{\bar{Q}} (\phi_{RR})^+ \right]_+ \tag{B13}$$

From Eq. A38,

$$W_b = \frac{-D}{QN} \cdot \frac{1}{(\phi_{dd})^+} \left[\frac{\bar{D}}{\bar{Q}\,\bar{N}} \cdot \frac{1}{(\phi_{dd})^-} \cdot \frac{\bar{N}Q}{\bar{D}}\ \phi_{dd} \right]_+ \tag{B14}$$

$$W_b = \frac{-D}{QN}\ \frac{1}{(\phi_{dd})^+} \left[\frac{Q}{\bar{Q}} \cdot G_2(\phi_{dd})^+ \right]_+ \tag{B15}$$

whence

$$W_2 = -G_2 + \frac{\bar{Q}}{Q} \cdot \frac{1}{(\phi_{dd})^+} \left[\frac{Q}{\bar{Q}} \cdot G_2(\phi_{dd})^+ \right]_+ \tag{B16}$$

B.2 EVALUATION OF MEAN SQUARE QUANTITIES

The contribution to $E(h_e^2)$ that comes from that part of h_e which is correlated with the command $E(h_e^2)_R$ is given by:

$$\phi_{RR} W_1 \bar{W}_1 = \phi_{rr} - \frac{\bar{Q}}{Q} \cdot (\phi_{RR})^- \left[\frac{Q}{\bar{Q}} \cdot (\phi_{RR})^+ \right]_+ - \frac{Q}{\bar{Q}} \cdot (\phi_{RR})^+ \left[\frac{\bar{Q}}{Q} \cdot (\phi_{RR})^- \right]_-$$

$$+ \left[\frac{Q}{\bar{Q}} \cdot (\phi_{RR})^+ \right]_+ \left[\frac{\bar{Q}}{Q} \cdot (\phi_{RR})^- \right]_- \tag{B17}$$

$$= \phi_{rr} - \bar{M}[M]_+ - M[\bar{M}]_- + [M]_+[\bar{M}]_- \tag{B18}$$

where

$$M = \frac{Q}{\bar{Q}} \cdot (\phi_{RR})^+$$

$$\int^* \phi_{RR} W_1 \bar{W}_1 = \int^* \Big(\phi_{RR} - \cancelto{0}{[\bar{M}]_+ [M]_+} - [\bar{M}]_- [M]_+ - [M]_+ [\bar{M}]_- - \cancelto{0}{[M]_- [\bar{M}]_-} + [M]_+ [\bar{M}]_- \Big) \tag{B19}$$

The terms marked $\cancelto{0}{\ }$ do not contribute to the integral since they have poles only in either the left or the right half plane. Hence:

$$E(h_e)_R^2 = \int^* \phi_{RR} W_1 \bar{W}_1 = \int^* \Big(\phi_{RR} - [M]_+ [\bar{M}]_- \Big) \tag{B20}$$

This can easily be evaluated by noting that $\phi_{RR} = M\bar{M}$, whence:

$$E(h_e)_R^2 = \int^* \Big([M]_+ + [M]_- \Big) \Big([\bar{M}]_+ + [\bar{M}]_- \Big) - [M]_+ [\bar{M}]_- \tag{B21}$$

$$= \int^* \Big(\cancelto{0}{[M]_+ [\bar{M}]_+} + [M]_+ [\bar{M}]_- + [M]_- [\bar{M}]_+ + \cancelto{0}{[M]_- [\bar{M}]_-} - [M]_+ [\bar{M}]_- \Big) \tag{B22}$$

$$= \int^* [M]_- [\bar{M}]_+ \triangleq \frac{1}{2\pi j} \int_{-j\infty}^{j\infty} \left[\frac{Q}{\bar{Q}} (\phi_{RR})^+ \right]_- \left[\frac{\bar{Q}}{Q} (\phi_{RR})^- \right]_+ d j\omega \tag{B23}$$

The above integral is simple to compute because typically $[(Q/\bar{Q})(\phi_{rr})^+]_+$ has only one denominator factor.

The second of the two contributions to $E(h_e)^2$ comes from that part of h_e which is correlated with the disturbance, $E(h_e^2)_d$, and is given by:

$$\phi_{dd}W_2\bar{W}_2 = \phi_{dd}G_2\bar{G}_2 - \bar{G}_2 \frac{\bar{Q}}{Q} (\phi_{dd})^- \left[\frac{Q}{\bar{Q}} G_2(\phi_{dd})^+\right]_+ - G_2 \frac{Q}{\bar{Q}} (\phi_{dd})^+ \left[\frac{\bar{Q}}{Q} \bar{G}_2(\phi_{dd})^-\right]_- + \left[\frac{Q}{\bar{Q}} G_2(\phi_{dd})^+\right]_+ \left[\frac{\bar{Q}}{Q} \bar{G}_2(\phi_{dd})^-\right]_- \quad \text{(B24)}$$

Put

$$L = \bar{G}_2 \frac{\bar{Q}}{Q} (\phi_{dd})^- \quad \text{(B25)}$$

$$\int^* \phi_{dd}W_2\bar{W}_2 = \int^* \left(L\bar{L} - \cancelto{0}{[L]_+[\bar{L}]_+} - [L]_+[\bar{L}]_- - [\bar{L}]_+[L]_- - \cancelto{0}{[\bar{L}]_-[L]_-} + [\bar{L}]_+[L]_- \right) \quad \text{(B26)}$$

$$= \int^* \left(L\bar{L} - [L]_+ [\bar{L}]_- \right) \quad \text{(B27)}$$

$$= \int^* \left([L]_+[\bar{L}]_- + \cancelto{0}{[L]_+[\bar{L}]_+} + [L]_-[\bar{L}]_+ + \cancelto{0}{[L]_-[\bar{L}]_-} - [L]_+[\bar{L}]_- \right) \quad \text{(B28)}$$

$$= \int^* [L]_+[\bar{L}]_- \quad \text{(B29)}$$

Thus the remaining contribution to the mean square error is:

$$E(h_e^2)_d = \int^* \left(\left[\frac{\bar{G}_2 \bar{Q} (\phi_{dd})^-}{Q} \right]_+ \left[\frac{G_2 Q (\phi_{dd})^+}{\bar{Q}} \right]_- \right) \tag{B30}$$

It is also of interest to compute the mean square control deflection associated with k = 0. This is given by:

$$E(\delta^2) = \int^* (W_a \phi_{RR} \bar{W}_a + W_b \phi_{dd} \bar{W}_b) \tag{B31}$$

The contribution to $E(\delta^2)$ that stems from the component of δ correlated with the command is:

$$E(\delta^2)_R = \phi_{RR} W_a \bar{W}_a = \int^* \left(\frac{D \bar{D}}{NQN\bar{Q}} \left[\frac{Q}{\bar{Q}} (\phi_{RR})^+ \right]_+ \left[\frac{\bar{Q}}{Q} (\phi_{RR})^- \right]_- \right) \tag{B32}$$

The remaining contribution, which stems from the component of δ correlated with the disturbance, is:

$$E(\delta^2)_d = \phi_{dd} W_b \bar{W}_b = \int^* \left(\frac{D \bar{D}}{NQN\bar{Q}} \left[\frac{Q}{\bar{Q}} G_2 (\phi_{dd})^+ \right]_+ \left[\frac{\bar{Q}}{Q} \bar{G}_2 (\phi_{dd})^- \right]_- \right) \tag{B33}$$

B.3 COMPUTATION OF RESULTS: MEAN SQUARE ERROR

Writing Eq. B23 in full:

$$E(h_e)_R^2 = \frac{1}{2\pi j} \int_{-j\infty}^{j\infty} \left[\frac{Q}{\bar{Q}} (\phi_{RR})^+\right]_- \left[\frac{\bar{Q}}{Q} (\phi_{RR})^-\right]_+ dj\omega \tag{B34}$$

The command spectrum is:

$$(\phi_{RR})^+ = \frac{818.9\ s^2}{(s + 6.3)^4} \tag{B35}$$

$$\frac{Q}{\bar{Q}} = \frac{-s - b}{s - b} = \frac{b + s}{b - s} \tag{B36}$$

$$\left[\frac{Q}{\bar{Q}} (\phi_{RR})^+\right]_- = \left[\frac{b + s}{b - s} \cdot \frac{818.9\ s^2}{(s + 6.3)^4}\right]_- = \frac{1}{b - s} \cdot \frac{2b(818.9)b^2}{(b + 6.3)^4} \tag{B37}$$

$$E(h_e)_R^2 = \left((818.9) \cdot \frac{2b^3}{(s + 6.3)^4}\right)^2 \cdot \frac{1}{2b} \tag{B38}$$

For the configurations of interest, we have:

Configuration	3GA	6GA	9GA
b	16.9799	21.7433	24.3630
$E(h_e)_R^2$ ft^2	21.944	17.0406	14.73

Writing Eq. B30 in full:

$$E(h_e)_d^2 = \frac{1}{2\pi j}\int_{-j\infty}^{j\infty}\left[\frac{\bar{G}_2\bar{Q}(\phi_{dd})^-}{Q}\right]_+\left[\frac{G_2Q(\phi_{dd})^+}{\bar{Q}}\right]_- dj\omega \tag{B39}$$

$$(\phi_{dd})^+ = \frac{14.043(s+4.5143)}{(s+7.819)^2} \tag{B40}$$

$$G_2 = \frac{R_{42}s + R_{43}}{s(s^2 + R_{34}s + R_{35})} \quad , \quad \frac{Q}{\bar{Q}} = \frac{b+s}{b-s} \tag{B41, B42}$$

$$\left[G_2\frac{Q}{\bar{Q}}(\phi_{dd})^+\right]_- = \left[\frac{R_{42}s+R_{43}}{s(s^2+R_{34}s+R_{35})}\cdot\frac{b+s}{1}\cdot\frac{14.043(s+4.513)}{(s+7.819)^2}\right]_{s=b}\frac{1}{b-s} \tag{B43}$$

$$= \frac{(R_{42}b+R_{43})2b\cdot 14.043(b+4.5143)}{b(b^2+R_{34}b+R_{35})(b+7.819)^2(b-s)} \tag{B44}$$

$$E(h_e)_d^2 = \left\{\frac{28.0876(R_{42}b+R_{43})(b+4.5143)}{(b^2+R_{34}b+R_{35})(b+7.819)^2}\right\}^2\cdot\frac{1}{2b} \tag{B45}$$

For all the configurations of interest we have:

Configuration	3GA	6GA	9GA
R_{42}	1.2276	2.2904	3.1404
R_{43}	1.0017216	3.31879	6.155184
R_{34}	1.7606	3.2372	4.4166
R_{35}	14.8089	37.79935527	63.83748685
b	16.9799	21.7433	24.3630
$E(h_e)_d^2$, ft^2	0.00012212	0.00013692	0.00014698

AD-A096 450 AERONAUTICAL CONSULTANT ASSOCIATES RANCHO PALOS VERDES CA F/G 16/4
APPLICATION OF THE JOINED WING TO CRUISE MISSILES.(U)
NOV 80 J WOLKOVITCH N00014-79-C-0953
UNCLASSIFIED ONR-CR212-266-1 NL

3 of 3
AD
A096450

END
DATE FILMED
4-81
DTIC

B.4 COMPUTATION OF RESULTS: MEAN SQUARE CONTROL DEFLECTION

Writing Eq. B32 in full:

$$E(\delta^2)_R^2 = \frac{1}{2\pi j} \int_{-j\infty}^{j\infty} \frac{D}{NQ} \left[\frac{Q}{\overline{Q}} (\phi_{RR})^+\right]_+ \cdot \frac{\overline{D}}{\overline{N}\,\overline{Q}} \left[\frac{\overline{Q}}{Q} (\phi_{RR})^-\right]_- dj\omega \tag{B46}$$

First, let us evaluate $[(Q/\overline{Q})(\phi_{RR})^+]_+$

$$\left[\frac{Q}{\overline{Q}} (\phi_{RR})^+\right]_+ = \frac{Q}{\overline{Q}} (\phi_{RR})^+ - \left[\frac{Q}{\overline{Q}} (\phi_{RR})^+\right]_- \tag{B47}$$

$$= \frac{b+s}{b-s} \cdot \frac{818.9\ s^2}{(s+6.3)^4} - \frac{818.9 \cdot 2b^3}{(b+6.3)^4} \cdot \frac{1}{b-s} \tag{B48}$$

$$= \frac{818.9}{(b-s)} \cdot \frac{1}{(s+6.3)^4} \left\{s^3 + bs^2 - \frac{2b^3}{(b+6.3)^4} (s+6.3)^4\right\} \tag{B49}$$

$$= \frac{818.9}{(b-s)(s+6.3)^4(b+6.3^4)} \left\{(s^3+bs^2)(b+6.3^4) - 2b^3(s+6.3)^4\right\} \tag{B50}$$

Put 6.3 = c. Then it can be shown that the (b - s) factor cancels, giving:

$$\left[\frac{Q}{\overline{Q}} (\phi_{RR})^+\right]_+ = \frac{-818.9\left\{-2b^3s^3 + [-b^4 - 4cb^3 + 6c^2b^2 + 4c^3b + c^4]s^2 + [8c^3b^2 + 2c^4b]s + 2c^4b^2\right\}}{(s+6.3)^4(b+c)^4} \tag{B51}$$

Note that this expression is third/fourth order in s.

To compute $E(\delta_R)_R^2$ the following quantity is required.

$$\frac{D}{NQ} \cdot \left[\frac{Q}{\bar{Q}} (\phi_{RR})^+\right]_+ = \frac{s(s^2 + 2\zeta\omega_n s + \omega_n^2)(818.92b^3s^2 + \cdots)}{(s+a)(s+b)(s+6.3)^4(b+6.3)^4} \tag{B52}$$

But since this expression has a numerator which is sixth order in s and a denominator which is also sixth order in s the corresponding integral $E(\delta_R)_R^2$ is unbounded. This is a consequence of the particular forms of G_1 and $(\phi_{RR})^+$ selected here. Within the limits of the short-period airframe dynamics approximation the form of G_1 is fixed, hence D/NQ must have a third order numerator and a second order denominator. To obtain a finite $E(\delta)_R^2$ it is thus necessary for $(\phi_{RR})^+$ to have a denominator which is of $(n+2)$th order, where n is the order of the numerator of $(\phi_{RR})^+$. This could be done by introducing a high-frequency break in the ϕ_{RR} spectrum.

From Eq. B33:

$$E(\delta^2)_d = \frac{1}{2\pi j} \int_{-j\infty}^{j\infty} W_2 \phi_{dd} \bar{W}_2 \, dj\omega \tag{B53}$$

But

$$W_2 = -G_2 + \frac{\bar{Q}}{Q} \frac{1}{(\phi_{dd})^+} \left[\frac{Q}{\bar{Q}} G_2 (\phi_{dd})^+\right]_+ \tag{B54}$$

$$G_2 = \frac{R_{42}s + R_{43}}{s(s^2 + 2\zeta\omega_n s + \omega_n^2)} = \frac{R_{42}s + R_{43}}{s(s^2 + R_{34}s + R_{35})} \tag{B55}$$

$$(\phi_{dd})^+ = \frac{14.0438(s + 4.5143)}{(s + 7.819)^2} \tag{B56}$$

$$(\phi_{dd})^{+}W_2 = -(\phi_{dd})^{+}G_2 + \frac{\bar{Q}}{Q}\left[\frac{Q}{\bar{Q}}\,G_2(\phi_{dd})^{+}\right]_{+} \tag{B57}$$

$$\int^{*}\phi_{dd}W_2\bar{W}_2 = \int^{*}\left(\phi_{dd}G_2\bar{G}_2 - (\phi_{dd})^{+}G_2\left[\frac{\bar{Q}}{Q}\,\bar{G}_2(\phi_{dd})^{-}\right]_{+}\right.$$

$$- (\phi_{dd})^{-}\bar{G}_2\,\frac{\bar{Q}}{Q}\left[\frac{Q}{\bar{Q}}\,G_2(\phi_{dd})^{+}\right]_{-}$$

$$\left. + \left[\frac{Q}{\bar{Q}}\,G_2(\phi_{dd})^{+}\right]_{+}\left[\frac{\bar{Q}}{Q}\,G_2(\phi_{dd})^{-}\right]_{-}\right) \tag{B58}$$

$$= \int^{*}\phi_{dd}G_2\bar{G}_2 - \left[\frac{Q}{\bar{Q}}\,G_2(\phi_{dd})^{+}\right]_{-}[\text{c.c.}]_{+} - \left[\frac{\bar{Q}}{Q}\,\bar{G}_2(\phi_{dd})^{-}\right]_{+}[\text{c.c.}]_{-}$$

$$+ \left[\frac{Q}{\bar{Q}}\,G_2(\phi_{dd})^{+}\right]_{+}\left[\frac{\bar{Q}}{Q}\,G_2(\phi_{dd})^{-}\right]_{-} \tag{B59}$$

where [c.c.] denotes the complex conjugate of the immediately preceding term in [ ]. Hence:

$$\int^{*}\phi_{dd}W_2\bar{W}_2 = \int^{*}\left(\phi_{dd}G_2\bar{G}_2 - \left[\frac{\bar{Q}}{Q}\,\bar{G}_2(\phi_{dd})^{-}\right]_{+}[\text{c.c.}]_{-}\right) \tag{B60}$$

To evaluate this expression note that:

$$\phi_{dd}{}^{+}G_2 = \frac{14.0438(s+4.5143)(R_{42}s+R_{43})}{(s+7.819)^2(s)(s^2+R_{34}s+R_{35})} = \frac{\text{2nd order}}{(s)(\text{4th order})} \tag{B70}$$

Note also that:

$$\left[\frac{\bar{Q}}{Q} G_2(\phi_{dd})^-\right]_+ = \frac{1}{s+b}\left\{\frac{2b(-R_{42}b+R_{43})(-b+4.5143)}{(-b)(b^2-R_{34}b+R_{35})(-b+7.819)^2}\right\} = \frac{\text{Constant}}{\text{1st order}} \tag{B71}$$

Hence $E(\delta^2)_d$ is unbounded, due to the free s in the denominator of $\phi_{dd}{}^+G_2$.

To obtain a finite $E(\delta^2)_d$ it would be necessary to modify the low-frequency end of the Dryden atmospheric turbulence spectrum, i.e., to replace

$$(\phi_{dd})^+ = \frac{14.0438(s + 4.5143)}{(s + 7.819)^2} \tag{B72}$$

by

$$(\phi_{dd})^+ = \frac{s}{(s + h)} \cdot \frac{14.0438(s + 4.5143)}{(s + 7.819)^2} \tag{B73}$$

where h is a small frequency (e.g., 0.1 rad/sec).

APPENDIX C

PROGRAM LISTINGS

```
 01♦LBL "OCT"
RCL 35  2  *  RCL 34
X↑2  -  STO 03  RCL 41
RCL 31  X↑2  *  RCL 33
X↑2  +  STO 02  RCL 31
RCL 33  *  3  *  RCL 32
X↑2  -  RCL 41  *
STO 01  RCL 33  X↑2
RCL 41  *  STO 00
XEQ "POLY"  END
```

PRP "QP"

```
 01♦LBL "QP"
RCL 01  RCL 03  +  -2  *
PRX  RCL 01  RCL 03  *
4  *  RCL 06  +  RCL 05
+  PRX  RCL 05  RCL 03
*  RCL 06  RCL 01  *  +
-2  *  PRX  RCL 05
RCL 06  *  PRX  END
```

PRP "AB"

```
 01♦LBL "AB"
-6.3  STO 00  RCL 01  *
RCL 02  -  RCL 00  +
RCL 03  +  STO 14
RCL 00  X↑2  *  STO 13
RCL 00  RCL 06  -
RCL 00  *  RCL 07  +
RCL 00  *  RCL 08  -
RCL 00  *  RCL 09  +
STO 10  1/X  RCL 13  *
STO 17  RCL 00  4  *
RCL 06  3  *  -  RCL 00
*  RCL 07  2  *  +
RCL 00  *  RCL 08  -
STO 11  RCL 00  12  *
RCL 06  6  *  -  RCL 00
*  RCL 07  2  *  +
STO 12  RCL 00  24  *
RCL 06  6  *  -  STO 13
RCL 01  2  *  RCL 00  *
RCL 02  -  STO 15
RCL 00  X↑2  *  RCL 00
RCL 14  *  2  *  +
RCL 17  RCL 11  *  -
RCL 10  /  STO 10
RCL 11  *  2  *  CHS
RCL 17  RCL 12  *  -
RCL 01  RCL 00  X↑2  *
2  *  +  RCL 00  RCL 15
*  4  *  +  RCL 14  3  *
+  RCL 10  /  2  /
STO 16  RCL 11  *  6  *
CHS  RCL 10  RCL 12  *
3  *  -  RCL 17  RCL 13
*  -  RCL 01  RCL 00  *
3  *  RCL 15  +  6  *  -
RCL 10  /  6  /  STO 15
RCL 00  CHS  STO 00
RCL 15  STO 10  RCL 00
*  3  *  RCL 16  +
STO 11  RCL 00  X↑2  3
*  RCL 15  *  RCL 00
RCL 16  *  2  *  +
RCL 10  -  STO 12
RCL 00  X↑2  RCL 00  *
RCL 15  *  RCL 00  X↑2
RCL 16  *  +  RCL 00
RCL 18  *  +  RCL 17  +
STO 13  25.2  STO 20
238.14  STO 21  1000.188
STO 22  1575.8961
STO 23  RCL 20  RCL 06
+  STO 24  RCL 21
RCL 06  RCL 20  *  +
RCL 07  +  STO 25
RCL 22  RCL 06  RCL 21
*  +  RCL 07  RCL 20  *
+  RCL 08  +  STO 26
RCL 23  RCL 06  RCL 22
*  +  RCL 07  RCL 21  *
+  RCL 08  RCL 20  *  +
RCL 09  +  STO 27
RCL 06  RCL 23  *
RCL 07  RCL 22  *  +
RCL 08  RCL 21  *  +
RCL 09  RCL 20  *  +
STO 28  RCL 07  RCL 23
*  RCL 08  RCL 22  *  +
RCL 09  RCL 21  *  +
STO 29  RCL 08  RCL 23
*  RCL 09  RCL 22  *  +
STO 30  RCL 09  RCL 23
*  STO 31  3.8.9  ENTER♦
RCL 41  *  STO 32
RCL 10  *  STO 33
RCL 11  RCL 04  RCL 10
*  +  RCL 32  *  STO 34
RCL 12  RCL 04  RCL 11
*  +  RCL 05  RCL 10  *
+  RCL 33  *  STO 35
RCL 13  RCL 04  RCL 12
*  +  RCL 05  RCL 11  *
+  RCL 32  *  STO 36
RCL 04  RCL 13  *
RCL 05  RCL 12  *  +
RCL 33  *  STO 37
RCL 05  RCL 13  *
RCL 32  *  STO 38  0
STO 39  STO 40  RCL 20
STO 42  RCL 21  STO 43
RCL 02  STO 44  RCL 03
STO 45  RCL 04  STO 46
RCL 05  STO 47  RCL 06
STO 48  RCL 07  STO 49
RCL 11  STO 50  RCL 12
STO 51  RCL 13  STO 52
RCL 14  STO 53  RCL 15
STO 54  RCL 16  STO 55
PRREG  STOP  XROM "INTG"
PRX  END
```

PRP "BC"

```
 01♦LBL "WBC"
7.818  STO 11  2  *
STO ..  RCL 11  X↑2
STO ..  RCL 04  RCL 10
-  STO 12  RCL 05
RCL 10  RCL 04  *  +
RCL 11  +  STO 13
RCL 10  RCL 05  *
RCL 11  RCL 04  *  +
STO 10  RCL 11  RCL 05
*  STO 11  RCL 42
RCL 01  *  STO 14
RCL 43  RCL 01  *
RCL 02  RCL 42  *  -
STO 15  RCL 42  RCL 03
*  RCL 43  RCL 02  *  -
```

```
STO 16  RCL 43  RCL 33
*  STO 17  4.5143
STO 18  RCL 15  RCL 13
RCL 14  *  +  STO 20
RCL 16  RCL 18  RCL 15
*  +  STO 15  RCL 17
RCL 18  RCL 16  *  +
STO 16  RCL 18  RCL 17
*  STO 17  RCL 09  /
STO 19  CHS  RCL 14  +
STO 14  RCL 19  RCL 06
*  RCL 20  +  STO 20
RCL 15  RCL 07  RCL 19
*  -  STO 15  RCL 16
RCL     RCL 19  *  +
ST      RCL 11  1/X
STO 17  RCL 10  RCL 11
X↑2  /  CHS  STO 18
RCL 16  X↑2  RCL 11
RCL 13  *  -  RCL 11
X↑2  /  RCL 11  /
STO 21  RCL 16  *
RCL 18  RCL 15  *  +
RCL 17  RCL 20  *  +
STO 20  RCL 16  RCL 16
*  RCL 15  RCL 17  *  +
STO 15  RCL 16  RCL 17
*  STO 16  RCL 17
RCL 09  *  STO 22
RCL 08  RCL 17  *  CHS
RCL 09  RCL 18  *  +
STO 23  RCL 17  RCL 07
*  RCL 18  RCL 08  *  -
RCL 21  RCL 09  *  +
STO 21  RCL 12  RCL 06
+  CHS  STO 24  RCL 07
RCL 13  -  STO 25
RCL 10  RCL 08  +  CHS
STO 26  RCL 09  RCL 11
-  STO 27  1  ENTER↑
RCL 22  -  STO 28
RCL 06  RCL 12  RCL 22
*  +  CHS  STO 29
RCL 07  RCL 13  RCL 22
*  -  STO 30  RCL 08
RCL 10  RCL 22  *  +
CHS  STO 31  RCL 23  CH
STO 32  RCL 23  RCL 12
*  RCL 22  +  CHS  1  +
STO 33  RCL 13  RCL 23
*  RCL 06  +  RCL 12
RCL 22  *  +  CHS
STO 34  RCL 07  RCL 10
RCL 23  *  -  RCL 13
RCL 22  *  -  STO 35
RCL 21  CHS  STO 36
RCL 12  RCL 21  *
RCL 23  +  CHS  STO 37
1  ENTER↑  RCL 13
RCL 21  *  -  RCL 12
RCL 23  *  -  RCL 22  -
STO 38  RCL 06  RCL 10
RCL 21  *  +  RCL 13
RCL 23  *  +  RCL 12
RCL 22  *  +  CHS
STO 39  RCL 14  RCL 10
RCL 20  *  -  RCL 13
RCL 15  *  -  RCL 12
RCL 16  *  -  STO 10
RCL 13  RCL 20  *  CHS
RCL 12  RCL 15  *  -
RCL 16  -  STO 11
RCL 15  CHS  RCL 12
RCL 20  *  -  STO 12
RCL 20  CHS  STO 13
RCL 29  *  RCL 12
RCL 28  *  -  RCL 24
RCL 29  *  RCL 28
RCL 25  *  -  STO 15  /
STO 16  RCL 24  RCL 12
*  RCL 25  RCL 13  *  -
RCL 15  /  STO 17
RCL 29  RCL 32  *
RCL 28  RCL 33  *  -
RCL 15  /  STO 12
RCL 33  RCL 24  *
RCL 25  RCL 32  *  -
RCL 15  /  STO 13
RCL 29  RCL 36  *
RCL 28  RCL 37  *  -
RCL 15  /  STO 14
RCL 24  RCL 37  *
RCL 25  RCL 36  *  -
RCL 15  /  STO 15
RCL 31  *  CHS  RCL 14
RCL 27  *  -  RCL 39  +
STO 23  RCL 35  RCL 27
RCL 12  *  -  RCL 31
RCL 13  *  -  STO 21
RCL 34  RCL 26  RCL 12
*  -  RCL 36  RCL 13  *
-  STO 20  RCL 38
RCL 26  RCL 14  *  -
RCL 30  RCL 15  *  -
STO 22  RCL 11  RCL 26
RCL 16  *  -  RCL 30
RCL 17  *  -  STO 11
RCL 10  RCL 27  RCL 16
*  -  RCL 31  RCL 17  *
-  STO 10  RCL 20
RCL 23  *  RCL 21
RCL 22  *  -  STO 24
RCL 23  RCL 11  *
RCL 22  RCL 10  *  -
RCL 24  /  STO 25
RCL 20  RCL 10  *
RCL 21  RCL 11  *  -
RCL 24  /  STO 10
RCL 25  STO 11  RCL 16
RCL 12  RCL 11  *  -
RCL 14  RCL 10  *  -
STO 14  RCL 17  RCL 13
RCL 11  *  -  RCL 15
RCL 10  *  -  STO 12
RCL 14  STO 13  RCL 19
STO 14  7.819  STO 16  2
*  STO 15  RCL 16  X↑2
STO 16  RCL 06  RCL 15
+  STO 20  RCL 07
RCL 15  RCL 06  *  +
RCL 16  +  STO 21
RCL 08  RCL 15  RCL 07
*  +  RCL 16  RCL 06  *
+  STO 22  RCL 09
RCL 15  RCL 08  *  +
RCL 16  RCL 07  *  +
STO 23  RCL 15  RCL 09
*  RCL 16  RCL 08  *  +
STO 24  RCL 16  RCL 09
*  STO 25  RCL 41
14.0438  *  CHS  STO 15
RCL 13  *  STO 26
RCL 12  RCL 15  *
STO 27  RCL 11  RCL 15
*  STO 28  RCL 10
RCL 15  *  STO 29
RCL 14  RCL 15  *
STO 30  0  STO 31
020.031  XEQ "PRREGX"
PRX  END
```

PRP "I8N"

```
 01♦LBL "I8N"
STO 11  RCL 11  X↑2
STO 12  RCL 33  CHS  *
RCL 35  +  RCL 12  *
RCL 37  -  RCL 12  *
RCL 39  +  RCL 11  *
STO 13  RCL 36  RCL 12
RCL 34  *  -  RCL 12  *
RCL 38  -  RCL 12  *
RCL 40  +  RCL 13  R-P
STO 14  RCL 12  RCL 25
-  RCL 12  *  RCL 27  +
RCL 12  *  RCL 29  -
RCL 12  *  RCL 31  +
STO 15  RCL 26  RCL 12
RCL 24  *  -  RCL 12  *
RCL 28  -  RCL 12  *
RCL 30  +  RCL 11  *
RCL 15  R-P  STO 16
RCL 14  RCL 16  /  X↑2
RTN  END
```

PRP "DE"

```
 01♦LBL "DE"
0.0  STO 33  818.9
STO 34  RCL 48  RCL 41
RCL 10  *  RCL 43  *  -
RCL 34  *  STO 35
RCL 43  RCL 50  *
RCL 44  RCL 10  *  +
RCL 41  *  CHS  RCL 49
+  RCL 34  *  STO 36
RCL 43  RCL 51  *
RCL 44  RCL 50  *  +
RCL 45  RCL 10  *  +
RCL 41  *  CHS  RCL 08
+  RCL 34  *  STO 37
RCL 43  RCL 52  *
RCL 44  RCL 51  *  +
RCL 45  RCL 50  *  +
RCL 41  *  CHS  RCL 09
+  RCL 34  *  STO 38
RCL 44  RCL 52  *
RCL 45  RCL 51  *  +
RCL 41  *  CHS  RCL 34
*  STO 39  RCL 41
RCL 45  *  RCL 52  *
RCL 34  *  CHS  STO 40
PRREG  STOP  XROM "INTG"
PRX  END
```

```
 01♦LBL "W3C"
4.5143  STO 15  RCL 42
*  RCL 43  +  STO 16
RCL 42  STO 17  RCL 15
RCL 43  *  STO 15
RCL 17  RCL 06  *
RCL 16  +  STO 18
RCL 17  RCL 07  *
RCL 16  RCL 06  *  +
RCL 15  +  STO 19
RCL 17  RCL 08  *
RCL 16  RCL 07  *  +
RCL 15  RCL 06  *  +
STO 26  RCL 17  RCL 09
*  RCL 16  RCL 08  *  +
RCL 15  RCL 07  *  +
STO 27  RCL 16  RCL 09
*  RCL 15  RCL 08  *  +
STO 16  RCL 15  RCL 09
*  STO 15  RCL 01
RCL 13  *  RCL 41  *
RCL 17  -  STO 17
RCL 01  RCL 12  *
RCL 02  RCL 13  *  +
RCL 41  *  RCL 18  -
STO 18  RCL 01  RCL 11
*  RCL 02  RCL 12  *  +
RCL 03  RCL 13  *  +
RCL 41  *  RCL 19  -
STO 19  RCL 01  RCL 10
*  RCL 02  RCL 11  *  +
RCL 03  RCL 12  *  +
RCL 41  *  RCL 26  -
STO 26  RCL 01  RCL 14
*  RCL 02  RCL 10  *  +
RCL 03  RCL 11  *  +
RCL 41  *  RCL 27  -
STO 27  RCL 02  RCL 14
*  RCL 03  RCL 10  *  +
RCL 41  *  RCL 16  -
STO 16  RCL 03  RCL 14
*  RCL 41  *  RCL 15  -
STO 15  XEQ "PRX"
RCL 26  STO 43  RCL 27
STO 42  0  STO 06
STO 07  STO 08  STO 09
STO 10  STO 11  STO 12
STO 13  STO 14  RCL 05
RCL 25  *  STO 31
RCL 04  RCL 25  *
RCL 24  RCL 05  *  +
STO 30  RCL 25  RCL 04
RCL 24  *  +  RCL 05
RCL 23  *  +  STO 29
RCL 24  RCL 04  RCL 23
*  +  RCL 05  RCL 22  *
+  STO 28  RCL 23
RCL 04  RCL 22  *  -
RCL 05  RCL 21  *  +
STO 27  RCL 22  RCL 04
RCL 21  *  +  RCL 05
RCL 20  *  +  STO 26
RCL 21  RCL 04  RCL 20
*  +  RCL 05  +  STO 25
RCL 20  RCL 04  +
STO 24  0  STO 41
14.0438  STO 15  RCL 16
*  STO 40  RCL 15
RCL 42  *  STO 39
RCL 15  RCL 43  *
STO 38  RCL 19  RCL 15
*  STO 37  RCL 18
RCL 15  *  STO 36
RCL 17  RCL 15  *
STO 35  0  STO 34
STO 33  024.040  PRREGX
STOP  XEQ "INTG"  END
```

```
 01♦LBL "I8N"
STO 11  RCL 11  X↑2
STO 12  RCL 26  RCL 12
*  RCL 28  -  RCL 12  *
RCL 30  +  RCL 11  *
STO 13  RCL 27  RCL 12
*  RCL 29  -  RCL 13  *
RCL 31  +  RCL 13  R-P
STO 14  RCL 20  RCL 12
*  RCL 22  -  RCL 12  *
RCL 24  +  RCL 11  *
STO 15  RCL 21  RCL 12
-  RCL 12  *  RCL 23  -
RCL 12  *  RCL 25  +
RCL 15  R-P  1/X  RCL 14
*  X↑2  RTN  END
```

POLY
Z11/K
INTG

ARE STANDARD
HP 41c MATHPACK
ROUTINES

DISTRIBUTION LIST

	Copies
Office of Naval Research 800 N. Quincy Street Arlington, VA 22217	
Attn: ONR 438	2
210	3
200	1
100M	1
Chief of Naval Operations Washington, D. C. 20350	
Attn: OP-506	1
OP-225	1
OP-354	1
OP-951G	1
OP-954D	1
OP-982E	1
Chief of Naval Material Washington, D. C. 20360	
Attn: NAVMAT 08T2	1
NAVMAT 071	1
NAVMAT 07C1	1
Naval Sea Systems Command Washington, D. C. 20362	
Attn: NAVSEA 63R	1
NAVSEA 63X2	1
NAVSEA 62ZB	1
NAVSEA 62Z4	1
Naval Air Systems Command Washington, D. C. 20361	
Attn: NAVAIR 530	1
NAVAIR 03PA	1
NAVAIR 320	1
NAVAIR 950D	1
PMA 242	1
PMA 258	1
Project Manager Joint Cruise Missile Project Office Department of the Navy Washington, D. C. 20361	
Attn: JCM-0011	1

	Copies
Technical Library Naval Surface Weapons Center Dahlgren Laboratory Dahlgren, VA 23448	2
National Academy of Sciences 2101 Constitution Avenue, NW Washington, D. C. 20418 Attn: Naval Studies Board	1
Assistant Secretary of the Navy (Research, Engineering & Ststems) Pentagon, Room 5E787 Washington, D. C. 20350	1
Office of Under Secretary of Defense for Research and Engineering (Naval Warfare) Pentagon, Room 3D1048 Washington, D. C. 20301	1
Defense Technical Information Center Cameron Station, Bldg 5 5010 Duke Street Alexandria, VA 22314	12
Director, Air Vehicles Technology Office Defense Advanced Research Projects Agency 1400 Wilson Boulevard Arlington, VA 22209	1
Commander David W. Taylor Naval Ship Research and Development Center Bethesda, MD 20084	1
Library Naval Postgraduate School Monterey, CA 93940	1
Commander Naval Weapons Center China Lake, CA 93555	1

DISTRIBUTION LIST (Continued)

	Copies
Technical Library Naval Missile Center Point Mugu, CA 93042	1
Director National Aeronautics and Space Administration Ames Research Center Moffett Field, CA 94035	1
Director National Aeronautics and Space Administration Langley Research Center Hampton, VA 23365	1
Director National Aeronautics and Space Administration 21000 Brooke Park Road Cleveland, OH 44135	1
Director Air Force Flight Dynamics Laboratory (ASD/ENFDH) Wright-Patterson AFB Dayton, OH 45433	1
Commander Air Force Aeronautical Systems Division Wright-Patterson AFB Dayton, OH 45433	1